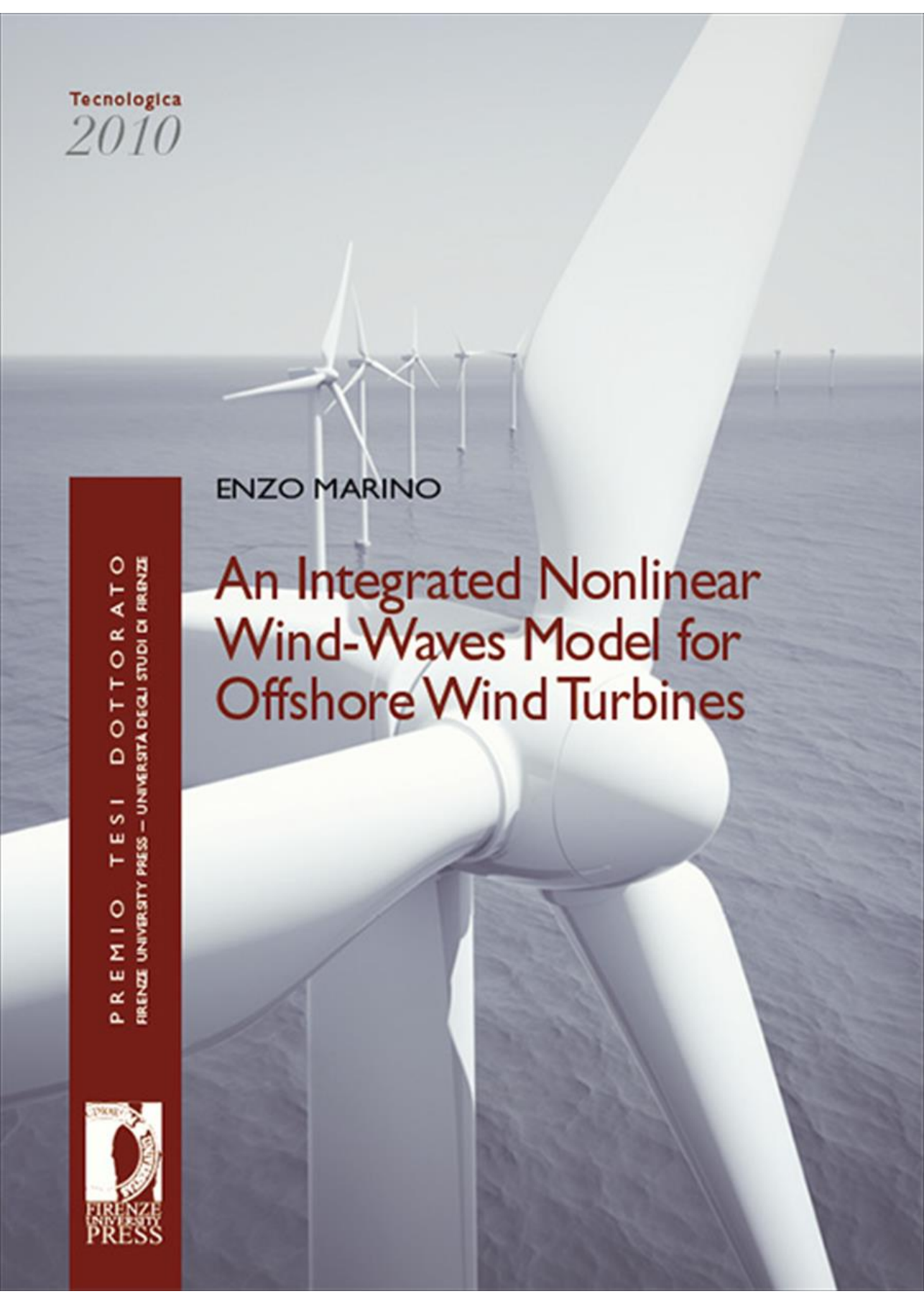

Tecnologica
2010

ENZO MARINO

An Integrated Nonlinear Wind-Waves Model for Offshore Wind Turbines

PREMIO TESI DOTTORATO
FIRENZE UNIVERSITY PRESS – UNIVERSITÀ DEGLI STUDI DI FIRENZE

FIRENZE UNIVERSITY PRESS

PREMIO FIRENZE UNIVERSITY PRESS
TESI DI DOTTORATO

– 22 –

COLLANA PREMIO TESI DI DOTTORATO
Commissione giudicatrice, anno 2010

Luigi Lotti, *Facoltà di Scienze Politiche* (Presidente della Commissione)

Fortunato Tito Arecchi, *Facoltà di Scienze MFN*
Vincenzo Collotti, *Facoltà di Lettere e Filosofia*
Paolo Felli, *Facoltà di Architettura*
Ada Fonzi, *Facoltà di Psicologia*
Pelio Fronzaroli, *Facoltà di Lettere e Filosofia*
Roberto Genesio, *Facoltà di Ingegneria*
Ferrando Mantovani, *Facoltà di Giurisprudenza*
Mario Pio Marzocchi, *Facoltà di Farmacia*
Salvo Mastellone, *Facoltà di Scienze della Formazione*
Adolfo Pazzagli, *Facoltà di Medicina e Chirurgia*
Giancarlo Pepeu, *Facoltà di Medicina e Chirurgia*
Franco Scaramuzzi, *Facoltà di Agraria*
Piero Tani, *Facoltà di Economia*
Fiorenzo Cesare Ugolini, *Facoltà di Agraria*

Enzo Marino

An integrated nonlinear wind-waves model for offshore wind turbines

Firenze University Press
2011

An integrated nonlinear wind-waves model for offshore wind turbines / Enzo Marino. – Firenze : Firenze University Press, 2011.
(Premio FUP. Tesi di dottorato ; 22)

http://digital.casalini.it/978866550532

ISBN 978-88-6655-051-8 (print)
ISBN 978-88-6655-053-2 (online)

Immagine di copertina: © Zentilia | Dreamstime.com

Università degli Studi di Firenze
Firenze University Press
Borgo Albizi, 28
50122 Firenze, Italy
http://www.fupress.com/

Printed in Italy

Acknowledgments

I wish to express my gratitude to my advisors Professor Claudio Borri and Professor Udo Peil for their support, suggestions and tutoring activity.

I am deeply grateful to Dr. Ing. Claudio Lugni, (CNR–INSEAN, Rome) for the extraordinary help he offered me in the development of the numerical model. I learned a lot from him and I will never forget those intense days spent at INSEAN.

A sincere thank goes to Jason Jonkman (NREL, Colorado) for being always so kind in giving me the full support in using FAST. Interfacing the model developed in the thesis with FAST would have not been possible without his help.

I am also particularly grateful to Professor Hocine Oumeraci for his crucial and encouraging suggestions and to Professor Gianni Bartoli for the very helpful discussions.

My gratefulness is finally addressed to all the people I met during this unique experience of the joint doctoral course University of Florence–TU-Braunschweig. The months spent in Braunschweig, the people I knew, the friendships grown during these three years significantly enriched my personality and now they all are part of me.

November 14, 2011

Enzo Marino

Enzo Marino, *An integrated nonlinear wind-waves model for offshore wind turbines*
ISBN 978-88-6655-051-8 (print) ISBN 978-88-6655-053-2 (online)

Contents

Enzo Marino, *An integrated nonlinear wind-waves model for offshore wind turbines*
ISBN 978-88-6655-051-8 (print) ISBN 978-88-6655-053-2 (online)

List of Figures

Enzo Marino, *An integrated nonlinear wind-waves model for offshore wind turbines*
ISBN 978-88-6655-051-8 (print) ISBN 978-88-6655-053-2 (online) © 2011 Firenze University Press

List of Tables

Enzo Marino, *An integrated nonlinear wind-waves model for offshore wind turbines*
ISBN 978-88-6655-051-8 (print) ISBN 978-88-6655-053-2 (online) © 2011 Firenze University Press

List of Algorithms

Enzo Marino, *An integrated nonlinear wind-waves model for offshore wind turbines*
ISBN 978-88-6655-051-8 (print) ISBN 978-88-6655-053-2 (online)

Abstract

This thesis presents a numerical model capable of simulating offshore wind turbines exposed to extreme loading conditions. External condition-based extreme responses are reproduced by coupling a fully nonlinear wave kinematic solver with a hydro-aero-elastic simulator.

First, a two–dimensional fully nonlinear wave simulator is developed. The transient nonlinear free surface problem is formulated assuming the potential theory and a higher-order boundary element method (HOBEM) is implemented to discretize Laplace's equation. For temporal evolution a second-order Taylor series expansion is used. The code, after validation with experimental data, is successfully adopted to simulate overturning plunging breakers which give rise to dangerous impact loads when they break against wind turbine substructures. The impact force is quantified by means of an analytical model and the total hydrodynamic action is finally obtained by adding the impulsive term to the drag and inertial ones.

In the second main core of the thesis, emphasis is placed on the random nature of the waves. Indeed, a global simulation framework embedding the numerical wave simulator into a more general stochastic environment is developed. Namely, first a linear irregular sea is generated by the spectral approach, then, only on critical space–time sub-domains, the fully nonlinear solver is invoked for a more refined simulation. The space–time sub–domains are defined as the wind turbine near field (space) times the time interval in which wave impacts are expected (time). Such a domain decomposition approach permits systematically accounting for dangerous effects on the structural response (which would be totally missed by adopting linear or weakly nonlinear wave theories alone) without penalizing the computational effort normally required.

At the end of the work the attention is moved to the consequences that the proposed model would have in the quantification of the structural risk.

Enzo Marino, *An integrated nonlinear wind-waves model for offshore wind turbines*
ISBN 978-88-6655-051-8 (print) ISBN 978-88-6655-053-2 (online) © 2011 Firenze University Press

Sommario

In questa tesi viene proposto un nuovo modello numerico in grado di simulare turbine eoliche in mare esposte a condizioni ambientali estreme. Le simulazioni, ottenute per via diretta (i.e. a partire da azioni estreme stabilite a priori fissando il periodo di ritorno), accoppiano un modello numerico di propagazione del moto ondoso con un solutore idro-aero-elastico dell'intero sistema.

Inizialmente viene sviluppato il modello numerico bidimensionale e completamente non–lineare di propagazione dell'onda formulato assumendo un flusso a potenziale. L'equazione di Laplace ad esso associata viene risolta numericamente attraverso il metodo degli elementi al contorno di ordine elevato (HOBEM). L'evoluzione temporale del moto viene effettuata implementando una serie di Taylor fino al secondo ordine. Il software, validato con dati sperimentali, è così in grado di riprodurre onde frangenti fino al rientro del getto. La forza di impatto, quantificata mediante un modello analitico, viene poi aggiunta alle componenti inerziale e di trascinamento in modo da stimare l'azione idrodinamica complessiva.

La seconda fase del lavoro è dedicata allo sviluppo di un modello di simulazione globale finalizzato alla integrazione del suddetto solutore numerico in un ambiente del tutto stocastico. In particolare, dapprima una mare lineare irregolare viene generato con approccio spettrale. Successivamente, solo su sotto–domini critici, i.e. nell'intorno della turbina e per intervalli di tempo in cui i frangimenti sono attesi, il simulatore non–lineare viene lanciato per un'analisi più raffinata. Questa strategia di decomposizione del dominio permette di mettere in conto in modo sistematico quegli effetti impulsivi, che verrebbero altrimenti ignorati dai modelli lineari, senza penalizzare lo sforzo computazionale normalmente richiesto.

Infine, il lavoro si chiude mostrando le ripercussioni che il modello proposto può avere in termini di affidabilità e sicurezza strutturale.

Enzo Marino, *An integrated nonlinear wind-waves model for offshore wind turbines*
ISBN 978-88-6655-051-8 (print) ISBN 978-88-6655-053-2 (online) © 2011 Firenze University Press

Kurzfassung

In dieser Arbeit wird ein numerisches Modell zur Simulation von Offshore-Windenergieanlagen unter extremen Lasteinwirkungen entwickelt. Dazu wird ein vollständig kinematisch nichtlineares Wellenmodell mit einem hydroaeroelastischen Modell kombiniert.

Zunächst wird das instationäre nichtlineare Problem der freien Wasseroberfläche unter Verwendung der zweidimensionalen Potentialtheorie beschrieben. Die sich ergebende Laplace-Gleichung wird mit einer Randelementmethode höherer Ordnung räumlich diskretisiert. Für die zeitliche Entwicklung wird eine Taylor Reihe zweiter Ordnung verwendet. Nach Abgleichung mit experimentellen Daten wird der entwickelte Algorithmus angewendet, um die für die Stoßbelastung von Windkraftanlagen ursächlichen überschlagenden brechenden Wellen zu simulieren. Die gesamte hydrodynamische Last wird schließlich durch ein analytisches Modell beschrieben, bei dem ein Term, der die Stoßwirkung der Wellen berücksichtigt, zu den Längs- und Trägheitskräften hinzugefügt wird.

Im zweiten Teil der Arbeit wird das Wellenmodell in eine Simulationsumgebung eingebettet, welche die stochastischen Natur des Wellengangs erfasst. Hierbei wird zuerst ein linear beschriebener breitbandiger Seegang mithilfe des Spektralansatzes erzeugt. Beschränkt auf kritische Bereiche in der räumlichen und zeitlichen Simulation wird im Anschluss das vollständig nichtlineare hydrodynamische Modell für eine genauere Lösung herangezogen. Die kritischen Bereiche sind auf die nähere Umgebung der Windenergieanlage beim Eintreffen der brechenden Welle begrenzt. Diese Substrukturtechnik erlaubt es, für die Strukturantwort maßgebende Effekte systematisch zu erfassen, die bei einer Verwendung von linearen oder schwach nichtlinearen Wellentheorien komplett vernachlässigt werden, ohne dabei den herkömmlichen Rechenaufwand substantiell zu erhöhen.

Zum Abschluss der Arbeit wird diskutiert, wie sich das vorgestellte Modell auf die Quantifizierung des Risikos der Struktur auswirkt.

Enzo Marino, *An integrated nonlinear wind-waves model for offshore wind turbines*
ISBN 978-88-6655-051-8 (print) ISBN 978-88-6655-053-2 (online) © 2011 Firenze University Press

Chapter1
Introduction

This introductive chapter presents the framework of the thesis and outlines the motivations and the organization of the work.

At the beginning it also tries to give a global view about the wind energy market with the aim of pointing out that research on (offshore) wind energy is nowadays truly crucial.

1.1 Wind energy

To introduce the topic of this thesis and to get a broader idea about the global energy system, it could be useful to start with some preliminary notions about the current worldwide and European energy consumption status as well as the objectives in matter of greenhouse gas emissions[1].

Only starting by clarifying the objectives and, above all, the departing point for each country, it is possible to understand how important is nowadays to invest research sources in wind energy.

1.1.1 European and world energy scenario

During the last decade with no doubt wind energy has been representing the leading renewable energy source. And, according to government plans, it will keep being the leading renewable source for many years.

The worldwide energy scenario is represented in figures 1.1 and 1.2 which show the global annual wind power installed capacity in the period 1996–2008 and the annual wind power capacity installed by region, respectively.

Wind power is the fastest growing power generation technology in the EU with more than 35% of all new energy installations in 2008. It is also interesting to note from figure 1.2 that European wind energy installation has been leading the global installation since 2003.

Figure 1.3 shows that in 2008 wind energy installation was definitely dominating other energy sources. Indeed, only in this year, upon a total installed capacity of 23.851 GW in Europe, approximately one third was represented by wind anergy.

Almost 8.9 GW of new wind turbines installed in 2008 brought European wind power generation capacity up to nearly 66 GW. Another promising sign, see figure 1.4, is the diversification of the European market. 2008, in fact, saw a much more balanced expansion with not negligible contributions given by Italy, France and the UK.

[1] Data and statistics here presented are all update to 2008. Currently, official data from EWEA and GWEC for 2010 are not yet available.

Enzo Marino, *An integrated nonlinear wind-waves model for offshore wind turbines*
ISBN 978-88-6655-051-8 (print) ISBN 978-88-6655-053-2 (online) © 2011 Firenze University Press

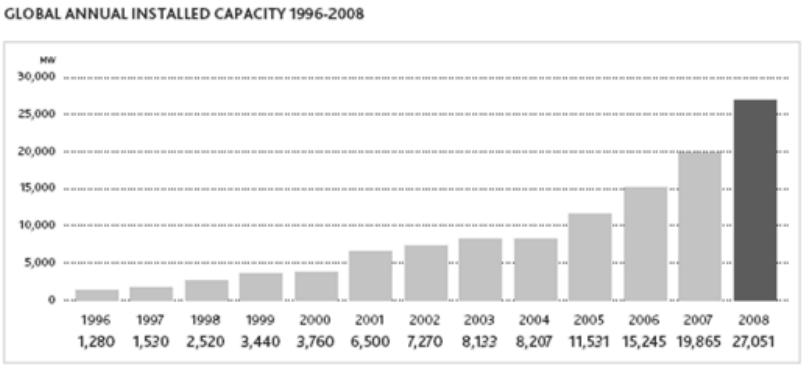

Figure 1.1: Global annual wind power installed capacity, 1996-2008.

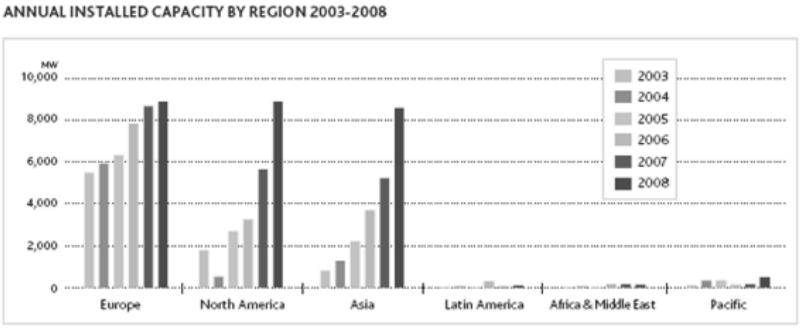

Figure 1.2: Annual wind power installed capacity by region, 2003-2008.

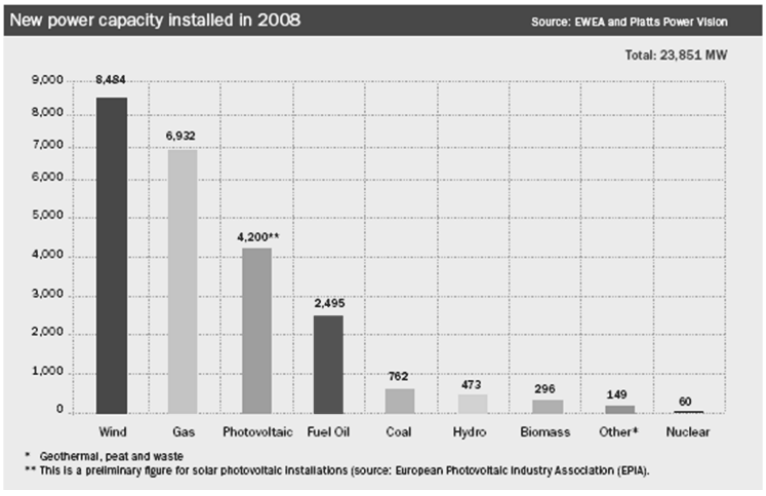

Figure 1.3: New power capacity installed in Europe in 2008.

However, Germany continues to be Europe's leading market, both in terms of new and total installed capacity. To confirm this, figure 1.4 shows that over 1.6 GW of new capacity was installed in 2008 and this brought the total German capacity up to nearly 24 GW.

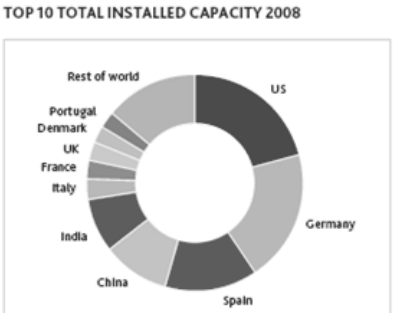

	MW	%
USA	25,170	20.8
Germany	23,903	19.8
Spain	16,754	13.9
China	12,210	10.1
India	9,645	8.0
Italy	3,736	3.1
France	3,404	2.8
UK	3,241	2.7
Denmark	3,180	2.6
Portugal	2,862	2.4
Rest of world	16,693	13.8
Total top 10	**104,104**	**86.2**
World total	**120,798**	**100.0**

	MW	%
USA	8,358	30.9
China	6,300	23.3
India	1,800	6.7
Germany	1,665	6.2
Spain	1,609	5.9
Italy	1,010	3.7
France	950	3.5
UK	836	3.1
Portugal	712	2.6
Canada	526	1.9
Rest of world	3,285	12.2
Total top 10	**23,766**	**87.8**
World total	**27,051**	**100.0**

Figure 1.4: Top 10 global capacity installed, total and in 2008.

As reported in [15], it is also worth mentioning that among the growing European markets in 2008, Italy experienced a significant leap: over 1 GW of new wind turbines came on line in 2008, bringing the total installed capacity up to 3.7 GW.

A more detailed map about the cumulative installed capacity state by state is given in figure 1.5.

	Installed in 2008	**Cumulative, end of 2008**
Total EU-27	8484 MW	64 935 MW
of which Offshore	357 MW	1471 MW

Table 1.1: European wind power capacity.

As shown in table 1.1, at the end of 2008, there were 65 GW of wind power capacity installed in the EU-27 producing 142 TWh hours of electricity which satisfies 4.2% of the whole EU electricity demand. This means that at the moment offshore wind energy is able to satisfy only 0.1% of the whole EU demand. This datum makes more understandable how challenging are the targets fixed by EU which will be shortly recalled in the next section.

Figure 1.5: State by state cumulative installed capacity at the end of 2008.

In 2008 US wind industry was able to install 8.36 GW marking an increase in generating capacity of 50% in a single calendar year. The 2008 US growth represented about 42% of new electricity generating capacity added in the United States during the year, establishing wind as a mainstream energy source for the country (second only to natural gas) in new generating capacity. US total wind generating capacity in 2008 was more than 25.17 GW, producing enough electricity to power the equivalent of close to 7 million households and to meet over 1% of total US electricity demand.

1.1.2 Short and long term objectives

Focusing on the European situation, in the Strategic Research Agenda (SRA) - a document prepared by the Wind Technological Platform (TPWind) in 2008 - fundamental objectives in matter of wind energy development have been fixed. They are divided into:

Short term targets: within 2020 reduction of greenhouse gas emission by 20% and ensure 20% of renewable energy sources in the EU;

Long term targets: decarbonization, 60 - 80% reduction of the greenhouse gas emission.

To meet the 2020 targets, among many other research lines, for the European Commission it is imperative to:

> "Double the power generation capacity of the largest wind turbines, with offshore wind as the lead application."

In particular for the offshore wind, the Strategic Research Agenda establishes the following special objectives to be achieved within 2030:

- More than 10% of Europe's electricity should come from offshore wind;
- Make the offshore generating costs competitive with other sources of power generation;
- Make commercially mature the technology for sites at any distance from shore with a water depth up to 50 m:
- Full–scale proven technology to dominate deep–water sites.

Moreover, together with the above targets, five research topics have been prioritized:

- Substructures;
- Assembly, installation and decommissioning;
- Electrical infrastructure;
- Turbines;
- Operations and maintenance;

With respect to on land standard designs, the offshore environment does introduce significant additional elements which have to be carefully considered, especially in designing the support structures. Knowledge about modeling the wind and rotor aerodynamics developed for onshore sites are generally enough and do not need deep changes when moving in the offshore environment. Some adjustments are made just due to the different wind characteristics of offshore sites (e.g. strong difference in the roughness length and turbulence intensity). Figure 1.6 gives an example of different wind shears for on– and off–shore sites, respectively.

On the contrary, for offshore plants, the concept of support structure has to be entirely rearranged. For this reason research on the substructure is always prioritized both directly, by improving the technology itself, and indirectly, that is by developing more accurate models to estimate the combined wind–waves action. In fact, in addition to the previous research topics, the Strategic Research Agenda establishes also the following priorities:

- Development of fully integrated wind–wave–current interaction models;
- Development of new substructure concepts;
- Development of improved design methodologies to extend the life of structures, to reduce costs and to incorporate risk-based life-cycle approaches.

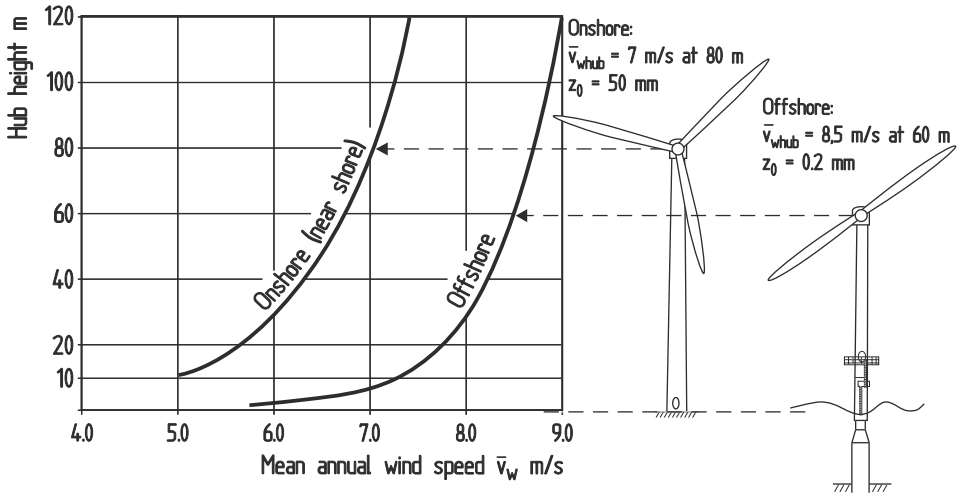

Figure 1.6: Typical wind shears for land and offshore sites. Figure from [1].

Consider that only the substructure represents approximately 25% of the whole investment and if we think that forces (and consequently costs) used to design the substructure increase with the square of wind/water velocity, then it appears clear the importance of accurate models for loads prediction.

The objectives described above for wind energy development are based on the central fact that Europe has a remarkable wind potential. Figure 1.7 shows the map of onshore wind potential. Considering that the minimum value of the mean wind speed to make cost–effective a wind power plant is approximately 4 m/s, it results that most of the European areas possess a wind energy potential.

The offshore potential is depicted in figure 1.8, which shows that in addition to the North and Baltic Seas, also some Mediterranean areas, for example between Greek and Italian coasts, the wind resource can be exploited.

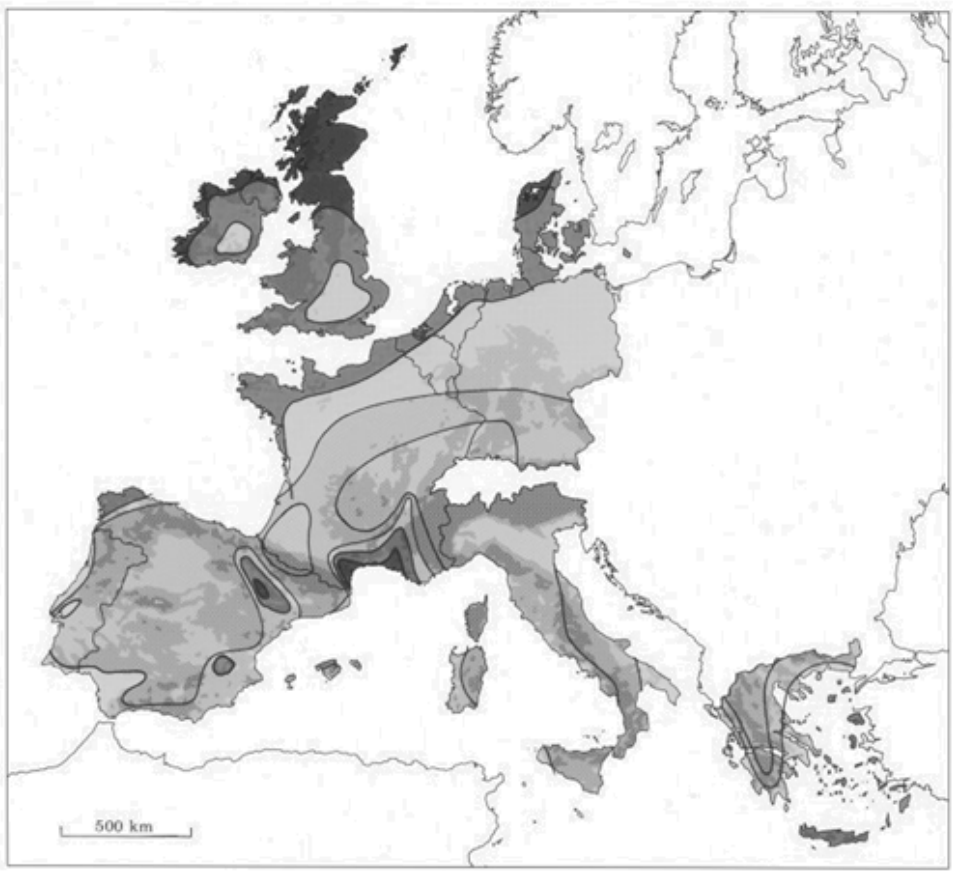

Wind resources[1] at 50 metres above ground level for five different topographic conditions

	Sheltered terrain[2]		Open plain[3]		At a sea coast[4]		Open sea[5]		Hills and ridges[6]	
	$m\,s^{-1}$	Wm^{-2}	$m\,s^{-1}$	Wm^{-2}	$m\,s^{-1}$	Wm^{-2}	$m\,s^{-1}$	Wm^{-2}	$m\,s^{-1}$	Wm^{-2}
	> 6.0	> 250	> 7.5	> 500	> 8.5	> 700	> 9.0	> 800	> 11.5	> 1800
	5.0-6.0	150-250	6.5-7.5	300-500	7.0-8.5	400-700	8.0-9.0	600-800	10.0-11.5	1200-1800
	4.5-5.0	100-150	5.5-6.5	200-300	6.0-7.0	250-400	7.0-8.0	400-600	8.5-10.0	700-1200
	3.5-4.5	50-100	4.5-5.5	100-200	5.0-6.0	150-250	5.5-7.0	200-400	7.0- 8.5	400- 700
	< 3.5	< 50	< 4.5	< 100	< 5.0	< 150	< 5.5	< 200	< 7.0	< 400

Figure 1.7: Onshore wind potential. European Wind Atlas. Copyright 1989 by Risø-National Laboratory, Roskilde, Denmark.

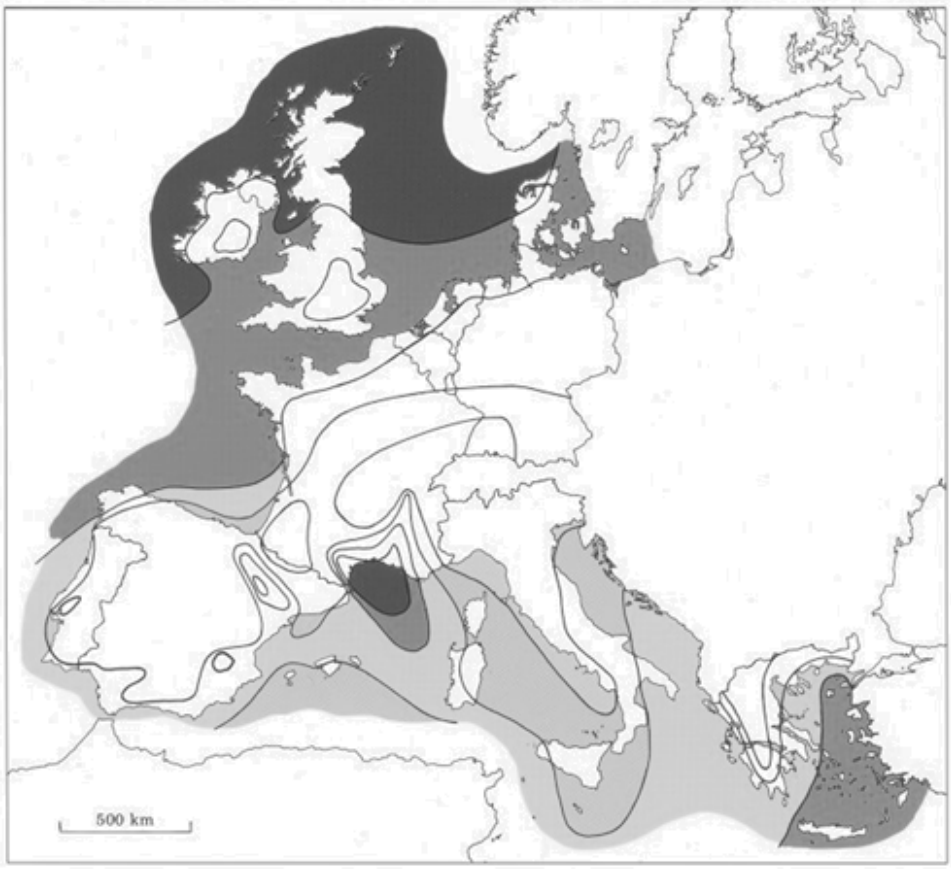

Wind resources over open sea (more than 10 km offshore) for five standard heights

	10 m		25 m		50 m		100 m		200 m	
	$m\,s^{-1}$	Wm^{-2}	$m\,s^{-1}$	Wm^{-2}	$m\,s^{-1}$	Wm^{-2}	$m\,s^{-1}$	Wm^{-2}	$m\,s^{-1}$	Wm^{-2}
	> 8.0	> 600	> 8.5	> 700	> 9.0	> 800	> 10.0	> 1100	> 11.0	> 1500
	7.0-8.0	350-600	7.5-8.5	450-700	8.0-9.0	600-800	8.5-10.0	650-1100	9.5-11.0	900-1500
	6.0-7.0	250-300	6.5-7.5	300-450	7.0-8.0	400-600	7.5- 8.5	450- 650	8.0- 9.5	600- 900
	4.5-6.0	100-250	5.0-6.5	150-300	5.5-7.0	200-400	6.0- 7.5	250- 450	6.5- 8.0	300- 600
	< 4.5	< 100	< 5.0	< 150	< 5.5	< 200	< 6.0	< 250	< 6.5	< 300

Figure 1.8: Offshore wind potential. European Wind Atlas. Copyright 1989 by Risø-National Laboratory, Roskilde, Denmark.

1.2 General nomenclature

Before entering further into the topic of this thesis, it would be useful to provide some general terminology which will be frequently used throughout the text. Figures 1.9 and 1.10 help in this task.

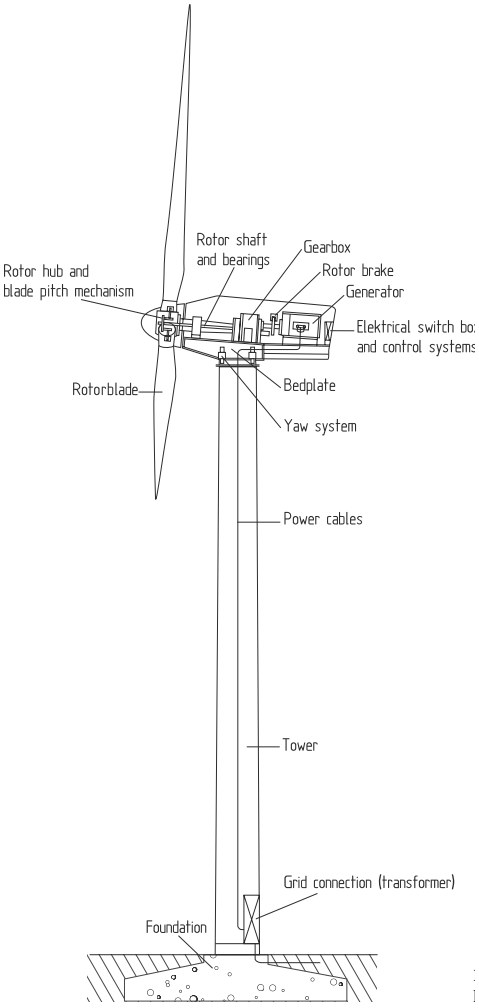

Figure 1.9: Main components of an horizontal axis wind turbine. Figure from [1].

Figure 1.9 in particular shows the essential components of the upper part of the wind turbine. It is referred to an onshore case with a superficial foundation. On the contrary, figure 1.10 provides more details about the substructure, which is defined as the structural subpart included between the sea bed and the platform. Among the three types of substructures sketched in the figure, the so called "monopile", the first from the left, is the one supporting the baseline reference model adopted in this work.

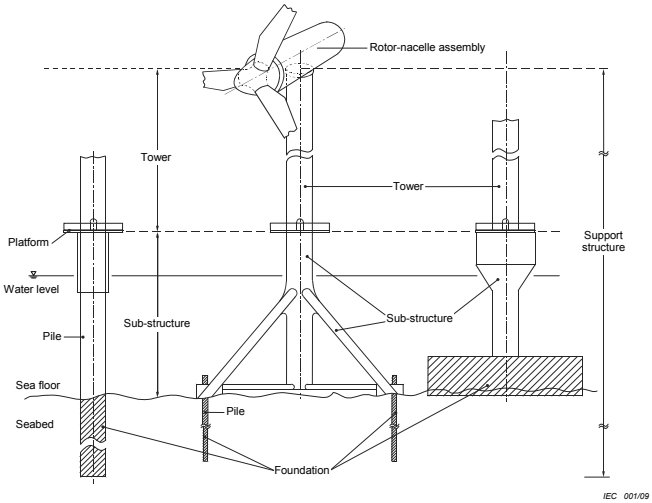

Figure 1.10: Main components of the support structures of an horizontal axis offshore wind turbine. Figure from IEC61400-3 [2].

Figure 1.11: Offshore wind farm Utgrunden off the southern Swedish North–Sea coast (7 wind turbines of 1.5 MW each).

An example of a wind farm made of monopile supported wind turbines is shown in figure 1.11.

1.3 Modeling offshore wind turbines

Together with the general motivations regarding the global need in boosting wind energy production, there are some more technical lines of reasoning which justify the research on offshore wind turbine.

Offshore wind turbines are very sophisticated systems that can be only analyzed by adopting integrated multi–physic models. There are four coupled disciplines involved: aerodynamics, structural dynamics, hydrodynamics, soil dynamics. Each of them relates to the rotor, the tower, the substructure, the foundation, respectively. Figure 1.12 tries to sketch this concept, indeed, moving from right to left, the four isolated subjects are applied to the four main parts of an offshore wind turbine and thus coupled into a unique system which should render the reality as much as possible.

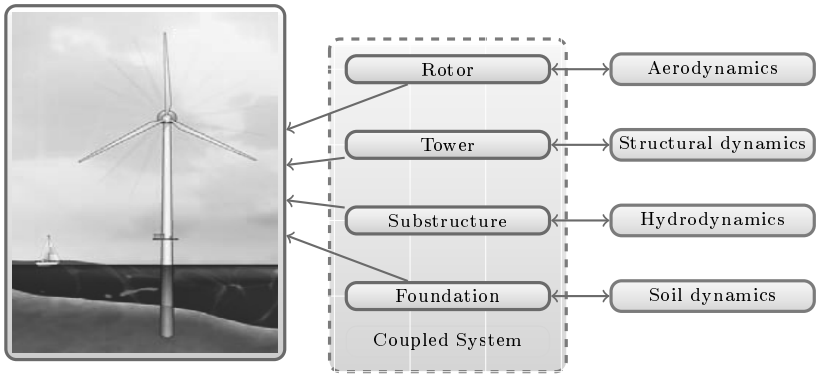

Figure 1.12: Coupled disciplines in a unique system.

The current standard technique to analyze and design offshore wind turbines starts from a real structure (or from a scheme if one is to design it) and, once all the structural and mechanical properties are known, the designer collects the system and environmental variables so that it is possible to provide input data for adequate numerical simulations.

In the present case, the time domain solver used is FAST, which gets the aerodynamic loads acting on the rotor blades by invoking AeroDyn, see scheme in figure 1.13. Both solvers have been developed at National Renewable Energy Laboratory (NREL). In some cases, however, solvers for simulating wind turbines implement some additional hydrodynamic routines which provide the wave kinematics and accordingly the hydrodynamic forces to reproduce also the offshore environment. The linear wave theory, together with Morison's equation, is commonly implemented and this permits to simulate most of the condition that a wind turbine may experience during operation. In fact, looking at the green rectangles in figure 1.13, it is clear that when the aim is to predict state of failure induced by long term fatigue accumulation, or more in general for all those cases characterized by relatively small wind speeds, this procedure is sufficient.

On the contrary, there are design load conditions characterized by extreme wind which in turn generates severe highly nonlinear waves that cannot be modeled by the

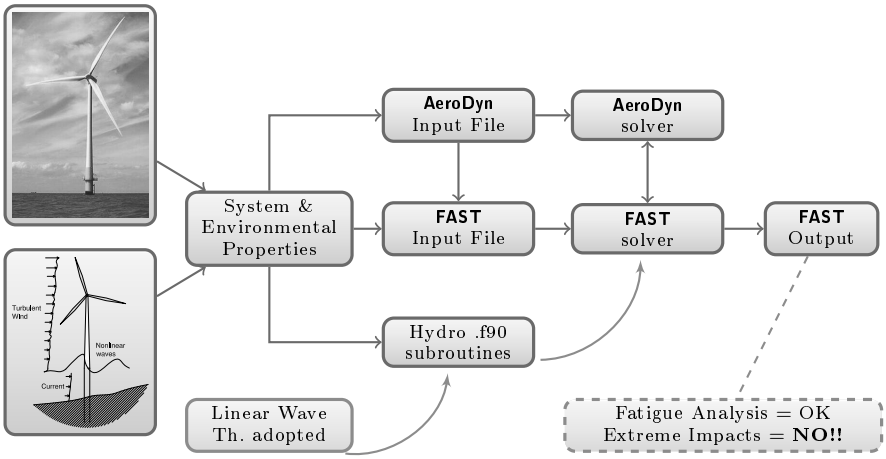

Figure 1.13: Commonly adopted scheme for offshore wind turbines simulations.

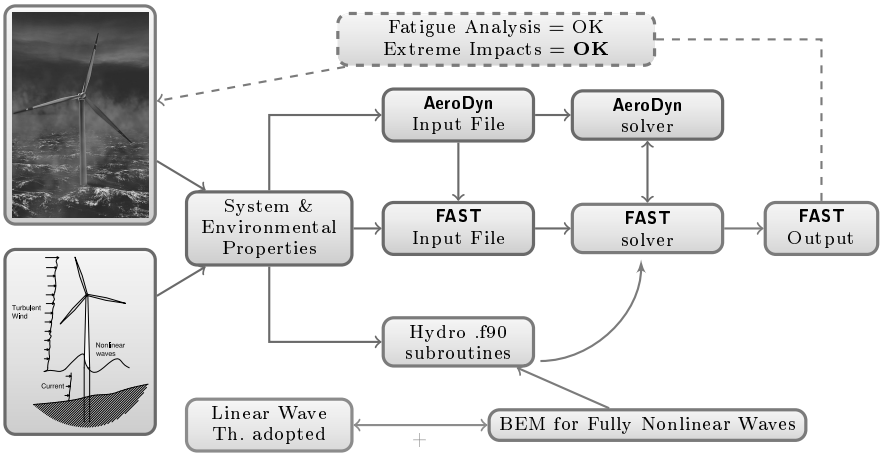

Figure 1.14: Proposed scheme for offshore wind turbines simulations capable of capturing both fatigue state of failure and ultimate limit states associated with extreme wind–waves actions.

linear theory anymore. Later on it will be also shown that for really extreme wind conditions also the most common (weakly) nonlinear wave theories are not sufficient when phenomenal events, such as plunging breaking waves, occur. Therefore, the simulation scheme alone sketched in figure 1.13 is no longer valid.

For this reason the present thesis attempts to give a contribution to fill the gap, so that, as highlighted by the red rectangles of figure 1.14, an improved hydrodynamic model is provided with the aim of setting up and advanced numerical simulator able to reproduce not only irregular linear random seas associate with the normal wind conditions, but also extreme winds which can give rise to very dangerous and destructive phenomena for an offshore wind turbine such as impacts due to plunging breakers.

1.4 Structure and scope of the thesis

The thesis is articulated in four main parts. After this introductory chapter, which attempts to point out both the general and scientific motivations of the whole work, firstly the general Risk Management Chain is tailored on the specific features characterizing offshore wind systems. The crucial point which is stressed in this context lies in the fact that any design of wind energy converters must always assure a certain minimum system reliability level. Therefore, to estimate the probability of failure of such systems, a systematic procedure needs to be applied.

Chapters 3, 4, and 5, as sketched in scheme 1.15, are devoted to the development of a new numerical code whose importance in terms of structural safety will be remarked in the concluding Chapter 6.

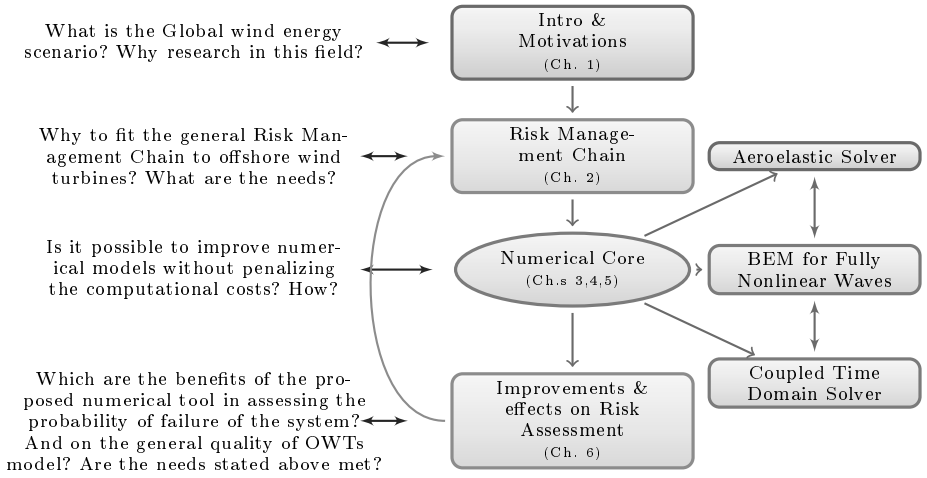

Figure 1.15: Scheme of the work. Blue: state of the art, red: development of a new numerical tool; green: initial targets and improvements evaluation.

Figure 1.15 helps to understand the structure of the work. The central column denotes the main parts of the thesis. Each of these parts tries to provide an answer to the key questions stated on the left–hand side. The blue elements in scheme 1.15 denote either what concerns the state of the art or anything which has been only

used in the present work but not investigated. The red parts (the ellipse and the two related sub-cores), on the contrary, refer to parts which have been either entirely developed (as the case of the Boundary Element code for fully nonlinear water waves simulation) or improved and embedded into a new design tool. Finally, the green rectangles represent the motivation and objectives achieved. In particular, Chapter 2 rises some issues concerning the structural risk of offshore wind turbines, then Chapter 6, by using results of the central core, attempts to answer the questions.

Chapter2
The risk management chain of offshore wind turbines

This chapter has the scope of applying the general probabilistic risk management chain to investigate the probability of failure of offshore wind turbines.

2.1 Cost and structural safety

In accordance with the new research lines in the field of offshore wind energy emphasized in the introductory chapter, fully probabilistic based design procedures are more and more necessary and desirable. However, it must be remarked that even the most sophisticated probabilistic model will return unsatisfactory results when the physical model being simulated is not well reflected in the numerical idealization.

As already anticipated, the major needs for offshore systems today are represented by novel design procedures, e.g. structural optimization, which assure the minimization of the costs under the constraint, among others, of a fixed *Structural Reliability* (SR). The latter is regarded as the probability that the structure under consideration exhibits a proper performance throughout its lifetime. The definition itself intrinsically contains a very sensitive point: what does it mean "proper performance"? A closer look at this issue will be taken in the next section.

Minimizing costs under a fixed *Structural Reliability* level can be thought as a constrained optimization problem

$$Cost\left(\bar{X}\right) \rightarrow \min \tag{2.1}$$

$$SR\left(\bar{X}\right) > SR^{*} \tag{2.2}$$

where $\bar{X}$ is the vector collecting all design variables involved both on the loading side and the structural strength side, while SR^{*} is the minimum acceptable structural safety level.

Establishing the lower structural reliability level SR^{*} mostly concerns cost–benefit analysis and lies beyond the goals of this work. On the contrary, the optimization problem shown in equations (2.1) and (2.2) highlights how strongly the cost reduction is linked to a proper estimation of SR. This concept results even clearer by recalling the general principle that the better the SR is evaluated, the larger its expected value [16].

Therefore, since SR is never an absolute measure - it considerably depends on many factors, such as the accuracy level of the idealized structural model, the number of uncertainties and their statistics, etc. - in this thesis the attention is most paid to restrict as much as possible the sources of uncertainties solely to those parameters which are intrinsically random (aleatory uncertainties) by providing a

Enzo Marino, *An integrated nonlinear wind-waves model for offshore wind turbines*
ISBN 978-88-6655-051-8 (print) ISBN 978-88-6655-053-2 (online) © 2011 Firenze University Press

more accurate numerical tool to account for the extreme hydrodynamic actions due to overturning breaking waves. It will be presented, in fact, a numerical model which, without assuming any *a priori* restriction about the magnitude of water waves nonlinearity, reduces the model uncertainties, especially those deriving from modeling the loads.

2.2 The risk management framework

More analytically, it is possible to quantify the structural reliability as $SR = 1 - P_f$ where P_f denotes the probability of failure of the *system*, or the Element at Risk (EaR), under consideration. Hence, the issue opened above concerning when it is possible to say that a structure is exhibiting a proper performance and when not, has now simply been shifted to determine the probability of failure of the *system*.

The difficult task of determining the probability of failure, especially when the *system* is very articulated as in the case of offshore wind turbines, can only be carried out by invoking a proved and systematic approach which is usually referred to as *Risk Management Process* [3], [17], [18], [19] [20].

As already mentioned, such a general approach needs to be adapted depending on the specific application. In fact, it might happen that not all the phases characterizing the *Process* are of primary interest for the current application.

The first level subdivision of the whole risk management framework is made up of the three following crucial steps [3]:

1. Risk Identification;
2. Risk Assessment;
3. Risk Treatment;

The first step, *Risk Identification*, is decisive for all the remaining procedure. In this phase the *system* must be declared and the sources of all possible *hazards* menacing the *system* should be carefully identified. In the present case the *system* could be represented by a group of components of which an offshore wind turbine is made. For example, one could focus on the rotor blades, the nacelle (including all the electrical and mechanical components such as generator, gear box, brake system, etc.), the tower and finally the foundation.

However, in the case being investigated in this thesis the *system* is represented by the tower and the performance we are interested in is its capability of safely carry all the loads acting on the entire structure. This choice is justified by the fact that since extreme environmental conditions are simulated, the rotor is always in the parked condition so that an ultimate load case condition will always involve primarily the support structure[1].

The threat which may endanger the *system* is represented by a combined wind–waves action. As in this work we only consider wind–generated waves, in the hazard identification we distinguish a "driver" (main) hazard, represented by the wind and a "driven" (induced) hazard represented by the waves. Note that this distinction

[1] In future the effects of the foundation should also be considered, but in the current application the monopile is considered rigidly connected to the sea bed.

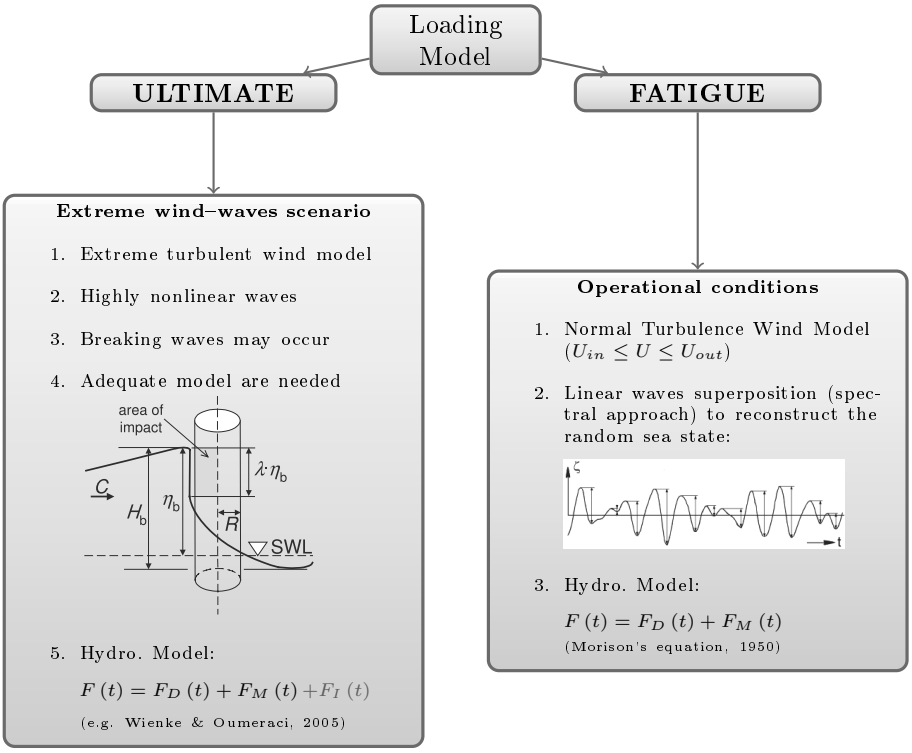

Figure 2.1: Schematic representation of the two main loading conditions an offshore wind turbine may experience. Different failure types have to be investigated with different tools.

by no means should lead to believe that waves are less dangerous or secondary in terms of load intensity compared with the wind.

These two hazards are not statistically independent and thus in the subsequent phase, *Risk Assessment*, the correlated multi–hazard scenario needs to be carefully analyzed.

The *Risk Identification* phase ends only when it is possible to answer the following question: given the system, what is the possible state of failure that it may experience? Figure 2.1 helps to answer this question. Indeed, the first most important distinction has to be made between ultimate failure condition and long-term damage accumulation failure. What is crucial to stress is that not only different statistics are involved depending on the failure type under investigation, but also the way of modeling the actions has to be be properly adjusted.

It is known that offshore structures are basically exposed to wind, wave and current loads, see the schematic representation in figure 2.2, and they may fail because of two different loading conditions: (i) extreme wind coupled with highly nonlinear extreme waves, which lead to the so called ultimate failure condition and (ii) long term fatigue accumulation that gives raise to the growth of cracks [21]. In general the fatigue failure results from the accumulation of damage induced by fluctuating loads. When the material is exposed to a continually changing internal state

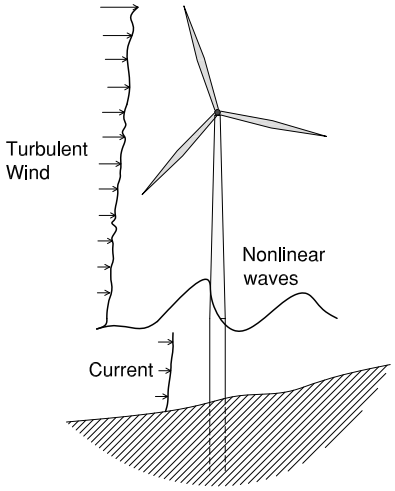

Figure 2.2: Schematic representation of the main loading actions on an offshore wind turbine.

of stress, it slowly deteriorates initiating cracks which will eventually lead to the material rupture. Such failures caused by damage accumulation are not investigated in this thesis. Contrarily, we will only focus on failures induced by extreme loading conditions. In particular, it will be assumed that our system reaches a state of failure whenever the state of internal forces due to the combined action of wind and waves attains a certain fixed value above which the bearing loads capability of the tower is compromised[2].

A deep understanding of the failure scenario paves the way for the next phase of the risk management framework: the Risk Assessment.

Risk Assessment

The *Risk Assessment* step represents the core of the whole risk management process and it is divided in two subparts:

- Risk Analysis;
- Risk Evaluation;

The above approach is referred to the model proposed in [3], see figure 2.3.

This phase aims at quantifying the *risk*. To this end it is of primary importance to employ as much accurate as possible prediction models to estimate both the hazard intensity and its frequency of occurrence. The risk is quantified by the following expression

$$Risk = Probability\ of\ failure \times Losses \qquad \text{[Losses unit/time]}$$

[2] Additional loads might be provided by ice impacts and earthquakes, but in this context they are not taken into account.

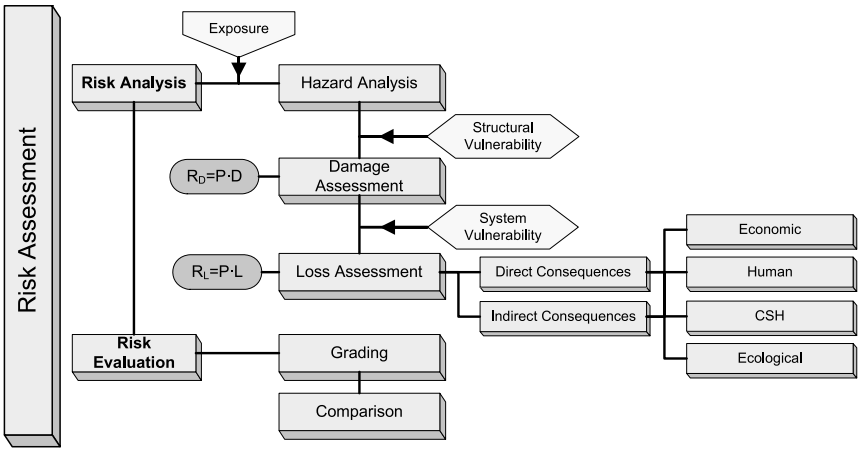

Figure 2.3: The Risk Assessment phase. Image from [3].

where *Losses* indicates all the expected consequences which may happen due to the failure of the system. Typical losses are: economical, fatalities, effects on the environment, etc. The estimation of consequences given the failure of the *system* remarkably relates to the nature of the *system*. Consequences associated with a failure of support structures of offshore wind turbines may be very significant in terms of monetary loss, while fatalities have less probability of occurrence than in the case of structural failures of civil buildings. Also the impact on the environment would not be dramatic as a failure of nuclear power plants. For these reasons, in the present work the risk analysis is restricted only to the first term of the risk, that is the the probability of failure of the system. The consequences - and thus the quantification of the losses in case of failure of the system - is not part of this thesis.

The probability of failure involves the *Vulnerability* of the *system*, the *Hazard* and the *Exposure*. According to [22], [23], [24], and assuming that the uncertainties associated with the loads are definitely dominating those related to the structure [25], for the specific case under consideration, the probability of failure can be expressed as follows

$$P_{fail} = P\left(LS\right) = \int P\left(LS|\boldsymbol{IM}\right) p\left(\boldsymbol{IM}\right) \mathrm{d}\boldsymbol{IM} \tag{2.3}$$

where LS denotes a limit state which in this case it is assumed to represent both the measure of the damage induced by the hazard and the structural response, while $\boldsymbol{IM}$ is the intensity measure of the hazards. In the light of equation (2.3) it is possible to understand the following conceptual equation for the probability of failure

$$P_{fail} = \mathit{Vulnerability} \times \mathit{Hazard} \times \mathit{Exposure}$$

where the *Vulnerability* is meant as the probability of a certain structural damage (or structural response) given the intensity measure of the hazard: $P\left(LS|\boldsymbol{IM}\right)$, while the *Hazard* is meant as the probability distribution the hazard intensities: $p\left(\boldsymbol{IM}\right)$,

finally the *Exposure* is intended as the probability that such a *Hazard* meets the *system*.

As already mentioned, in this work we are mainly interested in the bearing load capacity of the substructure so that the structural response is quantified by means of the tower base bending moment M_{yt} and, as a consequence, the *Limit State* function which identifies the state of failure is given by

$$Limit\ State\ (LS)\text{: } M_{yt} > M_{yt}^{*} \Leftrightarrow Failure$$

where M_{yt}^{*} is the ultimate resistant tower–base bending moment[3].

It has to be noted in equation (2.3) that the hazard intensity measure is a vector (typed in bold). Uncertainties from the load side are provided by several variables: the mean wind speed, the turbulence intensity, the wind shear exponent, yaw misalignment, significant wave height, zero up–crossing wave period, current speed, etc. However, in agreement with what observed in [25], the randomness in the load model is restricted only to the three variables which have the greatest influence on the response of support structures. These are: the mean wind speed U, the significative wave height H_s and the zero up–crossing wave period T_z. Thus, by setting $\boldsymbol{IM} = (U, H_s, T_z)$, equation (2.3) becomes

$$P_{fail} = P\left(M_{yt} > M_{yt}^{*}\right) = \int_{\mathcal{E}} P\left(M_{yt} > M_{yt}^{*} | U, H_s, T_z\right) p\left(U, H_s, T_z\right) \mathrm{d}U \mathrm{d}H_s \mathrm{d}T_z \tag{2.4}$$

where $\mathcal{E}$ is the environmental domain which represents all the possible variations of U, H_s and T_z.

The conditional distribution of the response given the set of sea state parameters is usually referred to as short–term distribution. By multiplying the conditional response times the joint probability density function of the sea state parameters U, H_s and T_z and integrating over the domain $\mathcal{E}$, the so called long–term distribution of the response is obtained.

According to [25] and as sketched in figure 2.4, the procedure to get the probability of failure conditioned on the environmental parameters is articulated in the following main steps:

- Definition of a joint wind–waves probabilistic model (from measurements or hindcast data);
- Generation of wind and waves time histories from which aerodynamic and hydrodynamic loads are derived;
- Time domain simulation and analysis of response time series;

At this point some statistics of the time series permits to obtain the distribution of the response conditioned on a given set of environmental parameters. To obtain such a conditional distribution several methods can be applied, for a detailed description we refer to [25], [26].

As already mentioned the long–term distribution is then obtained by the integration over the domain of all sea state. Finally, to extrapolate the response distribution

[3] Here this value is assumed to be deterministic.

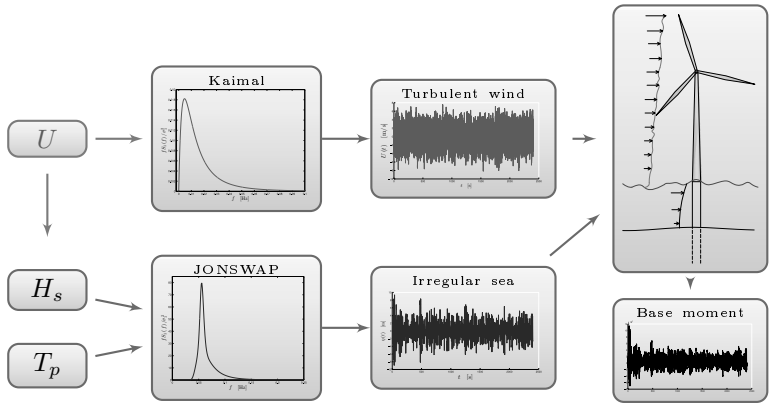

Figure 2.4: Schematic representation to obtain the short–term response given the environmental parameters intensity.

for longer period, e.g. 50 years, due to the hypothesis of independent sea states (once the sea state duration has been established), it is possible to calculate the number of independent sea state in a fixed time period and thus the probability distribution of the response for such a return period.

Finally, the probability of failure, i.e. the probability that in such a period of time the maximum response is higher than the ultimate strength, can be computed.

The methodology above described is known as "response–based" approach. Although it represents a rational method to estimate the probability of failure of the system, it has some disadvantages: it requires a considerable computational effort, it cannot be used in the early stage of the design; it usually adopts the same loading model independently on the intensity of the environmental parameters. Thus, no possibility of accounting the increasing waves nonlinearity as the wind speed increases.

An alternative procedure used to estimate the extreme response of offshore wind turbines is the so called "external conditions–based" approach. In this case it is assumed that the extreme response is induced by the extreme loads. In this thesis this methodology is used because our scope is to capture the response when the structure system is exposed to extreme events such as breaking waves. It will be shown in fact that, according to IEC61400-3, when 50–year return period storm are simulated, then breaking waves occur causing dangerous impacts against the substructure.

Within this second approach, first the joint probability distribution for the three main random variables U, H_s and T_z has to be built [21], [11], [27]. Then from the joint model the environmental contour may be obtained by fixing the requested

return period. Next, assuming that the turbine is parked or standstill[4], and that the extreme response is always proportional to the wind speed and the significative wave height, the triplet of environmental parameters which induce the maximum response can be easily found among the infinity triplets of U, H_s and T_z laying on the environmental contour [28], [21], [27], [26], [29], [30].

For the practical application in this thesis, however, because of lack of measured data and also because it is not central for our purpose, the extreme environment is established in a simplified way, that is by first setting the wind intensity in agreement with the extreme turbulent wind speed model (EWM) as in IEC61400-1, then by deriving the sea severity - associated with such a wind model - by using values for H_s and T_z recommended by literature [10], [31], [32], [11], [33], among others. Details on the wind–waves loading model are discussed in section 5.4.

The point we want to to stress in conclusion of this chapter is that the loading model employed to predict the system response needs to be adjusted according to the intensity measures of the hazard. Currently, appropriate numerical tools capable of systematically predicting the structural response when the hazard is characterized by fully nonlinear waves seem to lack in literature.

[4] In particular we will only focus on the substructure bearing load capacity rather than on the internal forces of the rotor blades. According to what said in the previous section, this restriction is reasonably justified because in case of extreme scenarios it will be assumed that the turbine is parked, so that blades are set with 90° pitch angle in order to be not affected by any lift force. On the contrary, in extreme environmental conditions tower and substructure result mostly involved.

Chapter3
Aerodynamic model

In this chapter the basic notions concerning the rotor blade aerodynamics on which the solver used in the next chapters is based are shortly recalled. The key concepts of the Blade Element Momentum are presented step by step starting from the disc theory.

3.1 Basics on wind turbines aerodynamics

The primary goal of a wind turbine is to subtract kinetic energy from the wind to transform it first into mechanical energy and then into electrical energy. The conversion of the wind kinetic energy into mechanical energy takes place when the air flows through the rotor disc. Given the upstream air flow velocity and making use of some basic fluid dynamics, it is possible to calculate both the velocity at the rotor disc and in the wake, provided that the axial flow induction factor a is known. The maximum achievable value of power coefficient is known as Betz limit and represents only a theoretical value. What so far introduced is usually named Momentum Theory and it is marked by the fact that it does not employ neither any event which occurs locally at rotor blades nor the shape and the number of blades.

To calculate the torque and power developed by the rotor a more sophisticated model involving lift and drag forces on the blades is adopted. To this aim, first the axial wind velocity at the disc is composed with the tangential velocity, which depends on the rotor angular velocity as well as on the tangential flow induction factor a', then, given the aerodynamic coefficients of each elemental segment of the blades, it is possible to compute the drag and lift forces. An iterative procedure permits to calculate the induction factors a and a' which finally lead to know the torque and, as a consequence, the power developed by the rotor. The latter, divided by the maximum available power, gives the expression of the power coefficient C_p. The variation of C_p versus the tip speed ratio represents the performance curve of a wind turbine.

In the following section details about the method will be presented and the meaning of the terminology here introduced will result clear.

3.2 Momentum theory

Let us start from the stream tube concept sketched in figure 3.1. The mass of fluid m passing a generic cross section A of the stream tube is given by $m = \rho V$, where ρ is the air density and V the volume of fluid. The *mass flow rate*, that is the *volume of fluid passing the cross–section A per unit time* is just given by $Q = AU$,

Enzo Marino, *An integrated nonlinear wind-waves model for offshore wind turbines*
ISBN 978-88-6655-051-8 (print) ISBN 978-88-6655-053-2 (online) © 2011 Firenze University Press

where U is the velocity of the air particles passing through the considered section[1].

3.2.1 Axial momentum

Of course, mass flow conservation imposes that

$$Q_\infty = Q_d = Q_w \tag{3.1}$$

where the subscripts ∞, d and w - according to figure 3.1, denote the far upstream undisturbed wind velocity, the disc, and the wake wind velocity, respectively.

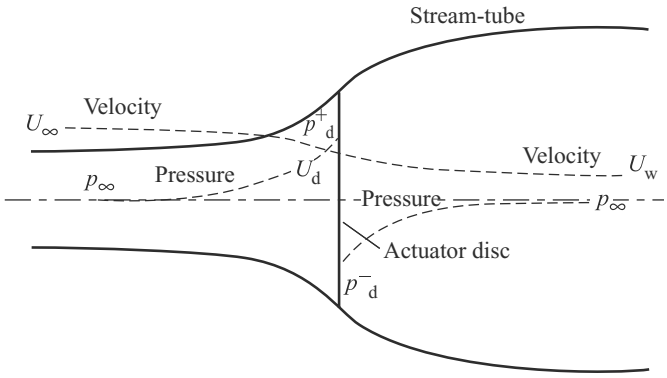

Figure 3.1: Stream tube. *Wind Energy Handbook*, Burton et al. Wiley 2001 [4].

Equation (3.1) can also be written as follows

$$A_\infty U_\infty = A_d U_d = A_w U_w \tag{3.2}$$

Newton's second law can be naturally applied at the disc by introducing the momentum $K = mU$. At the disc, the momentum rate writes as $\dot{K}_d = \rho A_d U_d U$. Thus, throughout the disc the momentum rate experiences an overall change given by

$$\Delta \dot{K}_d = \rho A_d U_d \Delta U = \rho A_d U_d \left(U_\infty - U_w\right) \tag{3.3}$$

and consequently the total forces acting at the disc, basically given by the pressure, must equal

$$A_d \left(p_d^+ - p_d^-\right) = \rho A_d U_d \left(U_\infty - U_w\right) \tag{3.4}$$

Now, by introducing the *axial flow induction factor* a, which permits to express the velocity at the disc through the far upstream undisturbed velocity U_∞ as $U_d = U_\infty (1-a)$, equation (3.4) turns into

$$\Delta p_d = \rho U_\infty (1-a) \left(U_\infty - U_w\right) \tag{3.5}$$

[1] $Q = \frac{d}{dt}(Ads) = A\frac{ds}{dt} = AU$, where ds is the disc thickness: the distance the air particles would cover in a time interval of dt.

The pressure gradient Δp_d can be computed by using twice Bernoulli's equation (once between the upstream undisturbed section and the disc section and once between the disc and the wake sections). This leads to write

$$\Delta p_d = \frac{1}{2}\rho\left(U_\infty^2 - U_w^2\right) \tag{3.6}$$

that replaced into equation (3.4) finally gives

$$U_w = (1-2a)\,U_\infty \tag{3.7}$$

Next, by making use of equation (3.7) into (3.4), the total force acting at the rotor disc (the thrust) is given by

$$F_d = 2\rho A_d U_\infty^2 a\,(1-a) \tag{3.8}$$

and, accordingly, the power developed is

$$P_{yield} = F_d U_d = 2\rho A_d U_\infty^3 a\,(1-a)^2 \tag{3.9}$$

It is straightforward now to see that from the all available power in the wind, machines can only extract a share given by the so called *power coefficient* C_p defined as follows

$$C_p = \frac{P_{yield}}{\frac{1}{2}\rho U_\infty^3 A_d} = 4a\,(1-a)^2 \tag{3.10}$$

The above coefficient is maximum when $a = 1/3$, therefore we have

$$C_{p_{\max}} = 0.593 \tag{3.11}$$

that is known as Bet's limit. It represents an ideal value which proves that the most exploitable energy is about 60 % of the available wind power.

3.2.2 Angular momentum

We are still not considering the blades aerodynamics. Since the final scope is to get the aerodynamic forces acting on the blades, it is necessary to go more in depth by adding some concepts about the angular momentum.

We assume that an air particle past the rotor disc has a tangential velocity $U_t = 2a'\Omega R$ where Ω is the angular velocity of the rotor, while a' is called *tangential flow induction factor*. Refer to figure 3.2.

It is easy thus to derive that, given an elemental volume of air, the infinitesimal angular moment writes as $\delta K^{ang} = \bar{r} \times dm\bar{U}_t = dm 2a'\Omega r$, where the elemental mass is $\delta m = \rho r \delta\vartheta\delta r$. By integrating along the circumference and taking the derivative with respect to time, we get

$$\delta\dot{K}^{ang} = \rho\delta A_d U_\infty\,(1-a)\,2a'\Omega r^2 \tag{3.12}$$

which represents the *change of angular momentum at the rotor disc* regarding an elemental annulus. Therefor, it is straightforward to obtain an alternative expression for the power yield[2]

$$\delta P_{yield} = \rho\delta A_d U_\infty\,(1-a)\,2a'\Omega^2 r^2 \tag{3.13}$$

[2]Power is given by the couple times the angular velocity.

Equating equation (3.9) with the above result we get

$$a'\lambda_r^2 = a\,(1-a) \tag{3.14}$$

where $\lambda_r = \Omega r/U_\infty$ is the local speed ratio.

Throughout the rotor disc thickness the tangential velocity of an air particle varies from zero (upstream) to $2a'\Omega r$ (downstream), so that in the middle a linear model permits to consider that the tangential velocity is $a'\Omega r$. See figure 3.2. The latter, along with the tangential velocity of the blades, gives rise to a net tangential flow experienced by the blade element equal to $\Omega r + a'\Omega r = \Omega r\,(1+a')$, therefore the total relative velocity experienced by the blade is the following. See figure 3.3.

$$W = \sqrt{U_\infty^2\,(1-a)^2 + \Omega^2 r^2\,(1+a')^2} \tag{3.15}$$

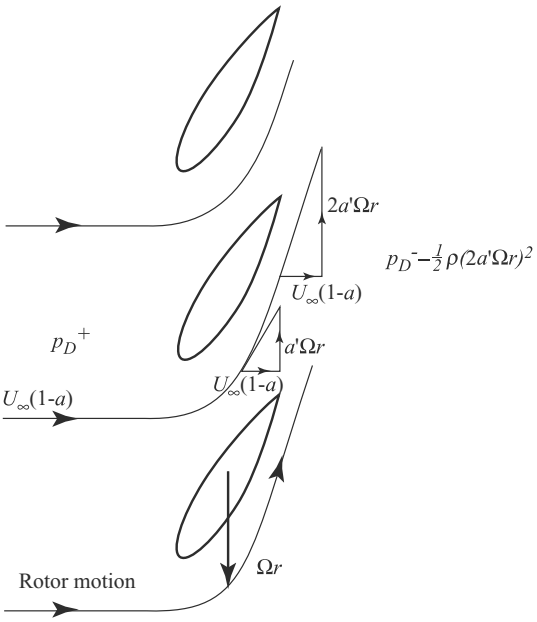

Figure 3.2: Tangential velocity growing across the rotor disc thickness. *Wind Energy Handbook*, Burton et al. Wiley 2001 [4].

Furthermore, from figure 3.3 it can also be readily set

$$W\sin\phi = U_\infty\,(1-a) \tag{3.16}$$

$$W\cos\phi = \Omega r\,(1-a') \tag{3.17}$$

where $\phi = \alpha + \beta$. The angle β amid the *airfoil zero lift line* and the plane of the rotor disc is named *pitch angle*, while α is the *angle of attack*.

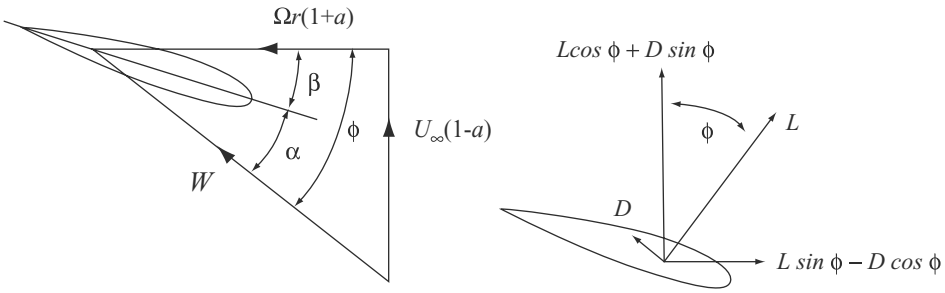

Figure 3.3: Velocity and forces on a blade element. *Wind Energy Handbook*, Burton et al. Wiley 2001 [4].

3.3 Blade Element Momentum theory

3.3.1 Drag and Lift forces

Once the total velocity W of air particles past the single blade element is known, see equation (3.15), it becomes relevant to compute the aerodynamic forces acting on it. To this aim, the aerodynamic properties of the blades, namely the drag and lift coefficients C_D and C_L, respectively, lead us to write

$$\delta D = \frac{1}{2}\rho W^2 c C_D \delta r \tag{3.18}$$

$$\delta L = \frac{1}{2}\rho W^2 c C_L \delta r \tag{3.19}$$

where δr denotes an elemental ring belonging to the rotor plane and c is the blade chord. See figure 3.4.

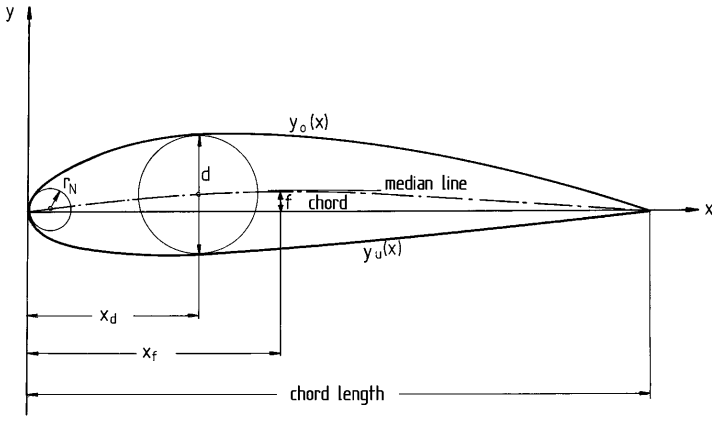

Figure 3.4: Typical geometry of NACA airfoil.

Together with the chord length c, the main geometric parameters which define an airfoil are shown in figure 3.4, where f is the maximum camber, x_f is the position

of the maximum camber, d is the maximum airfoil thickness, x_d is the position of maximum thickness, r_N is the nose radius and finally $y_o(x)$ and $y_u(x)$ are the coordinates of the upper and lower side contours.

As we are mainly interested in the forces normal and tangential to the rotor plane, the following projections are considered

$$P_n = \delta L \cos\phi + \delta D \sin\phi \tag{3.20}$$
$$P_t = \delta L \sin\phi - \delta D \cos\phi \tag{3.21}$$

which can be normalized with respect to $1/2\rho W^2 c$ to obtain

$$p_n = \delta l \cos\phi + \delta d \sin\phi \tag{3.22}$$
$$p_t = \delta l \sin\phi - \delta d \cos\phi \tag{3.23}$$

where

$$p_n = \frac{P_n}{\frac{1}{2}\rho W^2 c} \tag{3.24}$$
$$p_t = \frac{P_t}{\frac{1}{2}\rho W^2 c} \tag{3.25}$$

Projecting also the drag and lift coefficients we have

$$C_n = C_L \cos\phi + C_D \sin\phi \tag{3.26}$$
$$C_t = C_L \sin\phi - C_D \cos\phi \tag{3.27}$$

where C_n and C_t are such as

$$p_n = \frac{1}{2}\rho c C_n W^2 \tag{3.28}$$
$$p_t = \frac{1}{2}\rho c C_t W^2 \tag{3.29}$$

Now, if N_b denotes the number of blades, we obtain that the thrust and torque for an elemental volume of thickness δr are, respectively

$$\delta F = \frac{1}{2}\rho N_b \frac{W^2 (1-a)^2}{\sin^2\phi} c C_n \delta r \tag{3.30}$$
$$\delta M = \frac{1}{2}\rho N_b \frac{W (1-a) \Omega r (1+a')}{\sin\phi\cos\phi} c C_t r \delta r \tag{3.31}$$

By equating the two equations above, and by introducing the *solidity* $\sigma = crN_b/(2\pi r)$, the system for a and a' becomes

$$a = \frac{1}{\frac{4\sin^2\phi}{\sigma C_n} + 1} \tag{3.32}$$
$$a' = \frac{1}{\frac{4\sin\phi\cos\phi}{\sigma C_t} - 1} \tag{3.33}$$

Algorithm 1: Blade Element Momentum algorithm

Data: U_∞, β, Ω, r
Result: δF, δM
initialization ($a = 0$, $a' = 0$);
while $toll\,(a, a') <= toll^*$ **do**
  Compute flow angle ϕ;
  Read off $C_L\,(\alpha)$ and $C_D\,(\alpha)$ from tables;
  Compute C_n and C_t from equations 3.26 and 3.27;
  Calculate a and a' from equations 3.32 and 3.33;
end
Compute the local loads on the segment of the blades;

The above system concludes the so called Blade Element Momentum (BEM) model which can be translated into a computer code by the following algorithm 1 [34].

To sum up, the BEM theory just couples the momentum equations with the local element aerodynamics balance equations, involving drag and lift forces, to solve the complete system.

The BEM method requires two corrections in order to account for both the real number of blades and the case when the momentum theory is no longer allowed. Finally, the corrected BEM theory can be satisfactory used to compute the loads on the rotor as well as the annual energy production.

The aerodynamic solver used by the structural aero–elastic simulator which will be used in this thesis implements also the so called Generalized Dynamic Wake (GDW) model to compute the aerodynamic forces. This theory is also known as the Method of Acceleration Potential. It is an approach originally developed for helicopter industry and exhibits some advantages with respect to the above discussed BEM. It allows a more general distribution of pressure across the rotor plane than the BEM. The GDW model is based an a solution of Laplace'equation for potential problems. Details about the GDW theory are available in [35], [4]. The aerodynamic solver used in the next simulations will use both the BEM and the GDW theories depending upon the current wind speed.

3.4 Wind model

Forces acting on offshore wind turbines mostly stem from the aerodynamics of the rotor, the offshore environment (waves, tides, currents, ice, ect.), the gravitational and inertial loads. Modern turbine rotor blades are getting larger and larger and this gives rise to an increase of the dimensions of all others structural components (e.g. the tower height). Larger dimensions cause, in turn, an augmentation of dead weight (gravitational loading), inertial forces and, last but not least, the effects of unsteady turbulent wind becomes more and more evident. A sketch of a three bladed onshore wind turbine in a full field turbulent wind is given in figure 3.5.

In this thesis, as already pointed out in Chapter 1, an external condition–based extreme response analysis of offshore wind turbines is carried out. This means that

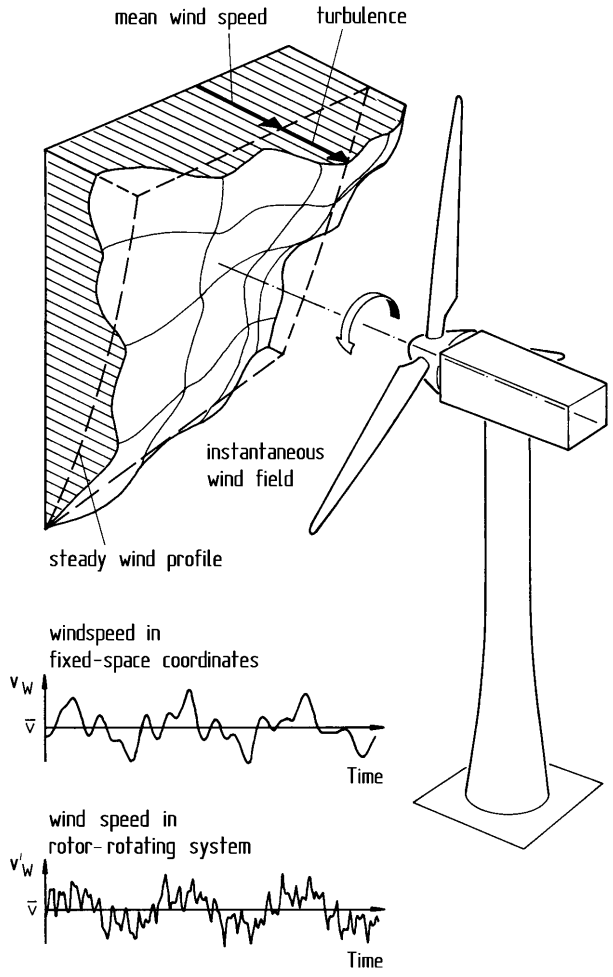

Figure 3.5: Effect of a turbulent wind speed distribution over the swept rotor area on the upwind velocity of the rotating rotor blades. Figure from [1].

extreme wind conditions are assumed according to recognized international standards, such as IEC61400-1 and -3.

Since the external conditions are dependent on the site, in IEC61400-1 wind turbines are divided in four classes. Each one is characterized by a reference wind speed U_{ref} and a turbulence intensity factor I_{ref}. These wind classes have the intent to cover most of the onshore applications. While, a special wind class, referred to as "S" is devoted to offshore applications. No prescription are made on this special class where all parameters are specified by the designer. However, for offshore wind turbines, to design the Rotor—Nacelle Assembly, the definition of wind classes as in IEC61400-1 remains valid. Due to a lack of data, for the sake of simplicity, in the present study the parameters defining the class "S" are always chosen like those for wind class III.

Much attention must be paid to the reference wind speed, in fact if a turbine belongs to a specific wind turbine class with a reference wind speed U_{ref}, it is designed to withstand climates for which the extreme 10 min average wind speed with a 50–year recurrence period at turbine hub height is lower than or equal to U_{ref}.

For the sake of simplicity, IEC61400-1 groups external condition in the so called Design Load Cases (DLCs) which are defined by combining:

- normal design situations and appropriate normal or extreme external conditions;
- fault design situations and appropriate external conditions;
- transportation, installation and maintenance design situations and appropriate external conditions.

It is worth pointing out that all structural and mechanical components are required to resist both the ultimate and the fatigue loading conditions. While the design of tower and foundation is governed by the ultimate load cases, the *design driver* for the rotor blades is usually contemplated by the fatigue load cases.

To each DLC it is assigned a specific type of analysis denoted by U (Ultimate), F (Fatigue). Ultimate analysis are additionally distinguished in Normal (N) or Abnormal (A) and partial safety factors are then assigned accordingly[3].

3.4.1 Extreme turbulent wind speed model EWM

As already pointed out, in this work the focus is on the extreme wind conditions, where the word "extreme" is referred to all those events with a 50–year return period. Offshore wind turbine must be designed to safely withstand wind conditions having intensity defined by such a return period.

The randomness of the wind is taken into account by adopting the appropriate turbulence model. Among the two recommended by IEC61400-1 3rd edition, the Kaimal model is here adopted. The single–sided velocity spectra for the three wind components, $k = u, v, w$[4] is given as follows

$$S_k(f) \frac{4\sigma_k^2 L_k/U_{hub}}{(1 + 6fL_k/U_{hub})^{5/3}} \tag{3.34}$$

where f is the frequency, σ_k is the standard deviation of the k–th velocity component and L_k is the integral scale parameter. See table 3.1

where

$$\Lambda_1 = \begin{cases} 0.7z & z \leq 60\,\text{m} \\ 42\,\text{m} & z \geq 60\,\text{m} \end{cases}$$

In this case the 10 min average wind speeds as functions of the elevation above the still water level, with 50–year and 1–year return period, respectively, are as-

[3] As 1.35 for N, 1.1 for A situations. All fatigue design situations assume 1.0 as partial safety factor.

[4] u is the longitudinal direction, v lateral and w vertical.

	Velocity components		
	u	v	w
σ_k	σ_u	$0.8\sigma_u$	$0.5\sigma_u$
L_k	$8.1\Lambda_1$	$2.7\Lambda_1$	$0.66\Lambda_1$

Table 3.1: Turbulence spectral parameter for the Kaimal model.

sumed as follows

$$U_{50}(z) = U_{ref}\left(\frac{z}{z_{hub}}\right)^{0.14} \tag{3.35}$$

$$U_1(z) = 0.8U_{ref} \tag{3.36}$$

The standard deviation in the longitudinal direction σ_u for the turbulent extreme wind speed model is

$$\sigma_u = 0.11U_{hub} \tag{3.37}$$

where U_{hub} is the wind velocity at hub height.

Note that for specific design load conditions when the turbine is parked or standstill (e.g. DLC 6.1a of IEC61400-3 [2]) the turbulent extreme wind model prescribed by the ICE61400-1 [36], see section 6.3.2.1, assumes that the turbulence standard deviation does not depend on the surface roughness. However, in general, this is not true and an appropriate model accounting for the effect of the sea surface roughness on the turbulence has to be adopted[5].

[5] Apart from the extreme wind model, for other design load conditions, according to [2], the turbulence standard deviation, whenever there are no site data available, is related to the sea surface roughness as follows

$$\sigma_u = \frac{U_{hub}}{\ln\left(\frac{z_{hub}}{z_0}\right)} + 1.28 \times 1.45 \times I_{15} \tag{3.38}$$

where I_{15} is the average value of the hub height turbulence intensity determined at hub height wind speed $U_{hub} = 15\,\mathrm{m/s}$. Offshore wind turbines are considered in the wind class "S" for which specific data regarding the wind and turbulence models have to be provided, see Annex A of [2].

While, the roughness length z_0 should be found by solving the following nonlinear equation

$$z_0 = \frac{A_C}{g}\left(\frac{\kappa U_{hub}}{\ln\left(\frac{z_{hub}}{z_0}\right)}\right)^2 \tag{3.39}$$

where g is the acceleration due to gravity, $\kappa = 0.4$ is the von Karman constant, A_C is the Charnock's constant whose recommended values are 0.011 for open sea conditions and 0.034 for near–costal areas. See [2] for further details.

Chapter4
Hydrodynamic model

This chapter describes the numerical model developed in this thesis for fully nonlinear water waves simulations. In addition to the aerodynamic loads discussed in the previous chapter, the offshore environment provides additional significant loading actions such as wave loads, current loads, ice impacts and tides. The numerical model here presented aims at the systematical inclusion (see next chapter) into the design procedures of the effects stemming from extreme waves breaking against offshore structures.

The first part is devoted to a brief review of the standard waves descriptions in order to adequately prepare the background for the new impact wave model.

4.1 Waves description

Sea waves are traditionally described by both a deterministic approach and a probabilistic model with respective advantages and disadvantage. For instance, the spectral approach permits to describe a random sea, but has the drawback that only linear waves can be represented. As a consequence, only forces stemming from linear wave theories can be derived.

On the contrary, some nonlinearity magnitude can be taken into account when a deterministic single-harmonic wave is used. In other words, the two commonly used approaches implement respectively either

- Regular nonlinear waves, or
- Irregular linear waves;

Fortunately, in most cases the nature of oceans can be very well described by the superposition of linear regular waves, and this makes the spectral approach an extraordinarily effective tool, in fact especially for long term loading condition, this approach fits fairly well the nature of the actions.

Contrarily, for ultimate failure conditions more representative models are required in order to capture the fully nonlinear contribution due to extreme (possibly breaking) waves.

Nowadays capabilities of modern computers permit to simulate fully nonlinear waves without penalizing the total simulation time, thus, whenever the fully nonlinear behaviour of waves plays a dominant role in designing offshore structures, it seems to be opportune to adopt a direct numerical solution of the governing equation without introducing any *a priori* hypotheses[1].

[1] Note that "*a priori* hypotheses" refers to the magnitude of nonlinearity, rather than to the assumptions on the physical characteristic of the fluid and flow type.

Enzo Marino, *An integrated nonlinear wind-waves model for offshore wind turbines*
ISBN 978-88-6655-051-8 (print) ISBN 978-88-6655-053-2 (online) © 2011 Firenze University Press

Analytical theories, such as Stokes–2nd and 5th order, fall in the weakly nonlinear group. In fact, what really distinguishes weak nonlinearity to the high (or strong) nonlinearity is essentially the asymmetry with respect to the vertical axis [31]. In the weakly nonlinear case we only deal with asymmetry with respect to the horizontal axis: crests become narrower and the troughs wider.

Figure 4.1(a) shows the two traditional approaches used to describe ocean waves: deterministic and stochastic. The advantage of the deterministic description is the capability of simulating nonlinear waves both through analytical and numerical tools. The main drawback however is that the real nature of oceans is not deterministic. On the other hand, as already pointed out, the stochastic approach permits to capture the real nature of the sea but only superimposing linear regular waves. To overcome the disadvantages of both methodologies, first a deterministic fully nonlinear Boundary Element Method–based simulator is developed, then it is linked with the wave energy spectra in order to account for the stochastic nature of the reality, see figure 4.1(b).

In this thesis the link between the probabilistic and deterministic approaches is used to get the advantages from both by virtue of their complementarity. In fact, in a random wave series there are some larger components, characterized by special energy contents, which have to be be captured and described separately because the importance of their strong nonlinearity is dominant with respect to the whole sea surface representation. These are the cases when exceptional events, such as rouge waves, occur. An example is shown in figure 4.2.

Figure 4.3, *The Great Wave*, shows how the danger represented by such extreme waves was also well impressed into artists' imaginary.

In the next section the fully nonlinear numerical wave model is described. Later on, in the next chapter, the numerical model is embedded into the stochastic environment.

4.1.1 Deterministic representation

There are several wave theories that provide a deterministic description of water waves. For most of them, three parameters are fundamental, while all the others can be derived from these. They are the period T, the wave height H and the water depth d.

The most used wave theories are shortly listed below:

Linear (or Airy) wave theory: the most important, useful and applied theory. It is also known as small amplitude wave theory and it is based on a strong linearization which makes the theory suitable for the probabilistic spectral representation of random seas. The analytical solution for the velocity potential and all the kinematic quantities is found by dropping all the second order terms in the dynamic and kinematic boundary conditions at the free surface.

It is always useful, especially for the scopes of Chapter 5, to have at hand all the kinematic and dynamic equations governing the propagation of a regular sinusoidal wave. For this reason, the essential formulas are listed in appendix A.

2nd and 5th order Stokes theories: these theories are also known as finite am-

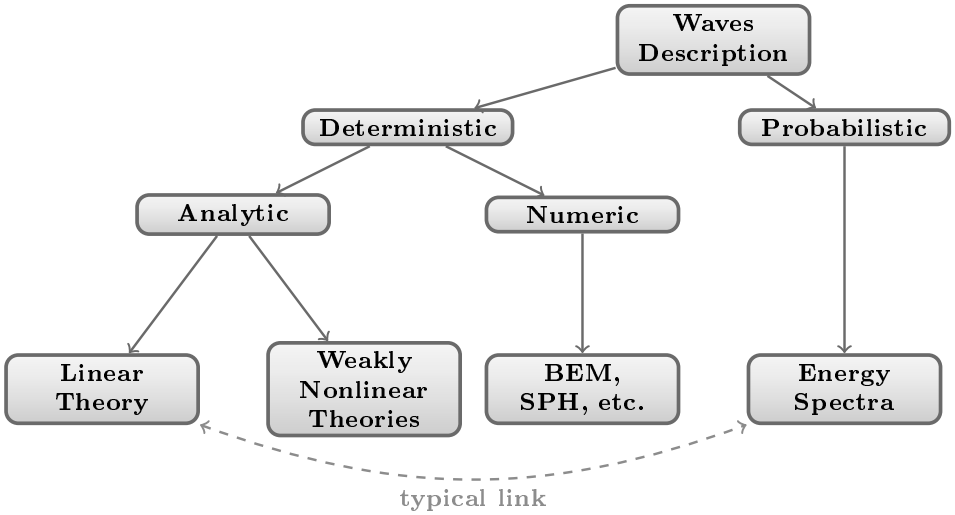

(a) Standard layout.

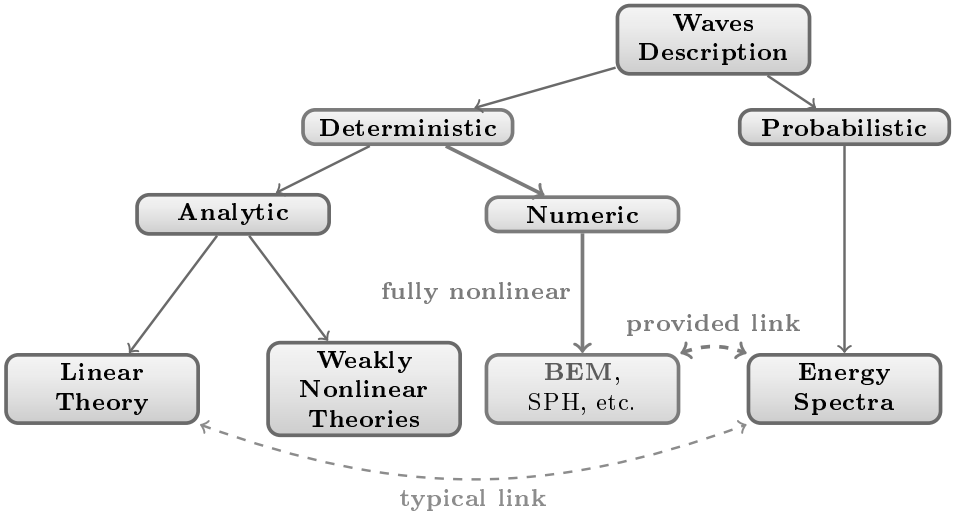

(b) Proposed approach.

Figure 4.1: Traditional scheme and proposed analysis approach adopted for describing ocean waves.

plitude wave theories. In fact, they employ a perturbation parameter called steepness $\epsilon = ka$, where k is the wave number and a the wave amplitude, which permits to describe steeper waves.

Cnoidal theory: the above Stokes theories have some restrictions on the applicability in shallow waters. The cnoidal theory supplies a proper description for

(a) Deep water rogue wave. (b) Shallow water freak wave.

Figure 4.2: Examples of freak waves.

Figure 4.3: *The Great Wave* by Katsushika Hokusai, 1760-1849.

finite amplitude long waves in shallow waters. A cnoidal wave has a typical shape consisting of sharper crest separated by wide troughs.

The importance of understanding the difference between several wave theories comes up if we look at the applicability diagram in figure 4.4.

A complete description of all the theories mentioned above is available in many books [37], [5], among others.

4.1.2 Probabilistic representation

As already mentioned, to design offshore structures both the stochastic and the deterministic approaches are necessary. To describe the random nature of ocean waves the only tool is represented by the wave energy spectrum. Energy density spectra represent the energy content of an ocean wave and how it varies on a certain range of frequencies.

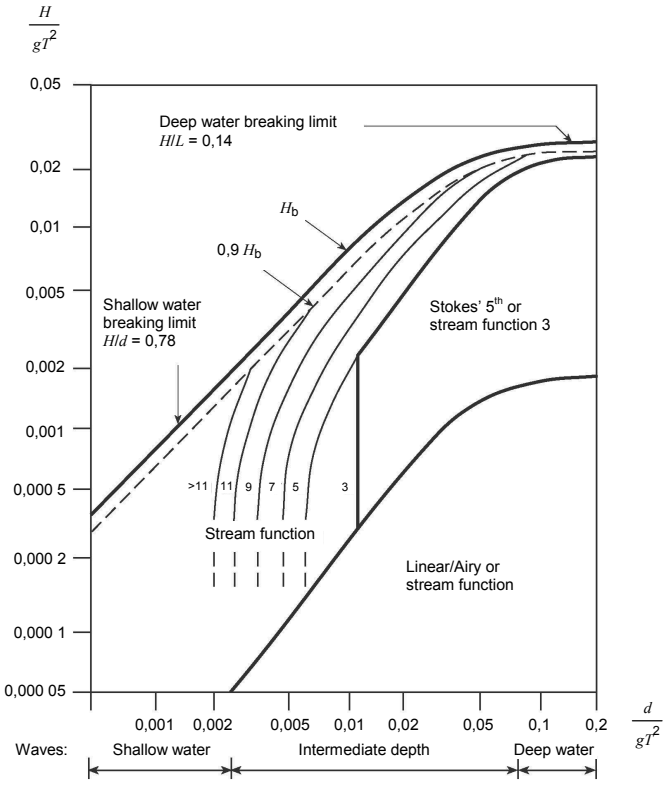

Figure 4.4: Wave theories applicability, from [5].

It is not our aim to repeat what is available in a very wide range of textbooks, but to have at hand some important concepts we just mention the two most important wave spectra which have been implemented in the numerical model discussed in the next chapter.

Standard wave spectra

After carrying out an environmental analysis, the key parameters which describe the sea severity can be established. They are: the wind velocity, the significant wave height, the mean zero–crossing wave period. Then, depending upon the type of sea to be simulated, the two most used wave spectra are [32], [11], [31], [38], [2], [7]:

Pierson–Moskowitz: The Pierson-Moskowitz spectrum was developed departing from data obtained in the North Atlantic in condition of fully developed sea. This is a single–parameter formulation, indeed it depends only on the wind velocity U measured at 19.5 m above the sea water level.

$$S_{\eta\eta}(\omega) = \frac{8.10}{10^3}\frac{g^2}{\omega^5}\exp\left[-0.032\frac{\left(\frac{g}{H_s}\right)^2}{\omega^4}\right] \tag{4.1}$$

where H_s is the significative wave height related to the wind velocity U as $H_s = 0.21\frac{U^2}{g}$.

JONSWAP: The Joint North Sea Wave Project spectrum is based on an extensive measurement campaign carried out between the 1968 and 1969 along a line of about 160 km in the area of Sylt Island, see [11] and its references. Contrarily to the Pierson–Moskowitz formulation, this spectrum is suitable for wind–generated fetch–limited seas. Therefore it requires as input both the wind velocity and the fetch length. The formulation is given as follows

$$S_{\eta\eta}(\omega) = \alpha\frac{g^2}{\omega^5}\exp\left[-\frac{5}{4}\left(\frac{\omega_p}{\omega}\right)^4\right]\gamma^{\exp\left[-\frac{(\omega-\omega_p)^2}{2(\sigma\omega_p)^2}\right]} \tag{4.2}$$

where

- ω_p is the peak circular frequency. According to [11] it is related to the fetch F and wind velocity U by the following relation
$$\omega_p = 7\pi\frac{g}{U}x_F^{-0.33} \tag{4.3}$$
- γ is the *peak–shape parameter*, it represents the ratio between the maximum spectral energy density and the maximum of the corresponding Pierson–Moskowitz spectrum
- α is a parameter related to the sea generation conditions, indeed it depends on the fetch F as follows
$$\alpha = 0.076x_F^{-0.22} \tag{4.4}$$
- $\sigma = 0.07$ for $\omega \leq \omega_p$ and $\sigma = 0.09$ for $\sigma > \omega_p$
- $x_F = \frac{gF}{U^2}$ is the nondimensional fetch length
- U is the mean wind speed
- F is the fetch length
- g is the gravity acceleration

It is always useful, however, to obtain the JONSWAP spectrum in terms of the sea severity H_s. In agreement with [11] and [12], we will assume the following relation

$$U = kF^{-0.615}H_s^{1.08} \tag{4.5}$$

where k depends on the peak shape parameter γ, as shown in table 4.1, F is the fetch in km and H_s must be expressed in m.

The line in red in table 4.1 highlights the values for k associated with the mean value of γ.

The value γ varies approximately from 1 to 5 randomly, it is usually normal distributed with mean value of 3.30. However, according to [2] and [10], the following formulation is adopted:

$$\gamma = \begin{cases} 5 & \text{for} \quad \frac{T_p}{\sqrt{H_s}} \leq 3.6 \\ \exp\left(5.75 - 1.15\frac{T_p}{\sqrt{H_s}}\right) & \text{for} \quad 3.6 < \frac{T_p}{\sqrt{H_s}} \leq 5 \\ 1 & \text{for} \quad \frac{T_p}{\sqrt{H_s}} > 5 \end{cases}$$

k	γ
96.2	1.75
88.3	2.64
83.7	3.30
80.1	3.96
76.4	4.85

Table 4.1: $k - \gamma$ relation, [11] and [12].

It is convenient sometime to get the JONSWAP spectrum as function of the two independent variables H_s and T_p. In this way we do not use neither table 4.1 nor the fetch F which is an information already contained in T_p and H_s. Indeed, given these two inputs, α is readily obtained as follows [39]

$$T_p = \left(\frac{1}{0.305\alpha}\right)^{\frac{1}{4}} 2\pi\sqrt{\frac{H_s}{4g}} \Rightarrow \alpha = \frac{1}{4.88}\omega_p^4\left(\frac{H_s}{g}\right)^2 \tag{4.6}$$

In conclusion, the formulation given in equation (4.2) would require as independent variables U and F. In other design situations H_s and T_p are assumed the two independent design parameters. From them, of course, it is possible to get back first α via (4.6), then F through (4.4) and finally U.

4.2 Fully nonlinear potential flow water waves

Most of the current approaches in designing offshore structures successfully adopt the linear wave theory, nevertheless in some design conditions nonlinear effects cannot be neglected, especially when the goal is evaluating the structural safety.

Although modern computer simulations of offshore wind turbines have made formidable progresses, the integration of a fully nonlinear numerical solution of gravity waves into the more general multi-physics framework characterizing the design of offshore wind turbines seems to be not yet a common practice.

One of the first contribution addressing the numerical simulation of nonlinear water waves was due to Longuet–Higgins and Cokelet in [40] who introduced for the first time the Mixed Eulerian–Lagrangian approach to describe such a free surface problem. Subsequently, in [41] it was proposed a new and time–effective procedure to integrate in time the dynamic and kinematic boundary conditions on the free surface. The advantage of this time-stepping procedure, indeed, lies in solving different Laplace's equation at each fixed time step making use of the same system matrices.

The numerical solution of the Boundary Value Problem (BVP) and the consequent time integration do not introduce any approximation neither on the velocity potential nor on the dimension of typical wave parameters such as wave height, wave period, water depth and wave length. Excellent results of this approach in the description of fully nonlinear water waves have been achieved in [42], [43], [44] and [45], just to mention a few.

Nowadays the implementation of this computational tool deserves attention for several reasons: firstly we detected a lack of fully nonlinear models in investigat-

ing structure-fluid interaction for offshore wind turbines substructures. Secondly because, especially in those seas where the water depth is fairly high, floating structures are desirable and in this case methods hereafter illustrated are quite promising [46], [47] and [48]. Moreover, as for long term loading actions the sea state needs to be described by a superposition of nonlinear waves, interesting developments are also in the direction proposed in [49].

4.2.1 On the validity of the potential flow model to describe breaking waves

The potential flow theory is regularly used to model water waves. The existence of a velocity potential stems from the hypothesis that the fluid is irrotational. In the model used in this work the condition of non-rotational flow is guaranteed throughout the evolution of the wave up to the time instant when the water jet re-enters into the free surface. At the re-entry time instant, in fact, the domain becomes multi-connected and Kelvin's theorem does not hold anymore.

Kelvin's theorem states that for an ideal fluid subjected to conservative body forces, the circulation about any closed material contour moving with the fluid is constant in time, see e.g. [50].

So that, given a zero initial circulation, we are sure that it remains zero up to the re-entry. Moreover, Stokes' theorem assures that the condition of zero circulation on the closed contour is equivalent to the condition of irrotaional flow.

In addition to the theoretical justifications, experimental evidences (see e.g. [6, 51]) confirm that the irrotational model is valid to capture the evolution of plunging breakers (up to the re-entry).

The above argumentations lead to the conclusion that no relevant discrepancies from the real flow situation are caused by the assumption of a potential model.

As already mentioned, in addition to the hypotheses of incompressibility of the fluid and irrotational flow discussed above, the present model is based on the assumption of non-viscous fluid. It has been demonstrated that the effects of the viscosity on the kinematics of water waves is negligible for the cases we are interested in. In general, the viscosity might influence by acting through three mechanisms: 1) viscous effects at the free surface; 2) viscous effects inside the fluid; 3) viscous effects at the sea bottom. Concerning mechanisms 1) and 2), viscosity causes the progressive attenuation of the gravity waves, but this happens for time periods much longer than those typical for the propagation of gravity waves. In case 3), the effect could be taken in some consideration only in the case of very small water depth. Our simulations are all in intermediate water conditions, thus the effects of viscosity can be neglected without introducing significant errors. Further details on the effect of viscosity can be found in [52].

On the contrary, the viscosity plays a different role in the loading model. In fact, a non-viscous fluid would lead to no drag contribution in the hydrodynamic force exerted on the monopile. To avoid this, Morison's equation provides the drag term which accounts for the viscosity of the fluid.

4.2.2 Governing equations

From Euler's equations valid for an incompressible and inviscid fluid, the additional hypothesis of irrotational flow allows the description of fully nonlinear water waves by means of a potential model. At a fixed time t, the velocity field for each point belonging to the spatial domain $\Omega(t)$ can be expressed by means of a velocity potential $\phi(p,t)$ as follows

$$\bar{v}(p,t) = \nabla\phi(p,t) \quad \forall p \in \Omega(t) \tag{4.7}$$

Equation (4.7), together with the mass conservation ($\mathrm{div}(\bar{v}) = 0$) leads to the following Laplace's equation

$$\nabla^2\phi(p,t) = 0 \quad \forall p \in \Omega(t) \tag{4.8}$$

The domain $\Omega(t)$ is assumed bounded by four boundaries: $\Gamma_i(t)$, $\Gamma_b(t)$, $\Gamma_o(t)$, $\Gamma_f(t)$ being the inflow wall, the bottom, the outflow wall and the free surface, respectively. See figure 4.5.

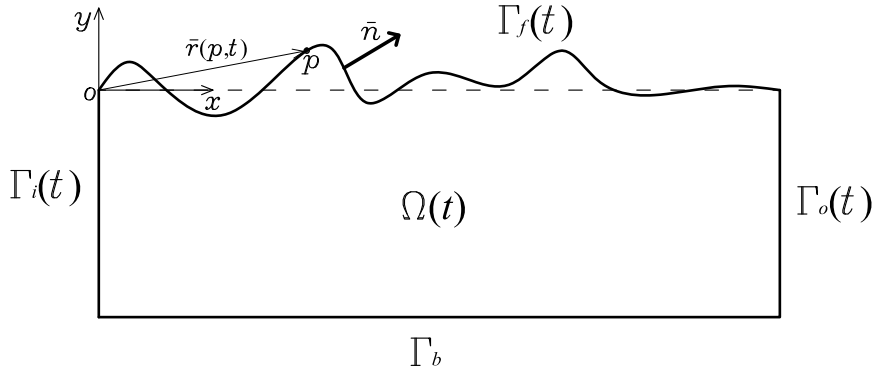

Figure 4.5: Two–dimensional domain of the potential problem.

Let $\bar{n}$ be the unit outward normal vector, the normal component of the velocity field (the flux) stems form (4.7), as follows

$$v^n(p,t) = \nabla\phi(p,t) \cdot \bar{n} \tag{4.9}$$

Equation (4.9) is used to provide Neumann boundary conditions on the boundary $\Gamma_i(t)$, $\Gamma_b(t)$, $\Gamma_o(t)$. The value to be assigned to the normal derivative of the velocity potential depends on the type of water wave to be simulated.

An inertial coordinate system is fixed with the x–axis along the Still Water Level (SWL) and the y–axis vertical and upwardly oriented. See figure 4.5. At a fixed time, points $p \in \Gamma_f$ are tracked by a Lagrangian position vector $\bar{r}(p) = p - o = x_f\bar{e}_x + y_f\bar{e}_y$. Where $\bar{e}_x$ and $\bar{e}_y$ denote the unit normal basis.

Boundary conditions

On the free surface $\Gamma_f(t)$ the dynamic boundary condition, which represents the Bernoulli equation for unsteady flow, reads as follows

$$\frac{D\phi(p,t)}{Dt} = -\frac{p_a}{\rho_w} - gy_f + \frac{1}{2}\nabla\phi(p,t)\cdot\nabla\phi(p,t) \quad \forall p \in \Gamma_f(t) \tag{4.10}$$

where y_f is the free surface instantaneous elevation, often also denoted by η, p_a is the atmospheric pressure, which can be neglected, and ρ_w the water density.

Moreover, the profile of the free surface is governed by the following kinematic boundary condition which stems directly from equation (4.7)

$$\frac{D\bar{r}(p,t)}{Dt} = \bar{v}(p,t) = \nabla\phi(p,t) \quad \forall p \in \Gamma_f(t) \tag{4.11}$$

The above free surface kinematic boundary condition can be written in components as follows

$$\frac{Dx_f}{Dt} = v_f^x \tag{4.12}$$

$$\frac{Dy_f}{Dt} = v_f^y \tag{4.13}$$

To solve the time-depending potential problem (4.8), initial conditions must be also assigned. Namely, at the beginning of the simulation the potential along the free surface and its geometry have to be known.

4.2.3 Time integration scheme

There are several methods to integrate the dynamic and kinematic boundary conditions on the free surface. A review of the possible approaches is proposed in [53], [54]. One of the most effective time integration scheme for this type of problems was first proposed by Dold and Peregrine [41]. It is based on Taylor series truncated at a certain order which permits to approximate, and consequently to update, both the free surface profile and the velocity potential from the current time t to the subsequent time step $t + \mathrm{d}t$. Namely, the series are

$$\bar{r}(p,t+\mathrm{d}t) = \bar{r}(p,t) + \frac{D\bar{r}(p,t)}{Dt}\mathrm{d}t + \frac{1}{2}\frac{D^2\bar{r}(p,t)}{Dt^2}\mathrm{d}t^2 + o\left(\mathrm{d}t^3\right) \tag{4.14}$$

$$\phi(p,t+\mathrm{d}t) = \phi(p,t) + \frac{D\phi(p,t)}{Dt}\mathrm{d}t + \frac{1}{2}\frac{D^2\phi(p,t)}{Dt^2}\mathrm{d}t^2 + o\left(\mathrm{d}t^3\right) \tag{4.15}$$

Figure 4.6 shows the Lagrangian updating of the free surface water particles position.

The above series are truncated at the second order. It seems that such a choice is optimal considering the numerical effort necessary to compute the third order coefficients [55]. The procedure to get up to the second order coefficients of the above series is rather simple and has some remarkable advantages with respect to other time-stepping schemes. The following two paragraphes describe how to proceed.

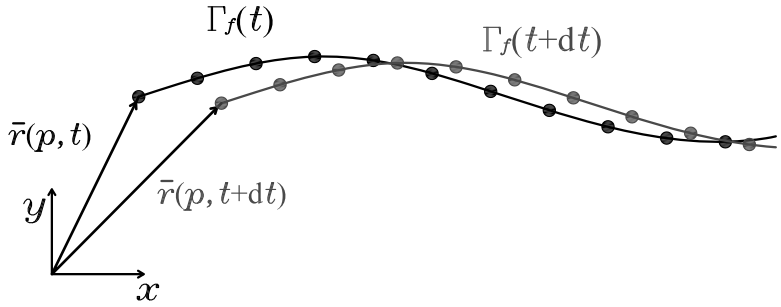

Figure 4.6: Lagrangian updating of the free surface particles position.

First order Lagrangian derivatives

No special effort is required to compute the first–order coefficients in equations (4.14) and (4.15). Indeed, the first–order total derivative of the position vector $\bar{r}$, i.e. the velocity components v_f^x and v_f^y, can be computed by accounting for both the contributions of normal and tangential components

$$v_f^x = v_f^n n^x + v_f^t t^x \tag{4.16}$$

$$v_f^y = v_f^n n^y + v_f^t t^y \tag{4.17}$$

where, in turn, v_f^n stems directly form the solution of the BVP, while the tangential component v_f^t is obtained by differentiating the shape functions. See section B.2 of appendix B.

In equations (4.16) and (4.17), n^x, n^y and t^x, t^y denote the Cartesian components of the normal and tangential unit vectors, respectively.

In addition to this, the first–order coefficient for the integration of the velocity potential, that is its total derivative, see equation (4.15), can be directly computed by means of the dynamic boundary condition (4.10)

$$\frac{D\phi\,(p,t)}{Dt} = -gy_f + \frac{1}{2}\left(v_f^{x2} + v_f^{y2}\right) \tag{4.18}$$

Second order Lagrangian derivatives

A bit more articulated procedure is invoked to compute the second–order coefficients involved in equations (4.14) and (4.15), [45]. Let us start from the particle acceleration

$$\frac{D^2\bar{r}}{Dt^2} = \frac{D\bar{v}}{Dt} = \frac{\partial\bar{v}}{\partial t} + (\nabla\bar{v})\,(\bar{v}) \tag{4.19}$$

By means of equation (4.7), the temporal derivative $\frac{\partial\bar{v}}{\partial t}$ can be written as follows

$$\frac{\partial\bar{v}}{\partial t} = \nabla\dot{\phi} \tag{4.20}$$

where it has been set $\dot{\phi} = \frac{\partial\phi}{\partial t}$. Therefore, the particle acceleration becomes

$$\frac{D\bar{v}}{Dt} = \nabla\dot{\phi} + (\nabla\bar{v})\,(\bar{v}) \tag{4.21}$$

To solve the above problem it is necessary to know $\dot{\phi}$. By differentiating equation (4.8) with respect to time, it is immediate to realize that for a fixed time, $\dot{\phi}$ satisfies another potential problem stated as follows

$$\nabla^2 \dot{\phi}\,(p) = 0 \quad \forall p \in \Omega \tag{4.22}$$

$$\dot{\phi} = \frac{D\phi}{Dt} - \left(v_f^{x2} + v_f^{y2}\right) \quad \forall p \in \Gamma_f \tag{4.23}$$

$$\dot{v}_b^n = \frac{\partial v_b^n}{\partial t} \quad \forall p \in \Gamma_b \tag{4.24}$$

$$\dot{v}_o^n = \frac{\partial v_o^n}{\partial t} \quad \forall p \in \Gamma_o \tag{4.25}$$

$$\dot{v}_i^n = \frac{\partial v_i^n}{\partial t} \quad \forall p \in \Gamma_i \tag{4.26}$$

Note that the right–hand side of equation (4.23) is completely known since the total derivative of the potential stems directly form the dynamic boundary condition and the velocity field on Γ_f has already been computed by using equations (4.16) and (4.17). By solving this second BVP, with the same distribution of Dirichlet and Neumann boundary conditions, we get the unknowns $\dot{v}_f^n$. Furthermore, by numerical differentiation it is possible to calculate also $\dot{v}_f^t$ and thus it is straightforward to compute the gradient of $\dot{\phi}$ as follows

$$\frac{\partial \dot{\phi}}{\partial x} = \dot{v}_f^x = \dot{v}_f^n n^x + \dot{v}_f^t t^x \tag{4.27}$$

$$\frac{\partial \dot{\phi}}{\partial y} = \dot{v}_f^y = \dot{v}_f^n n^y + \dot{v}_f^t t^y \tag{4.28}$$

The above approach is particularly effective because the system matrix needs to be computed only once at each time–step as the geometry of the domain Ω is the same for both BVPs. Namely, this permits to use again the same matrices H and G, see equation (B.28) in appendix B. The difference between the two BVPs lies only in the boundary condition value (not type!), and so no new integration over the boundary elements is required.

The second–order coefficient for Taylor series (4.14) still need the last contribution $(\nabla \bar{v})\,(\bar{v})$. The procedure to compute this involves nothing but some basic vector calculus where the irrotational hypothesis of the flow and the continuity equation are used [45]. However, details on the calculation of this term are discussed in section B.3 of appendix B.

Concerning the second–order coefficient $\frac{D^2\phi}{Dt^2}$ necessary to update the velocity potential at time $t+\mathrm{d}t$, it is required to differentiate the dynamic boundary condition with respect to time as follows

$$\frac{D^2\phi}{Dt^2} = \frac{D}{Dt}\left(-gy_f + \frac{1}{2}\bar{v}_f \cdot \bar{v}_f\right) = -gv_f^y + v_f^x \frac{Dv_f^x}{Dt} + v_f^y \frac{Dv_f^y}{Dt} \tag{4.29}$$

4.2.4 Method of solution

As already mentioned, the fully nonlinear potential flow initial-boundary-value problem is solved by using the Mixed Eulerian Lagrangian (MEL) approach which

consists in a repeated two-step procedure. See [56] for a wide literature survey.

After the notions introduced in the previous sections, the MEL approach can now be better highlighted.

For the sake of brevity let $\Gamma_N = \Gamma_i \cup \Gamma_b \cup \Gamma_o$ denote the region of the boundary where Neumann boundary conditions are assigned. Note that the dependency of the boundary curve Γ on time has been suppressed. This abuse in notation is here justified by the fact that at each time step the problem is regarded as a steady case.

The two steps are:

1. *Eulerian step:* at a fixed time t, the free surfac Γ_f and the velocity potential $\phi\,(p \in \Gamma_f)$ on it are known. The flux $\nabla\phi\,(p \in \Gamma_f) \cdot \bar{n}$ on Γ_N and Γ_N itself are also known. Two steady Laplace's equations are solved for the fluxes $\nabla\phi\,(p \in \Gamma_f) \cdot \bar{n}$ and $\nabla\dot{\phi}\,(p \in \Gamma_f) \cdot \bar{n}$ on the free surface and for the velocity potentials ϕ and $\dot{\phi}$ on Γ_N.

2. *Lagrangian step:* making use of equations (4.14) and (4.15), the velocity potential and the free profile are updated in time providing boundary conditions for the next Eulerian step. See figure 4.6.

At the second step, when all the unknowns have been found, each particle of the boundary of the Eulerian frame is updated in a Lagrangian manner.

It is worth pointing out that the particular type of time-integration adopted requires that at each time step the number of steady Laplace's equations to be solved depends on the order of Taylor's series, so that, in accordance with equations (4.14) and (4.15), in the current code two BVPs are solved at each time–step.

The steady solution at each time–step is achieved by discretizing the BVP by using the direct Boundary Elements Method. See appendix B.1.

Note that in the above procedure the analytic linear solution (Airy wave theory for irregular waves) plays a twofold role: it is used to initialize the solver by providing the free surface elevation and the velocity potential on the free surface, and it is used to provide Neumann boundary conditions (involved in the Eulerian step) on the upstream and downstream walls during the simulation. Moreover, the transition from the linear solution to the fully nonlinear one is made by using a ramp function which is required to be long not more than ten times one boundary element length. In Chapter 5, in particular in section 5.4.3, such a domain decomposition strategy will be extensively discussed.

4.2.5 Smoothing and regridding

According to [57] in our model the two most important and typical numerical instabilities occurred: (i) *strong instability* due to a too large time–step; (ii) *steep wave* instability, also known as "sawtooth" instability. The Boundary Element Method used to discretize Laplace's equation implements second order elements along all the four boundaries. Hence, the sawtooth instabilities look like a bit different to the classical one shown in literature. Figure 4.7 gives an example of what this instability causes.

While the *strong instability* can be fixed by setting a proper time–step, to remove the sawtooth behavior of the free surface a smoothing procedure is necessary. The

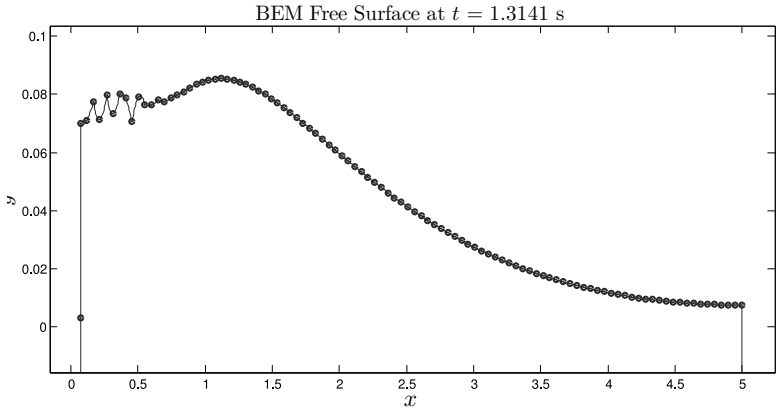

Figure 4.7: Typical sawtooth instability affecting the free surface in the case of a steep wave generated by a piston wavemaker.

are many possibilities to smooth the free surface, here the one proposed in [40] has been chosen. Every a variable number of time steps the free surface and the velocity potential are smoothed by the following 5–point smoothing formula

$$f_j^{smt} = \frac{1}{16}\left(-f_{j-2} + 4f_{j-1} + 10f_j + 4f_{j+1} - f_{j+2}\right) \tag{4.30}$$

where f_j^{smt} is the smoothed value in the j–th node of the function f which can be ϕ, y_f and x_f.

The above smoothing formula is valid for equally spaced points and does not apply to the first (and last) two nodes of the free surface. When nodes tend to gather in the large velocity gradient regions, the equally spaced condition is no longer sufficiently accurate, hence the smoothing subroutine also implements the generalized form of the 5–point scheme in accordance with [58].

When dealing with overturning waves, however, the formation of a water jet causes nodes to concentrate near the cusp where very high velocity fields are associated with high curvatures. In this situation a more refined mesh could be needed but it must also be avoided that nodes undergo displacement so large to step over the neighbor particles. A regridding subroutine has been thus implemented with the aim of avoiding the latter inconvenient. When necessary, the regridding is also used to refine the free surface discretization as it allows the augmentation of the boundary elements on selected boundary patches. The regridding makes use of cubic splines.

Smoothing and regridding have to be used together carefully. For both there are advantages and drawbacks which can lead to inaccurate solutions.

4.3 Validation

4.3.1 Periodic waves

The first simplest case used to test the numerical model regards a period wave. It will result clear later on the importance of demanding excellent performance to the code in simulating linear periodic waves. In fact, when the goal will be the simulation of an irregular sea, it will be just matter of the number of harmonics of which the velocity potential and the other kinematic entities are made up, but the global framework of the numerical solver is absolutely identical to this case. However, in this specific case, to check also the capability of the code of capturing nonlinear effect, a periodic 2nd–order Stokes wave has been simulated. Care needs to be devoted to the inflow and outflow boundaries where periodicity guarantees no reflection. Although the analytical solution for such a problem is spread into an unbounded number of textbooks, e.g. [37], here the initial and boundary conditions are recalled and adapted to the present numerical scheme.

Boundary conditions on Γ_b

The boundary condition on the bottom is the no flux condition, so that

$$v_b^n = \nabla\phi \cdot \bar{n} = 0 \quad \forall p \in \Gamma_b \tag{4.31}$$

Boundary conditions on Γ_i *and* Γ_o

The velocity along the inflow and outflow boundary are consistent with Stokes 2nd–order theory. They are

$$\begin{aligned} v_i^n(\Gamma_i, t) = {} & \frac{H\pi}{T}\frac{\cosh(ks)}{\sinh(kd)}\cos(k(x_i - ct)) + \\ & + \frac{3}{4c}\left(\frac{H\pi}{T}\right)^2 \frac{\cosh(kd)}{\sinh^3(kd)}(2 + \cos(2kd))\cos(2k(x_i - ct)) \end{aligned} \tag{4.32}$$

$$\begin{aligned} v_o^n(\Gamma_o, t) = {} & \frac{H\pi}{T}\frac{\cosh(ks)}{\sinh(kd)}\cos(k(x_o - ct)) + \\ & + \frac{3}{4c}\left(\frac{H\pi}{T}\right)^2 \frac{\cosh(kd)}{\sinh^3(kd)}(2 + \cos(2kd))\cos(2k(x_o - ct)) \end{aligned} \tag{4.33}$$

where $s = d + y$.

Initial conditions

The initial conditions are assigned to the free surface as follows

$$\phi(p,0) = \frac{Hg}{2\omega}\frac{\cosh(ks)}{\cosh(kd)}\sin(kx) + \\ + \frac{3}{8}\frac{H^2\pi^2}{kTL}\frac{\cosh(2ks)}{\sinh^4(kd)}\sin(2x) \quad \forall p \in \Gamma_f(0) \tag{4.34}$$

$$y_f(x,0) = \frac{H}{2}\cos(kx) + \\ + \frac{\pi H^2}{8L}\frac{\cosh(kd)}{\sinh^3(kd)}(2+\cos(2kd))\cos(2kx) \quad \forall p \in \Gamma_f(0) \tag{4.35}$$

where y_f (often denoted also by η) is the elevation of the free surface with respect to the still water level.

4.3.2 Solitary wave

The second numerical experiments to test our code addresses the propagation of a solitary wave as described in [59]. Actually, several kinds of solitary waves have been simulated, e.g. [55] among others, and for all cases excellent results have been attained. Here, for the sake of brevity, only the solitary wave simulated in [59] is shown.

Boundary conditions on Γ_i, Γ_o and Γ_b

To generate a solitary wave we give some specific initial conditions on the free surface, while all the remaining boundaries are assumed impervious and kept at rest by setting the following Neumann boundary conditions

$$v_b^n(\Gamma_i,t) = v_i^n(\Gamma_i,t) = v_o^n(\Gamma_o,t) = 0 \quad \forall t \in [t_i,t_f] \tag{4.36}$$

where t_i and t_f are the initial and final instants of the simulation.

Initial conditions

The motion is generated by initial conditions obtained by the following second–order analytical solution setting $t = 0$

$$\phi(x,t) = \frac{1}{\lambda}\left[1 - 1/4H + 1/3H\tanh^2(\mu - k\lambda t)^2\right] \times \\ \tanh(\mu - k\lambda t)\sqrt{4/3H(1-5/4H)} + \\ + 1/\lambda\,\mathrm{sech}^2(\mu - k\lambda t)^2\tanh(\mu - k\lambda t)\sqrt{3/4H^3(1-5/4H)} \tag{4.37}$$

$$\eta(x,t) = H\left[1 - 3/4H\tanh^2(\mu - k\lambda t)\right]\mathrm{sech}^2(\mu - k\lambda t) \tag{4.38}$$

where

$$k = \sqrt{3/4H\,(1 - 5/4H)} \tag{4.39}$$

$$\lambda = 1 + 1/2H - 3/20H^2 \tag{4.40}$$

$$\mu = kx \tag{4.41}$$

4.3.3 Piston wavemaker

Here a fully nonlinear numerical wave tank is simulated. See [60], [61], [62], [63], [43], [42], [51], [46], [6], [64], [45], [44], [65], among others.

Two fundamental cases have been tested: (i) when the paddle is moving generating single harmonic wave and (ii) the motion of the piston is given by the superposition of several harmonics.

The numerical piston starts moving at the initial time $t_i = 0$ when the fluid lies in a state of rest with the free surface being horizontal.

Boundary conditions on Γ_b *and* Γ_o

The outflow wall Γ_o and the bottom Γ_b are not time-depending and for both of them the no-flux condition is assigned as follows

$$v_b^n = \nabla\phi \cdot \bar{n} = 0 \quad \forall p \in \Gamma_b \tag{4.42}$$

$$v_o^n = \nabla\phi \cdot \bar{n} = 0 \quad \forall p \in \Gamma_o \tag{4.43}$$

Boundary conditions on the wavemaker Γ_i

According to [51], [6], [64], in the case of single harmonic, the piston moves with the following general law

$$x_p\,(t) = -\frac{A}{2}\cos\,(\omega t) \tag{4.44}$$

so that the position of the piston at the initial instant is given by the negative semistroke $-A/2$. From equation (4.44), the upstream flux assumes the following expression

$$v_p\,(t) = \frac{A}{2}\omega \sin\,(\omega t) \tag{4.45}$$

Note that since the unit normal vector is always outwardly oriented from the domain $\Omega\,(t)$, the Neumann boundary condition assumes the negative sign: $v_i^n\,(t) = -v_p\,(t)$.

Initial conditions

The fluid in the water tank is at rest, so that the initial conditions on the free surface are assumed as follows

$$\phi\,(p, 0) = 0 \quad \forall p \in \Gamma_f\,(0) \tag{4.46}$$

$$f\,(x, 0) = 0 \quad \forall p \in \Gamma_f\,(0) \tag{4.47}$$

where f is the elevation of the free surface with respect to the still water level, indeed we have $y_f\,(x_f, t) = f\,(x, t)$.

4.3.4 Absorbing beach

To reproduce a real wave tank, especially when simulating waves generated by piston wavemakers, it is necessary to avoid the reflection of the energy introduced into the system by the piston. This can be done by means of a damping layer which can be tuned in order do dissipate a certain amount of energy. See figure 4.8.

Thus, the waves are gradually attenuated along the beach which has a fixed length. Along this sponge layer both the kinematic and dynamic free surface boundary conditions have been modified by introducing the dissipative term as suggested in [64] as follows

$$\frac{D\phi\left(p,t\right)}{Dt} = -\frac{p_a}{\rho_w} - gy_f + \frac{1}{2}\nabla\phi\left(p,t\right)\cdot\nabla\phi\left(p,t\right) - \nu\left(p\right)\left(\phi - \phi_e\right) \quad \forall p \in \Gamma_f\left(t\right) \tag{4.48}$$

and for the free surface kinematic boundary condition (4.11), we have

$$\frac{D\bar{r}\left(p,t\right)}{Dt} = \bar{v}\left(p,t\right) = \nabla\phi\left(p,t\right) - \nu\left(p\right)\left(\bar{r} - \bar{r}_e\right) \quad \forall p \in \Gamma_f\left(t\right) \quad \forall p \in \Gamma_f(t) \tag{4.49}$$

where ϕ_e and $\bar{r}_e$ denote the velocity potential and the free surface particle position at the reference configuration, that is when no waves are being generated.

The absorbing piston located downstream at Γ_o as described in [61] is not necessary for our purposes.

Setting the function $\nu\left(p\right)$ is crucial as its strength makes the filter more or less effective. The scope of absorbing the incident wave energy before it reaches the wall and thus being reflected depends on the parameters which tune the following expression

$$\nu\left(x\right) = \alpha\omega\left[\frac{k}{2\pi}\left(x - x_0\right)\right]^2 \quad \forall x \in \left[x_0, x_1\right] \tag{4.50}$$

where x_0 is the starting point of the beach and $x_1 = x_0 + \frac{2\pi\beta}{k}$ is the channel length.

To fully absorb a wave characterized by ω and k as angular frequency and wave number respectively, the parameters α and β should both equal one.

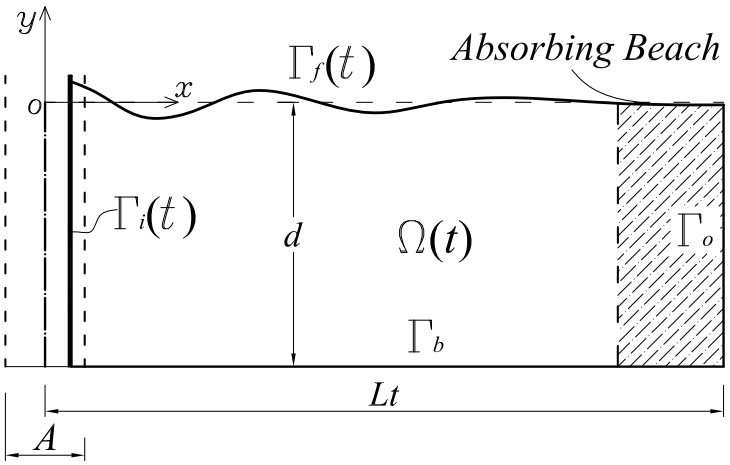

Figure 4.8: Sketch of the numerical wave tank equipped with a sponge layer.

4.4 Results

4.4.1 Stokes 2nd–order

The simulated wave is characterized by $H = 0.2\,\mathrm{m}$, $d = 2.5\,\mathrm{m}$, $L = 6.28\,\mathrm{m}$, $T = 2.019\,\mathrm{s}$. Where H denotes the wave height, d the water depth, L the wave length and T the period. The harmonic wave is simulated considering a numerical tank $4L = 25.12\,\mathrm{m}$ long[2].

Figure 4.9 shows the comparison between analytical and numerical free surface evolution obtained with $NE_f = 60$, $NE_b = 20$, $NE_i = NE_o = 10$, $dt = 0.05\,\mathrm{s}$. Where NE_α denotes the number of boundary elements on the α–boundary with $\alpha = i, b, o$ and i: inflow (upstream); b: bottom; o: outflow (downstream). Moreover, the smoothing scheme introduced above has been used.

4.4.2 Solitary wave

The parameters defining the solitary wave and the geometry of the numerical tank are

- wave height $H = 0.1\,\mathrm{m}$;
- water depth $d = 1\,\mathrm{m}$;

The number of elements on the free surface is $NE_f = 48$, while on the upstream, downstream and on the bottom there are $NE_i = NE_o = 8$ and $NE_b = 24$ elements, respectively. The time–step adopted to integrate the boundary conditions is $\mathrm{d}t = 0.05\,\mathrm{s}$.

[2]Note that $H/\left(gT^2\right) = 0.005$ and $d/\left(gT^2\right) = 0.0625$. These values make the simulated wave falling in the Stokes second order theory applicability, [37].

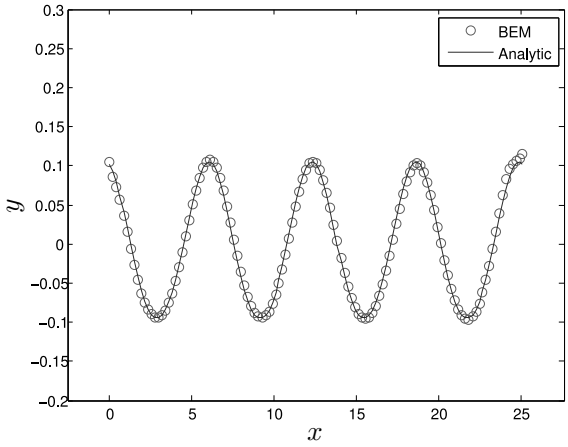

Figure 4.9: Analytical and numerical free wave propagation of a second order Stokes periodic wave. Free surfaces taken at $t = 2\,\mathrm{s}$.

To generate a solitary wave we assigned initial conditions from the analytical solution for $t = 0$. As said earlier, on the upstream, bottom and downstream walls the boundary conditions are defined by the impervious (no flux) condition.

Figure 4.10 shows the excellent agreement between the numerical results and the analytical solution. In addition to this, a proof of the efficiency of the code is given by computing both the total mass of the system and the flux trough the free surface. In the former the mass conservation is always guaranteed and in the latter zero flux balance is also preserved (with 10E-7 approximation).

The comparison presented in figure 4.10 has been intentionally limited to $t = 11$, because just further this dimensionless instant the run up starts, as shown in figures 4.11(c) and 4.11(d), and the comparison becomes meaningless.

A complete propagation is presented in figure 4.11 where also the run up is well visible. The simulation has been stopped at $t = 30$.

Simulation in figure 4.11 has been run with the following parameters: $NE_f = 64$, $NE_b = 20$; $NE_i = NE_o = 10$; $dt = 0.05$; $d = 1$. All the parameters have been made dimensionless by using water depth d for lengths and $\sqrt{gd}$ for time.

As already mentioned, along with fundamental comparisons with analytical results, some global quantities are also controlled to be in agreement with the theoretical expected values, naturally within some tolerance.

First, the total mass involved in the system has to be unchanged and this is shown in figure 4.12. Another useful check of the numerical reliability concerns the total flux balance. By using the divergence theorem, indeed, given Laplace's equation on a domain with boundary Γ, then it is possible to prove that

$$\int_{\Gamma} \frac{\partial \phi}{\partial \bar{n}} \mathrm{d}\Gamma = \sum_{j=1}^{NE_f} \int_{\Gamma_j} \sum_{k=1}^{3} \varphi_k(s)\, \mathrm{d}\Gamma q^{(j)} = 0 \tag{4.51}$$

where $\varphi_k(s)$ is the k–th shape function and NE_f the number of quadratic elements used to discretize the free surface. See appendix B for further details. Figure 4.13

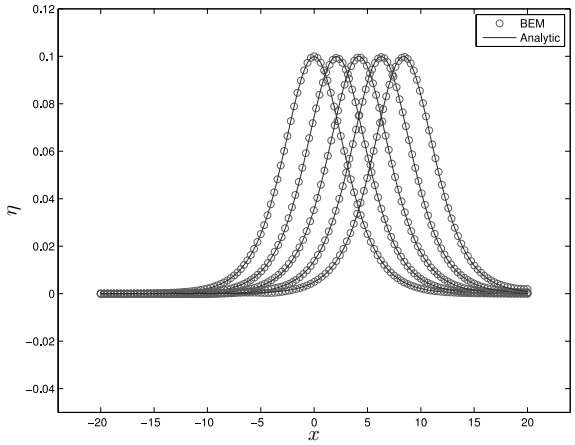

Figure 4.10: Analytical and numerical free wave propagation of a solitary wave. Free surfaces taken at each 40 time steps ($\Delta t = 40dt = 2$, from $t = 0$ to $t = 11$.

shows total flux balance during the propagation of the solitary wave.

4.4.3 Piston wavemaker: regular wave

The parameters concerning this simulation are itemized in the following. Note that all depends on the wave length L and the piston stroke S. The remaining parameters have been derived accordingly. The wave height in particular has been computed by invoking the linear transfer function.

- tank length $L_t = 32\,\mathrm{m}$;
- water depth $d = 1\,\mathrm{m}$;
- wave length $L = 8\,\mathrm{m}$;
- piston stroke $S = 2.0 \times 10^{-1}\,\mathrm{m}$
- wave number $k = 7.854 \times 10^{-1}$;
- angular frequency $\omega = 2.248\,\mathrm{rad/s}$;
- wave period $T = 2.795\,\mathrm{s}$
- celerity $c = 2.862\,\mathrm{m/s}$;
- wave height $H = 1.559 \times 10^{-1}\,\mathrm{m}$;
- $d/\left(gT^2\right) = 1.305 \times 10^{-2}$;
- $H/\left(gT^2\right) = 2.034 \times 10^{-3}$
- initial simulation time $t_i = 0$;

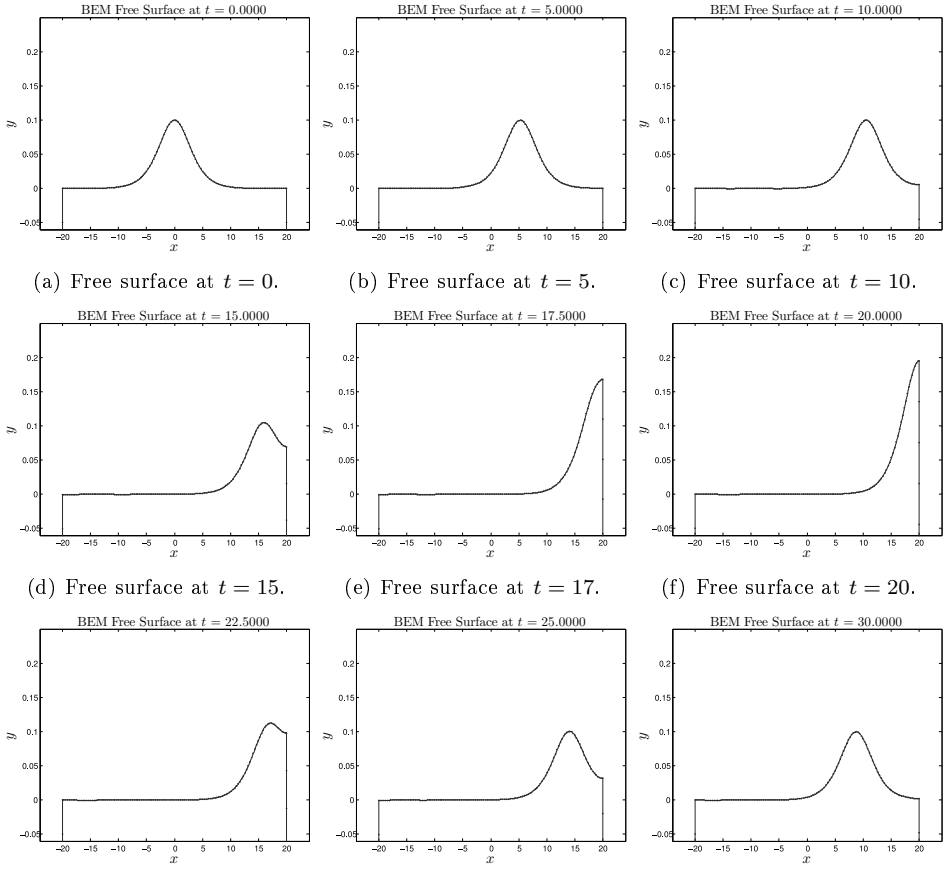

(a) Free surface at $t = 0$. (b) Free surface at $t = 5$. (c) Free surface at $t = 10$.

(d) Free surface at $t = 15$. (e) Free surface at $t = 17$. (f) Free surface at $t = 20$.

(g) Free surface at $t = 22.5$. (h) Free surface at $t = 25$. (i) Free surface at $t = 30$.

Figure 4.11: Propagation and run–up on an vertical wall of a solitary wave.

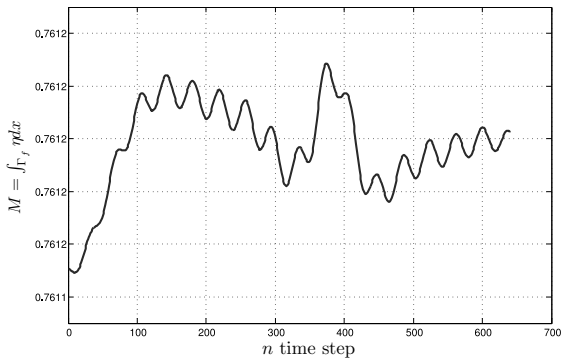

Figure 4.12: Mass conservation during the propagation of a solitary wave.

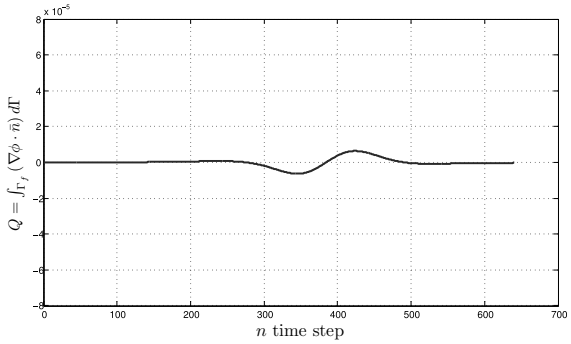

Figure 4.13: Total flux through the boundary during the propagation and runup of a solitary wave.

- final simulation time $t_f = T$;

Figures 4.14 to 4.18 show the evolution of a nonlinear regular wave generated by a piston wavemaker. They show the transient and the beginning of the stationary evolution. Even though linear theory is adopted for the transfer function, expected results in terms of wave length and wave height are excellently met.

This simulation implements also the absorbing beach which is fundamental in these type of simulations in order to avoid reflection. When a regular wave is being simulated, setting the numerical beach parameters is straightforward as the sponge layer is calibrated to absorb the whole energy associated with that single harmonic. In this case we have in fact

- $\alpha = 1$;
- $\beta = 1$;
- $x_0 = 24\,\mathrm{m}$;
- $x_1 = 32\,\mathrm{m}$;

where it results that the beach length just equals the wave length.

The number of elements on the free surface is $NE_f = 60$, while on the upstream (the paddle) and downstream boundaries we have $NE_i = NE_o = 2$. On the bottom there are $NE_b = 15$ elements. The time–step adopted to integrate the boundary conditions is $\mathrm{d}t = 0.05\,\mathrm{s}$.

4.4.4 Piston wavemaker: breaking wave

In this paragraph we show the capability of the code of simulating breaking waves induced by wave–wave interaction. Contrarily to the previous cases, where the augmentation of steepness is well controlled by the stroke of the piston, in this case we are to face a real fully nonlinear phenomenon which is characterized by very rapid increase of velocity together with high curvature regions of the free surface. This scheme is numerically very sensitive and a high resolution is required both in

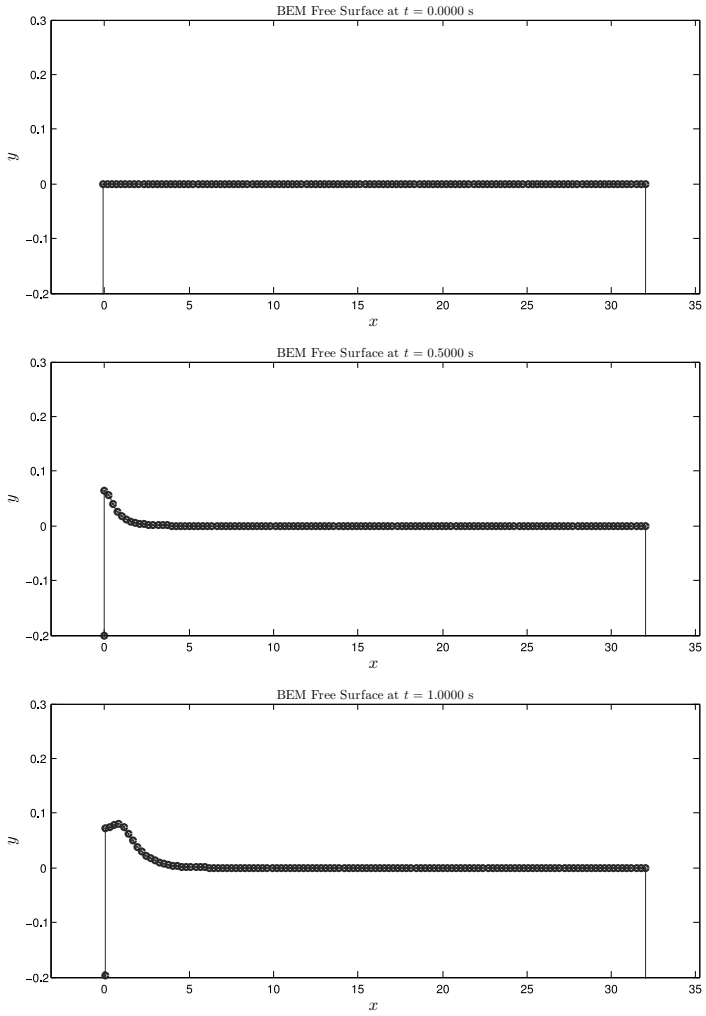

Figure 4.14: Propagation of a regular wave generated by a piston wavemaker.

space and in time whenever the wave becomes unstable. The refinement in space is gained by implementing a local mesh refinement subroutine while the latter is achieved by halving the integration time step when each node moves more than a fixed percentage of the adjacent elements length.

A deep water plunging breaking wave is here simulated according to [6], where an irregular wave field is generated by the following motion of the paddle

$$v_p(t) = \sum_{n=1}^{72} U_n \cos(\omega_n t - \theta_n) \tag{4.52}$$

where v_p is the velocity of the piston. The velocities U_n, the angular frequencies ω_n and θ_n the phases induce a breaking wave due to wave–wave interaction at 11.5 m

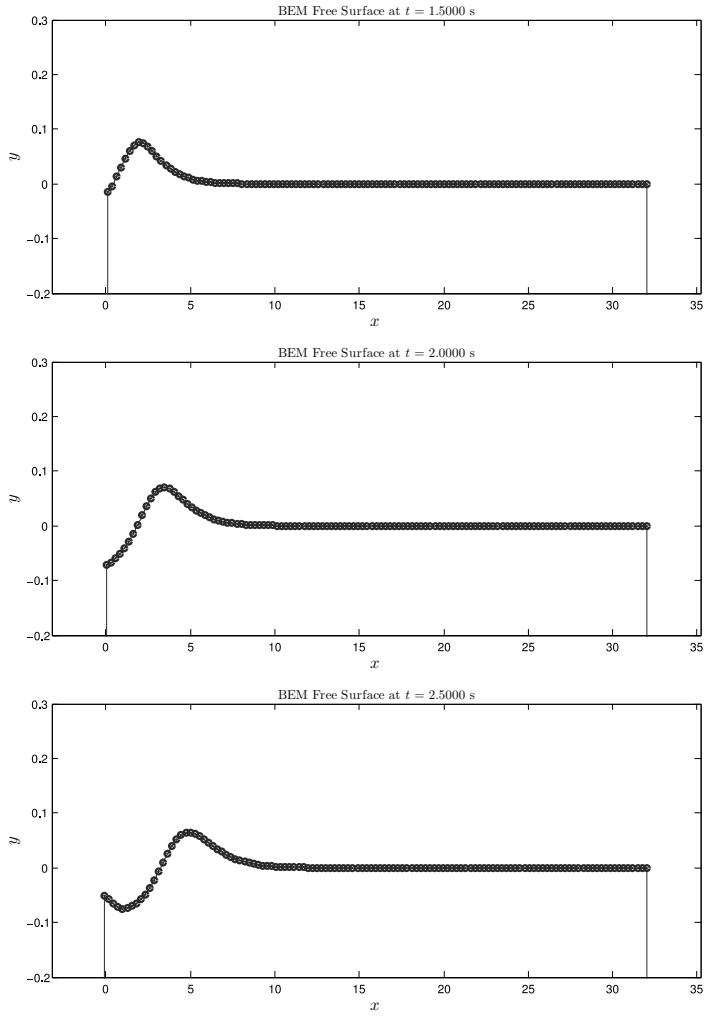

Figure 4.15: Propagation of a regular wave generated by a piston wavemaker.

approximately apart from the paddle and after 51.10 (non–dimensional) time from the beginning of the motion. All data necessary to implement equation (4.52) are available in [6].

The numerical tank has the following dimensions

- tank length $L = 20\,\mathrm{m}$;
- water depth $d = 1\,\mathrm{m}$;

Some selected snapshots of the free surface evolution are presented in figures 4.19 to 4.21. In particular, subplots of figure 4.19 show up to $t = 25$ (nondimensional time), while in figure 4.20 it is shown up to $t = 49.5$, which is just few instants before the steepness attains the critical value. Indeed, the three remaining subplots

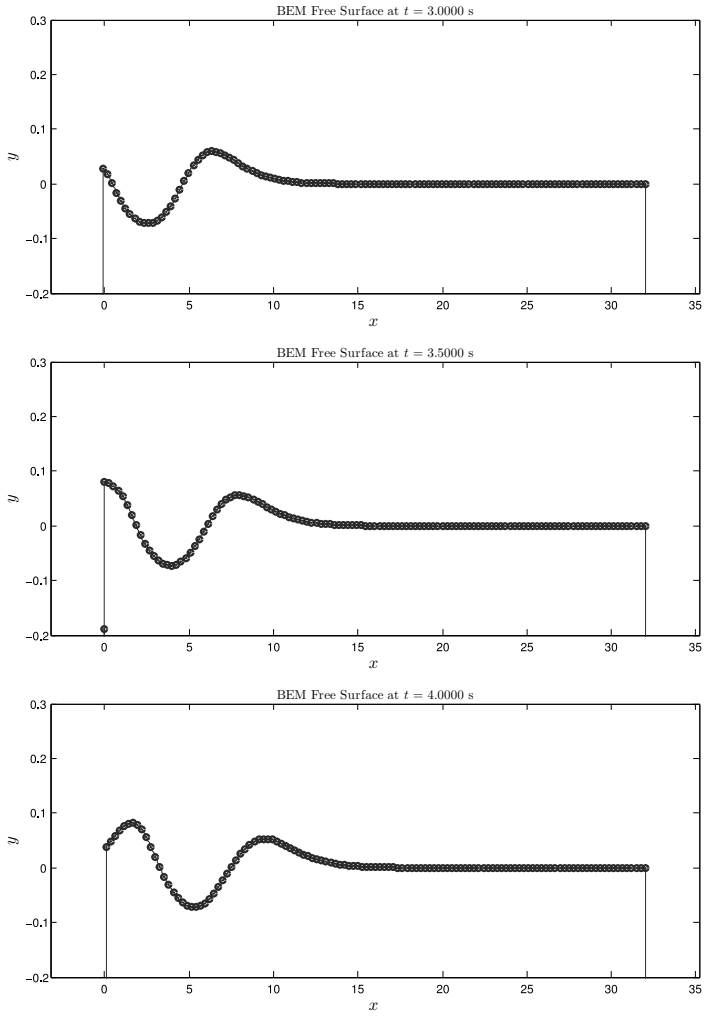

Figure 4.16: Propagation of a regular wave generated by a piston wavemaker.

shown in figure 4.21 depict the formation of the jet. From the figure it is also possible to note that the mesh has been refined a lot in the area where the cusp is forming. From this instant on it makes more sense to follow the evolution of the plunging breaker in an undistorted scale as in figure 4.22.

To validate the code and its capability of correctly simulating fully nonlinear waves, a comparison with experimental results obtained in [6] is presented in the following. Six numerical gauges are set at nondimensional distances of $x = 3.17$, 5.00, 6.17, 9.17, 10.83, 11.83 from the paddle and the time histories there numerically evaluated are compared with the experimental measurements. Figure 4.23 shows the free surface elevation over time for each probe.

The initial number of boundary elements of the free surface was $NE_f = 120$, then they self-adaptively increased whenever mesh refinement was needed. On the

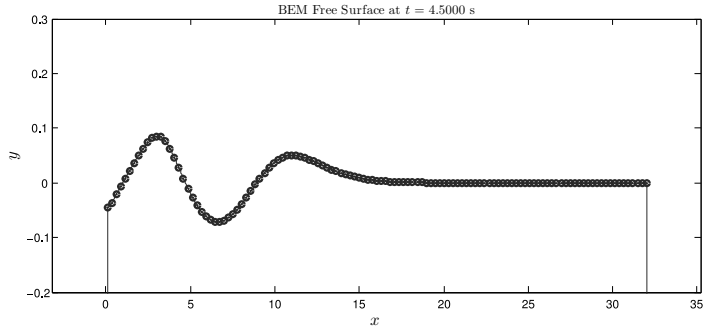

(a) Free surface at $t = 1s$.

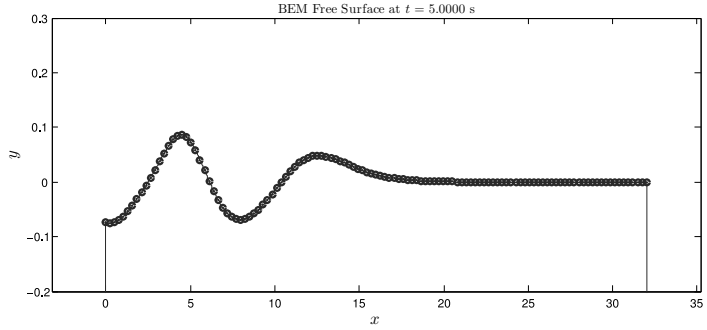

(b) Free surface at $t = 2s$.

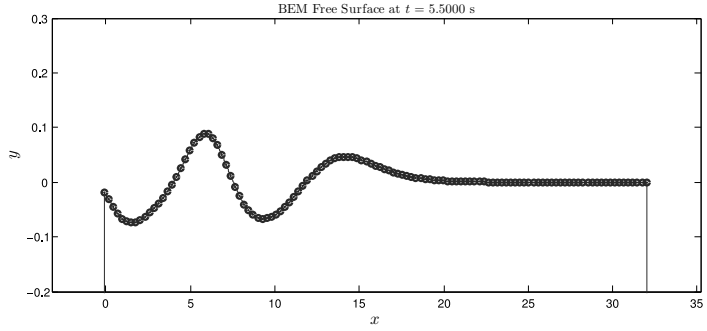

(c) Free surface at $t = 3s$.

Figure 4.17: Propagation of a regular wave generated by a piston wavemaker.

other boundaries there were $NE_i = NE_o = 3$, $NE_b = 30$ quadratic elements. The initial time–step adopted to integrate the boundary conditions was $\mathrm{d}t = 0.05\,\mathrm{s}$.

For the purpose of this thesis it is crucial to describe the water particles velocity during overturning. Figure 4.24 gives an example on how accurately it is possible to investigate such velocities with the present code.

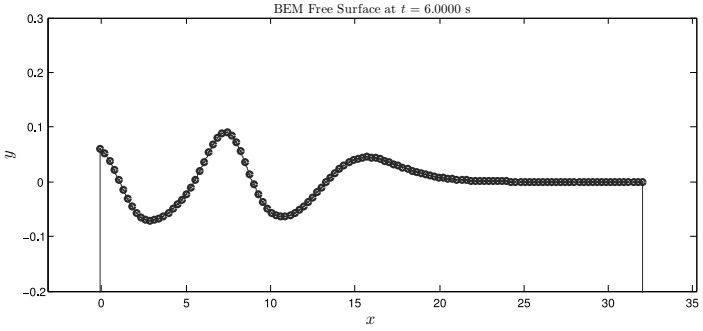

(a) Free surface at $t = 1s$.

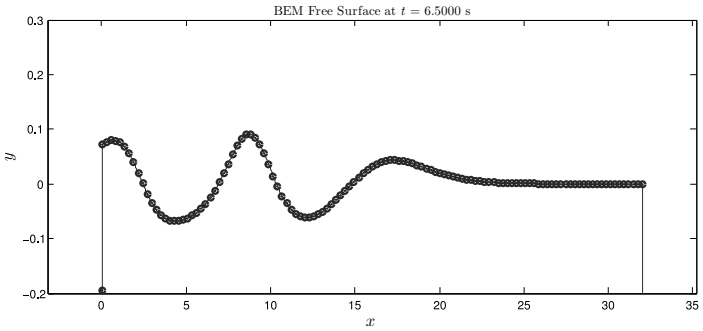

(b) Free surface at $t = 2s$.

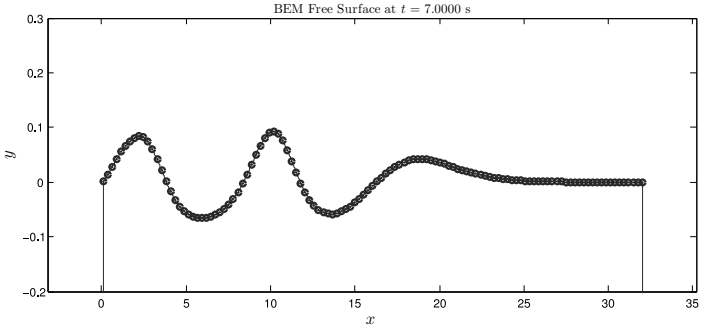

(c) Free surface at $t = 3s$.

Figure 4.18: Propagation of a regular wave generated by a piston wavemaker.

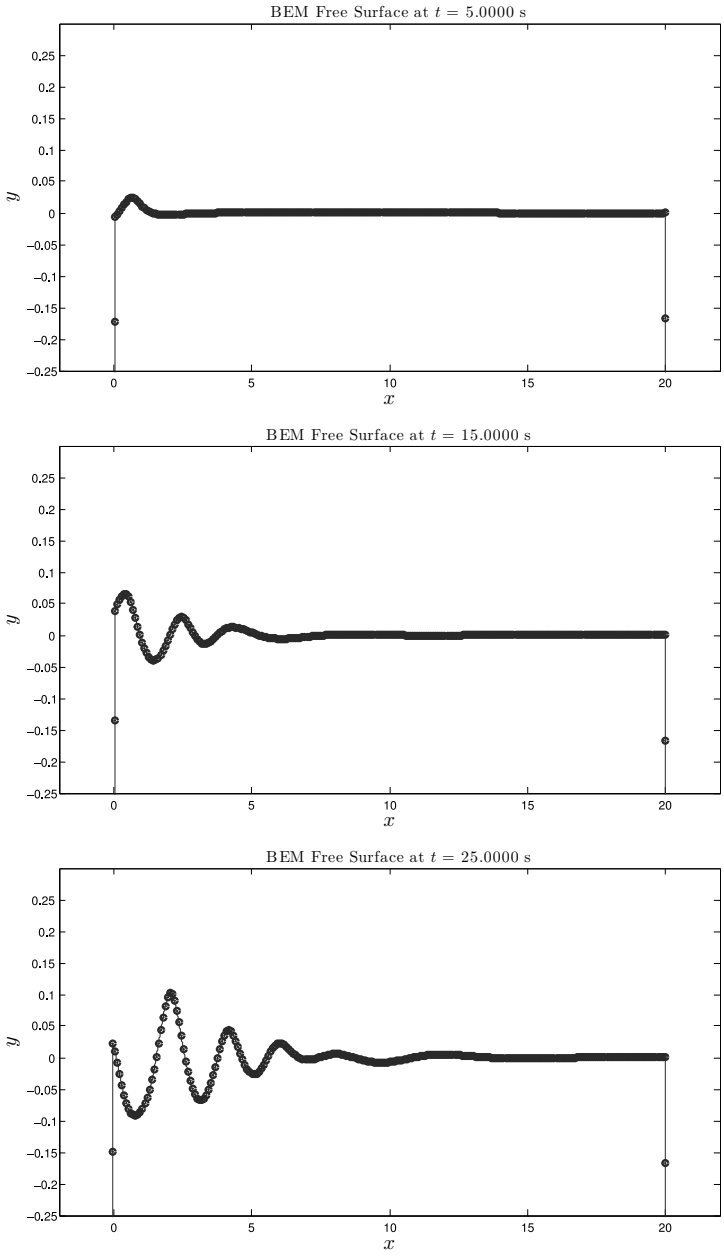

Figure 4.19: Propagation of a wave packet generated by a piston wavemaker.

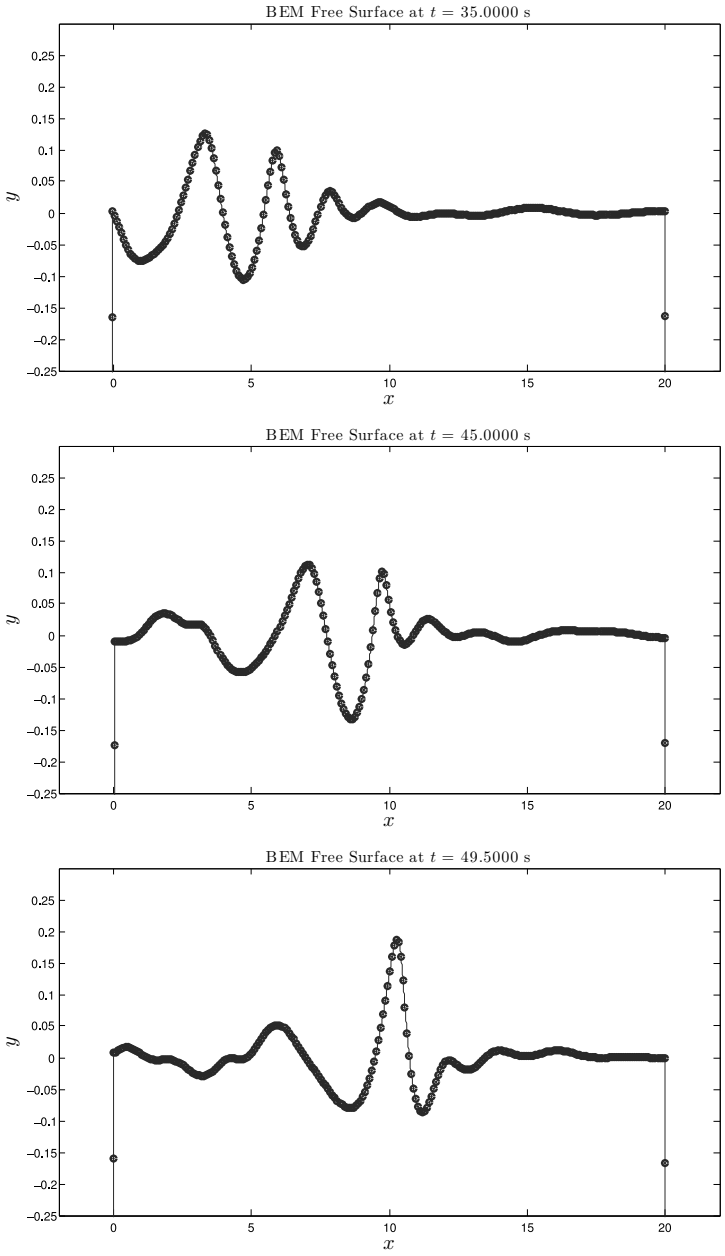

Figure 4.20: Propagation of a wave packet generated by a piston wavemaker.

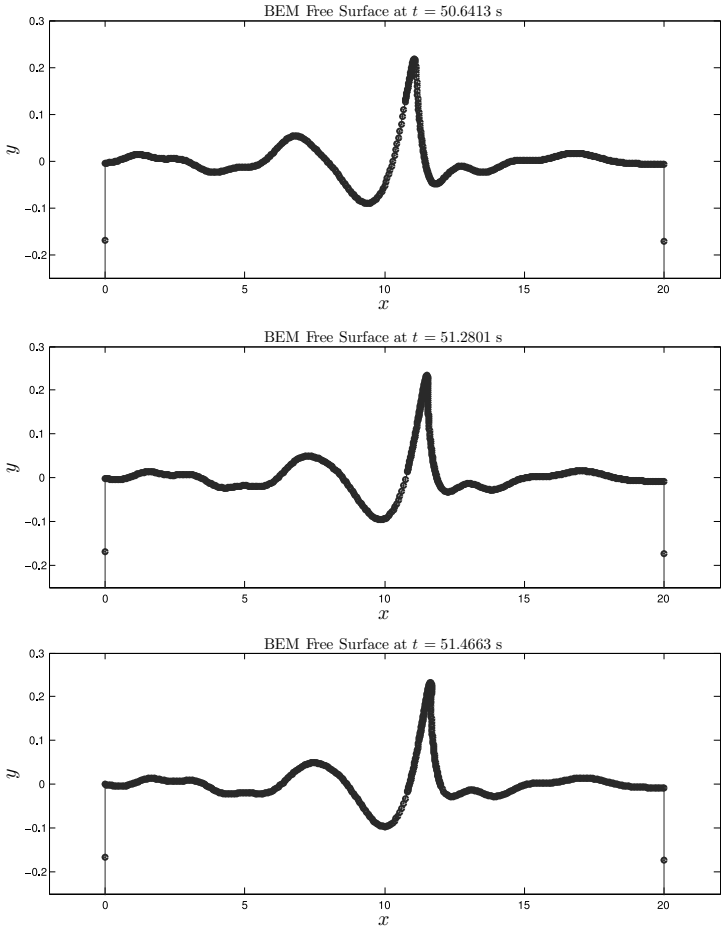

Figure 4.21: Propagation of a wave packet generated by a piston wavemaker.

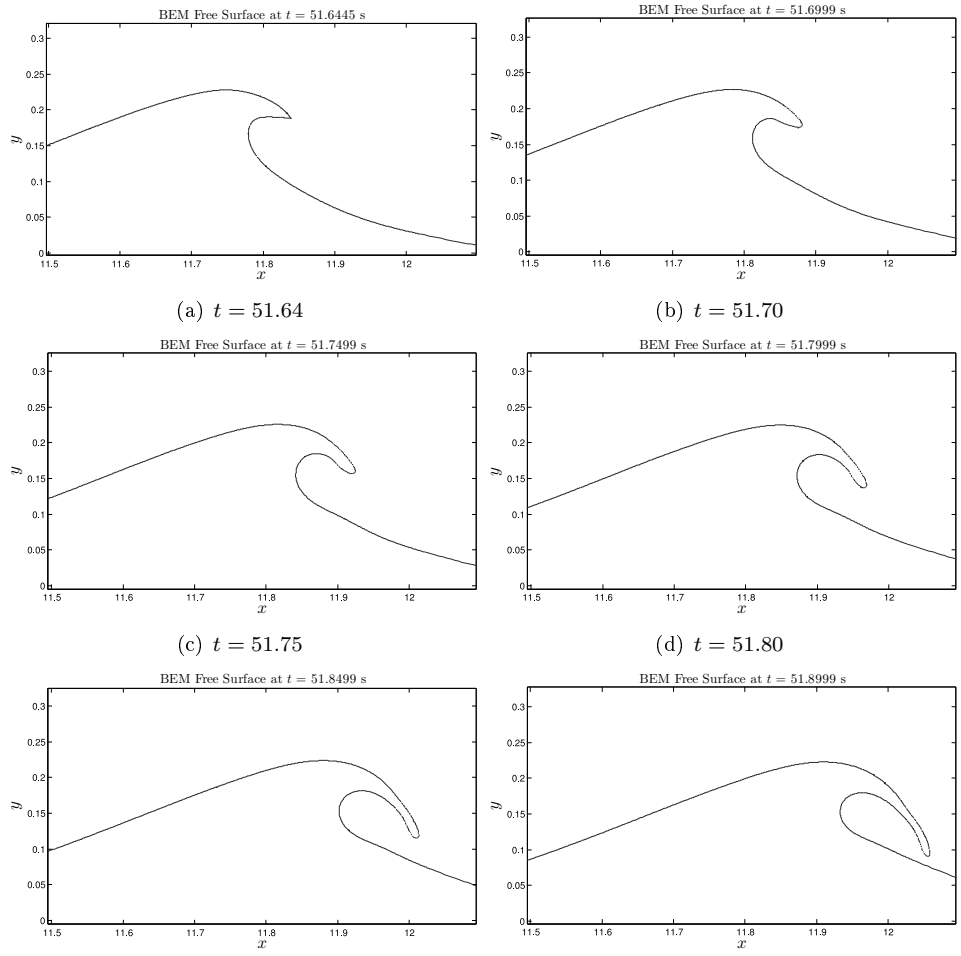

(a) $t = 51.64$ (b) $t = 51.70$

(c) $t = 51.75$ (d) $t = 51.80$

(e) $t = 51.85$ (f) $t = 51.90$

Figure 4.22: Evolution of the plunging breaker.

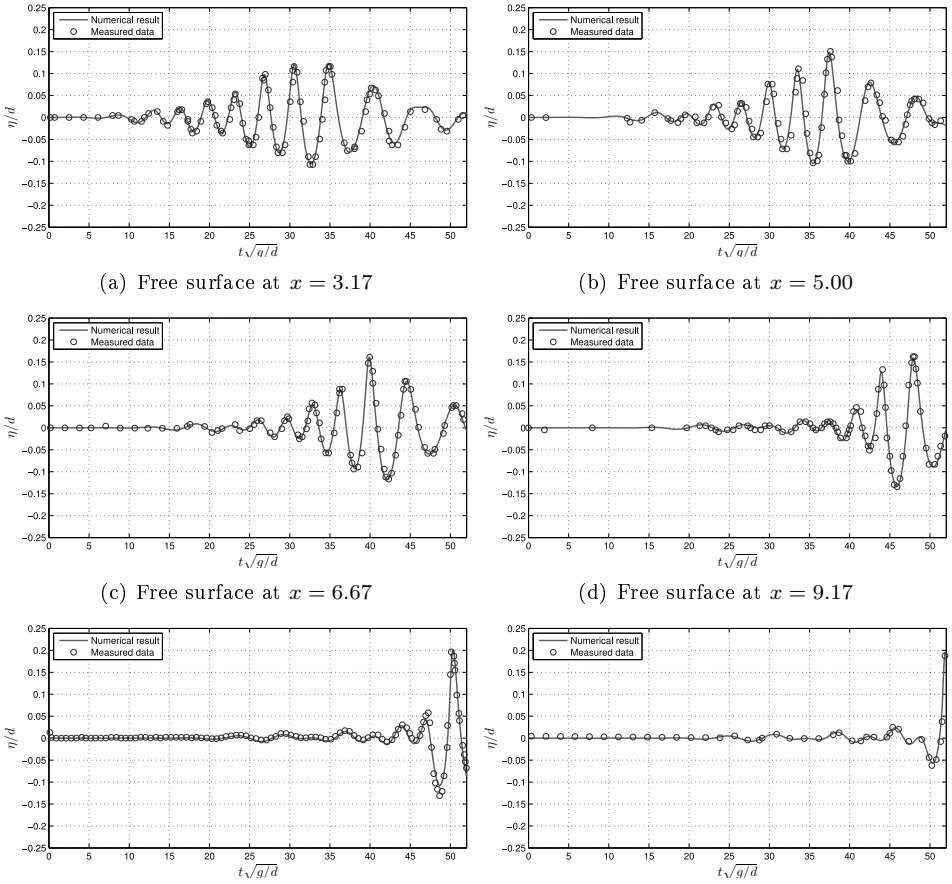

(a) Free surface at $x = 3.17$

(b) Free surface at $x = 5.00$

(c) Free surface at $x = 6.67$

(d) Free surface at $x = 9.17$

(e) Free surface at $x = 10.83$

(f) Free surface at $x = 11.83$

Figure 4.23: Numerical and experimental time histories of the free surface elevation at six probes.

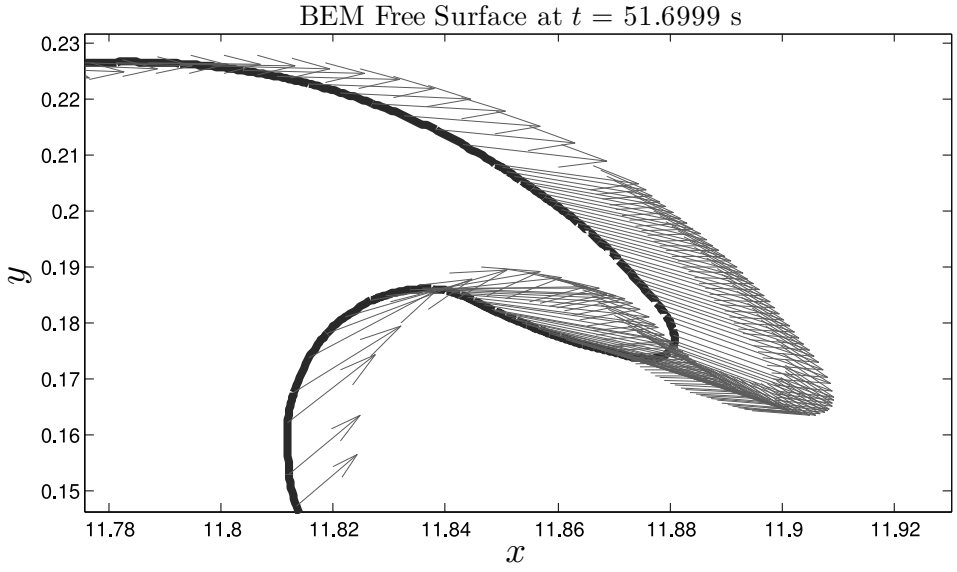

Figure 4.24: Velocities (red arrows) of the water particles at $t = 51.70$ of the spout evolution. Overturning wave generated by wave–wave interaction according to [6].

4.5 Impact wave model

The impact wave model adopted in the simulations performed in the next chapter is based on the Winke and Oumeraci's work [8]. The model applies to overturning deep water breaking waves. Before introducing the impact model, a very short review of breaking waves is presented in the next section. After this, Morison's equation will be recalled in order to prepare the background for the analysis of slapping wave loads.

4.5.1 Breaking waves

Among various special sea events present in nature, breaking waves definitively represent one of the most dangerous phenomenon. They may occur both in deep water and in shallow water, whenever the stability of the free surface is compromised by some reasons. In costal engineering the hazard represented by shallow water breaking waves is of primary interest, while when designing offshore structures deep water overturning breakers need to be taken into account carefully due their destructive potentiality. The shallow water instability is reached when the ratio wave height/water depth attains the theoretical value of 0.78 [5].

While the deep water breaking condition is reached when the wave steepness $\epsilon_b = H/L$ increases above the theoretical limit of 0.142. In the case of finite depth d, as it will be our case, the breaking limit becomes $\epsilon_b = 0.142 \tanh(kd)$ where k is the wave number. When a water wave becomes unstable it may break in four different ways, giving rise to the so called *spilling*, *plunging*, *collapsing*, *surging* breaking wave profiles, as shown in figure 4.25.

The most dangerous for the safety of offshore structures is definitely the plunging type which can cause strong and potentially destructive impacts.

Currently, there is no systematic methodology to take into account such extreme events when designing offshore structures and, above all, unless using computationally heavy CFD codes, they are only reconstructed by using empirical formula mostly suitable for deterministic design approaches. On this point it is worth quoting S.K. Chakrabarti who, in Chap. 3 of [10], says:

> "The theories described earlier for regular waves, including nonlinear Stokes waves and stream function theory, do not predict the kinematics and dynamic properties of very steep waves well. These waves are not only vertically unsymmetric, but also have large horizontal unsymmetry. If the design is based on these single steep waves, then a numerical theory need to be utilized. There are current attempts in describing such waves by the numerical wave tank methods and the method of New Waves [see Tromans, et a1 (1991) and Kim, et a1 (1999) for details]. These methods have not reached the design stage yet and are not commonly used in the design of offshore structures".

Plunging breakers definitely belong to the group the above quotation refers to when it mentions the horizontal asymmetry. Hence, what really deserves to be pointed out here is the fact that this thesis attempts to overcome what said in the last sentence of the above quotation. In fact, an *efficient* and *computationally*

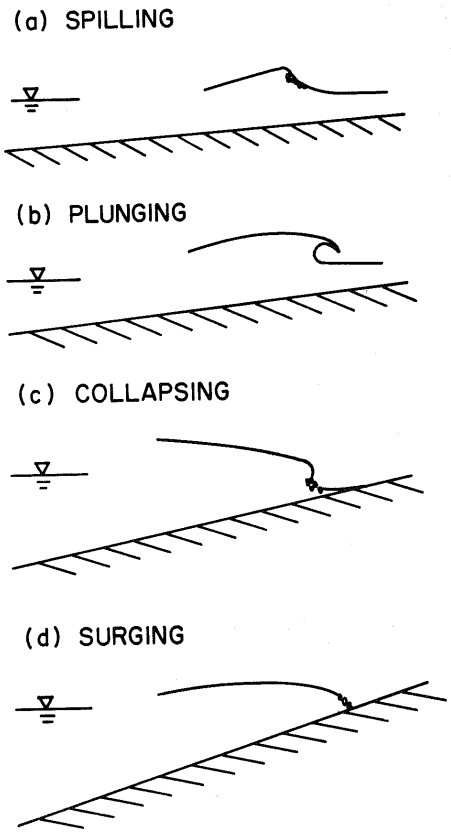

Figure 4.25: Different types of breaking waves, source [5].

effective numerical tool able to simulate very steep waves in a systematic way, overturning plunging breakers included, is offered to improve the standard design procedures.

4.5.2 Morison's equation

Wave forces on structures depend on many parameters, among which there are: time t, mean wave period T_z, mean wave length L, horizontal water particles velocity v, member diameter D, kinematic viscosity μ, member roughness κ, etc. All of these variables can be rearranged and somehow normalized to define some conventional quantities

- Keulegan–Carpenter's number: $KC = vT/D$;
- Reynolds' number: $Re = vD/\mu$;
- Diffraction parameter: D/L;
- Relative surface roughness: $\varepsilon = \kappa/D$;

Morison's equation applies only to those members which are considered slender, that is with the diffraction parameter lower than 0.2. Generally, we have

$$\frac{D}{L} \quad \begin{cases} < 0.2 & \text{Morison's equation} \\ \geq 0.2 & \text{Diffraction/Radiation theory} \end{cases}$$

Note that the KC number is also related to members main dimension. Consider in fact that for a fixed location, at the SWL, we have $\eta_{\max} = H/2$ and $v_{\max} = (gk/\omega)\,\eta_{\max}$. Recalling also the dispersion relation in deep water $\omega^2 = kg$, the KC number becomes

$$KC = \pi \frac{H}{D} \tag{4.53}$$

This means that the larger KC, the smaller the diffraction parameter. A general rule suggests that Morison's equation is valid for $KC > 6$ [14].

To develop the impulsive wave impact model it is necessary to start by analyzing how Morison's equation is composed [66]. The model takes into account the drag and inertia contributions induced by an undisturbed wave on a cylindrical member. Morison's equation is a useful and simple engineering tool because it has the great advantage of considering the whole wave kinematics as *if the cylinder were absent*. On the other hand it presents some important limitations and drawbacks. For example it does not take into account wave run–up and it is questionable its validity for all wave theories, especially for highly nonlinear cases. In particular, by adopting Morison's equation alone, extreme events like breaking waves cannot be considered at all.

The force per unit–length given by Morison in [66] is the following

$$f(t) = f_D(t) + f_M(t) = \frac{1}{2}\rho C_D D v(t)\,|v(t)\,| + \frac{\pi}{4}\rho C_M D^2 \dot{v}(t) \tag{4.54}$$

where C_M and C_D are the mass and drag coefficients, respectively; ρ_w is the water density.

The **drag** component in equation (4.54) would actually vanish if we had strictly to follow the the assumption of potential flow theory. Indeed, by virtue of this theory, one would end up into the famous *D'Alebert's paradox*. Nevertheless, by assuming the real pressure distribution around a cylinder, once accounted for the dependency on Reynolds' number, it is possible to describe the real drag force on the cylinder.

Concerning the **inertial** contribution in equation (4.54), by virtue of the pure potential theory one would find $C_M = 2$. Looking at the inertial term f_M we realize that $(D/2)^2\,\pi = \mathrm{vol}$ is the unit–length volume of the cylinder, and thus

$$f_M(t) = 2\rho\,\mathrm{vol}\,\dot{v}(t) \tag{4.55}$$

which is nothing but twice the inertial force associated with a "slice" of the cylinder under consideration. In the reality it has been proved that the inertial coefficient is not really equal to 2 but it is given as $C_M = 1 + k_M$. The sub coefficient "1" represents the inertial force owned by the flow able to move an amount of fluid having the volume vol, which is actually replaced by the material member. This contribution assumes an undisturbed flow.

However, the presence of the cylinder modifies the flow forcing the water particles to encircle the pile. Thus, particles undergo an acceleration which is provided by a force called *added mass*. k_M represents the added mass coefficient and depends on the shape of the object. See [67] and [33] for further details.

There are many researchers who proposed values for these hydrodynamic coefficients and of course it is not our intent to comment or list all of them. We just mention very few in order to get a practical idea. According to [13] typical values for the drag and inertial coefficients are given in table 4.2.

	$Re < 10^5$		$Re < 10^5$	
KC	< 10	≥ 10	< 10	≥ 10
C_D	1.2	1.2	0.6	0.6
C_M	2	1.5	2	1.5

Table 4.2: C_D and C_M proposed in [13].

Values proposed by the American Petroleum Institute API and by the Society of Naval Architects and Marine Engineers (SNAME) are shown in table 4.3

	smooth		rough	
	API	SNAME	API	SNAME
C_D	0.65	0.65	1.05	1
C_M	1.6	2	1.2	1.8

Table 4.3: C_D and C_M proposed by API and SANME.

Coefficients recommended by Det Norske Veritas (DNV) in [7] are only related to the KC number and the relative surface roughness ε. See figure 4.26.

However, as most of the recommended values in this work follow instructions given in [2], reference values for hydrodynamic coefficients may be found also in the International Standard ISO 13819 - 2, Part 2: Fixed Steel Structures.

The total force $F = F(t)$ acting on the member is then obtained by integrating the unit length force along the member up to the free surface elevation as follows

$$F(t) = F_D(t) + F_M(t) =$$
$$= \int_{-d}^{\eta} \frac{1}{2}\rho C_D D v(t)\,|v(t)|\,\mathrm{d}y + \int_{-d}^{\eta} \frac{\pi}{4}\rho C_M D^2 \dot{v}(t)\,\mathrm{d}y \tag{4.56}$$

To perform the integral in equation (4.56) it is necessary to extend the solution of the wave kinematic model up to the free surface, therefore the commonly linear and weakly nonlinear theory need to be adjusted because they provide solution up to the SWL. In the numerical model developed in the next chapter, Wheeler stretching is usually adopted, [68] and [10].

4.5.3 Impulsive load due to plunging breakers

Impact forces acting on offshore wind turbines can be two to four times larger than the non–impact forces stemming from waves of similar amplitude. And the

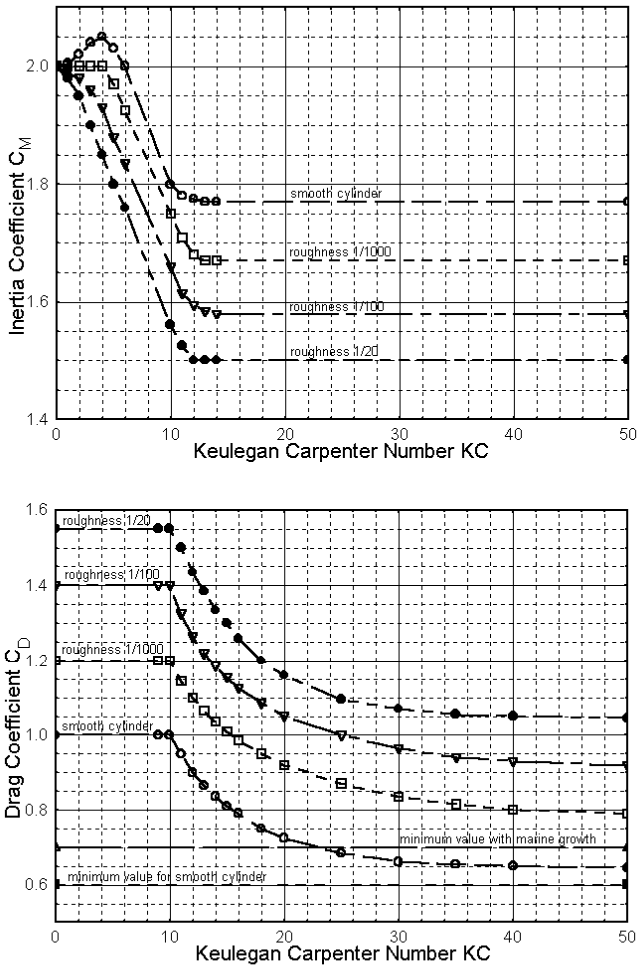

Figure 4.26: Hydrodynamic coefficients recommended by DNV, [7].

pressure due to impacts may be ten times larger than the non-impact pressure and it rises in a fraction of second.

Traditionally, the contribution of slamming waves is accounted for in a deterministic sense without considering its temporal development. Indeed, the drag component of Morison's equation (4.56) is just amplified by a factor which has a wide range of variation, typically from 2.5 to 5.15 [8], [69], [10]. [70].

Without considering the real time–history (though very short) of the impulsive contribution it is of course not possible to integrate such type of action in a full time domain analysis which accounts the global dynamic behaviour of the system.

Contrarily, the slapping contribution due to plunging breakers can be described by adjusting the original Morison's equation as follows

$$F(t) = F_D(t) + F_M(t) + F_I(t) \tag{4.57}$$

where F_I is the impulsive term. Wienke and Oumeraci in [71] and [8] developed a new analytical model to determine the impact force which results very accurate such as to represent a valid alternative to the earlier models proposed in [72], [32], [73], [74], among others.

Adopting a potential flow model and neglecting the surface tension as well as the the forces due to gravity, they found that for a rigid cylinder of radius R the impulsive force for unit length in 2D is given by

$$f_I(t) = \rho R v^2 \cos\gamma \left[2\pi\cos\gamma - 2\sqrt{\cos\gamma \frac{v}{R}t}\right] \cdot \cdot \left[\operatorname{arctanh}\sqrt{1 - \frac{1}{4}\frac{1}{\cos\gamma}\frac{v}{R}t}\right] \tag{4.58}$$

for

$$0 \le t \le \frac{1}{8}\frac{1}{\cos\gamma}\frac{R}{v} \tag{4.59}$$

And

$$f_I(t) = \rho R v^2 \cos\gamma \left[\pi\sqrt{\frac{1}{6}\cos\gamma\frac{1}{\frac{v}{R}t'}} - \left(\frac{8}{3}\cos\gamma\frac{v}{R}t'\right)^{\frac{1}{4}}\right] \cdot \cdot \left[\operatorname{arctanh}\sqrt{1 - \frac{v}{R}t'\sqrt{\frac{6}{\cos\gamma}\frac{v}{R}t'}}\right] \tag{4.60}$$

for

$$\frac{3}{32}\frac{1}{\cos\gamma}\frac{R}{V} \le t' \le \frac{12}{32}\frac{1}{\cos\gamma}\frac{R}{V} \tag{4.61}$$

where

$$t' = t - \frac{1}{32}\frac{1}{\cos\gamma}\frac{R}{V} \tag{4.62}$$

The duration T_i of the impact considered from the immersion time of the front line to the time of complete immersion of the half ellipse, see figure 4.27, is given by the following equation

$$T_i = \frac{13}{32}\frac{1}{\cos\gamma}\frac{R}{v} \tag{4.63}$$

Figure 4.28 shows the fundamental sketch the above formulation is referred to.

4.5.4 Numerical treatment of the plunging jet

The subroutine implementing equations (4.58) and (4.60) will need, as passed variables, both v and η_b. These two values are obtained from the numerical simulator discussed earlier. To this end, the forming water jet has to be analyzed carefully.

We start saying that for each time step of the simulation the free surface $\Gamma_f(t)$ is numerically known. So that in the space–time neighborhood of the expected impact event, a dedicated subroutine finds at which time the impact would happen. Let us imagine that the turbine is located at $x_t = 35\,\mathrm{m}$, see figure 4.29.

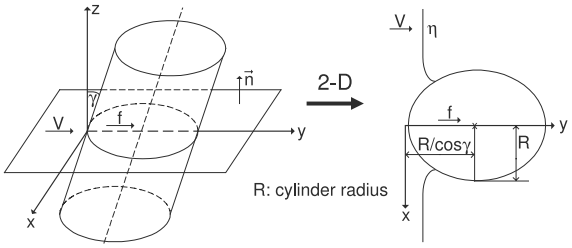

Figure 4.27: Sketch of the impact against an inclined cylinder. Image from [8].

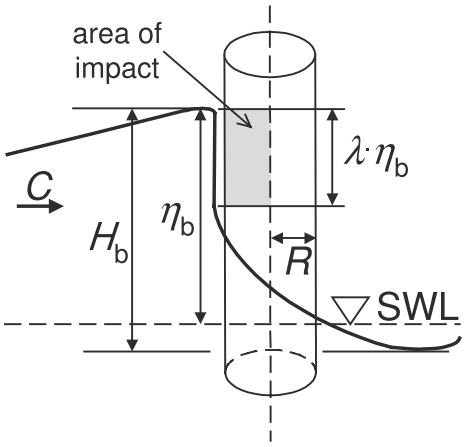

Figure 4.28: Sketch of the wave impact model. Image from [8].

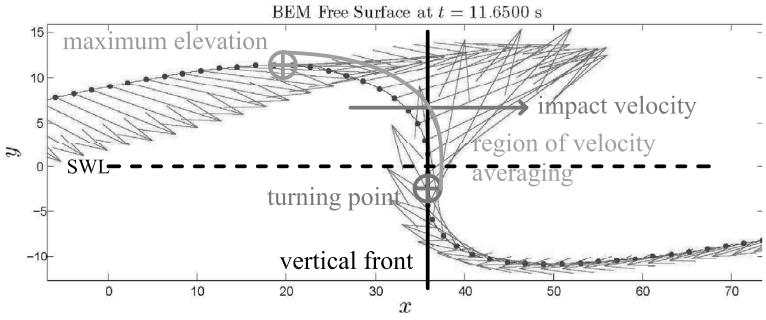

Figure 4.29: Example of the imminent overturning wave hitting the structure. At this time, η_b and $\bar{v}$ are computed.

At this impact time, the free surface looks like the example shown in figure 4.29. To get the maximum wave height η_b is trivial, while to compute the impact velocity v an "averaging region should be identified".

After many numerical runs we discovered that averaging the horizontal velocity components over a region included by the maximum wave elevation node and the

node being the turning point for the free surface curvature, gives acceptable results in estimating the impact velocity v. The turning point is found internally by the subroutine by checking for each element when a change of the curvature sign occurs[3]. See figure 4.29.

[3]For the j–th boundary elements the curvature $k^{(j)}$ is computed by using the well known formula

$$k^{(j)} = \left[\left(\dot{x}\ddot{y} - \dot{y}\ddot{x} \right) / \left(\dot{x}^2 + \dot{y}^2 \right) \right]^{3/2}$$

where the derivatives are trivially carried out due to the simplicity of the shape functions.

Chapter5
Coupled wind–fully nonlinear waves model

This chapter represents the second main part the thesis, where the fully nonlinear water waves simulator developed in Chapter 4 is coupled with a hydro-aero-elastic solver of the whole system. The chapter begins by describing the solvers, then it enters into the details of the wind and wave loads simulations, and finally the fully coupled analyses are presented.

5.1 Solvers description

Here we will introduce the basic features of FAST: a combined modal and multi–body dynamics simulator [9]. The version used in this thesis is FAST_v602c–jmj which is a not–yet–released version. As it is an alpha version all the the new capabilities of the software, in particular the hydrodynamic module, are not yet documented.

However, due to the support provided by the National Renewable Energy Laboratory (NREL, Colorado)[1], it was possible not only to use the new modules but also to set up and implement the new impact model developed in this thesis. A detailed description of this new capability is presented in the next section.

For three–bladed wind turbines FAST has up to 24 DOFs. All DOFs come from modeling rigid and flexible system components: tower, blades, etc. Reference [9] offers a detailed description of each DOF. The modus operandi of FAST (the parts relevant for our case) is sketched in figure 5.1, which also shows the input/output structure of the code.

The aeroelastic forces acting on the rotating blades are computed by AeroDyn which is internally called by FAST's main program at each time step. To compute the aerodynamic forces, AeroDyn implements both the Blade Element Momentum theory and the Generalized Dynamic Wake model [35], see Chapter 3.

To give an overview of the fundamental features of the solver we will shortly describe all the input files which are necessary to the simulations, see figure 5.1.

5.1.1 FAST input

- **Primary input file: **.fst***: contains many sets of the parameters which have to be entered. We mention just the following:
  - PLATFORM which calls an additional input file containing the platform properties (.dat)

[1] In the person of Jason Jonkman.

Enzo Marino, *An integrated nonlinear wind-waves model for offshore wind turbines*
ISBN 978-88-6655-051-8 (print) ISBN 978-88-6655-053-2 (online) © 2011 Firenze University Press

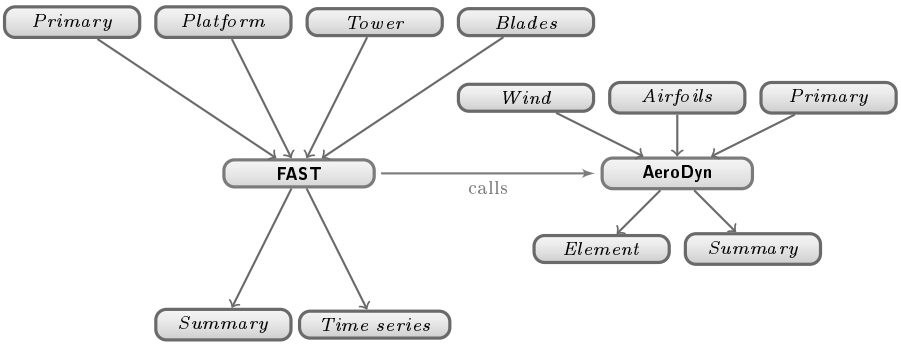

Figure 5.1: Selected files involved in FAST and AeroDyn.

  - TOWER which calls an additional input file containing the tower properties (.dat)
  - BLADE which calls additional input file(s) containing data about the blades (.dat)
  - AERODYN which calls an additional input file containing AeroDyn input parameters (.ipt)
    * the .ipt file calls the file containing the wind data (.wnd)
    * the .ipt file calls the file containing the airfoil data (.dat)
  - OUTPUT which itemizes the output channels required

- **Platform (monopile) input file **.dat***: also in this case we mention the blocks more relevant for our scope:
  - MASS AND INERTIA (relative to the platform)
  - PLATFORM (loading model 0: none, 1: user-defined from routine UserPtfmLd (switch))
  - TOWER (Loading model)
  - WAVES
  - CURRENT
  - OUTPUT

- **Tower input file **.dat***: the data sets required in this file are:
  - TOWER PARAMETERS
  - TOWER ADJUSTMUNT FACTORS
  - TOWER FORE-AFT MODE SHAPES
  - TOWER SIDE-TO-SIDE MODE SHAPES

- **Blade input file **.dat***:
  - BLADE PARAMETERS
  - BLADE ADJUSTMENT FACTORS
  - DISTRIBUTED BLADE PROPERTIES
  - BLADE MODE SHAPES

5.2 5–MW Baseline reference model

This section is devoted to a brief description of the model adopted in all the simulations carried out to test the new hydrodynamic model proposed.

The turbine model is the 5–MW Reference Wind Turbine for Offshore System Development. See Figure 5.2 for its general layout.

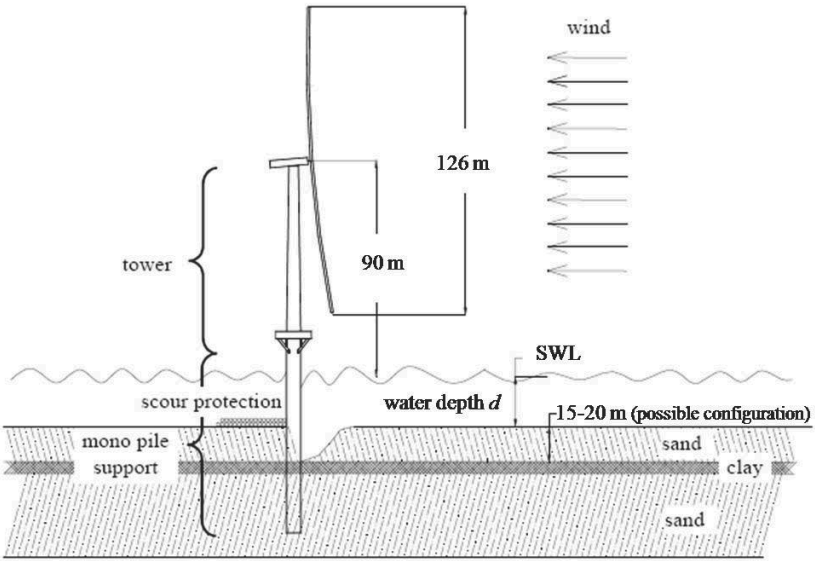

Figure 5.2: Layout of the model.

This model has been created by J. Jonkman et al. at the National Renewable Energy Laboratory (NREL, Colorado) with the aim of creating a common reference basis to pave the way for further investigations concerning offshore wind turbines located both in shallow and deep waters. In [75] the authors specified all the technical characteristics of the hypothetical, but realistic, multi-megawatt large wind turbine model by combining some available data from different machines (e.g. REpower 5–MW and Arveva Multibrid 5000) together with data assumed in some conceptual models of projects like RECOFF, etc. NREL 5–MW Baseline Wind Turbine gross properties are itemized in table 5.1.

In the following sections a short description of the model is given. Further details are available in [75], [76] and their bibliography.

5.2.1 Rotor and support structure

Rotor blades

The turbine has three blades with structural properties of the 62.6 m–long LM Glasfiber blade used in the DOWEC study. As this type of blade is 1.1 m longer than the 61.5 m–long LM Glasfiber blades adopted on the actual REpower 5–MW machine, in [75] they truncated the 62.6 m–long blades at 61.5 m span to obtain the

Rating Power	5 MW
Rotor Orientation, Configuration	Upwind, 3 Blades
Control	Variable Speed, Collective Pitch
Drivetrain	High Speed, Multiple-Stage Gearbox
Rotor, Hub Diameter	126 m, 3 m
Hub Height	90 m
Cut-In, Rated, Cut-Out Wind Speed	3 m/s, 11.4 m/s, 25 m/s
Cut-In, Rated Rotor Speed	6.9 rpm, 12.1 rpm
Rated Tip Speed	80 m/s
Overhang, Shaft Tilt, Precone	5 m, 5°, 2.5°
Rotor Mass	110 t
Nacelle Mass	240 t
Tower Mass	347.460 t
Coordinate Location of Overall CM	(−0.2 m, 0.0 m, 64.0 m)

Table 5.1: Key properties of the NREL 5–MW Baseline Wind Turbine.

structural properties of the NREL 5–MW baseline blades. Then properties at 61.5 m have been found interpolating the two properties at 61.2 m and 61.7 m stations. More exhaustive data are available in [77]. Each single blade is made up of three different varying geometries. Each different geometry is described in its special file where the aerodynamical properties are assigned. See table 5.2. Appendix B of [75] reports all the mentioned files.

Tower and pile

The tower adopted in the NREL baseline model is tubular shaped and has the same geometric characteristics of the tower used in the DOWEC study [76]. Table 5.3 summarizes the key geometric parameters. The tower diameter and wall thickness are assumed to vary linearly. The base diameter of 6 m is equal to the diameter of the monopile.

Regarding the substructure, the main properties are itemized in table 5.4.

Note that in general FAST uses the following variables to model the platform. As shown in Figure 5.3, TwrDraft denotes the downward distance from the Still Water Level (SWL) to the tower base platform connection. PtfmCM and PtfmRef represent the distance from the SWL and the platform center of mass and the platform reference point, respectively. The latter is the point where the platform DOFs are located. These three parameters are useful for modeling floating platforms, in our case they all equal the water depth $d = 20\,\mathrm{m}$.

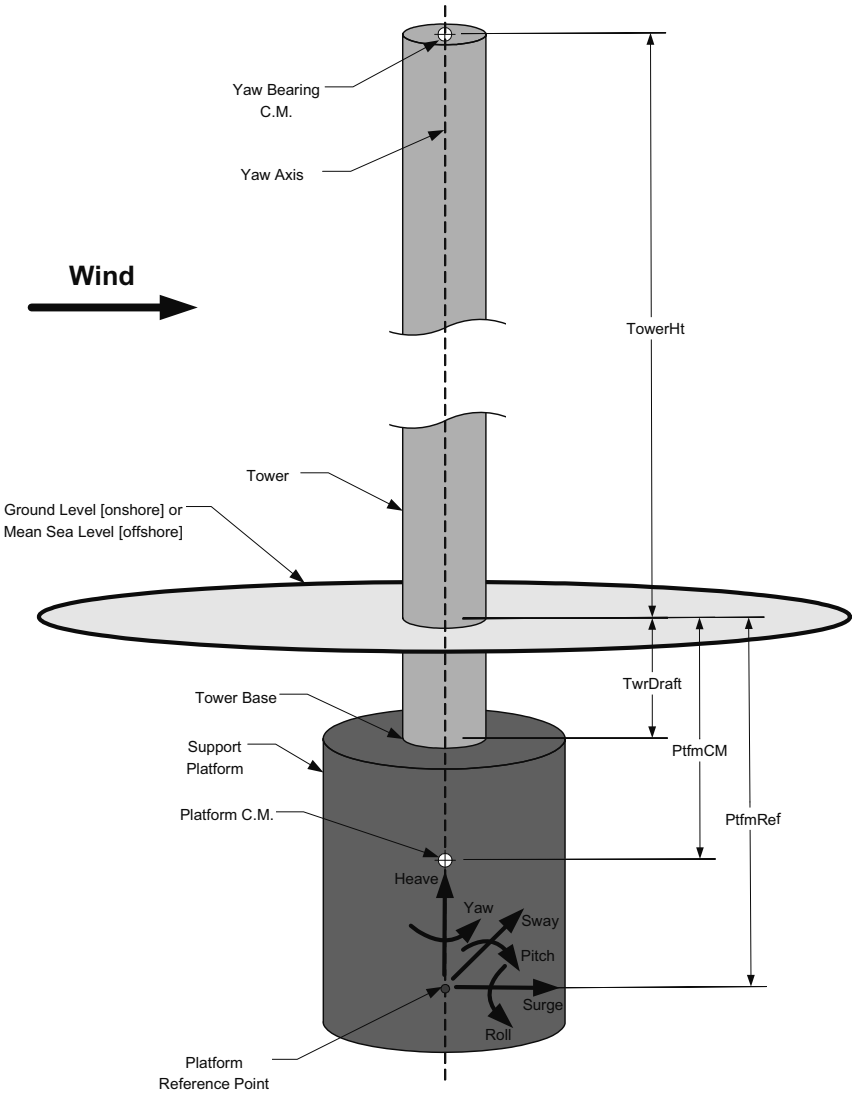

Figure 5.3: Platform scheme. Image from from [9]

Node	RNode	AeroTwist	ΔRNode	Chord	Airfoil Table
1	2.8667	13.308	2.7333	3.542	Cylinder1.dat
2	5.6000	13.308	2.7333	3.854	Cylinder1.dat
3	8.3333	13.308	2.7333	4.167	Cylinder2.dat
4	11.7500	13.308	4.1000	4.557	DU40_A17.dat
5	15.8500	11.480	4.1000	4.652	DU35_A17.dat
6	19.9500	10.162	4.1000	4.458	DU35_A17.dat
7	24.0500	9.011	4.1000	4.249	DU30_A17.dat
8	28.1500	7.795	4.1000	4.007	DU25_A17.dat
9	32.2500	6.544	4.1000	3.748	DU25_A17.dat
10	36.3500	5.361	4.1000	3.502	DU21_A17.dat
11	40.4500	4.188	4.1000	3.256	DU21_A17.dat
12	44.5500	3.125	4.1000	3.010	NACA64_A17.dat
13	48.6500	2.319	4.1000	2.764	NACA64_A17.dat
14	52.7500	1.526	4.1000	2.518	NACA64_A17.dat
15	56.1667	0.863	2.7333	2.313	NACA64_A17.dat
16	58.9000	0.370	2.7333	2.086	NACA64_A17.dat
17	61.6333	0.106	2.7333	1.419	NACA64_A17.dat

Table 5.2: Distributed blade aerodynamic properties.

Tower base diameter, wall thickness	6 m, 0.027 m
Tower top diameter, wall thickness	3.87 m, 0.019 m

Table 5.3: Tower geometric properties.

Pile length[2], diameter	20 m, 6 m
Pile wall thickness, total weight	0.060 m, 187.90 t

Table 5.4: Monopile properties.

5.3 New slamming wave module in FAST

As already mentioned, FAST is a Fortran open source code developed at NREL with the extraordinary feature of having some subroutines which can be defined by the user upon their specific needs. This was, indeed, the case of this work where the impact forces associated with some probable extreme seas, first computed externally by dedicated simulations, are passed to the time marching solver by means of the used defined subroutine UserTwrLd. This subroutine provides user defined tower loading in the case of monopile substructure.

Before describing how the impact model has been implemented, it is useful to give just an overview about the subroutine MorisonTwrLoading. The latter is stored in the *HydroCalc.f90* file and provides the forces acting on the tower calculated by means of Morison's equation. File *HydroCalc.f90* also contains all the necessary subroutines to generate the requested sea: linear regular or linear irregular. The latter can be generated by adopting either the Pierson–Moskowitz or the JONSWAP

spectrum. However we will always use our external sea generator.

The most important input parameters that control the wave kinematics are provided by the "platform monopile" input file (see previous section). In the present case the following parameters are frequently invoked: TwrLdMod (from block TOWER), which sets the tower loading model (0: none, 1: Morison's equation, 2: user-defined from routine UserTwrLd).

From block WAVES, the parameters WaveMod, WaveStMod WaveTMax, WaveDT are crucial to develop the new impact model. The first, WaveMod, sets the type of incident wave kinematics (0: none, that is still water, 1: plane regular, 2: irregular with JONSWAP or Pierson–Moskowitz spectra, 3: user–defined spectrum from routine UserWaveSpctrm, 4: GH Bladed wave data). WaveStMod sets the type of stretching, that is how to extend the linear solution, which is valid only up to the still water level, up to the instantaneous free surface elevation. Switches for WaveStMod are 0: no stretching, 1: vertical stretching, 2: extrapolation stretching, 3: Wheeler stretching. WaveTMax and WaveDT set the total simulation time and the time step, respectively.

To implement the new slapping wave module we first need to pass to FAST the wave kinematics consistent with the actual extreme sea which may contain some breaking wave events. Hence, the random sea is generated externally, see section 5.4 for details, then it is passed to FAST by the same way it reads in the wave kinematics files generated by GH Bladed. Namely, three files are necessary. They all have the same name root which can be assigned as input.

- *FNL_FAST.txt*
- *FNL_surface.txt*
- *FNL_kinematics.txt*

where *FNL* (in this case) is the passed name root.

FNL_FAST.txt contains the coordinates of the points where the kinematics is provided. The coordinates are expressed with respect to a planar system with the vertical axis y upward oriented and passing by the center of the monopile, while the x–axis points in the direction of the wave propagation. The origin is fixed at the still water level. *FNL_surface.txt* stores the free surface elevation at the wind turbine location ($x_t = 0$) during the whole simulation time WaveTmax, while *FNL_kinematics.txt* provides:

- particles velocity along x–axis , v^x
- particles velocity along z–axis , v^z (always zero in 2D model)
- particles velocity along y–axis , v^y
- particles acceleration along x–axis , a^x
- particles acceleration along z–axis , a^z (always zero 2D model)
- particles acceleration along y–axis , a^y
- dynamic pressure p_D

To understand the structure that *FNL_ kinematics.txt* must have to be correctly read in by FAST, here there is an example of the Matlab function generating it:

```
function [] = write_kinematics(Elevx0,time,y)

global Aw omega k_w phase rho_w g d
% NOTE: xt = 0!

fid = fopen('fast\FNL_kinematics.txt','w'); for i = 1:length(time)
    for h = 1:length(y)
        % With Wheeler stetching
        eta = Elevx0(i);
        if y(h) <= eta
        q = d/(d+eta);
        vx = sum(Aw.*omega    .* cosh( k_w.*( d + q*y(h) + d*(q-1)) )./sinh(k_w.*d).*cos(-omega.*time(i)+phase));
        vy = sum(Aw.*omega    .* sinh( k_w.*( d + q*y(h) + d*(q-1)) )./sinh(k_w.*d).*sin(-omega.*time(i)+phase));
        ax = sum(Aw.*omega.^2 .* cosh( k_w.*( d + q*y(h) + d*(q-1)) )./sinh(k_w.*d).*sin(-omega.*time(i)+phase));
        ay =-sum(Aw.*omega.^2 .* sinh( k_w.*( d + q*y(h) + d*(q-1)) )./sinh(k_w.*d).*cos(-omega.*time(i)+phase));
        p  = rho_w*g*sum(Aw   .* cosh( k_w.*( d + q*y(h) + d*(q-1)) )./cosh(k_w.*d).*cos(-omega.*time(i)+phase));
        else
        vx = 0;
        vy = 0;
        ax = 0;
        ay = 0;
        p  = 0;
        end
        fprintf(fid,'%d   %d   %d   %d   %d   %d   %d\r\n',vx, 0, vy, ax, 0, ay, p);
    end
end fclose(fid);
```

To check whether the wave kinematics provided by using external text files were correct, a very simple test comparing results obtained adopting both simulators has been carried out.

A simple regular wave has been generated first by using the internal wave solver, then by passing data provided by our external solver. For the sake of simplicity no wind is assumed to blow and the turbine is parked. The incident regular periodic wave is characterized by the following wave height and wave period: $H = 12\,\mathrm{m}$ and $T = 12\,\mathrm{s}$.

For both the simulations shown in figures 5.4 and 5.5, hydrodynamic forces are computed by using Morison's equation, i.e. TwrLdMod: 2, while WaveMod is 1 when the wave is simulated internally and 4 when read in from text files. Note that WaveMod 4 means loading GH Bladed wave files, but in the present case our own simulator is used. Only the file format and their organization is passed according to GH Bladed file type.

By comparing the tower base forces shown in figure 5.4(a) and 5.5(b), it is evident that the kinematics passed gives the same results than WaveMod 1. In fact, forces have the same period and amplitude.

Moreover, as expected, the same agreement is observed by comparing the tower base moments. Indeed, also for them, the structural response shown in figures 5.5(a) and 5.4(b) is basically the same.

Note that both for tower base forces and moments, meaningful comparisons are made between M_{yt} and F_{yt}. The remaining internal forces are reported just for the sake of completeness.

At this stage, once it has been proved that the external wave solver developed in the framework of this thesis works well, it is possible to move on to the impact model. As already said, a short introduction of MorisonTwrLd may be helpful as Morison's equation is the starting point for the impulsive contribution, see section 4.5. The subroutine needs as input variables the current tower node, the tower diameter, the inertial and drag coefficients, the three components of the translational and the three components of the rotational displacements, the three components of the translational and the three components of the rotational (angular) velocities. Moreover, the current simulation time is also needed.

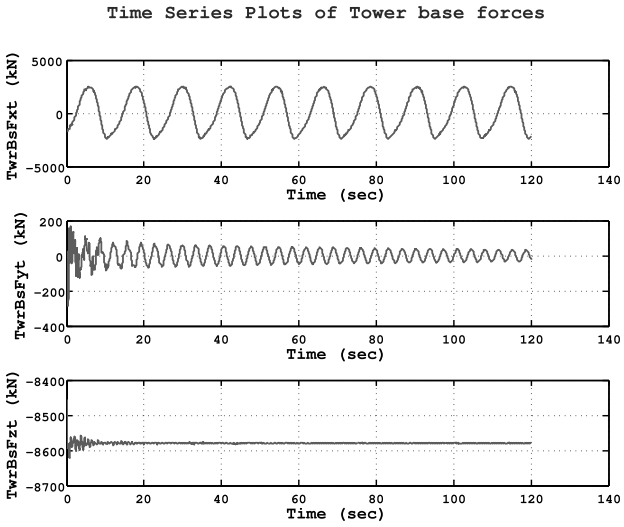

(a) Tower base forces computed by using FAST's internal wave simulator.

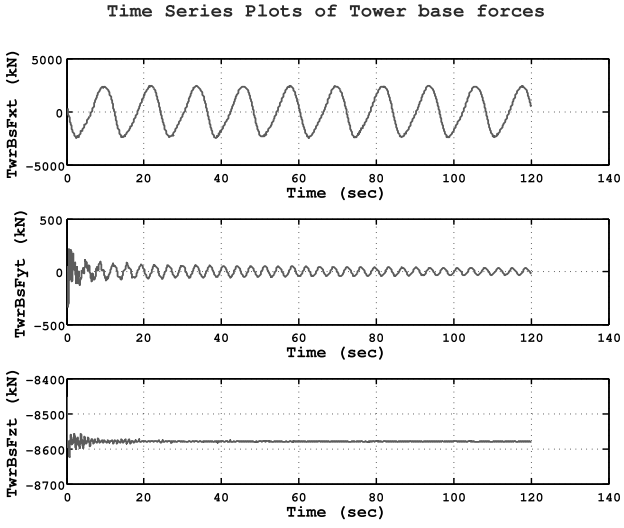

(b) Tower base forces computed by using the external wave kinematic solver and passed via text files.

Figure 5.4: Tower base forces obtained with wave kinematics computed internally by FAST (WaveMod: 1) and passed form outside (WaveMod: 4).

MorisonTwrLd subroutine outputs the force vector TwrFt, which is formed by the x (surge), y (sway) and z (heave) components of the portion of the tower force per unit length at the current tower element and the roll, pitch, and yaw components of the portion of the tower moment per unit length acting at the current tower element.

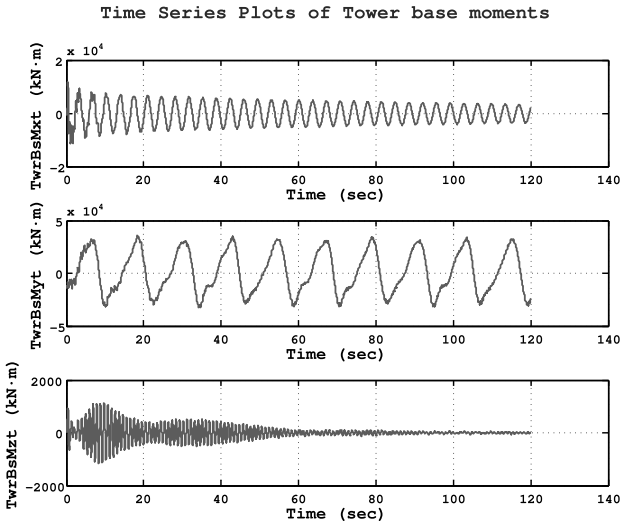

(a) Tower base moment computed by using FAST's internal wave simulator.

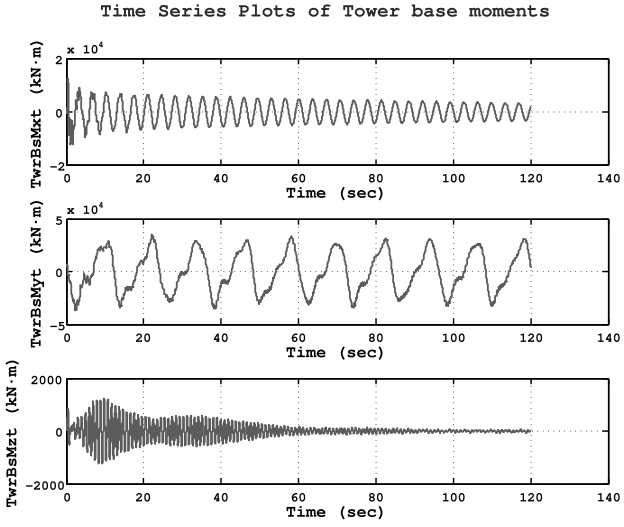

(b) Tower base moment computed by using the external wave kinematic solver and passed via text files.

Figure 5.5: Tower base moments obtained with wave kinematics computed internally by FAST (WaveMod: 1) and passed form outside (WaveMod: 4).

5.3.1 Slamming tower loading subroutine

The slamming tower load subroutine developed in this thesis adds a new feature to FAST. In fact, whenever under extreme climates a designer detects that highly nonlinear wave are present in the simulated sea and then the risk of impacts is pretty

hight, it is possible to switch the input parameter TwrLdMod to 2 in order to call the special user–defined subroutine implementing the theoretical model discussed in section 4.5.

It was necessary to introduce MorisonTwrLd subroutine because our user defined one contains a call to it. This should not surprise as the impulsive contribution is just added to the drag and inertial ones already provided by Morison's equation [8].

So the idea is: if breaking wave events are expected, then switch TwrLdMod to 2, else switch TwrLdMod to 1. Algorithm 2 summarizes this logic.

Algorithm 2: Basic logical scheme on how the variable TwrLdMod makes FAST compute tower loads.

input : TwrLdMod
output: TwrFt

if *TwrLdMod* $= 1$ **then**
  No impacts are expected, TwrFt $= f_D(t) + f_M(t)$
  MorisonTwrLd is called;
else if *TwrLdMod* $= 2$ **then**
  Impacts may occur, TwrFt $= f_D(t) + f_M(t) + f_I(t)$
  UserTwrLd is called;

According to algorithm 2, when UserTwrLd is called by switching TwrLdMod to 2, the first thing the routine does is to read in the following text files:

- *NtNb.txt*
- *eta_ b.txt*
- *curl.txt*
- *Tb.txt*
- *f_Impact*

To understand the logic of the routine, the above files need to be shortly described. *NtNb.txt* just contains the two parameters: Nt and Nb, which denote the number of total time steps concerning the sea simulation (Nt = Tsim/WaveDT + 1) and the number of expected impact events in that sea state, respectively.

File *eta_ b.txt* provides the maximum wave heights during the impacts and of course the file consists in Nb values. To remind the importance of the variable η_b (known as eta_b in the code) it is useful to recall the impact scheme proposed by Wienke and Oumerci in [8] and shown again in figure 5.6.

To properly compute the impact load, it is also extremely important to define the so called *impact area*. See figure 5.6. This can be done by means of the curling factor λ which basically gives the portion of tower being hit by the overturning spout of water. It would be very interesting in future to use the fully nonlinear solver here developed to asses and compare with experiments this factor, but in this application it has been fixed according to literature as $\lambda = 0.46$ [78], [79], [8].

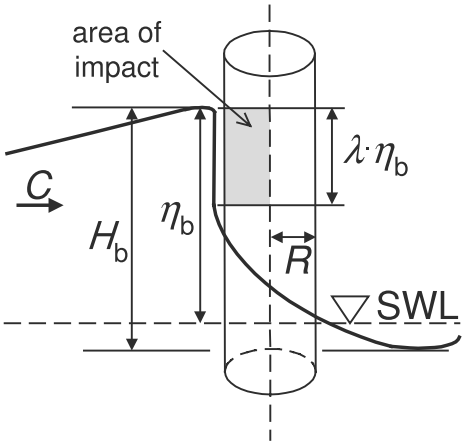

Figure 5.6: Sketch of the wave impact model. Image from [8].

File *Tb.txt* provides the vector gathering the times at which the impacts are expected. During an extreme sea state, in fact, several plunging breakers may occur at the structure location, thus, to take into account all of them, this variable needs to be known[3].

Finally, reading in the file *f_Impact*, the subroutine will create an allocatable variable called f_Impact. This variable has Nt rows and three columns: time, force in x direction (main direction of the impact), force in y direction. Of course the third column is always zero for the present model.

Now, when all the input data have been read in by the routine, the fraction of the current tower element included in the impact area is computed (this is necessary because the impact force applies of course only to those elements, or portion of them, included in the range $\lambda\eta_b$). To do this a logic similar to that used in MorisonTwrLd to find out which elements fall between the mudline and the instantaneous free surface has been implemented.

A selection of the most relevant lines of UserTwrLd are listed in the following:

```
!========================================================================
!!!!Some key lines of: SUBROUTINE UserTwrLd ( JNode, X, XD, ZTime,
DirRoot, TwrAM, TwrFt ) ! Select eta_b and curl corresponding to the
current impact event

CALL MorisonTwrLd ( JNode, TwrDiam, TwrCA, TwrCD, X, XD, ZTime, TwrAM, TwrFt )

      ! Initialize eta_b and curl

         eta_b = 0
         curl  = 0

 DO I = 1,Nb ! Loop through the impact events
     IF ( ( Ztime >= Tb(I) - 1 ) .AND. ( Ztime <= Tb(I) + 1 ) ) THEN
         eta_b = eta_b_vec(I)
         curl  = curl_vec(I)
     END IF
 END DO
```

[3]Note that this file provides the variable Tb to the subroutine, and it is nothing but what we will call $\bar{t}_b$ later on in section 5.5 of this chapter.

```
IF (     ( WaveKinzi0(JNode) - 0.5*DZNodes(JNode) ) >= eta_b )  THEN
   DZFractW = 0.0
ELSEIF ( ( WaveKinzi0(JNode) + 0.5*DZNodes(JNode) ) <= eta_b )  THEN
   DZFractW = 1.0
ELSE
   DZFractW = ( ( eta_b - ( WaveKinzi0(JNode) -
                            0.5*DZNodes(JNode) ) )/DZNodes(JNode) )
ENDIF

IF (        ( WaveKinzi0(JNode) - 0.5*DZNodes(JNode) ) >= (1.0-curl)*eta_b ) THEN
   DZFractS = 1.0
ELSEIF (    ( WaveKinzi0(JNode) + 0.5*DZNodes(JNode) ) <= (1.0-curl)*eta_b ) THEN
   DZFractS = 0.0
ELSE
   DZFractS = ( ( ( WaveKinzi0(JNode) + 0.5*DZNodes(JNode) ) -
                  ( (1.0-curl)*eta_b )   )/DZNodes(JNode) )
ENDIF

DZFract = DZFractW*DZFractS

! Compute the impact load (for the moment it is simply read from
outside):



IF ( DZFract > 0.0 )  THEN
   f_imp(1) = InterpStp ( ZTime, f_Impact(1,:), f_Impact(2,:), LastInd, Nt)
   f_imp(2) = InterpStp ( ZTime, f_Impact(1,:), f_Impact(3,:), LastInd, Nt)

   DO K = 1,2     ! Loop through the xi- (1) and yi- (2) directions

      TwrFt(K) = TwrFt(K) + f_imp(K)*DZFract

   ENDDO          ! K - The xi- (1) and yi- (2) directions

ENDIF
```

It is important to observe that in the subroutine UserTwrLd, first MorisonTwrLd provides the drag and inertial terms, then the remaining part adds the impulsive contribution. In addition to this, two important things should be pointed out from the above subroutine: first, it makes use of an additional subroutine named InterpStp which provides the value of f_impact interpolated at Ztime. This interpolation permits to compute the impact force with its own time step, which normally is WaveDT and then to be included in FAST main solver which has a different time step DT. It should also be considered that dealing with impulsive events, let us say with an average duration of magnitude 0.01 s, to capture the impulsive load it is necessary that a minimum number of time steps have to be included in the impact duration time. This induces some restriction both on WaveDT and DT. On the contrary, to generate the wave kinematics a time step of 0.5 s would be enough, but it could not capture the impact events. For this reason the impact force is always given with a proper time step.

The last remark about the above routine (see the last lines) is that the interpolated values of f_Impact, f_imp(1) and f_imp(2) are added to Morison's contributions at each time step. This can be done because f_Impact is nonzero only for the duration of the impact(s).

5.3.2 Test of the slamming load subroutine

At this point of the work, all the necessary tools to set up a preliminary test of a slamming wave have been provided. Plots showed in figures 5.4 and 5.5 were the time histories of the structural response subjected to a weakly nonlinear regular wave characterized by a wave height $H = 12\,\mathrm{m}$ and a wave period $T = 12\,\mathrm{s}$. This regular wave was rather far from the breaking limit, indeed its steepness is $\epsilon = 0.079$.

In this section, on the contrary, we need to increase the wave steepness in order to generate a plunging breaker from which, by following the scheme described in section 4.5.4, the input data to be passed to subroutine UserTwrLd can be derived.

A satisfactory high value of the steepness is achieved by doubling the wave height of the previous case, so that $H = 24\,\mathrm{m}$, while the wave period is unchanged: $T = 12\,\mathrm{s}$. Therefore the steepness becomes $\epsilon = H/L = 24/152.365 = 0.1575$. The free surface evolution with the formation of the overturning wave is shown in figure 5.7.

With a tower diameter of 6 m, the resulting impact force due to the breaker of figure 5.7 is plotted in figure 5.8.

The impact force vector, after being written in *f_Impact.txt*, is passed as variable f_Impact to FAST and it has the classical impulsive form as shown in figure 5.10.

According to this time history, indeed, the second column of file *f_Impact.txt* is nonzero only in a proper neighborhood of $t_b = 12\,\mathrm{s}$. The scale of figure 5.10 is too large to capture the real distribution of the impulsive force (which is shown in figure 5.8) but, as already said, FAST integration time step has been chosen in such a way to sample the impulsive contribution in an enough number of points.

Finally, it is possible to move to the structural response. As did earlier when we tested the wave kinematic solver, here we want to show the effect of the tower base internal forces, basically the shear force F_{xt} (that is in the same direction of the incident wave) and the bending moment M_{yt} rotating around the y–axis. The other internal forces and moments are also presented just to check that nothing occurs in the remaining directions.

The first subplot of figure 5.11(a) clearly describes that the periodical response due only to one single–harmonic loading action is suddenly shocked by the impulsive action associated with the slamming wave. The shear forces in the direction of the wave motion, indeed, presents a peak right at $t = 12\,\mathrm{s}$, compare with figure 5.10, while the force orthogonal to the main direction of the wave F_{yt} is not affected at all by this contribution. Another clear effect is registered by the time history of the vertical force F_{zt} at the tower base. In this direction, see the lower subplot of figure 5.11(a), the impulsive force also gives a relevant effect because the structure, after being hit, starts oscillating and this activates the the rotor mass, which, together with the mass of the tower, starts exciting the structure also in the vertical direction giving rise to a transient response. After a few seconds such a transient behaviour is damped. The vertical force comes back to the structure self weight after approximately 25 s, while a shorter damping period is necessary for F_{xt} to recover its periodicity. However, more details about the effects of the slam upon the vertical tower base force will be provided in the last paragraph of this section.

Observing in depth F_{xt}, however, a short delay between the peak due to the impact and the maximum fore due to Morison's contributions alone occurs. This is due to the fact that the impact force is computed with a nonlinear solver, while

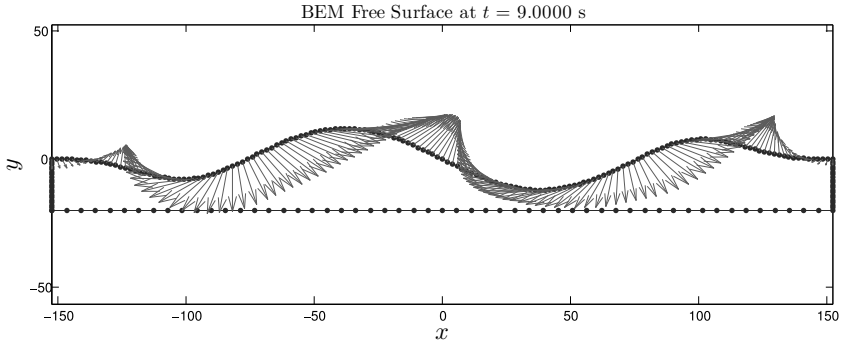

(a) Initial configuration.

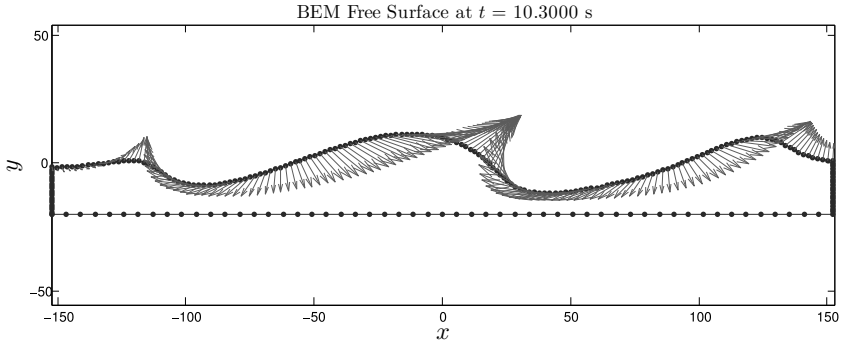

(b) Snapshot of the evolution at $t = 10.3\,\mathrm{s}$.

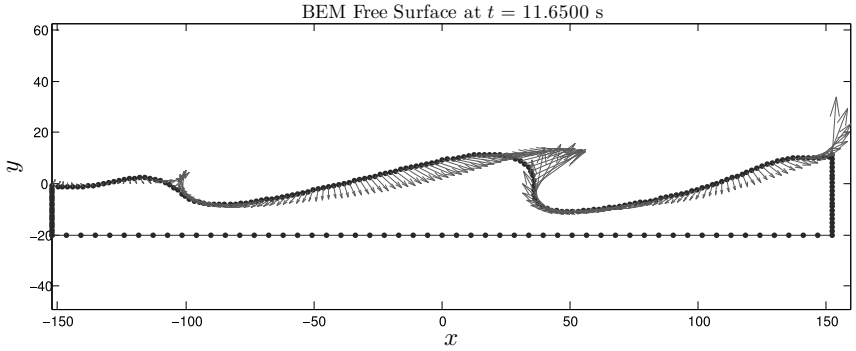

(c) Vertical front forming.

Figure 5.7: Free surface evolution of a steep regular breaking wave. Red arrows denote the free surface particles velocity and the blue dots the boundary element mesh. Input data from table 5.12.

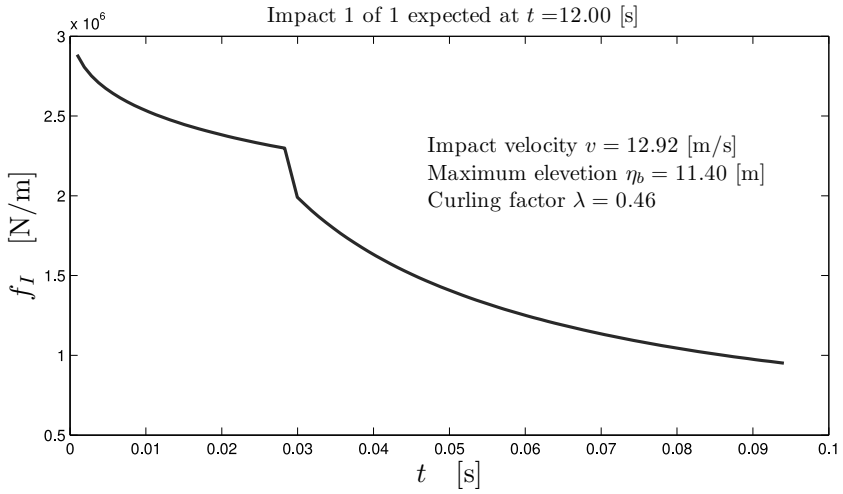

Figure 5.8: Impact force per unit length associated with the breaking wave shown in figure 5.7(c). The impact duration is $T_i = 0.094\,\mathrm{s}$.

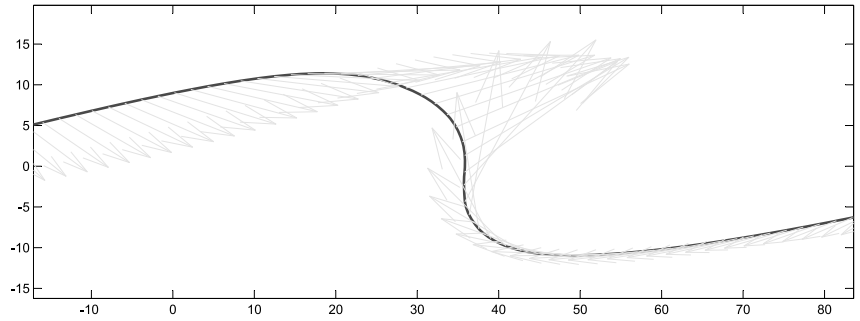

Figure 5.9: Closer view of the forming plunging breaker shown at the same time of figure 5.7(c). From this configuration the impact velocity and maximum wave height have been extracted in order tho get the time history of the impact load shown in figure 5.8.

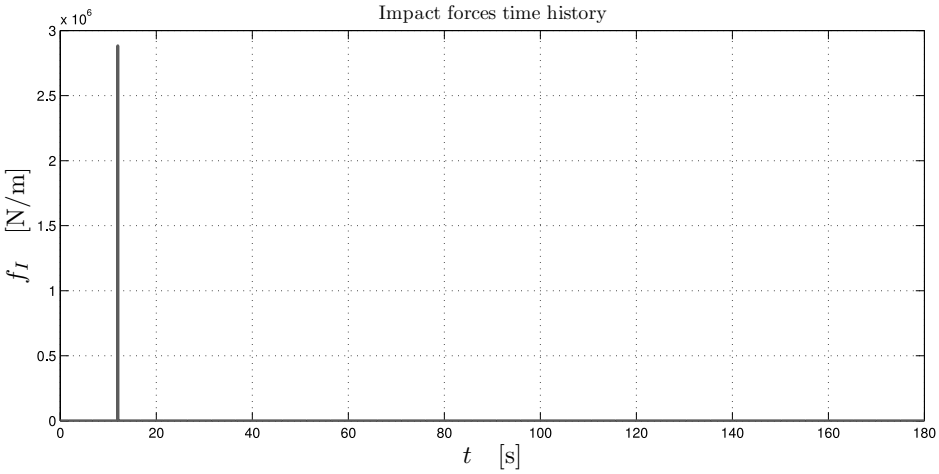

Figure 5.10: Impact force time history stemming from a steep regular wave breaking at $t = 12\,\mathrm{s}$, with $\eta_b = 11.40\,\mathrm{m}$, $\lambda = 0.46$. Total simulation time Tsim is 180 s.

Morison's force stems from a linear wave model. This delay is probably even more increased due to an excessive use of smoothing, which tends to dissipate some energy. A more careful use of both smoothing and regridding subroutines has been done in the next simulations.

Likewise, looking at figure 5.11(b), the results are pretty encouraging as neither the yaw moment nor the bending moment around the main direction of the incoming wave are affected by the hit, while, on the contrary, maximum effects is produced on the bending overturning moment. Here, in the middle subplot of figure 5.11(b), a clear peak occurs at 12 s which dissipates approximately after 10 s. Note that the damping period gives an idea of how much the whole structure suffers the shock.

It is also interesting to observe the tower top displacement in the incident wave direction. This displacement is shown in figure 5.12.

Also for the tower top displacement at $t = 12\,\mathrm{s}$, when the impact occurs, an increase of the tower deflection is registered. The series plotted in figure 5.12 is too short to really compare the transient effect with the stationary behavior. It seems that after a peak of about 26 cm due the slam, a progressive decay of the following peaks is registered.

Further considerations on F_{zt} time–history

To be sure that the above reasoning to justify the effect on F_{zt} is correct, the same simulation has been run disabling the tower degrees of freedom. Therefore, by assuming that the tower cannot undergo any displacement, that is no fore–aft oscillation is permitted, then no excitation is caused in the vertical direction. Evidences of this are given in figure 5.13.

The explanation given above about the transient effect also in F_{zt} time history is absolutely confirmed. Due to the absence of tower oscillations the impact effect is even clearer than before. The lower subplot of figure 5.13(a) shows that in this

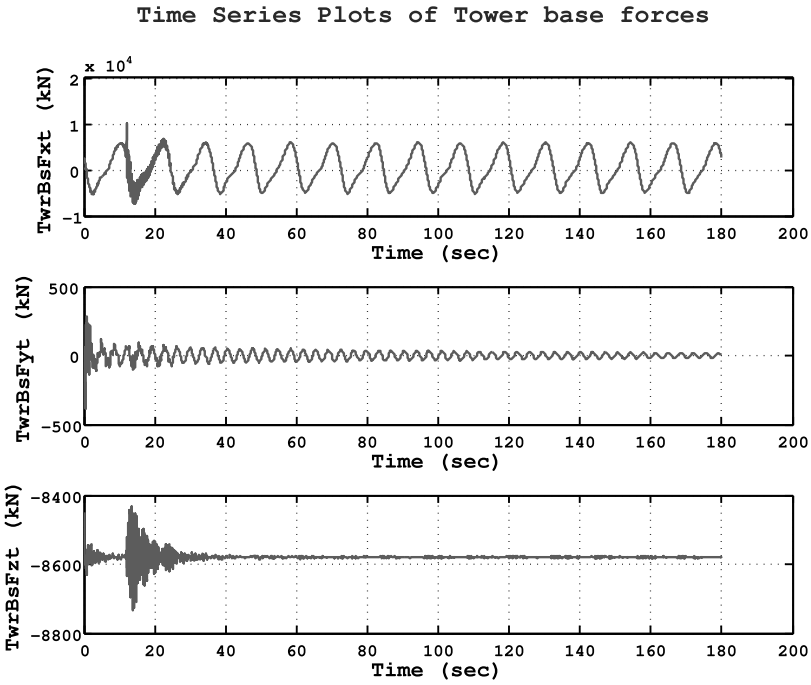

(a) Tower base forces.

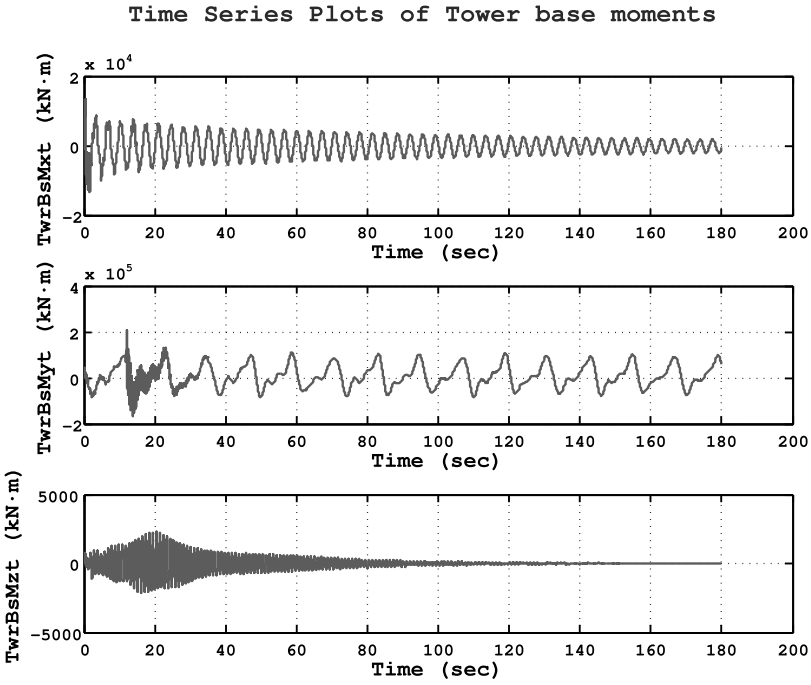

(b) Tower base moments.

Figure 5.11: First test on the structural response accounting for the impulsive load generated by a plunging breaker obtained from a very steep regular wave. (WaveMod: 4, TwrLdMod 2).

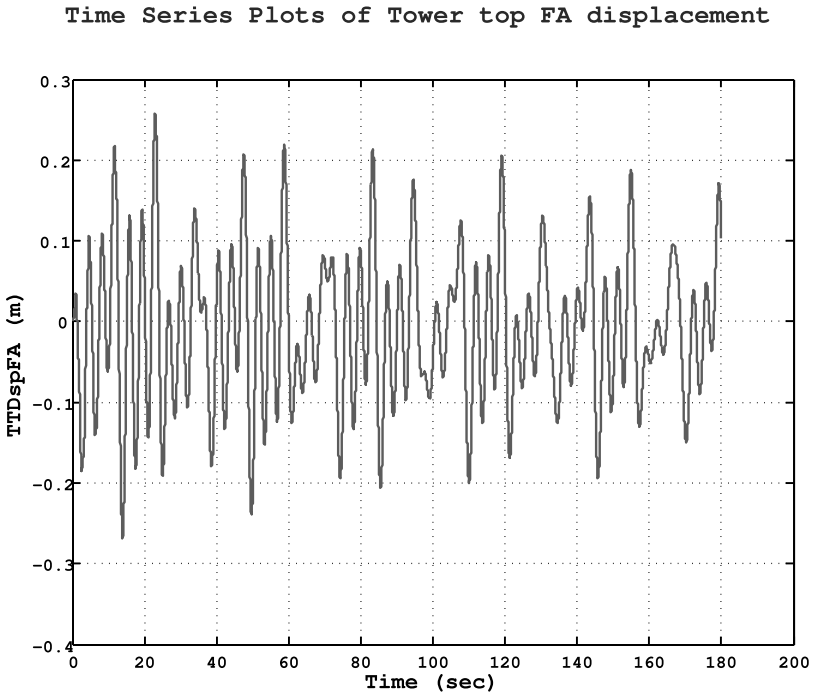

Figure 5.12: Tower top fore–aft displacement of the turbine parked and subjected only to hydrodynamic loads including the impact force associated with a plunging breaker.

case no transient effect is induced in z–direction and, as expected, the tower base vertical force remains constant on 8578 kN (as after the transient of figure 5.11(a)) which represents the self weight.

The last remark before closing this important test of the new impact model implemented in FAST regards the peaks of F_{xt} and M_{yt} plotted in the upper and middle subplots of figures 5.13(a) and 5.13(b), respectively.

The peak value of the shear force is $F_{xt_{pk}} = 1.8 \times 10^4$ kN, while the maximum shear force during the stationary phase is $F_{xt} = 5.8 \times 10^3$ kN. Thus, the impact increases in the shear force by 210%. While the peak value of the bending moment is $M_{yt_{pk}} = 4.8 \times 10^5$ kNm and the maximum value during the stationary phase is $M_{yt} = 8.7 \times 10^3$ kNm. This means that due to the impact, the fore-aft bending moment undergoes an augmentation of 451%, that is $M_{yt_{pk}} \simeq 5.5 M_{yt}$. Note that these amplifications should be treated carefully at this stage of the work, because the plunging wave has been generated without taking into account a realistic sea state. Indeed, the aim of this section is only to test the efficiency of the numerical model.

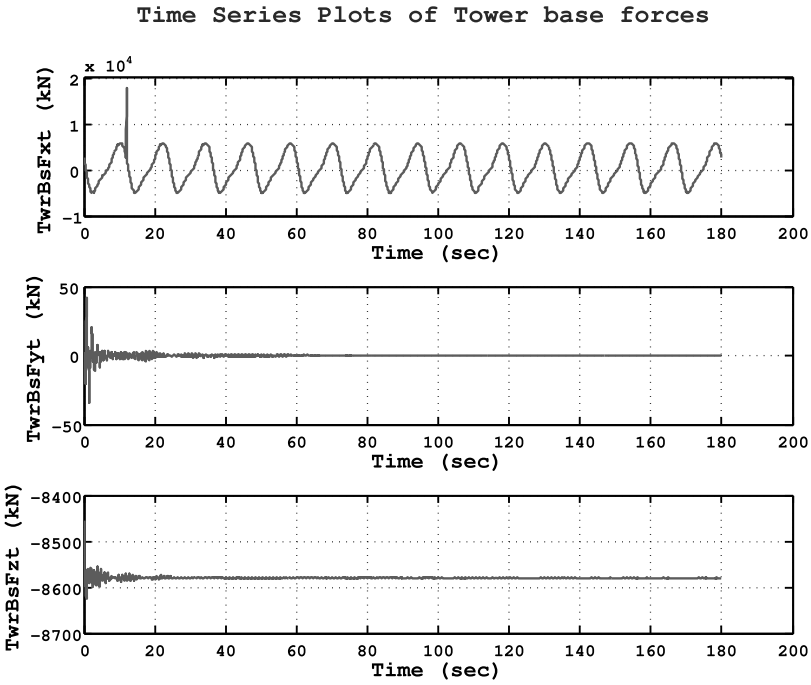

(a) Tower base forces.

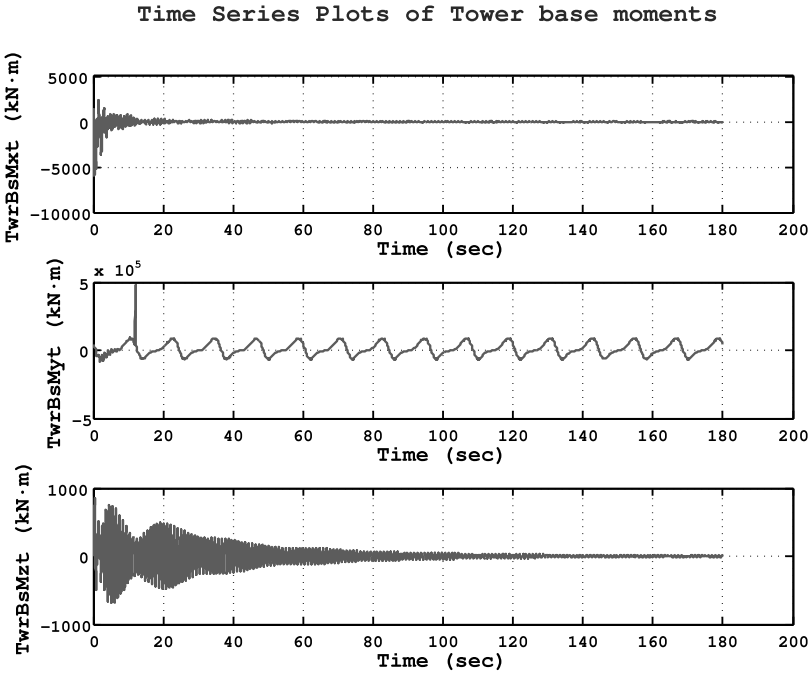

(b) Tower base moments.

Figure 5.13: The same impact load of figure 5.8, but in order to better investigate the nature of F_{zt}, this figure shows the tower base forces and moments when the tower degrees of freedom are disabled.

5.4 Wind and wave loads generation

According to IEC61400-1 [36], an Extreme Wind Speed Model (EMW) is assumed to estimate the wind loading conditions experienced by the offshore wind turbine. Consequently, as we are here mainly interested in extreme events, the relevant sea conditions are basically made up of wind–generated waves. So that, based upon the assumed wind, the most probable sea state around the offshore monopile, defined in terms of significant wave height and mean wave period, is reproduced in the time domain through a linear spectral approach. In particular the JONSWAP spectrum is adopted as the most suitable in case of wind–waves. For a generic time instant t the extreme scenario looks like the sketch in figure 5.14.

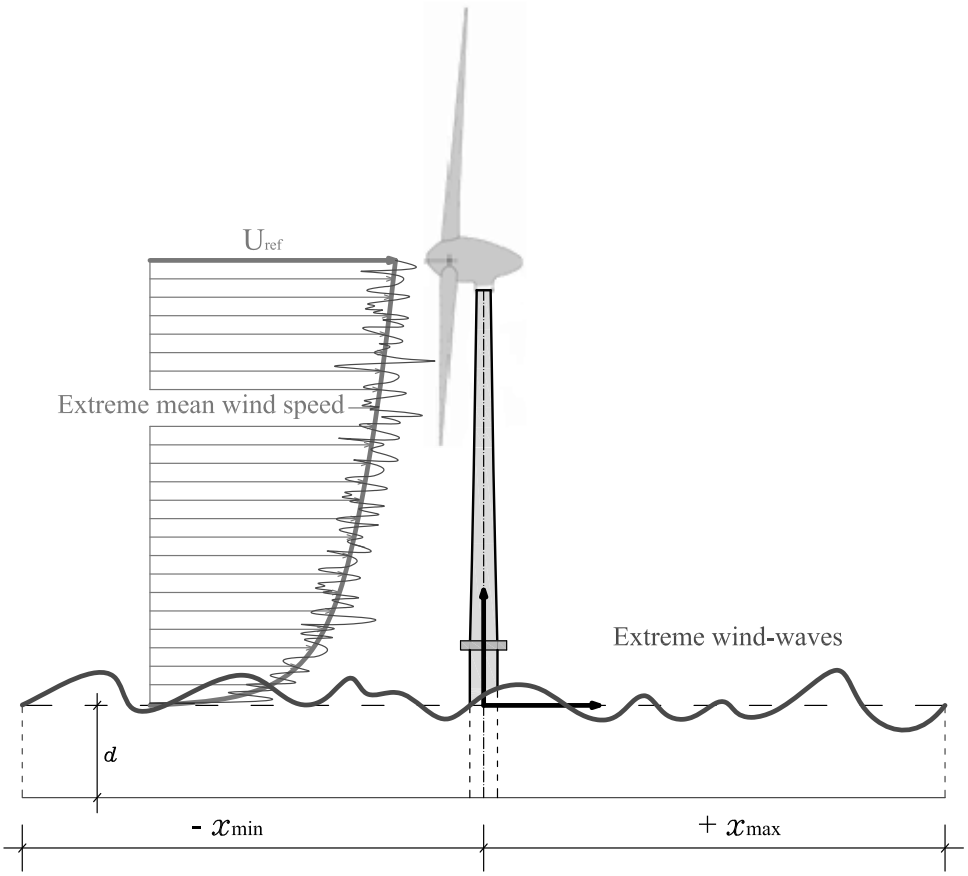

Figure 5.14: Sketch of the wind turbine located at $x_t = 0$ in the 2D spatial domain $\mathcal{D}_t = [x_{\min}, x_{\max}]$ for a given time instant t.

Figure 5.14 describes the main load sources for the whole structure acting together and in a continuous mutual interaction.

Once the wind–generated irregular sea is known in space and time, a suitable breaking wave criterion is used to check whether plunging breakers occur. And

thus, only when the steepness becomes large enough to induce wave instabilities, the fully nonlinear simulator is called in order to follow the sea evolution with an higher resolution in a narrower neighborhood of the substructure. This procedure is analyzed in depth on section 5.4.3.

The wind speeds at each blade element at the current time are computed from the hub–height turbulent value by accounting only for the assumed wind shear. As the rotor lies in the parked configuration (all the three blades are set with 90° pitch angle), the conservative assumption of not considering a full field turbulent wind generated by means of coherence functions can be accepted.

5.4.1 Wind loads

As already mentioned an extreme turbulent wind speed model (EWM) is adopted according to IEC61400-1. The turbulent wind is generated at the hub–height by using TurbSim which is an utility developed at NREL capable of generating both hub–height and full field wind data according to several spectral formulation. For our simulations the Kaimal model will always be adopted, see section 3.4 for details.

Extreme wind speed generation

In FAST's primary input file (i.e. **.fst*), in the AERODYN block, AeroDyn input file (i.e. **.ipt*) must be specified. In **.ipt* (line 10) at least two additional input files have to be provided: the wind file, containing either the hub-height wind speed (steady or time varying) or a full–field data file.

AeroDyn automatically detects the wind data type: if no file extension is specified (but only the root), then AeroDyn treats it like a full-field file and it expects to find both the files **.wnd* and **.sum*. Otherwise, a hub-height wind file, **.hh*, is assumed. This will always be our case. To summarize the input data necessary to generate a turbulent hub–height wind file, a part of TurbSim input file is shortly commented in the following.

TurbSim's input file is made up of five blocks:

- Runtime Options;
- Turbine Model Specifications;
- Meteorological Boundary Conditions;
- Non–IEC Meteorological Boundary Conditions;
- Coherent Turbulence Scaling Parameters;

Parameters provided in the above blocks are related both to the turbine type being simulated and the Design Load Case requested. In particular, in the first block settings about pseudorandom number generation and output type are specified. In the second block, parameters concerning the grid size and density, hub height, analysis time, etc. are to be specified. Most of these parameters depend on the turbine type for which the wind is simulated.

To set up the Kaimal model described in section 3.4, it might be opportune to show the forth block about "Meteorological Boundary Conditions":

```
--------Meteorological Boundary Conditions-------------------
"IECKAI"  TurbModel\\
"1-ED3"   IECstandard\\
"C"       IECturbc\\
"3WM50"   IEC_WindType\\
default   ETMc\\
"PL"      WindProfileType\\
90        RefHt\\
37.5      URef\\
...
```

Even though offshore wind turbines fall in the wind class "S", whose wind parameters are specified by the designer (see Annex A of [2]), here for the sake of simplicity we assume the wind turbine is designed according with parameters valid for wind class III. Therefore we have $U_{ref} = 37.5\,\mathrm{m/s}$ and for the turbulence intensity we choose the group "C", that is $I_{ref} = 0.12$, see [36]. As already mentioned in section 3.4, the simulations performed to test the coupled wind–fully nonlinear waves here developed, employ an extreme turbulent wind model. As in this case the standard deviation of the turbulence is always assumed to be depending only on the hub height wind speed, the turbulence intensity is not actually used in the following simulations.

Given the hub height of 90 m measured from the still water level, for the turbulent extreme wind speed model, the 10–min average wind speed profile with recurrence periods of 50 years and 1 year, respectively, are those given in section 3.4. The extreme mean wind profiles both for a 50 years and one year return period are shown in figure 5.15.

Of course, such wind velocities are far beyond the cut–out wind speed, which is 25 m/s, indeed in these two cases the turbine is parked or standstill.

Note that in FAST, in order to set the turbine in a parked condition, it is necessary (i) to turn off all controllers; (ii) to put the blade pitch angles at 90° (basically no lift forces); (iii) deactivate the induction model.

5.4.2 Wind-correlated sea states

An extreme sea state is defined by its significant wave height and mean zero–upcrossing wave period which should be estimated by taking into account the actual correlation between the whole environmental processes. As already discussed in Chapter 2, this requires a joint probabilistic model for the weather parameters relevant to the problem under consideration: wind speed, significant wave height, mean wave period.

As described in Chapter 2, the most suitable tool to this end is the so called Inverse FORM (First Order Reliability Method). Such a tool provides an environmental contour defining, for a required return period, environmental variables combinations at which the most extreme response lies. In other words, it is necessary to search along the contour in order to determine the point at which the conditional expected extreme response becomes the most extreme. The idea of investigating a contour, hence all combinations, is particularly effective because in most cases the *critical environment* is structure-dependent. For instance, assume to have found a contour of significant wave height and current velocity, then in the case of shallow water, it will be more dangerous the combination which maximize the significant wave height rather than the one which maximize the current velocity, [80].

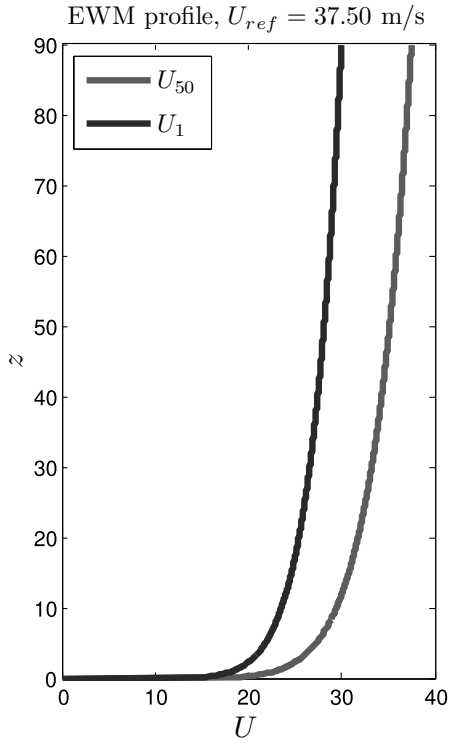

Figure 5.15: Extreme Wind Model velocity profiles.

A joint probabilistic model of mean wind speed, significant wave height and spectral peak period needs to be built. The wind speed is chosen as the primary parameter, the significant wave height is assumed to have second most influence. The joint model is used to establish a contour surface, giving combinations of the environmental variables with return period of 50 years according the recommendations in [2].

The reliability of the probabilistic model, however, lies mostly on the quality of available data. Indeed it is necessary to know the mean value of the significative wave height conditional on the wind velocity $\mu_{H_s|U} = f(U)$ and the standard deviation of H_s conditional on the wind velocity U, $\sigma_{H_s|U} = f(U)$. Thus, such a stochastic model is strictly recommended when reliable estimates of $\mu_{H_s|U}$ and $\sigma_{H_s|U}$ are available. Unfortunately this is not our case. And, in addition to this, in the present thesis it is not decisive to have at our disposal real data to implement the IFORM because it is not central for the research.

In similar circumstances, in accordance with [2], the significant wave height H_s defining the sea state state severity, can be assumed independent on the mean wind speed, so that $H_{s_{50}}$ is found from the marginal distribution of H_s and with the same sea state duration as the sea state duration used for the construction of the environmental contour.

Several distribution models for H_s and T_z are available, [81], [82] [83] [84] [85],

[86], [87], [88], among others. Often the Generalized Gamma distribution proposed in [12] gives a reliable description.

Extreme Sea State, simplified definition

Setting up a probabilistic model to estimate H_s and T_p (or T_z) departing from the 50–year return period wind velocity U_{50}, even by assuming an uncorrelated model, would be a mere exercise in this context because we are not aiming at a real design. In fact, we are more interested in constructing a valid model that, however determined the extreme values for U, H_s and T_p, is able to simulate with a higher accuracy the extreme offshore environment and the induced response.

The simplified approach consists in defining a sea state by assigning a severity rank depending on the wind velocity. Each severity class is characterized by a range of significant wave height and wave period.

By virtue of this simplification, the only random variable is the mean wind speed U, while H_s and T_p are deterministically determined from the wind velocity, see figure 5.16. Thus, equation (2.4) presented in Chapter 2 becomes

$$P_{fail} = \int P\left(M_{yt} > M_{yt}^{*} | U\right) p\left(U\right) \mathrm{d}\left(U\right) \tag{5.1}$$

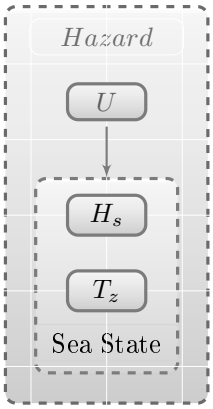

Figure 5.16: Simplified environmental model: the sea state is defined deterministically depending on the mean wind speed U.

In the present case the mean 50–year return period wind speed at 19.5 m above the sea level, obtained by using the profile in figure 5.15, is 31.69 m/s (61.61 Kn) which, referring to table 5.5 [10], makes the storm fall in the class of "hurricane–type storm".

This class is characterized by the following ranges for the significative wave-height and mean wave period, respectively

$$H_s = \{21.34 \text{ to } 35.05\,\mathrm{m}\} \tag{5.2}$$

$$T_z = \{10 \text{ to } 30\,\mathrm{s}\} \tag{5.3}$$

Sea states	Description of sea	Wind speed range	Significant wave height	Wave period range
		Knots	ft	s
1	Small wavelets	5–10	0.3–1.4	0.5–5
2	Large wavelets	10–14	1.4–3	1–7.5
3	Small waves	14–18	3–6	1.4–8.8
4	Small to moderate waves	18–19	6–7	2.5–10.6
5	Moderate waves	19–24	7–13	2.8–13.5
6	Large waves	24–30	13–22	3.8–15.5
7	Moderate gale	30–40	22–45	4.7–21
8	Strong gale	40–55	45–70	6.5–25
9	Hurricane type storm	55–70	70–115	10–30

Table 5.5: Definition of sea states according to [10].

Since this values are quite general, they could result too conservative and not very consistent with those specific for the North Sea, where our turbine is supposed to be located.

Hence, referring again to [10] (table 3.19), specific values for the North Sea extreme sea state associated with extreme wind of 37 m/s are

$$H_s = 14\,\mathrm{m} \tag{5.4}$$

$$T_p = \{15 \text{ to } 17\,\mathrm{s}\} \tag{5.5}$$

Moreover, as no consideration about the water depth has been made so far, we can refer to the diagram proposed in [10] where for the three exposure levels L-1, L-2, L-3 of an offshore platform, the relation between water depth and wave height has been found.[4]

In our simplified model we just need to collect some realistic values, so if we consider our offshore wind turbine like an unmanned platform (L-3), then from figure 5.17 it is immediate to see that for a water depth of 20 m (approximately 65.6 ft) the corresponding wave height is about 40 ft (12.19 m). And for such a design condition, the recommended extreme wind velocity and wave period are 58 Kn (29.84 m/s) and 11.6 s.

On the other hand, if we refer to Beaufort scale, see table 5.6, we have that for a Wind Force 11 (i.e. wind speed grater than 30.60 m/s) and Wind Force 12 (i.e.

[4] The three exposure levels are defined as follows:

- L-1: manned, non-evacuated;
- L-2: manned, evacuated;
- L-3: unmanned.

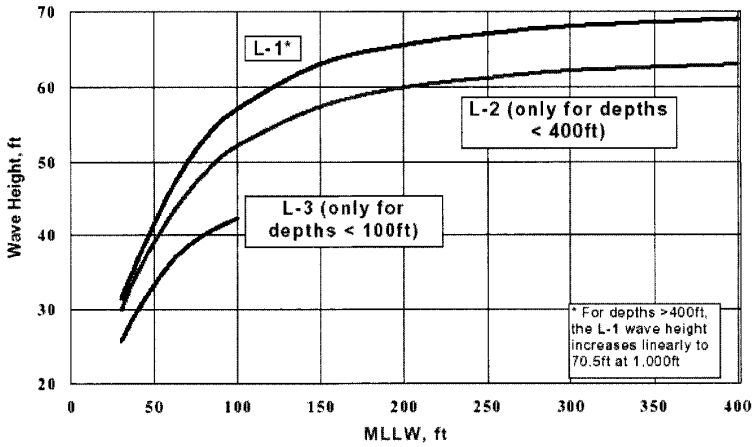

Figure 5.17: Water depth dependent wave height for different platform types, [10].

wind speed in the range of 29 to 33 m/s) the suggested values are, respectively

$$H_s = 10.25\,\mathrm{m} \tag{5.6}$$
$$T_p = 12.59\,\mathrm{s} \tag{5.7}$$

and

$$H_s = 8.70\,\mathrm{m} \tag{5.8}$$
$$T_p = 11.99\,\mathrm{s} \tag{5.9}$$

Note that with respect to table 5.6, the peak spectral period for the JONSWAP spectrum is given by $T_p = 1.199T_1$ or $T_p = 1.287T_2$, where T_1 and T_2 are some characteristic periods.

Although the above data present some differences, a deeper investigation to know which are the most suitable parameters for our case is not necessary. Also because in real design context a probabilistic model as described in the preceding section should be implemented.

In literature there are many other proposed tables and diagrams to get sea state parameters following the simplified approach. Among others we cite also diagrams proposed in [89] and [33].

5.4.3 Domain decomposition and breaking waves simulations

In this paragraph a detailed description of the procedure adopted to simulate the coupled wind–waves extreme environment is presented. The procedure has been implemented in a computer code which basically executes a certain number of instructions which can be grouped into the following steps:

1. **Environmental Analysis**

Wave Spectrum Parameter Estimates								
Scale of Beaufort	Wind Speed at 19.5 m above sea (kn)	Open Ocean Areas (Bretschneider)			North Sea Areas (JONSWAP)			
		$H_{1/3}$ (m)	T_1 (s)	T_2 (s)	$H_{1/3}$ (m)	T_1 (s)	T_2 (s)	γ (-)
1	2.0	1.10	5.80	5.35	0.50	3.50	3.25	3.3
2	5.0	1.20	5.90	5.45	0.65	3.80	3.55	3.3
3	8.5	1.40	6.00	5.55	0.80	4.20	3.90	3.3
4	13.5	1.70	6.10	5.60	1.10	4.60	4.30	3.3
5	19.0	2.15	6.50	6.00	1.65	5.10	4.75	3.3
6	24.5	2.90	7.20	6.65	2.50	5.70	5.30	3.3
7	30.5	3.75	7.80	7.20	3.60	6.70	6.25	3.3
8	37.0	4.90	8.40	7.75	4.85	7.90	7.35	3.3
9	44.0	6.10	9.00	8.30	6.10	8.80	8.20	3.3
10	51.5	7.45	9.60	8.80	7.45	9.50	8.85	3.3
11	59.5	8.70	10.10	9.30	8.70	10.00	9.30	3.3
12	$>$64.0	10.25	10.50	9.65	10.25	10.50	9.80	3.3

Table 5.6: Definition of sea states according to Beaufort scale. Table from [14].

2. **Spectrum choice**
3. **Irregular sea generation for a requested space–time domain**
4. **Setting the wind turbine location**
5. **Free surface elevation and zero–crossing analysis**
6. **Solve dispersion relations**
7. **Check breaking wave limit**
   (a) if **NOT**: Use standard Morison's equation.
   (b) if **YES**: Identify all the possible time instants at which waves break and:
      i. **Define space–time subdomains**
      ii. **Invoke the fully nonlinear solver**
      iii. **Perform fully nonlinear simulations**
      iv. **Plunging breakers analysis**
      v. **Get parameters to compute impact loads**
      vi. **Pass impact loads to FAST**
      vii. **Perform the fully coupled aero–hydro–elastic analysis**

From the *environmental analysis*, data about wind and wave conditions should be collected. However, in a pure conceptual design phase, it is possible to start

from the IEC wind class which provides both the U_{ref} and the turbulence intensity. As already said in the pervious section, in this work a wind turbine in class III is assumed.

The power law wind profile permits to get the mean extreme wind speed at 19.5 m above the still sea level. The sea state correlated to such an extreme wind condition can be derived by implementing one of the statistical model described above, but as the lack of data justifies, here we use the simplified approach. In fact we adopt the sea severity parameters among those recommended by [10].

From the *environmental analysis* we basically get $\{U_{ref}, H_s, T_p\}$ and after having chosen the most suitable wave spectrum, it is possible to move to phase 3. Here, first we consider a space–time domain $\mathcal{D}(t) = [0, T_{\text{sim}}] \times [x_{\min}, x_{\max}]$, where T_{sim} is the total simulation time, $x_{\min}$ and $x_{\max}$ are the lower and upper bounds of the two–dimensional spatial domain.

Since the focus is devoted to wind–generated waves and also because we imagine that the wind turbine is located in the North Sea, the JONSWAP spectrum is adopted. See section 4.1.2 for details.

By using the spectral formulation it is possible to determine the kinematics, the velocity potential and the free surface elevation of every water particle $p \in \mathcal{D}(t)$. The so called inverse approach permits in fact to come back to the temporal domain from the frequency domain provided that the phase angle ε, lost during the Fourier transform, is now assigned in such a way to get a different signal but with the identical statistical properties. To this end a uniform normal distributed phase angle is assumed.

The two–dimensional time–depending domain $\mathcal{D}(t)$ is reduced by one dimension by fixing the wind turbine location x_t. For all cases we will have $x_t = 0$ as shown in figure 5.14. Moreover, as already mentioned, for all simulations the water depth is always $d = 20$ m.

Subroutine 5 performs a zero–crossing analysis of the free surface elevation at x_t

$$\eta(x_t, t) = \sum_n a_n \cos(-\omega_n t + \varepsilon_n) \tag{5.10}$$

where a_n is the n–th wave amplitude stemming from the JONWASP spectrum

$$a_n = \sqrt{2 S_{\eta\eta}(\omega)\, \Delta\omega_n} \tag{5.11}$$

The time series $\eta(x_t, t)$ is analyzed by means of a special subroutine which computes all the wave periods and the corresponding wave heights. Firstly all the time instants up–crossing the still water level are collected into a vector called $\bar{t}_{up}$. Then the wave periods can be easily computed as the difference between two successive zero up–crossing time instants, while the wave heights are obtained by taking the difference between the highest and lowest points of the free surface (crests and troughs) within the corresponding period. Hence, for each time series these data are stored in two vectors, $\bar{T}$ and $\bar{H}$, respectively. In step 6, *Solve dispersion relations*, as many linear dispersion relations as the dimension of $\bar{T}$ (or $\bar{H}$) are solved in order to get the vector of wave numbers $\bar{k}$ which finally leads to the vector of wave lengths $\bar{L}$. Step 6 ends with the computation of the steepness vector

$$\bar{\epsilon} = \frac{\bar{H}}{\bar{L}} \tag{5.12}$$

Point 7, *Check breaking wave limit*, performs a comparison between the steepness vector $\bar{\epsilon}$ and the limit steepness vector $\bar{\epsilon}_b$. By computing the mean value of $\bar{H}$ and $\bar{T}$ it is not difficult to verify that the condition of deep water is not always guaranteed, thus in establishing the breaking limit the water depth is also taken into account by the well known relation [5]

$$\bar{\epsilon}_b = 0.142 \tanh\left(\bar{k}d\right) \tag{5.13}$$

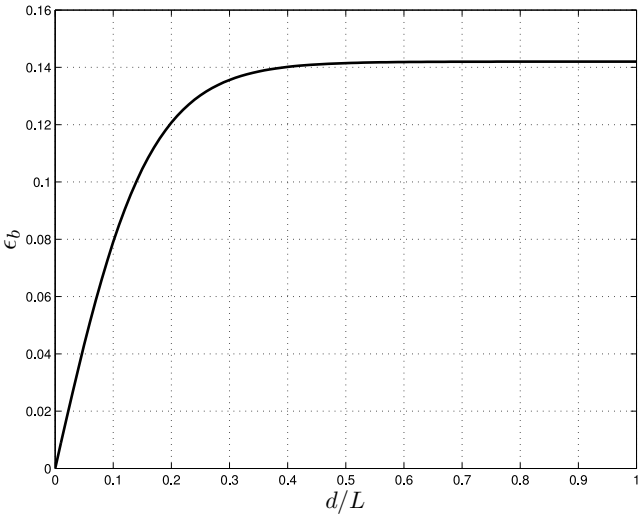

Figure 5.18: Limit breaking steepness ϵ_b for different wave lengths and water depth.

From step 7 there could be two outcomes: either the breaking limit is never achieved by any of the steepness in $\bar{\epsilon}$, or there could be a certain number of waves which violate the breaking limit.

In the first case, which is not the focus here, nothing should be done in particular. It is reasonable, in fact, to presume that since no impact will take place, Morison's equation remains valid without any alteration. The benefit stemming from the use of the fully nonlinear simulator is anyway not negligible because a more accurate wave kinematics can be obtained.

On the contrary, a different scenario occurs when the breaking limit is violated.

Referring to figure 5.19, and assuming that the vector $\bar{\epsilon}$ has dimension n, it is possible the identify a number nb of times $\bar{t}_b = \{t_{b1}, t_{b_2}, \ldots, t_{b_{nb}}\}$ at which waves will theoretically break. In this way all possible breaking events can be analyzed.

To visualize the importance of detecting the times at which breaking waves may occur we can refer to figure 5.14 and notice that it represents a snapshot taken at a generic time when, despite of the heavy storm in action, no wave is breaking against the substructure. In contrast, at a generic time t_{b_j}, or in particular at $t_{b_{\max}}$, an impact may occur as sketched in figure 5.20.

To perform some preliminary simulations aiming mainly at testing the global scheme, we start analyzing only the strongest event among nb possible. In the next

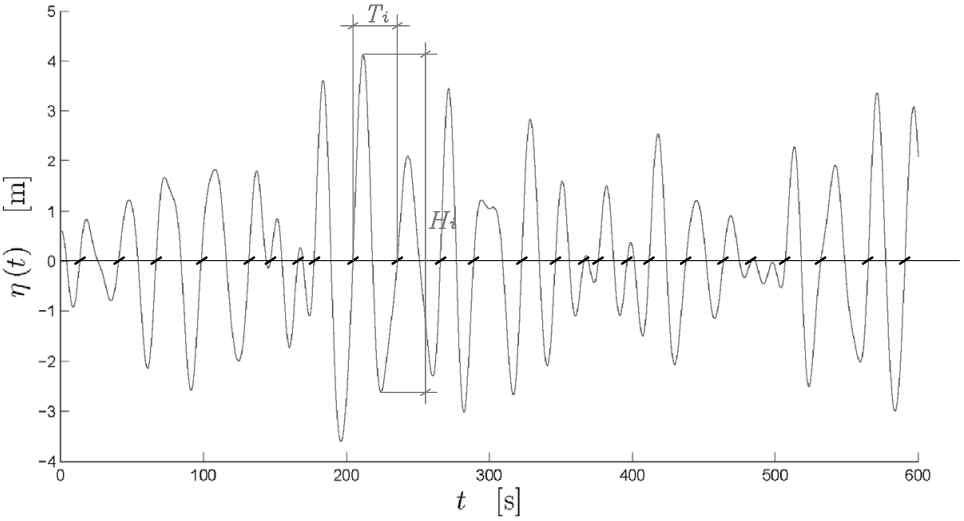

Figure 5.19: Example of free surface elevation. All zero up–crossing time instants are marked with a black dash and the i–th, with $i = 1, \ldots nb$, wave period and wave height are highlighted red.

section, when extreme wind and waves will be coupled, all the possible events will be taken into account.

Focusing the attention only on the stronger event, we just need to find the maximum value of $\bar{\epsilon}$ and then compute the associated time instant $t_{b_{\max}}$ as

$$t_{b_{\max}} = t_{up}(1) + \sum_{h=1}^{i_{b_{\max}}-1} T(h) + T(i_{b_{\max}})/4 \tag{5.14}$$

where $i_{b_{\max}}$ is the vector index corresponding to the maximum steepness, $\bar{t}_{up}$ is the vector collecting the zero up–crossing time instants, $\bar{T}$ collects all the wave periods in the signal $\eta(x_t, t)$.

Once the vector $\bar{t}_b$ or the time $t_{b_{\max}}$ are known, phase 7b ends and data to be passed as input for the fully nonlinear solver can be prepared.

In fact, in step 7(b)i *Define space–time subdomain*, neighborhoods of x_t and $t_{b_{\max}}$ have to be found in order to define a specific space–time subdomain $\Omega(t) \subset \mathcal{D}(t)$ on which Laplace's equation and the fully nonlinear kinematic and dynamic boundary conditions can be numerically solved.

Note that, whenever not ambiguous, the subscript max will be removed so that $t_{b_{\max}}$ will be simply denoted by t_b.

The subdomain is defined as follows

$$\Omega(t) = [t_b - \delta t_b, t_b + \delta t_b] \times [x_t - \delta x_t, x_t + \delta x_t] \tag{5.15}$$

where $\Omega(t)$ has the same meaning of section 4.

Upper and lower bounds of the sub-domain $\Omega(t)$ are crucial to set the initial and boundary conditions to be passed to the fully nonlinear solver. Caution has to be

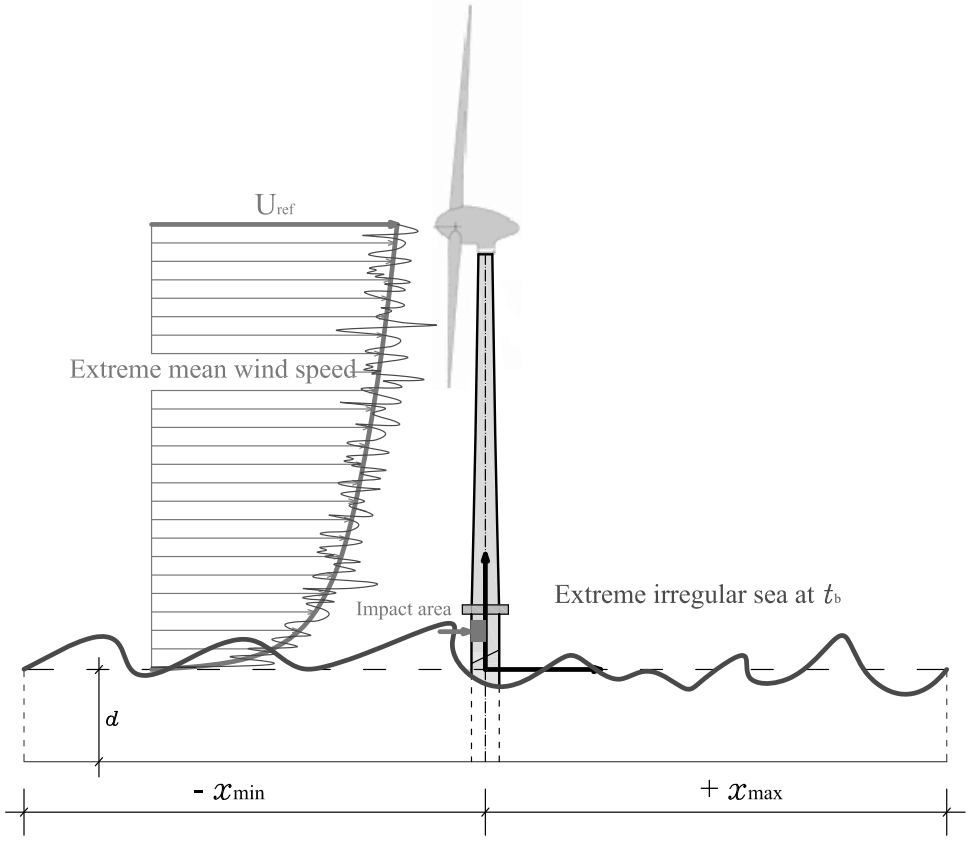

Figure 5.20: Sketch of the wind turbine located at $x_t = 0$ in the 2D spatial domain $\mathcal{D}_t = [x_{\min}, x_{\max}]$ for a time $t = t_b$.

paid when starting the nonlinear numerical solver by assigning initial and boundary conditions derived from the linear theory. To avoid numerical instabilities induced by a sudden transition from the linear to nonlinear solution, a spatial ramp function is applied in a very short space range.

The radii δx_t and δt_b of the neighborhood $\Omega(t)$ are chosen in order to assure a good compromise between the accuracy of the nonlinear wave propagation and the computational cost. In particular, it has been found that good values to define the sub-domains are twice the mean value of the wavelengths (spatial radius) and ranging between 2 and 4 s for the temporal radius

$$\delta x_t = 2 \times \mathsf{mean}\left(\bar{L}\right) \tag{5.16}$$

$$\delta t_b = 2 - 4\,\mathrm{s} \tag{5.17}$$

where, as already mentioned, vector $\bar{L}$ collects all the wave lengths contained in the signal $\eta(x_t, t_b)$.

It should be noted, however, that the temporal radius δt_b may significantly be increased without the global numerical scheme loses its efficiency. For the sole sake

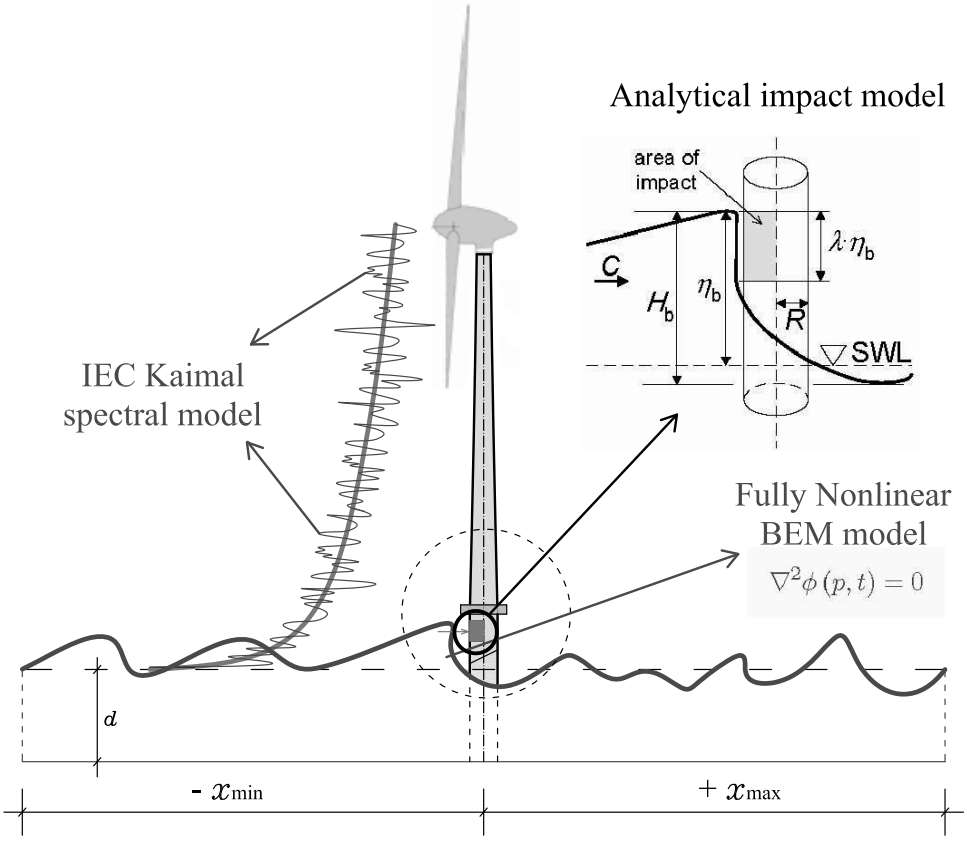

Figure 5.21: The three main models involved in the simulation. Wind: IEC Kaimal turbulence model; waves: fully nonlinear Boundary Element Method model; impact: analytical model.

of limiting the computational time, in all the applications presented later on, the temporal radius is fixed according to the above range.

Finally, it is possible to move to point 7(b)ii where the fully nonlinear solver is invoked. Before doing this, however, it is necessary to set the initial and the boundary conditions which have to be passed to the Boundary Element Method solver discussed in section 4.2.

Initial conditions

The spectral initial conditions, namely the initial free surface elevation and the velocity potential, are calculated as follows

$$\eta(x,t_i)=\sum_{n=1}^{N}a_n\cos\left(k_nx-\omega_nt_i+\varepsilon_n\right) \tag{5.18}$$

$$\phi(x,t_i)=g\sum_{n=1}^{N}\frac{a_n}{\omega_n}\frac{\cosh\left(k_n\left(d+\eta'(x)\right)\right)}{\cosh\left(k_nd\right)}\sin\left(k_nx-\omega_nt_i+\varepsilon_n\right) \tag{5.19}$$

where $x\in\Omega_t=[x_t-\delta x_t,x_t+\delta x_t]$ and $t_i=t_b-\delta t_b$ is the initial time of the numerical simulation. The subscript t on the domain $\Omega(t)$ just denotes the space-time domain at a given time instant, namely Ω_t turns out to be a spatial domain. In addition to that, as customary, a_n, k_n, ω_n, ε_n, denote respectively the wave amplitude, circular frequency, wave number and random phase angle associated with the n–th wave component. The meaning of these symbols will not be repeated in the remaining of the work.

Moreover, note that in equation (5.19) Wheeler's stretching [68] has been used. Accordingly, let $q(x)=d/\left(d+\eta(x,t_i)\right)$, then

$$\eta'(x)=q(x)\,\eta(x,t_i)+d\left(q(x)-1\right) \tag{5.20}$$

In general, the code enables users to chose the most preferred extension of the linear solution up to the actual free surface elevation. Indeed, Wheeler, extrapolation, constant and no stretching, are all possible switches.

Boundary conditions

The transition from the linear to the fully nonlinear solution at both ends $\Gamma_i(t)$ and $\Gamma_o(t)$ of the sub-domain $\Omega(t)$ is made using a two–sided ramp function R_s, which is required to be long not more than 10 times one boundary element length. The spatial ramp function is defined as follows

$$\mathsf{R}_s(x)=\begin{cases}\frac{1}{2}\left[\sin\left(\frac{x-x_i}{L_{\mathrm{rmp1}}}\pi-\frac{\pi}{2}\right)+1\right] & \text{for} \quad x\in[x_i,x_i+L_{\mathrm{rmp1}}]\\ 1 & \text{for} \quad x\in(x_i+L_{\mathrm{rmp1}},x_o-L_{\mathrm{rmp2}})\\ \frac{1}{2}\left[\sin\left(\frac{x_o-x}{L_{\mathrm{rmp2}}}\pi-\frac{\pi}{2}\right)+1\right] & \text{for} \quad x\in[x_o-L_{\mathrm{rmp2}},x_o]\end{cases}$$

where the shorter notation $x_i=x_t-\delta x_t$, $x_o=x_t+\delta x_t$ has been introduced.

This ramp function is necessary because it should be kept in mind that the we are setting up a numerical solver by assigning boundary conditions stemming from the linear solution. Thanks to this expedient we can safely assume that the solution inside the reduced sub-domain

$$\hat{\Omega}(t)=[t_b-\delta t_b,t_b+\delta t_b]\times[x_t-\delta x_t+L_{\mathrm{rmp1}},x_t+\delta x_t-L_{\mathrm{rmp2}}] \tag{5.21}$$

is fully reliable as the effects of the linear boundary conditions are all confined in the transition zones L_{rmp1} and L_{rmp2}. Note, in particular, that the area of our main focus is the very close surrounding of the turbine x_t, therefore as it lies always in the reduced sub-domain $\hat{\Omega}(t)$, we can totally relay on the accuracy of the numerical solution.

A simple explanatory example on how the ramp function (5.4.3) works is given in figure 5.22, where the ramp function R_s is applied to a generic function $g = g(x)$.

The boundary conditions on $\Gamma_i(t)$ and $\Gamma_o(t)$ are derived from the linear theory as follows

$$v_i^n(x_i,t) = \sum_{n=1}^{N} a_n\omega_n \frac{\cosh\left(k_n\left(d+y'(x)\right)\right)}{\sinh\left(k_n d\right)} \cos\left(k_n x_i - \omega_n t + \varepsilon_n\right) \tag{5.22}$$

$$v_o^n(x_o,t) = \sum_{n=1}^{N} a_n\omega_n \frac{\cosh\left(k_n\left(d+y'(x)\right)\right)}{\sinh\left(k_n d\right)} \cos\left(k_n x_o - \omega_n t + \varepsilon_n\right) \tag{5.23}$$

where $t \in \Omega_x = [t_b - \delta t_b, t_b + \delta t_b]$ and y' is given by the general form of equation (5.20)

$$y'(x) = q(x)\, y(x,t_i) + d\,(q(x) - 1) \tag{5.24}$$

with

$y' \in [-d, 0]$ is the computational vertical axis;

$y \in [-d, \eta(x,t)]$ is the actual vertical coordinate up to the free surface elevation;

q is a dimensionless factor;

$\eta(x,t)$ the elevation of the actual free surface elevation up to which the solution is sought.

The subscript x on the domain $\Omega(t)$ just denotes the space-time domain for a given location, so that Ω_x turns out to be a time domain.

To compute the second–order Lagrangian derivatives, used in the solution of the second Boundary Value Problem, refer to section 4.2 for details, also the accelerations need to be assigned as boundary conditions on Γ_i and Γ_o, therefore we have

$$\dot{v}_i^n(x_i,y,t) = \sum_{n=1}^{N} a_n\omega_n^2 \frac{\cosh\left(k_n\left(d+y'\right)\right)}{\sinh\left(k_n d\right)} \sin\left(k_n x_i - \omega_n t + \varepsilon_n\right) \tag{5.25}$$

$$\dot{v}_o^n(x_o,y,t) = \sum_{n=1}^{N} a_n\omega_n^2 \frac{\cosh\left(k_n\left(d+y'\right)\right)}{\sinh\left(k_n d\right)} \sin\left(k_n x_o - \omega_n t + \varepsilon_n\right) \tag{5.26}$$

After the initialization, all the kinematic quantities computed by the fully nonlinear numerical solver at each time step are made compatible with the linear boundary conditions by using the ramp function over the transition zones in the following fashion.

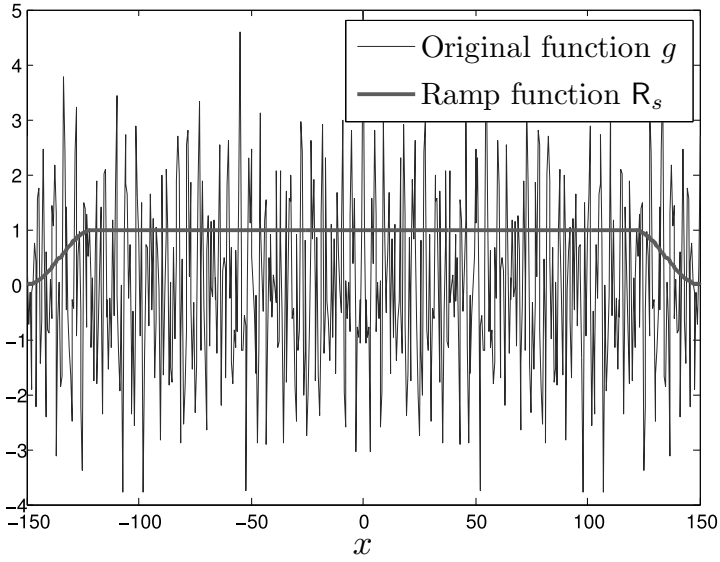

(a) Generic function $g = g(x)$ and two-side ramp function R_s.

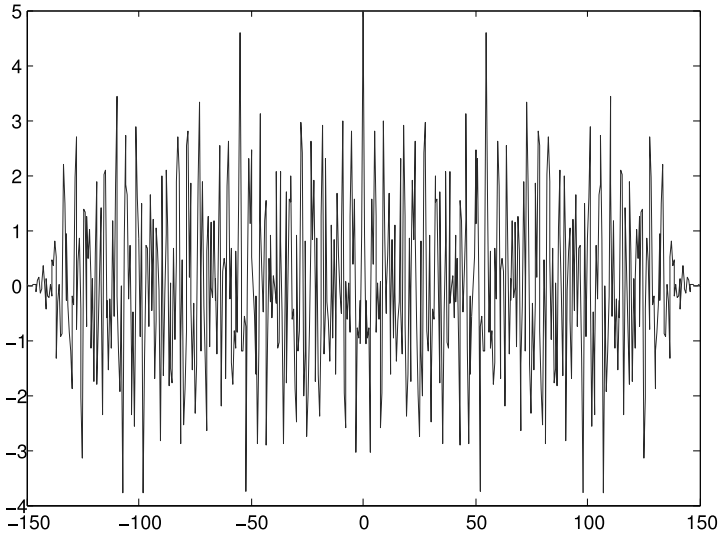

(b) Function g after the application of the ramp function.

Figure 5.22: Example of application of the space ramp function R_s on a domain $\Omega_t = [-150, 150]$ with $L_{\text{rmp1}} = L_{\text{rmp2}} = 30$.

Let $f^n = f^n(p,t)$ be a generic quantity numerically computed by the fully nonlinear solver, with the pair $(p,t) \in \Omega(t)$. For a given time instant $t \in [t_b - \delta t_b, t_b + \delta t_b]$ and for the points lying on the free surface, i.e. $y = y_f = \eta$, the function $f^n(p,t)$ turns out to be depending only on the the x–coordinate and it will be denoted by $\hat{f}^n = \hat{f}^n(x)$ with $x \in [x_t - \delta x_t, x_t + \delta x_t]$. Note that $\hat{f}^n$ is used for ϕ_f, v_f^x, v_f^y and η

itself.

Moreover, let $\hat{f}^a$ be the respective linear quantity computed analytically.

Then we have

$$\hat{f}(x) = \hat{f}^a(x)(1 - \mathsf{R}_s(x)) + \hat{f}^n(x)\,\mathsf{R}_s(x) \quad \forall x \in [x_t - \delta x_t, x_t + \delta x_t] \tag{5.27}$$

Notice that in the present case it is not necessary to have two different transition zones so that, from now on, we will always assume $L_{\text{rmp1}} = L_{\text{rmp2}} = L_{\text{rmp}}$. See figure 5.23.

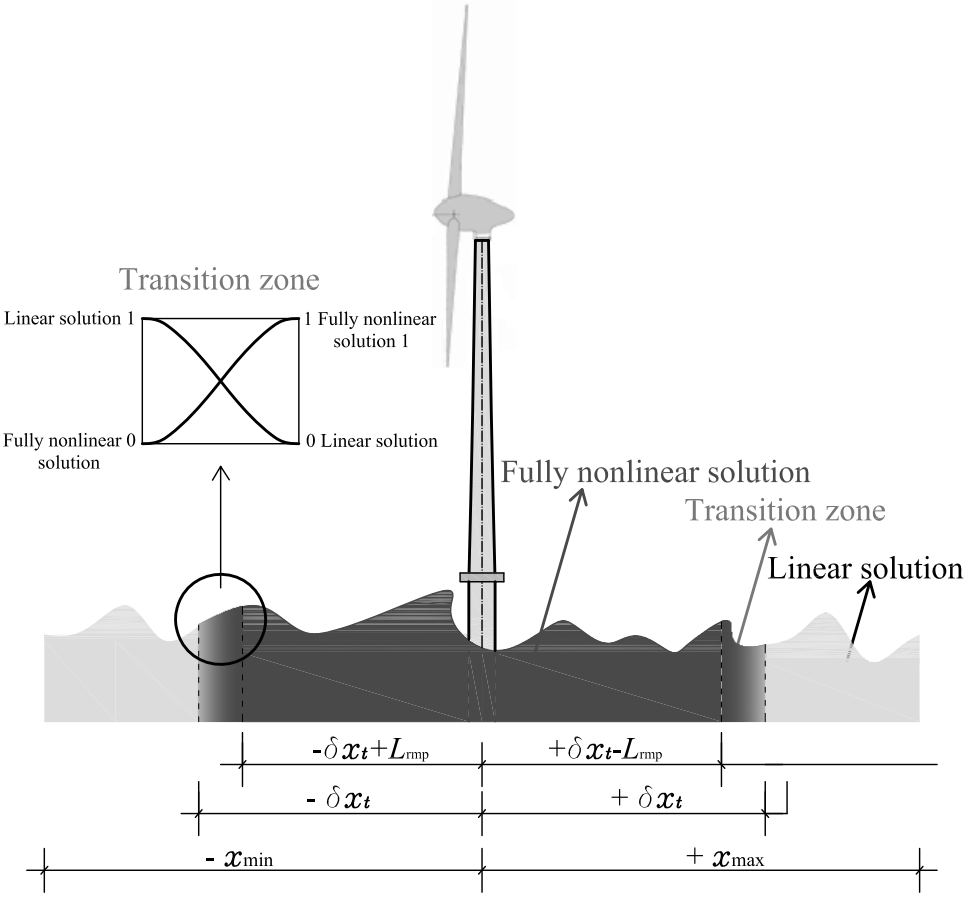

Figure 5.23: Schematic representation of the transition between the linear and fully nonlinear solution. The figure is out of scale.

To summarize, figures 5.24 and 5.25 show a schematic representation of the the main steps discussed above about the the global simulation scheme.

5.4.4 Applications

Before coupling the the fully nonlinear wave kinematic solver with the hydro-aero-elastic simulator, some applications are here preliminary presented in order to

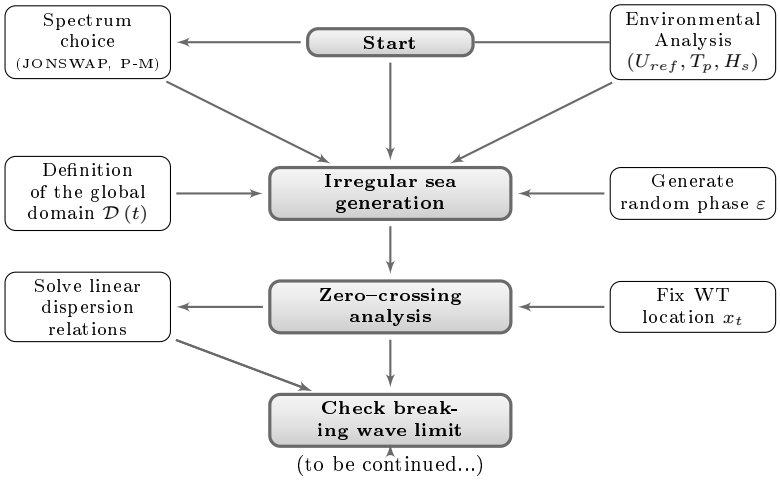

Figure 5.24: Diagram of the simulation. Part I

test the reliability of the numerical scheme summarized in figures 5.24 and 5.25.

Applications 1 and 2

In the first example a strong gale is simulated and all the relevant parameters are listed in table 5.7.

Sea severity[5]	"Strong gale" (rank 8)
U_{ref}, H_s, T_p	37.5 m/s, 18 m, 12 s
Spectrum Type	JONSWAP
T_{sim}, $x_{\min}$, $x_{\max}$	300 s, −200 m, 200 m
Turbine Location x_t	0
Maximum breaking wave time t_b	8.20 s (but not relevant!)
δx_t	146.59 m
δt_b	3 s

Table 5.7: Data relevant to application 1.

In this case no special time instant t_b has been requested to start the nonlinear numerical solver. In other words a generic time t has been assigned. The purpose is only to check the quality of the global scheme for the simulation.

The second simulation also shows a case of a strong gale and similarly to the previous example no special time instant t_b is requested to start the nonlinear solver. It interesting to notice, indeed, in the subdomain under analysis there could be multiple plunging breakers. Data relevant to this application are listed in table 5.8

Figures 5.26 and 5.27 show the evolution of the fully non linear seas for the

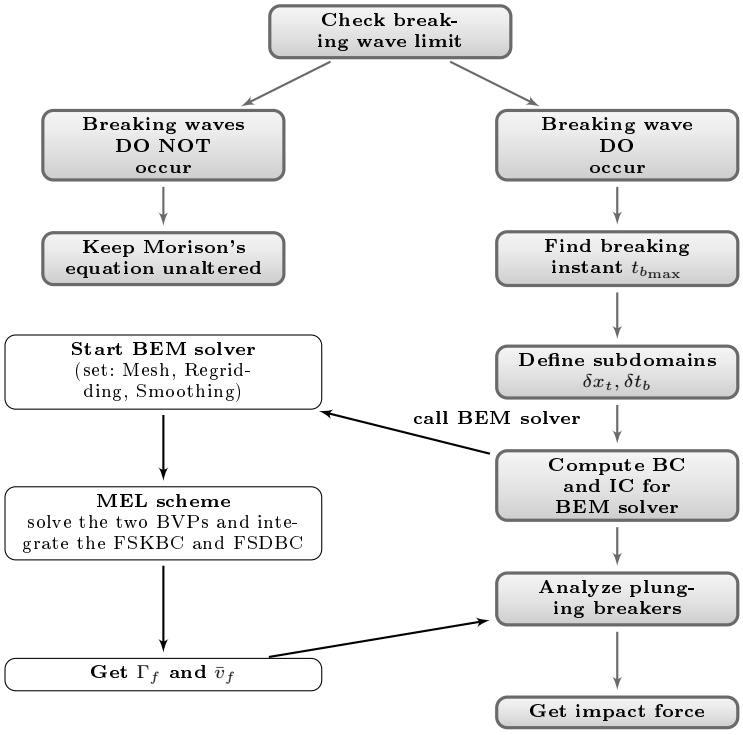

Figure 5.25: Diagram of the simulation. Part II.

Sea severity[6]	"Hurricane type storm" (rank 9)
U_{ref}, H_s, T_p	42.5 m/s, 22 m, 12 s
Spectrum Type	JONSWAP
T_{sim}, $x_{\min}$, $x_{\max}$	600 s, −200 m, 200 m
Turbine Location x_t	0
Maximum breaking wave time t_b	123.58 s (but not relevant!)
δx_t	137.24 m
δt_b	2 s

Table 5.8: Data relevant to application 2.

two examples above (tables 5.7 and 5.8, respectively). It is immediate to realize the transition from the linear solution to the fully nonlinear one work pretty well. Moreover, as the initial conditions have been assigned at a generic time instant,

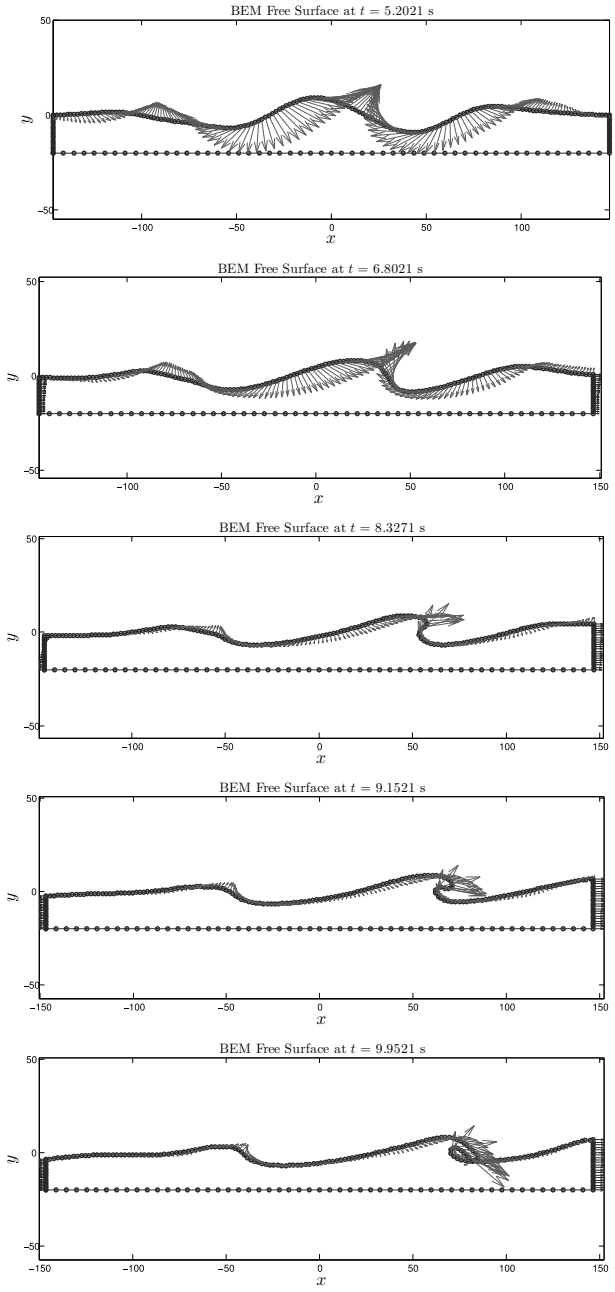

Figure 5.26: Five snapshots of a "Strong gale". Multiple plunging breakers scenario. Red arrows denote the free surface particles velocity and the blue dots the boundary element mesh. Input data from table 5.7.

waves break anywhere into the sub–domains.

Application 3

In the third case we show a simulation having a specified time t_b. All parameters are listed in table 5.9

Sea severity[7]	"Hurricane type storm" (rank 9)
U_{ref}, H_s, T_p	37.5 m/s, 18 m, 12 s
Spectrum Type	JONSWAP
T_{sim}, $x_{\min}$, $x_{\max}$	600 s, −200 m, 200 m
Turbine Location x_t	0
Maximum breaking wave time t_b	35.38 s (relevant!)
δx_t	128.28 m
δt_b	2 s

Table 5.9: Data relevant to application 3.

This simulation, see table 5.9 and figure 5.28, is extremely important and shows that the model described above works well and meet all the expectations. Such a result is actually not trivial because the breaking waves prediction tool elaborated above (see scheme in figures 5.24 and 5.25) starts form linear boundary and initial conditions to simulate a fully nonlinear event.

The first subfigure (the upper one) in 5.28 is a snapshot taken at $t = t_b - \delta t_b$, namely it shows the free surface configuration when we started the fully nonlinear solver. The last subfigure (the lower one) in 5.28 shows the free surface at $t = t_b + \delta t_b$, that is at the end of the refined simulation or, consistently with the concept of sub–domains $\hat{\mathcal{D}}$, at the end of the "sub–simulation". So as expected in the middle of the temporal sub–domain, i.e. at t_b (figure in the middle), we see exactly what expected: the plunging breaker is "crashing" against the virtual turbine substructure causing ad additional load to be carefully considered. From this time on, say up to the re–entry, the free surface experience very large curvatures and highest velocity at the water jet. This is very well seen in the three lower subplot of figure 5.28. These three instants are zoomed–out and reported in figure 5.29.

A clearer representation of the overturning tongue of water is given in figure 5.30 where the same of figure 5.29 is shown without velocity vectors and grid markers.

Application 4

To test further the stability and reliability of the first part of the numerical tool developed in this thesis another application is presented. Simulation parameters are listed in table 5.10. The main differences here with respect to results associated with data in table 5.7 are a larger wave period which tends to reduce the steepness in the average and a longer simulation time. In particular, here we have $T_p = 16\,\text{s}$ and $T_{\text{sim}} = 600\,\text{s}$. Moreover, also in this case, as did in the last two, we require to investigate the strongest breaker at x_t, that means the time t_b is relevant. The free surface evolution is presented in figure 5.31. The last three snapshots are zoomed

Sea severity[8]	"Strong gale" (rank 8)
U_{ref}, H_s, T_p	37.5 m/s, 14 m, 16 s
Spectrum Type	JONSWAP
T_{sim}, $x_{\min}$, $x_{\max}$	1200 s, −200 m, 200 m
Turbine Location x_t	0
Maximum breaking wave time t_b	464.15 s (relevant!)
δx_t	184.34 m
δt_b	3 s

Table 5.10: Data relevant to application 4.

and reported in figure 5.32.

A clearer representation of the overturning tongue of water is given in figure 5.33 where the same of figure 5.32 is plotted without velocity vectors and grid markers.

Also this application confirms the reliability of the global numerical model. From the second and third subplots presented in figure 5.31 it is clear that the predicted time of breaking, $t_b = 464.15$ s, is satisfactory observed and to compute the maximum impact force it is possible to use the most severe combination between wave elevation and water velocity among all the configurations around t_b.

Application 5

This simulation consist of a particular sea state which is not related to exceptional events. Highly nonlinear events may occur also with moderate wind speed. Indeed, by considering the rated wind speed of our wind turbine, that is 11.4 m/s, possibly after some reduction because that value is referred to the hub height 90 m and not to the conventional value of 19.5 m above the mean sea level, we realize to fall in a "Moderate Sea" again according to [10]. This sea severity rank (number 5) is characterized by the following ranges

$$H_s = \{2.13 \text{ to } 3.96\,\text{m}\} \tag{5.28}$$

$$T_p = \{2.8 \text{ to } 13.5\,\text{s}\} \tag{5.29}$$

The wave period range is meant to cover all possible periods over which measurable energy of the random wave for the particular sea state exists.

Now, by assuming the median value for the significative wave height and a wave period in the lower part of its "energy range" it has been observed that overturning breaking waves occur as well.

Table 5.11 lists all the relevant data for this simulation. Four breaking waves are detected in this realization and, as did for the previous cases, we isolate the stronger event which is expected to occur at $t_b = 33.99$ s.

We chose a larger sub–domain 500 m long in space and 12.5 min long in time. At the location of the wind turbine, i.e. $x_t = 0$, the free surface elevation is represented by the time series in figure 5.34.

Sea severity[9]	"Moderate waves" (rank 5)
U_{ref}, H_s, T_p	11.4 m/s, 3.05 m, 4.75 s
Spectrum Type	JONSWAP
T_{sim}, $x_{\min}$, $x_{\max}$	900 s, −250 m, 250 m
Turbine Location x_t	0
Maximum breaking wave time t_b	33.99 s (relevant!)
δx_t	33.99 m
δt_b	3 s

Table 5.11: Data relevant to application 5.

The three subplots reported in figure 5.35 show that a very steep and unstable wave is forming. The lower one clearly shows the vertical profile of the free surface just few instants before overturning.

Looking at what happens in the second group of snapshots, figure 5.36, the classical plunging overturning breaker takes place. However, the wave breaks some meters before reaching exactly the turbine location. By comparing this numerical experiments with the other presented in this section, it should not lead to wrong conclusions. Indeed, in this specific case the resolution is much higher because of the dimension of the space sub–domain $\hat{\mathcal{D}}_t$. In this case the numerical domain is 68 m long (which is $2\delta x_t$), while in the previous cases the domain was in the range of 200 m up to 360 m, approximately. Within this scale, few meters of approximation are definitely acceptable.

Anyhow, to judge the quality of this simulation, it is also crucial to stress that we are simulating a *fully nonlinear* phenomenon by departing from boundary and initial conditions which have been produced by a the *linear spectral theory*. Therefore, it is reasonable that breaking waves my not occur exactly where and when predicted by the linear theory.

Figure 5.37 shows what already presented in figures 5.35 and 5.36, but by removing the free surface particles velocity and the mesh markers a clearer representation of the water jet is offered.

Application 6

The very last case which deserves some attention is a non–breaking circumstance. This additional applications confirms once again the reliability of the numerical tool. Table 5.12 collects all key input parameters for this simulation.

What makes singular this application is that in the "Moderate waves" random sea we have generated, none of the harmonics reaches such a high steepness to violate the breaking limit. However, we fixed as center for the temporal domain t_b the time instant at which the maximum steepness is reached.

In the signal, plotted in figure 5.38, there are 242 wave components with mean steepness 0.051, mean wave length 39 m, mean wave period 4.94 s.

With the same scheme proposed above to identify t_b, we proceeded by consid-

Sea severity[10]	"Moderate waves" (rank 5)
U_{ref}, H_s, T_p	11.4 m/s, 3.05 m, 5.75 s
Spectrum Type	JONSWAP
T_{sim}, $x_{\min}$, $x_{\max}$	1200 s, −300 m, 300 m
Turbine Location x_t	0
Maximum breaking wave time t_b	**NO breakers are detected!**
δx_t	39.62 m
δt_b	6 s

Table 5.12: Data relevant to application 6.

ering the maximum steepness and we found that it is $t_b = 560.90\,\text{s}$. According to the general scheme discussed above, we launched the fully nonlinear solver with an initial time $t_i = t_b - \delta t_b = 557.90\,\text{s}$ and we ended the simulation at a final time given as $t_b + \delta t_b = 563.90\,\text{s}$.

The maximum steepness $\max(\bar{\epsilon}) = 0.1150$, which is below the limit in equation (5.13), has been used to start the simulator and as it can be seen form the third subplot (from above or below) of figure 5.39 the wave is really very steep and asymmetric also with respect to the vertical axis. Moreover, even though there is no overturning, a nearly vertical front forms approximately at x_t. This kind of ambiguous situation, where there is no real breaking phenomenon but the velocity of water increases a lot storing a large amount of kinetic energy - which could be released on the structure - should be investigated further. In our opinion such kind of non–overturning waves should also be counted among the impact events as they could also induce impulsive contribution.

The three subplots in figure 5.39 are shown again in figure 5.40 without the boundary mesh and the velocity vectors.

Some remarks on the numerical solver

We observe that in general all simulations may stop by obeying two criteria: a "natural" one, that is when the simulation time reaches the $t_b + \delta t_b$; a "forced" one, which applies when the water tongue re–enters into the sea surface. In this circumstance, in fact, the irrotational hypothesis on which the entire mathematical model is founded vanishes and thus the scheme breaks down.

The numerical instability of the system at the re–entry is shown in figures 5.41 and 5.42.

The zoom–in of the subplots in figure 5.41 are shown in figure 5.42. They clearly prove that the simulation is stable up to the contact of the water jet with the free surface.

An additional consideration regards also the utilization of local refinement and smoothing subroutines. Notice in fact that a multi–breaking waves scenario may occur (e.g. the case shown in figure 5.41). In these circumstances, the refinement subroutine should work at the same time on different regions of the boundary.

It should be pointed out that all the above results have been obtained by employing a number of quadratic boundary elements on the free surface NE_f adaptively computed as follows

$$NE_f = \mathsf{ceil}\left(\frac{L_f}{\mathsf{mean}\left(\bar{L}\right)} NE_f^*\right) \tag{5.30}$$

where ceil and mean simply compute the larger integer and the mean value of their arguments, respectively. NE_f^* is number of quadratic elements per wave length and as already said, $\bar{L}$ collects all the wave lengths contained in $\eta\left(x = x_t, t\right)$. The optimum value for NE_f^* has been found to be included in the range of 30-60.

Furthermore, it is remarkable the fact that during the simulations above the regridding subroutine has been called every five time steps, while the smoothing was applied every two time steps. Nevertheless, the code presents an extraordinary stability because neither restarting nor local refinements in the regions of the cusps were necessary.

Also surprising is to note that the time step is for nearly all the simulation time T_{sim} kept constant on the value 0.05 s. When the water jet is forming however, a specific subroutine halves the time step span any time a node of the boundary mesh undergoes a displacement larger than 50% of the element's length. This expedient permits to circumvent possible instabilities related to very high velocity gradient. See section 4.2 for further details.

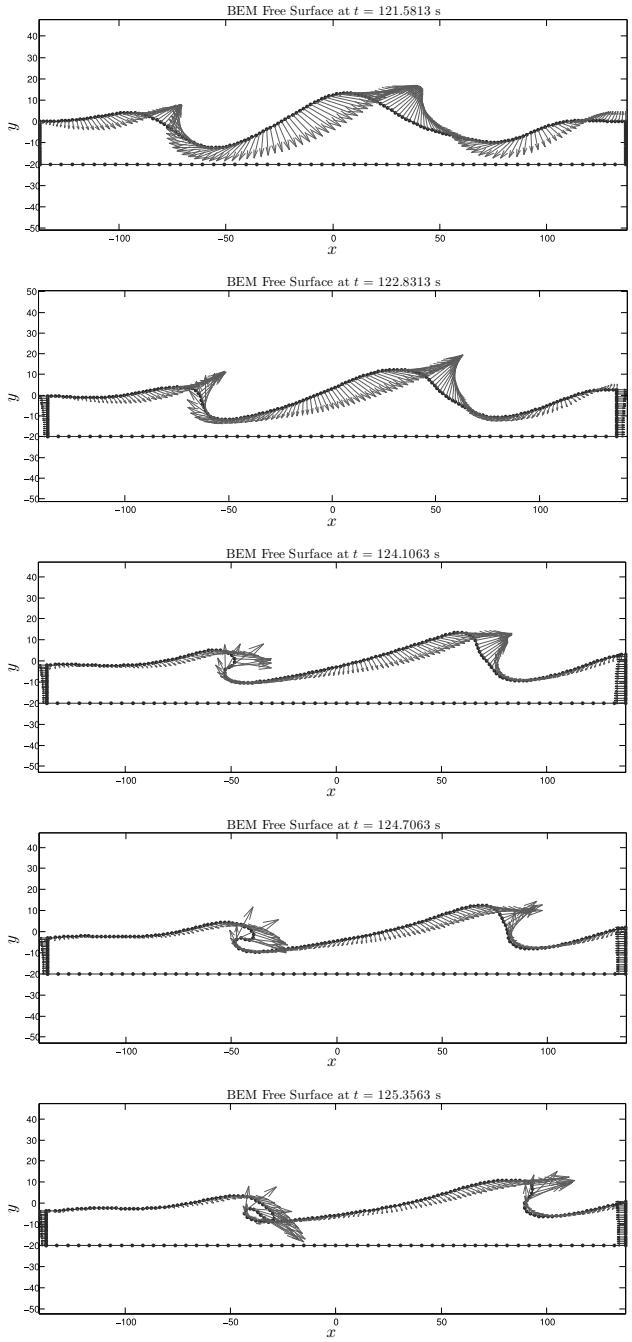

Figure 5.27: Five snapshots of a "Hurricane type storm". Multiple plunging breakers scenario. Red arrows denote the free surface particles velocity and the blue dots the boundary element mesh. Input data from table 5.8.

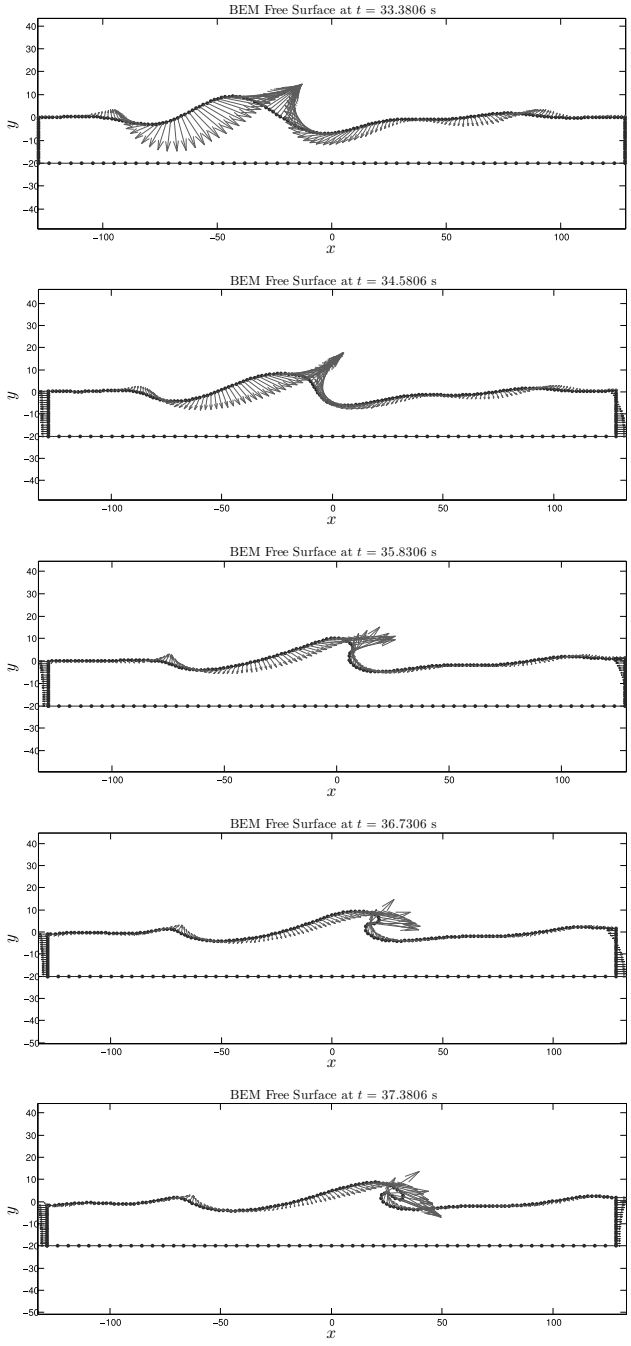

Figure 5.28: Five snapshots of a "Strong gale". Plunging breaker approximately at x_t and t_b. Red arrows denote the free surface particles velocity and the blue dots the boundary element mesh. Input data from table 5.9.

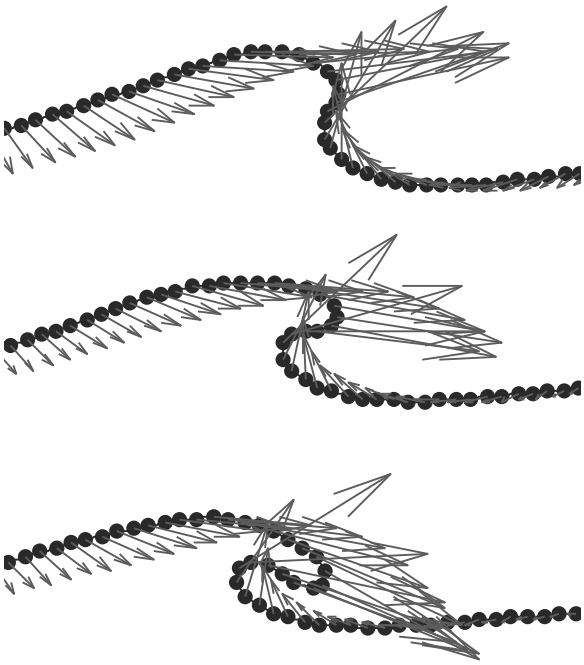

Figure 5.29: Plunging breaker: zoom of the lower three subplots of figure 5.28, from t_b to $t_b + \delta t_b$.

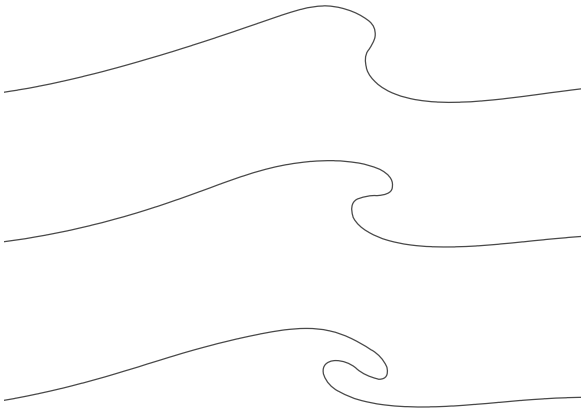

Figure 5.30: Plunging breaker: zoom of the lower three subplots of figure 5.28, from t_b to $t_b + \delta t_b$. Free surface profiles alone.

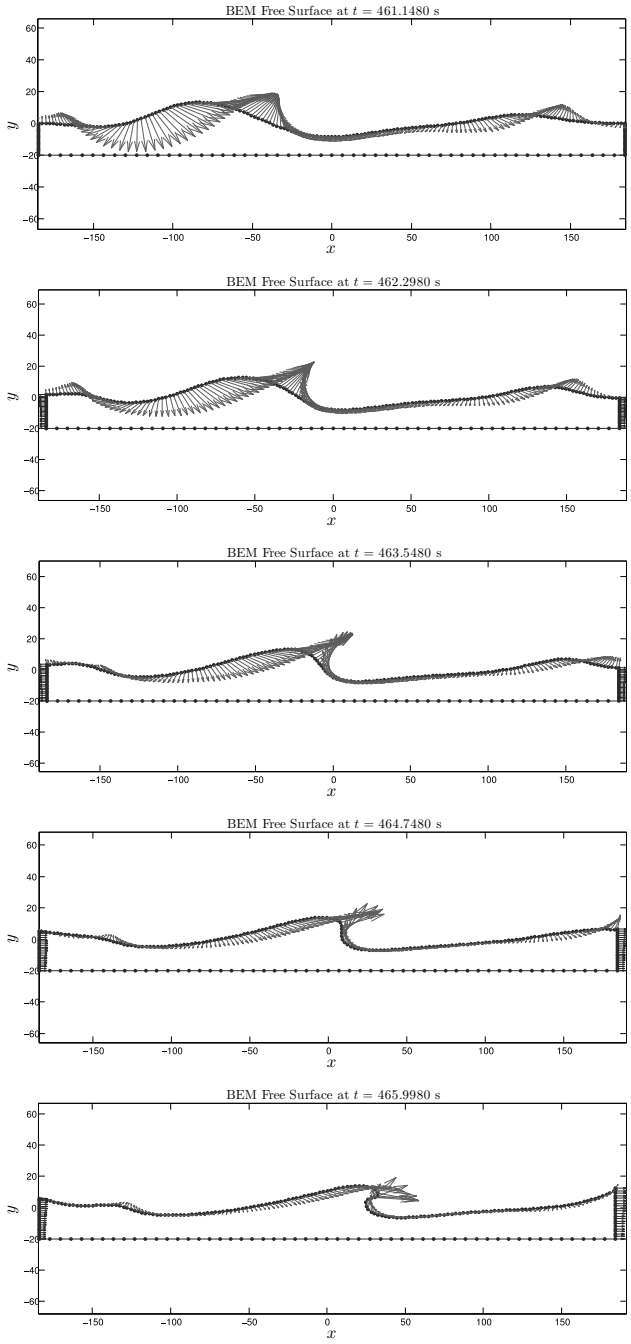

Figure 5.31: Five snapshots of a "Strong gale" sea state. Plunging breaker at predicted values of x_t and t_b . Red arrows denote the free surface particles velocity and the blue dots the boundary element mesh. Input data from table 5.10.

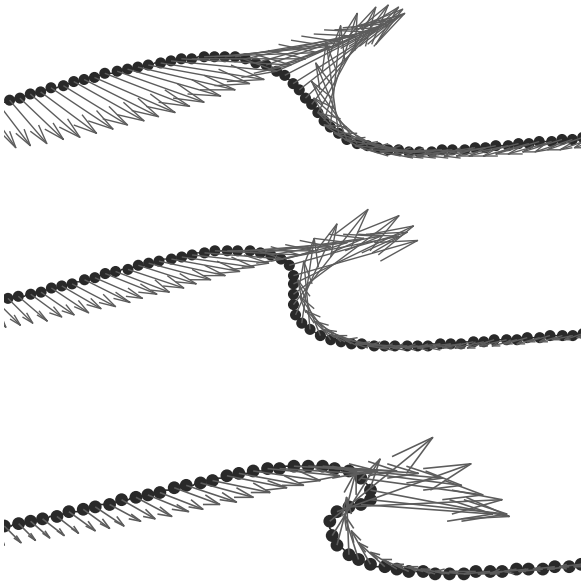

Figure 5.32: Plunging breaker: zoom of the lower three subplots of figure 5.31, from t_b to $t_b + \delta t_b$.

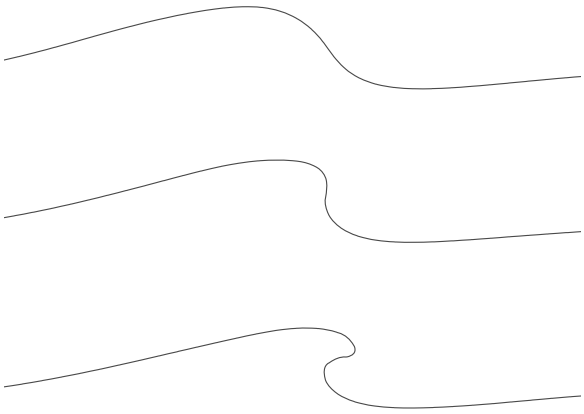

Figure 5.33: Plunging breaker: zoom of the lower three subplots of figure 5.31, from t_b to $t_b + \delta t_b$. Free surface profiles alone.

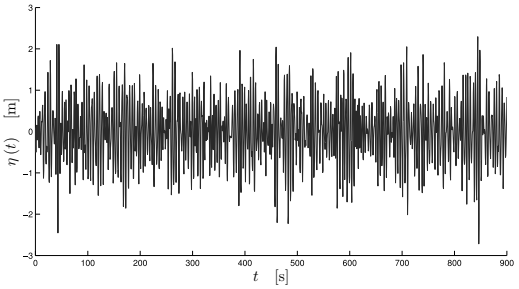

Figure 5.34: Time series of the free surface elevation at $x_t = 0$ for a "Moderate sea". More input data in table 5.11.

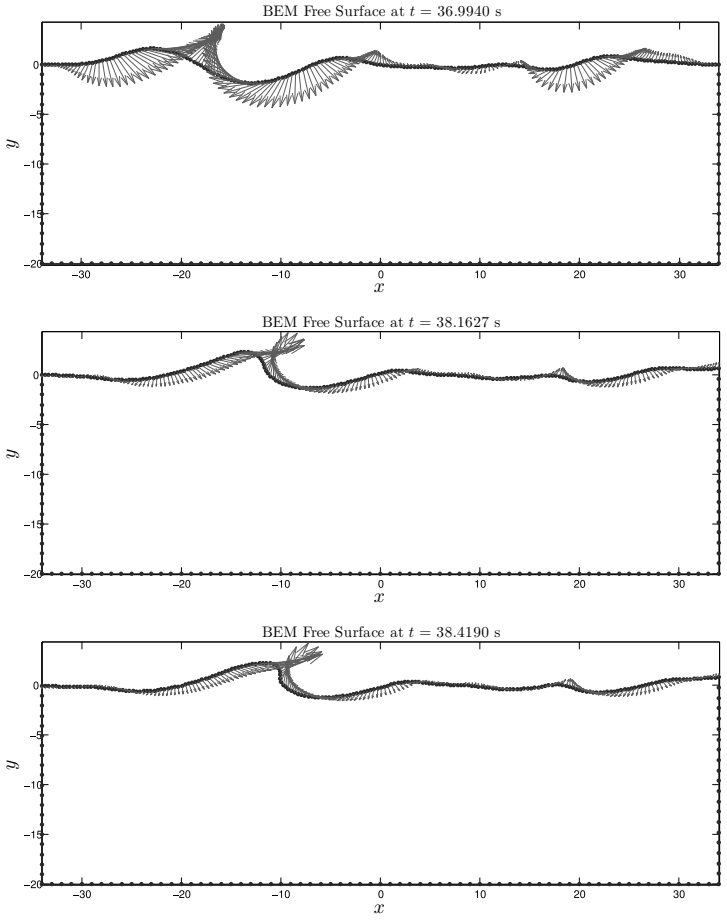

Figure 5.35: First three snapshots of a "Moderate waves" sea state. Red arrows denote the free surface particles velocity and the blue dots the boundary element mesh. Input data from table 5.11.

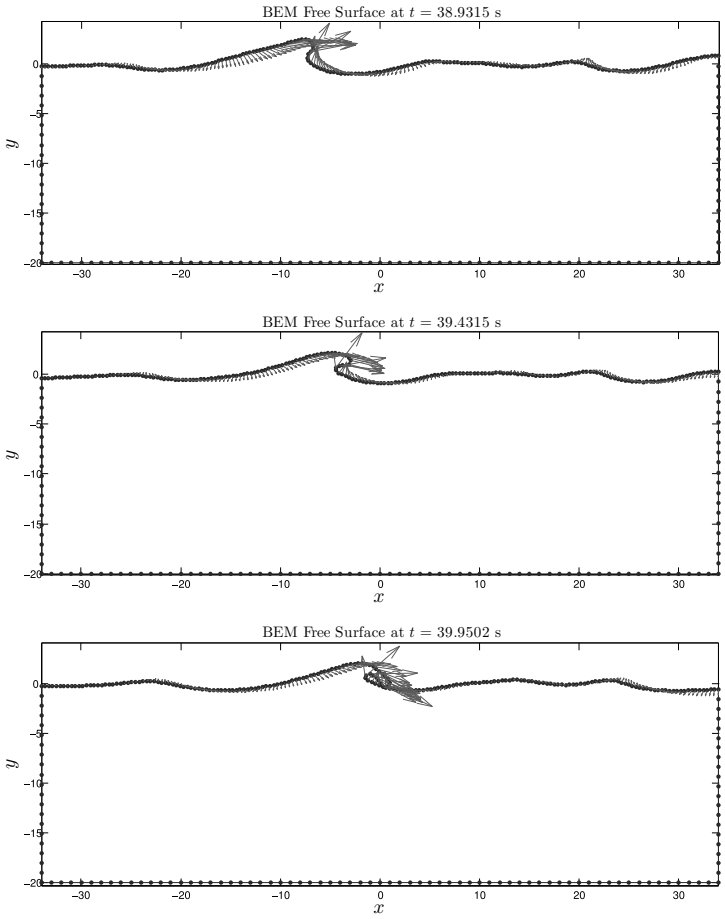

Figure 5.36: Second three snapshots of a "Moderate waves" sea state. Red arrows denote the free surface particles velocity and the blue dots the boundary element mesh. Input data from table 5.11.

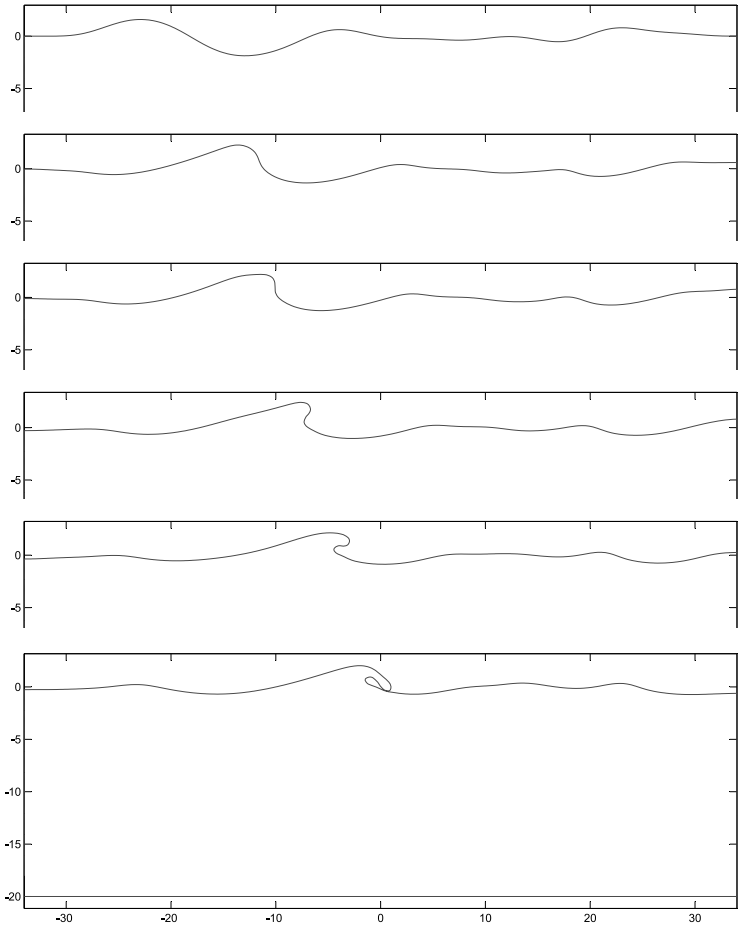

Figure 5.37: Application 5: free surface elevations for the six time instants associated with a "Moderate waves" sea state. Input data from table 5.11.

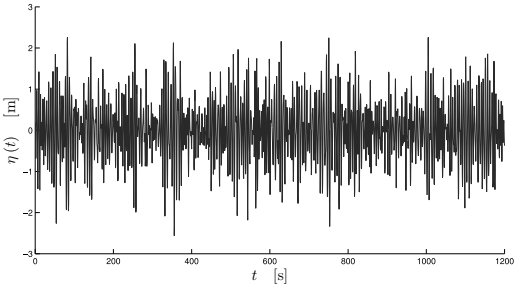

Figure 5.38: Time series of the free surface elevation at $x_t = 0$ for a "Moderate sea". More input data in table 5.12.

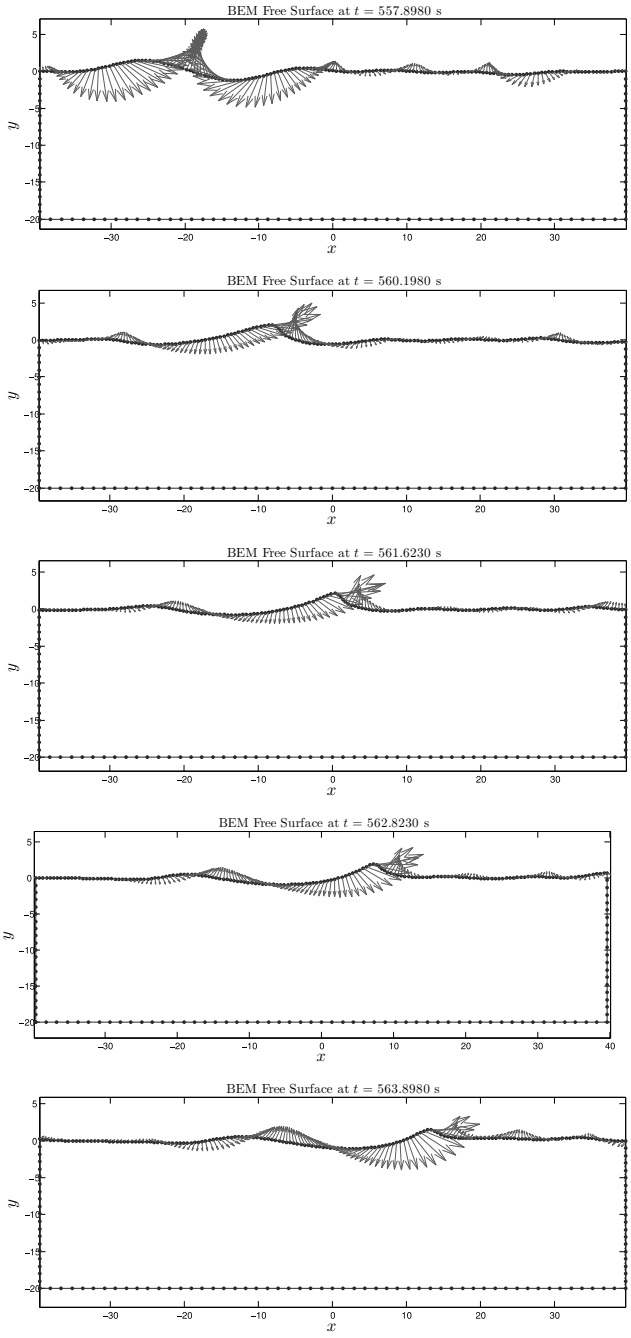

Figure 5.39: Five snapshots of a "Moderate waves" sea state. No breaking waves occur and t_b is fixed by the maximum steepness. Red arrows denote the free surface particles velocity and the blue dots the boundary element mesh. Input data from table 5.12.

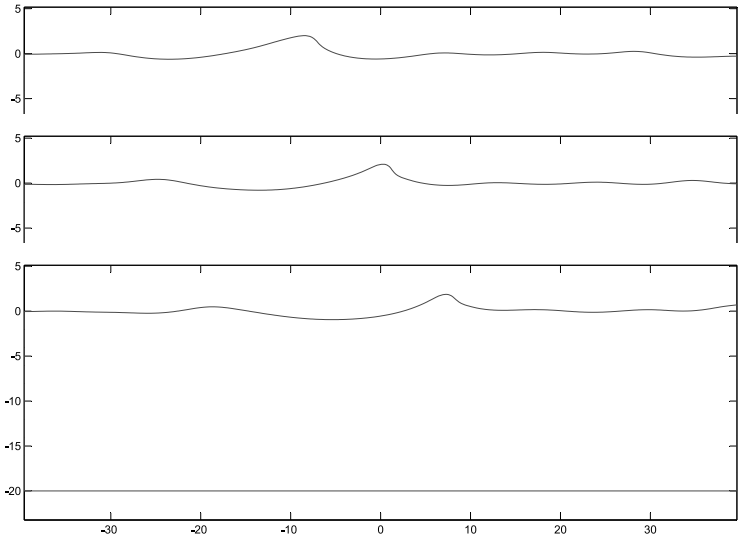

Figure 5.40: The three central snapshots of figure 5.39. Free surface evolution in the surrounding of x_t for a non–breaking wave case. The entire subdomain is shown only in the lower subplot. Input data from table 5.12.

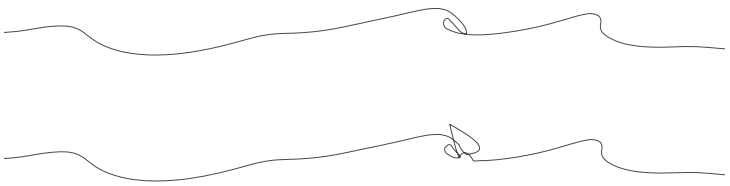

Figure 5.41: Breaking down of the numerical scheme due to re–entry of the water jet in the sea surface.

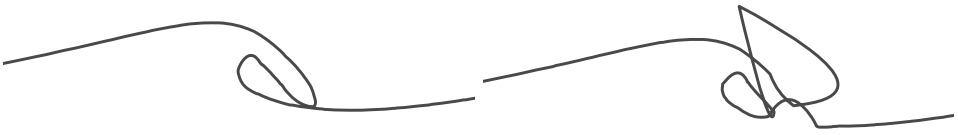

(a) Last time step before breaking down. (b) Re–entry and simulation breaking down.

Figure 5.42: Details of the overturning spout. Zoom–in of figure 5.41.

5.5 Fully nonlinear aero-hydro-elastic coupled model

In this section the complete fully integrated wind–waves simulation model is presented. The main steps and the global numerical framework shown in figures 5.24 and 5.25 is here generalized and extended in order to include all the possible breaking wave events occurring during the extreme sea state. The main implication of this feature is that the call to the fully nonlinear solver is made as many times as the number nb of plunging breakers detected.

Moreover, in this section the interface of the numerical wave simulator with FAST is developed.

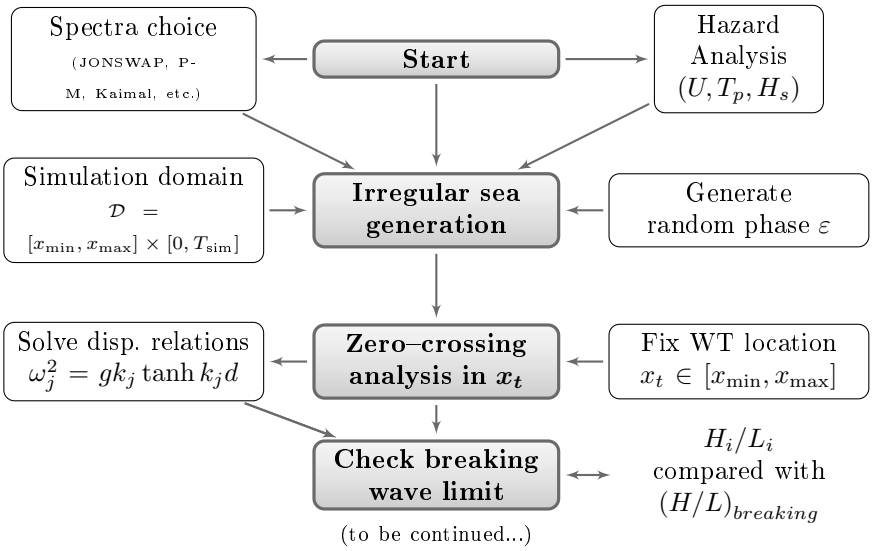

Figure 5.43: First part of the complete aero–hydro–elastic simulation.

The diagram shown in figure 5.43 does not present any significant difference compared with the scheme already seen in figure 5.24. It is just repeated for the sake of completeness.

On the contrary, a substantial difference appears in the second part of the complete simulation scheme depicted in figure 5.44. Here in fact all the instants at which a breaking wave is expected are collected in the vector $\bar{t}_b$ and nb sub–domains have to be defined. In fact, while in the previous section only the strongest event was considered, here we need to account for all the possible impacts which may occur during a storm. Therefore, nb possible overturning breakers are simulated by calling nb times the fully nonlinear solver. Note that the procedure shown earlier to compute the time instant at which braking occur needs to be slightly adjusted in order to get the vector $\bar{t}_b$

$$t_{b_i} = t_{up}(1) + \sum_{h=1}^{\mathsf{BrLm}(i)-1} T(h) + T(\mathsf{BrLm}(i))/4 \tag{5.31}$$

where BrLm is the vector selecting only elements of $\bar{\epsilon}$ which breaks, $\bar{t}_{up}$ is the vector

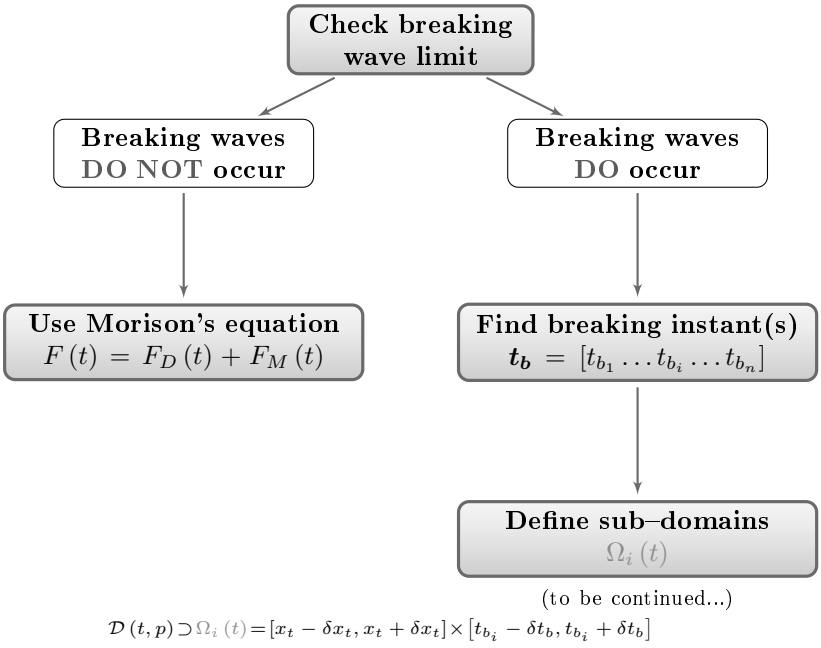

Figure 5.44: Second part of the complete aero–hydro–elastic simulation.

collecting the zero up–crossing time instants, $\bar{T}$ collects all the wave periods in the signal $\eta(x_t, t)$.

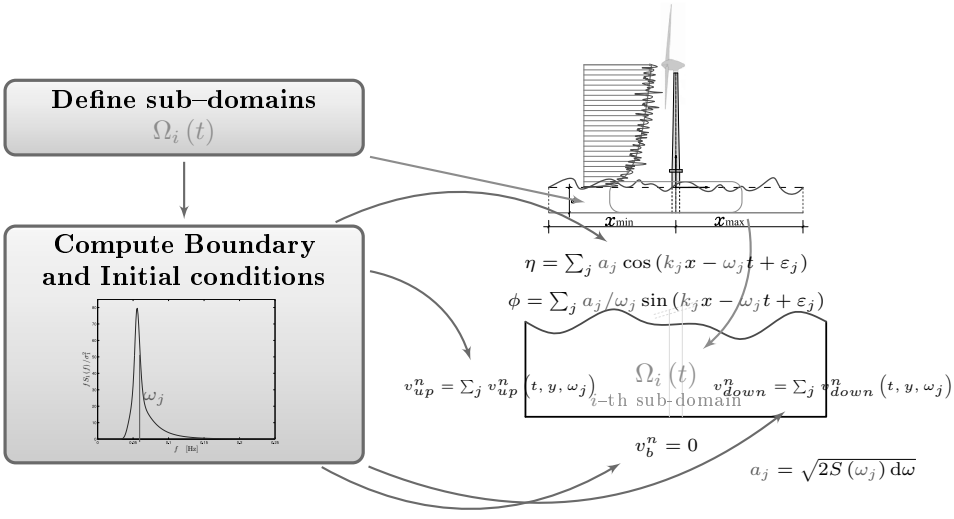

Figure 5.45: Definition of subdomains and initial and boundary conditions assignment form JONSWAP spectrum.

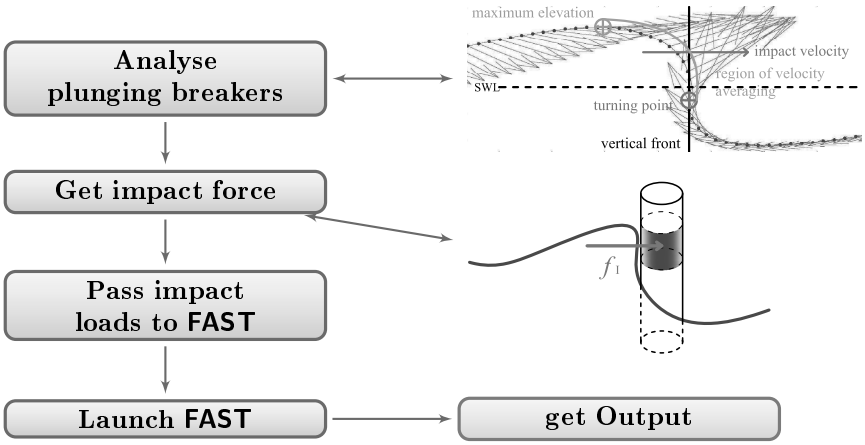

Figure 5.46: Last part of the global simulation scheme: interface with FAST.

The definition of sub-domains is well depicted in figure 5.45 where it is clear how the BEM–based code is activated to solve the fully nonlinear Laplace's equation on the domain Ω_i (relative to the i–th braking event) by assigning initial and boundary conditions derived by the linear spectral approach.

The last group of subroutines of the global simulation code execute the instructions sketched in figure 5.46, where the kinematic properties of each plunging breaker are derived. Impact forces are computed and subsequently passed to FAST which performs the time marching analysis.

The instructions executed by the software are also summarized in the algorithm 3 which gives a simplified representation of the whole procedure. Note that the environmental analysis is carried out externally from algorithm 3.

In the above algorithm WaveDT denotes the time step for the irregular sea simulation, the argument $input_i$ passed to the subroutine CallBEMSolver collects all the data related to the i–th breaking wave necessary to run the fully nonlinear code. See section 4.2 for details.

A global view of all the main steps of the code is presented in the scheme on figure 5.47.

Before presenting the applications of the software, we just stress that fact that in the light of the considerations and values proposed in the previous section about the simplified extreme sea states definition, given a wind turbine located in a generic region of North Sea with water depth of 20 m designed to withstand an 50–year return period extreme mean wind velocity of 37.5 m/s (wind class III, [36]), it seems to be reasonable to perform most of the simulations by assuming variations of the input parameters in the neighborhoods of the "most probable" sea state characterized by the following values of significative wave height and peak period

- $H_s = 12\,\mathrm{m}$
- $T_p = 12\,\mathrm{s}$

Now it is possible to start simulating irregular seas coupled with realistic turbulent wind.

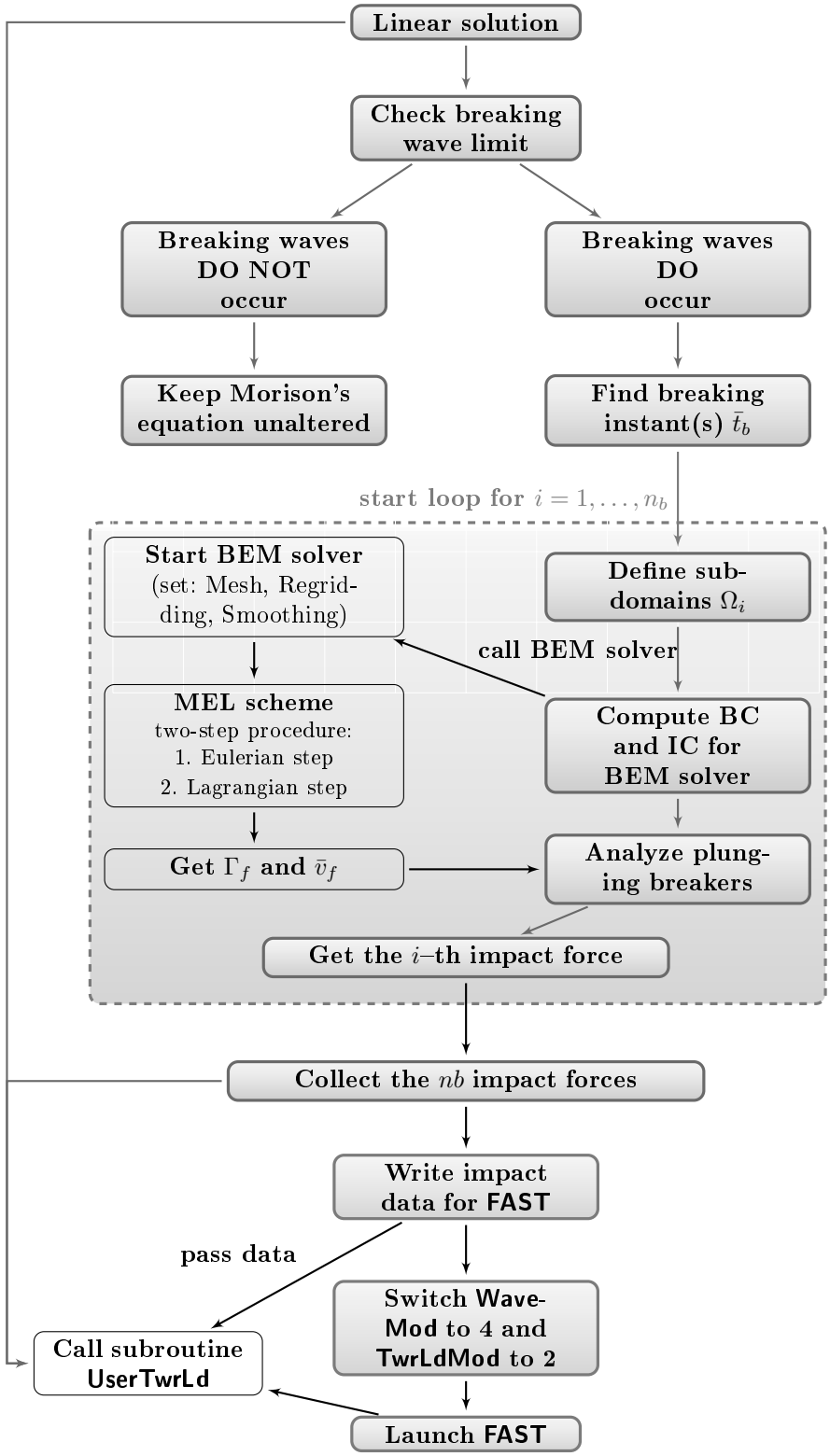

Figure 5.47: Framework of the whole simulation scheme.

Algorithm 3: Global simulation scheme.

input : Environmental variobles: U_{ref}, H_s, T_p
input : Total simulation time: T_{sim}
output: Impact force: $\bar{f}_I$
Initialization: $\bar{f}_I = \mathsf{zeros}\,(0 : \mathsf{WaveDT} : T_{\text{sim}}, 3)$;

Spectrum choice;
Irregular sea generation;
Setting the wind turbine location;
Zero–crossing analysis;
Solve dispersion relations;
Check breaking waves limit;
if *breaking waves occur* **then**
  Identify all possible breakers: get nb;
  for $i = 1$ **to** nb **do**
    Define space–time subdomains: fix δt_{b_i} and δx_t;
    $[v_i, \eta_{b_i}] = \mathsf{CallBEMSolver}\,(input_i)$;
    $\left[\bar{f}_{I_i}\right] = \mathsf{ComputeImpactForce}\,(v_i, \eta_{b_i})$;
else
  Morison's eq. unaltered;
Get final impact force $\bar{f}_I = \sum_{i=1}^{nb} \bar{f}_{I_i}$;

5.5.1 Fully coupled `Simulation #01`

Before approaching the final coupled simulations, a preliminary model is set up with no wind blowing, while an extreme irregular sea is generated. We should point out that this scenario is unrealistic because, as stated many times throughout this work, the focus is on wind–generated waves and not swells. However this preliminary simulation allows to test whether the software, until now only tested with regular waves, is stable and reliable.

In table 5.13 all the input data characterizing this simulation, form now on denoted by `Simulation #01`, are provided.

Note that WaveDT, DT, dt in the above table refer to time step for the linear irregular sea generation, FAST time step, our BEM simulator, respectively. Moreover, values δx_t and δt_b will always be constant for each breaking event occurring in one simulation.

First of all we start by showing the time series of the free surface elevation at the turbine location. The first time the breaking wave limit is achieved is at 68.12 s when, as confirmed in figure 5.48, a clear peak of about 13 m is registered.

Since $nb = 2$, the fully nonlinear wave kinematic solver is called two times. The most significative snapshots of the free surface evolution for each call are shown in figures 5.49 and 5.51, respectively.

Data passed to the subroutine computing the impact force are extracted at the time shown in figure 5.50.

It is interesting to observe that the predicted breaking wave time matches very

U_{ref}, I_{ref}	0 m/s, 0
$U_{19.5}$, H_s, T_p	0 m/s, 12 m, 12 s
Spectrum type, γ	JONSWAP, 3.3
Water depth	Intermediate Water
T_{sim}, $x_{\min}$, $x_{\max}$	600 s, −300 m, 300 m
WaveDT, DT, dt[11]	0.05 s, 0.01 s, 0.05 s
Turbine location x_t	0
Predicted number of breaking wave events	2
Number of breaking wave events occurred nb	2
Predicted breaking waves time vector $\bar{t}_b$ s	68.118, 105.376
BrLm	8, 11
δx_t	252.7681 m
δt_b	3 s
NE_f	80

Table 5.13: Input data for `Simulation #01`.

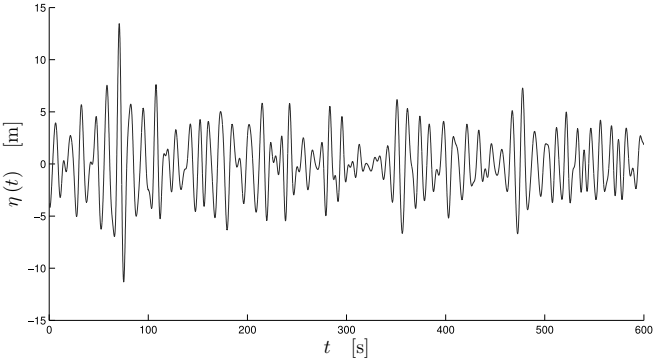

Figure 5.48: Time series of the free surface elevation at $x_t = 0$ for `Simulation #01`. Input data in table 5.13.

well the instant at which the impact occurs. However, it will not always be like this.

It must be pointed out that the predicted time at which the breaking wave would occur is just an indication to define the initial time to start the BEM solver. In fact, as it happens for the second breaker, the predicted time was 105.38 s but the simulation reveals that the wave crest starts overturning (say when the front forms) later at $t = 107.70$ s. From figure 5.53, it is clear that the overturning is taking place approximately 20 m further the turbine location.

This example reveals how inaccurate the linear model can be in predicting breaking waves.

The total impact force vector read in FAST is shown in figure 5.55. This plot

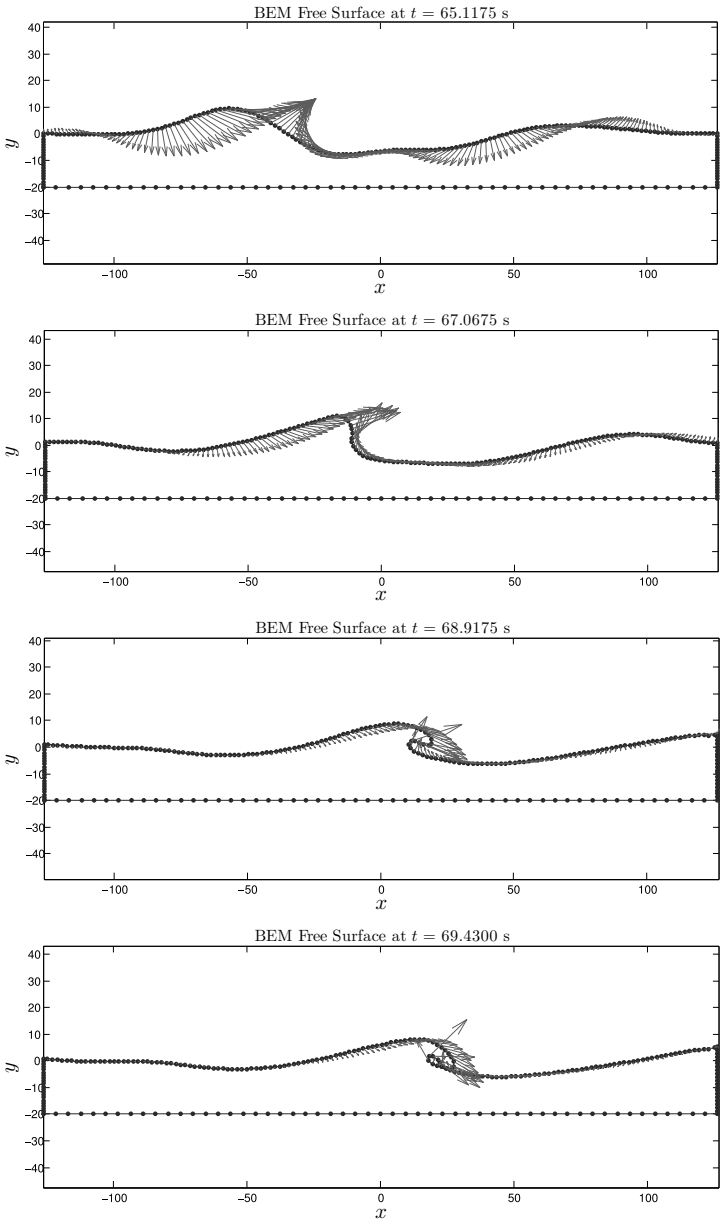

Figure 5.49: `Simulation #01`, first breaking wave event. Three snapshots of fully nonlinear free surface evolution.

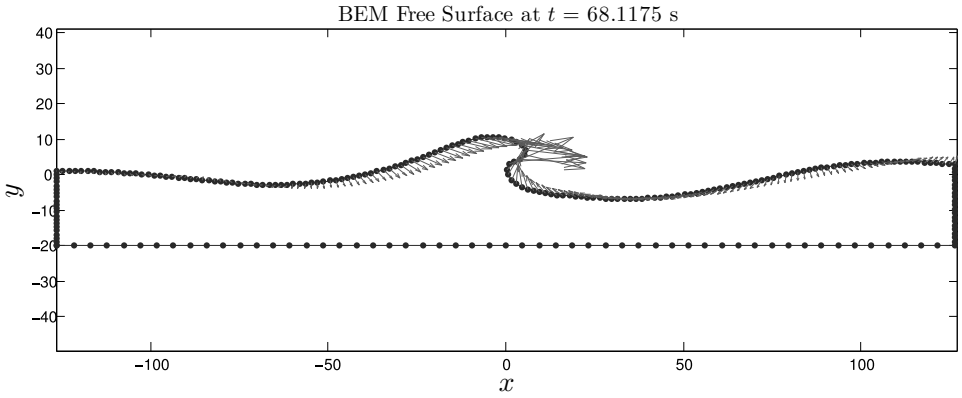

Figure 5.50: `Simulation #01`, first breaking wave event. Time at which the slam is supposed to happen.

is rather useful in understanding how the impulsive contributions are distributed during the whole simulation.

The structural response is presented in figures 5.56 and 5.57. The two slamming loads which occur during 10 min simulation induce on the structure a remarkable additional state of internal stress. To have a proper idea of what really happens when these two impulsive actions act on the monopile, we first observe the time series of the tower top fore–aft displacements, figure 5.56. From a maximum value (either positive or negative) of 5 cm when the first impact takes place, the maximum peak displacement leaps to approximately 21 cm, then when the vibrations start decay suddenly the second hit arrives and, even though it has a lower intensity because of a smaller η_b and reduced impact velocity, a clear amplification is registered around 105 s which brings the peak displacement up to 24 cm.

Note that here ultimate strength conditions are investigated, therefore the peak values are really crucial in assessing the structural safety.

Also looking at the shear force and bending moment at the foot of the monopile, reported in figure 5.57, the two peaks associated with the respective plunging breakers are very clear. In this case, contrarily to what happens for the tower top fore–aft displacement, the second shock does not cause an amplification of the first one. Both F_{xt} and M_{yt}, indeed, seem to have the time to dissipate all the momentum induced by the first impact in about 35 s which is approximately the time interval between the two slams.

The remaining internal forces and moments are also slightly affected by the impacts, but of course, due to the main direction of the colliding waves, they register a negligible consequences and for this reason are not shown in this first simulation.

From this preliminary case analyzed interesting suggestions to set up the next case study are derived: first the simulation time should be increased, second it is fundamental now to activate the turbulent wind simulator in order to have a first more realistic extreme environment.

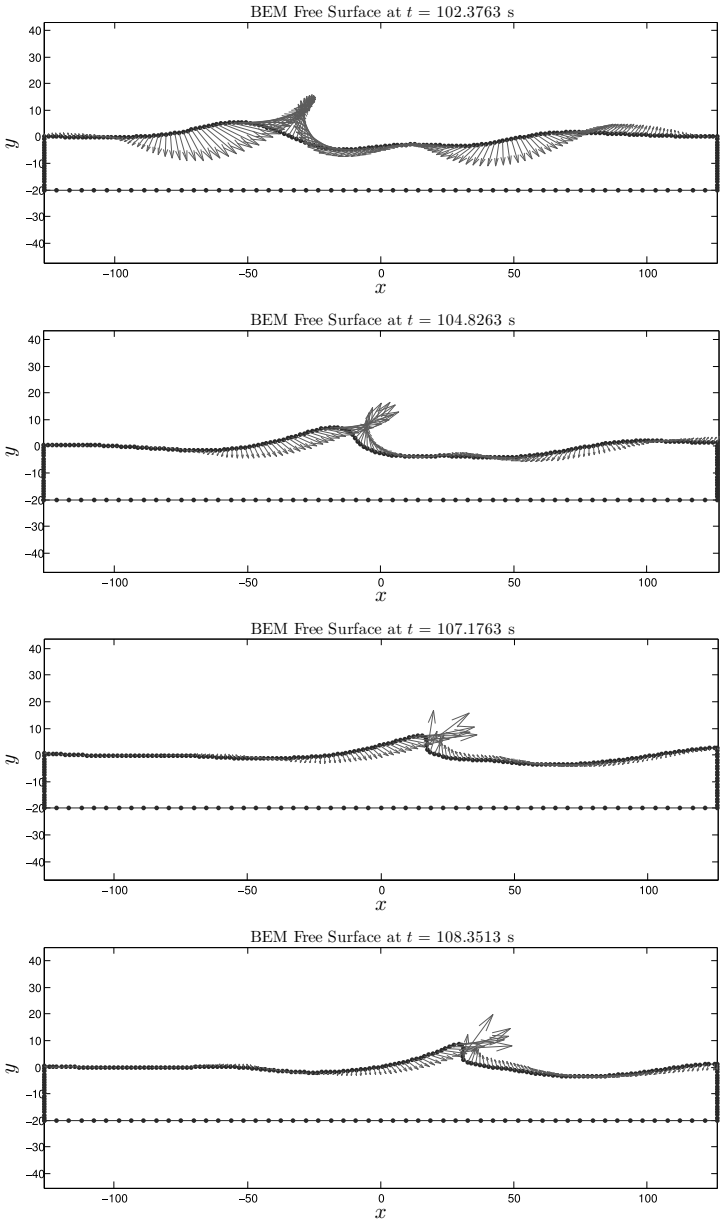

Figure 5.51: `Simulation #01`, second breaking wave event. Four snapshots of fully nonlinear free surface evolution.

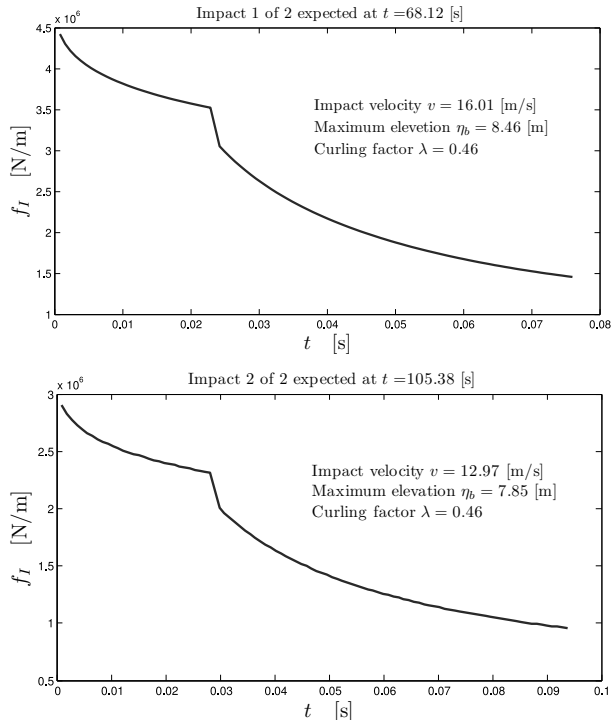

Figure 5.52: `Simulation #01`, impact forces computed according to section 4.5.

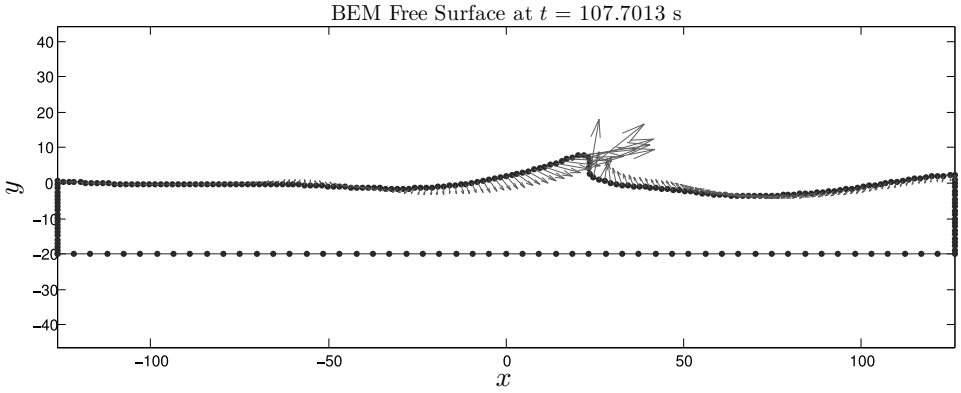

Figure 5.53: `Simulation #01`, second breaking event. Time at which the slam is supposed to happen.

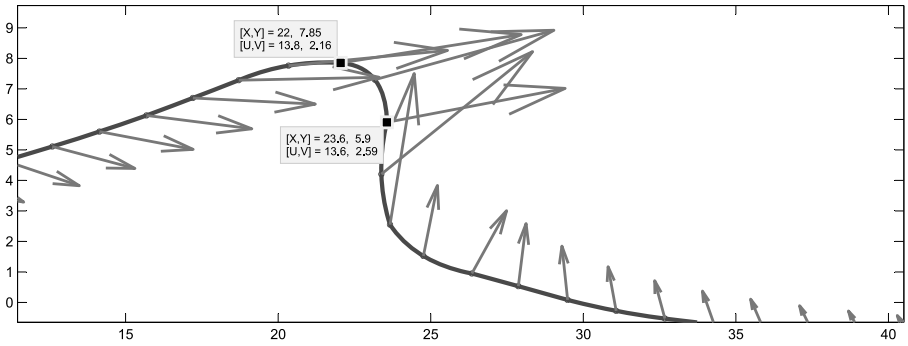

Figure 5.54: `Simulation #01`, second breaking event. Time at which the slam is supposed to happen. Detailed view of the impact front of the jet forming shown in figure 5.53.

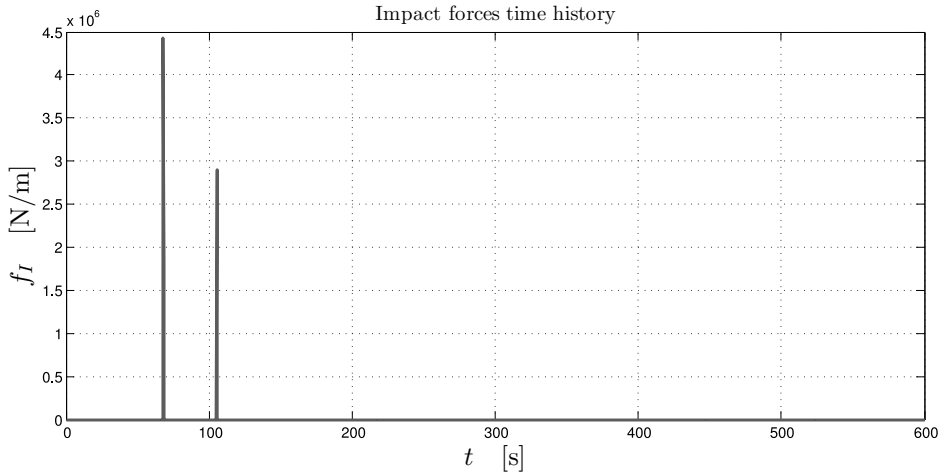

Figure 5.55: `Simulation #01`, time history of the impact forces throughout the total simulation time. On this scale the two impacts look like just two pins with intensity in agreement with figure 5.52.

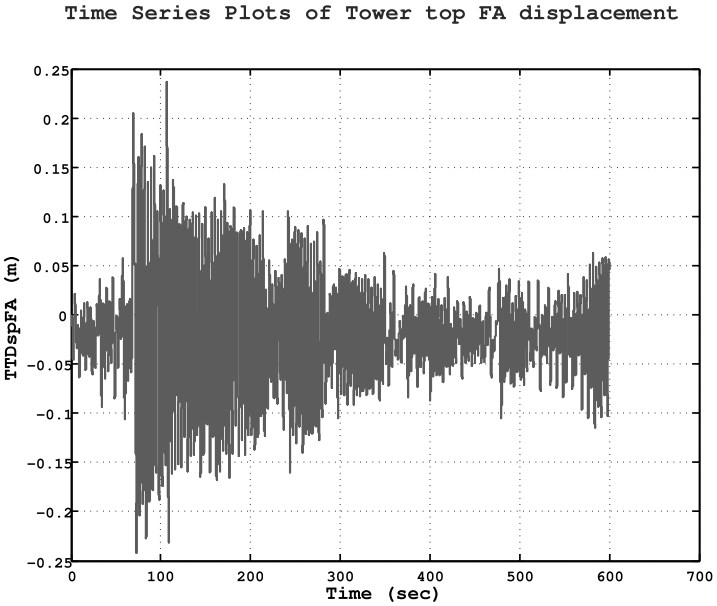

Figure 5.56: `Simulation #01`, Tower top fore–aft displacements time series.

5.5.2 Fully coupled `Simulation #02`

Table 5.14 lists all the input data characterizing this second simulation, form now on referred to as `Simulation #02`. This case is much more realistic than the previous one because here we really have for the first time the coupled wind and wind–waves extreme actions together.

The turbulent wind is generated by means of TurbSim, already introduced in section 5.4 of this chapter. The three 50–year recurrence period turbulent wind velocity components are plotted in figure 5.58.

Such a severe wind condition gives rise to an extreme irregular sea modeled by a JONSWAP spectrum characterized by a significative wave height $H_s = 12\,\mathrm{m}$ and a peak period $T_p = 12\,\mathrm{s}$ as reported in table 5.14. This sea has a free surface elevation at the turbine location shown in figure 5.59.

The software developed in this thesis at this point performs a zero–crossing analysis from which it results that in 10 min simulation and upon the severity environmental conditions assumed, one breaking wave event may occur, i.e $nb = 1$.

Thus the fully nonlinear wave kinematic solver is called only once. The most significative snapshots of the free surface evolution for the call are shown in figure 5.60.

Figure 5.60 shows four frames of the simulation. The upper subplot represents the initial time t_i, see equation (5.15), at which the BEM solver is started. The two intermediate sub–figures show the augmentation of the steepness until the "cusp" starts overturning, while the lower one describes the re–entry of the water jet which is completely curled. The latter is also the last time step the software in able to integrate the boundary conditions, in fact after this, the multi–connected domain

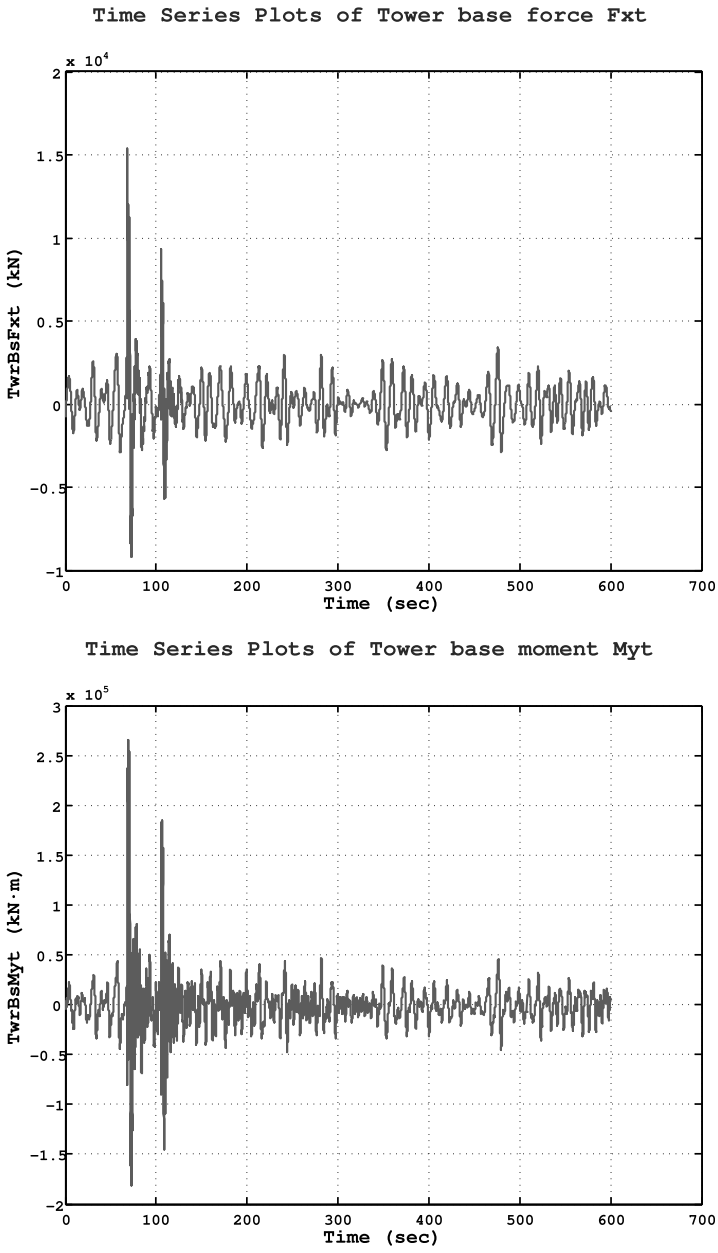

Figure 5.57: `Simulation #01`, tower base shear force F_{xt} and overturning moment M_{yt}.

occurs, the irrotational flow hypothesis is no longer valid and the numerical scheme breaks down as shown in the example of figure 5.41.

Data passed to the subroutine that computes the impact force are extracted

U_{ref}, I_{ref}	37.5 m/s, 0.12
$U_{19.5}$, H_s, T_p	31.69 m/s, 12 m, 12 s
Spectrum type, γ	JONSWAP, 3.3
Water depth	Intermediate Water
T_{sim}, $x_{\min}$, $x_{\max}$	600 s, −300 m, 300 m
WaveDT, DT, dt[12]	0.05 s, 0.01 s, 0.05 s
Turbine location x_t	0
Predicted number of breaking wave events	1
Number of breaking wave events occurred nb	1
Predicted breaking waves time vector $\bar{t}_b$ s	516.10
BrLm, Steepness ϵ	48, 0.1473
δx_t	263.304 m
δt_b	3 s
NE_f	100

Table 5.14: Input data for `Simulation #02`.

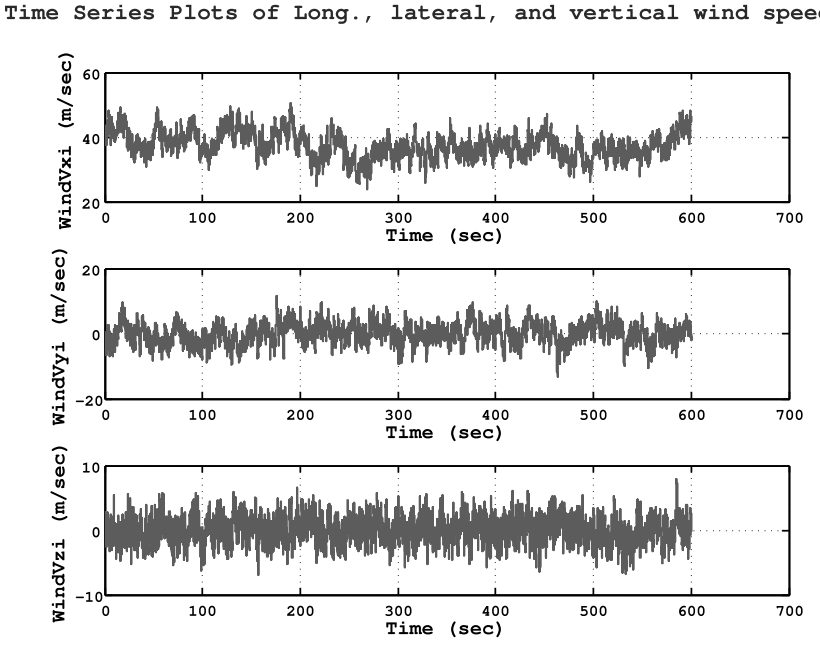

Figure 5.58: Time series of three turbulent wind speed components according to the Extreme Wind speed Model (EWM) of IEC61400-1 3rd ed. Time histories used in `Simulation #02`.

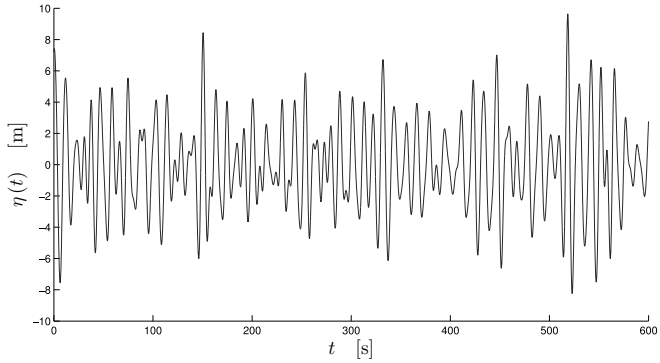

Figure 5.59: Time series of the free surface elevation at $x_t = 0$ for `Simulation #02`. Input data in table 5.14.

when the worst condition among maximum elevation and maximum impact velocity is reached. This condition is shown in figure 5.61.

Also in this circumstance the predicted breaking wave time matches extremely well the instant at which maximum wave elevation and impact velocity are extracted. The predicted value is 516.10 s, while the time at which the crest starts overturning and may likely exert the strongest impact force is $t = 516.85$ s. The two value are surprisingly close each other and this confirms the validity of the approach hereby implemented. A zoom–in of the free surface elevation with its kinematic features is offered in figure 5.62.

Note also that the spatial agreement between the expected location $x_t = 0$ (where the turbine is supposed) and the simulated impact.

The elevation η_b and the velocity v characterizing this impact are 12.44 m/s and 7.73 m, respectively; the impact duration is 0.0978 s and this means that approximately 10 time steps of FAST integration scheme account for such an impulsive contribution.

The total impact force vector read–in by FAST is plotted in figure 5.63(b). This plot permits to better understand the following results about the structural response. Figures 5.64 shows the tower top fore–aft displacement time series and, contrarily to what happened in `Simulation #01`, in this case impulsive load does not bring the tower top displacement too mach beyond its normal maxima. Where with "normal maxima" is intended as the peaks in the displacement time series before t_b.

The reason why this happens lies in the fact that `Simulation #01` was performed *without* wind and, of course, this made the structural displacement only depend on the the hydrodynamic loads where the impulsive action was generated. On the contrary, in `Simulation #2` a turbulent extreme wind (with mean value of 37.5 m/s) is blowing in the same direction of the slamming wave. Therefore, the tower is already vibrating with an average maximum displacement of 20 cm (it was 5 cm for `Simulation #01`) and when the impact occurs it can even be out of phase. We want to point out that the frequency of the impulsive loads are very high, therefore they are far beyond the first system fore–aft natural frequency. For this reason, the

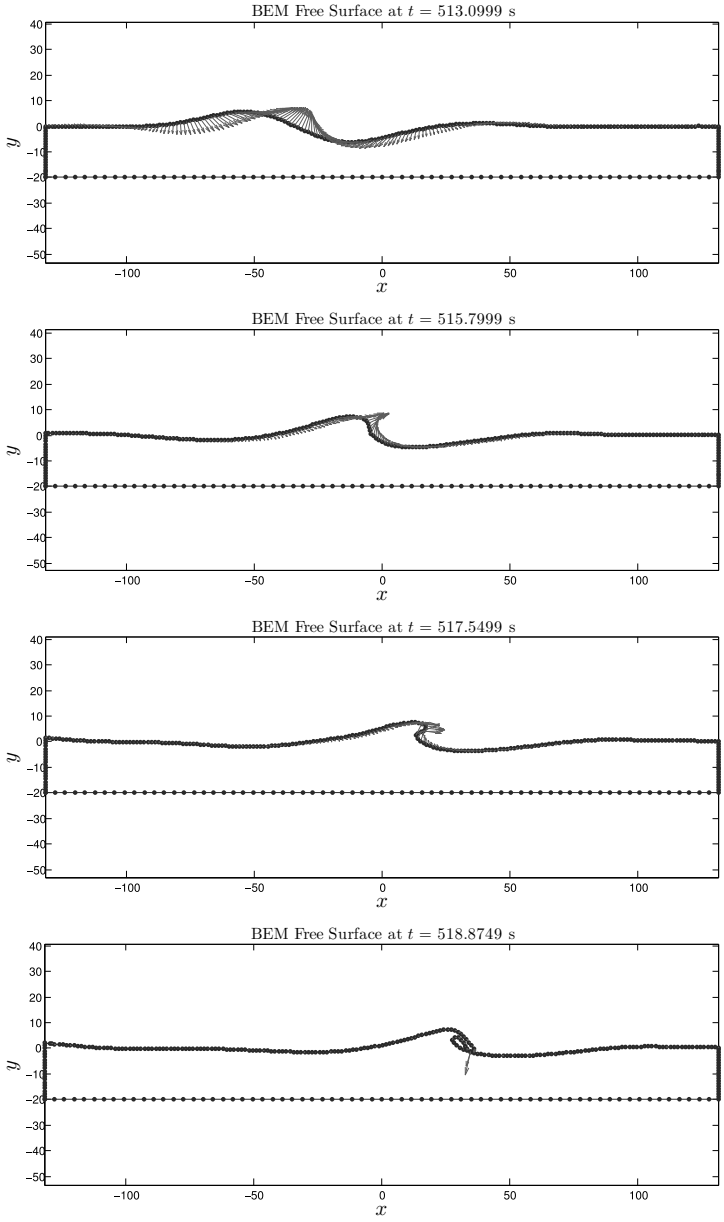

Figure 5.60: `Simulation #02`, first breaking wave event. Four snapshots of fully nonlinear free surface evolution.

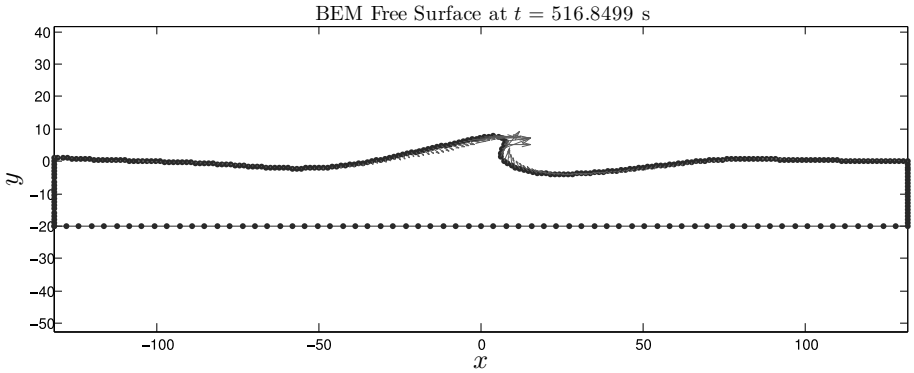

Figure 5.61: `Simulation #02`, maximum wave elevation η_b and impact velocity v are those associated with this instantaneous frame.

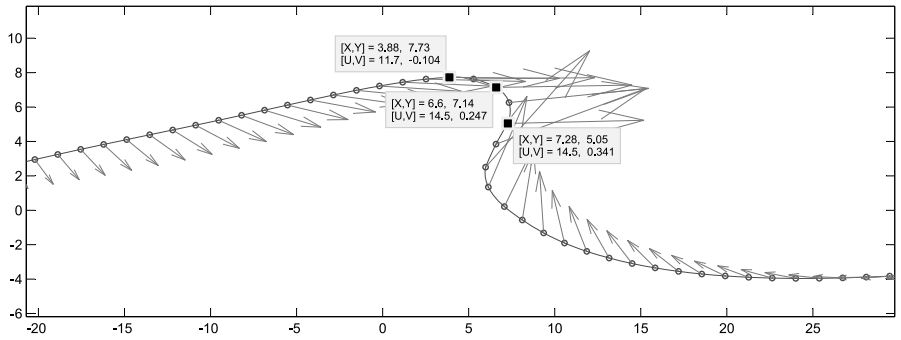

Figure 5.62: `Simulation #02`, second breaking wave event. Time at which the slam is supposed to happen. Detailed view of the impact front of the jet forming shown in figure 5.61.

consequences of the impacts are almost negligible on the global dynamics of the system.

The slamming wave which may occur during 10 min simulation induces on the structure a remarkable additional state of internal stress. And likewise to what pointed out for `Simulation #01`, peaks of internal forces and moments are absolutely relevant for our scopes.

It is impressive but not surprising to see the instantaneous augmentation of both the shear tower base force F_{xt} and the bending tower base moment M_{yt} plotted in figure 5.65. The force undergoes a leap from a peak of 4×10^3 kN to nearly 10×10^3 kN (positive sign), while the bending moment has extreme peaks of about 0.5×10^5 kNm and the impact brings the value up to nearly 1.5×10^5 kNm.

Another interesting structural output which deserves attention is the internal bending moment at the still water level. In this cross–section the structure registers the additional couple due to the impact given by the impact force $M_I = F_I d_I$, where $F_I = f_I \lambda \eta_b$ is the impact force described in section 4.5 and d_I denotes the

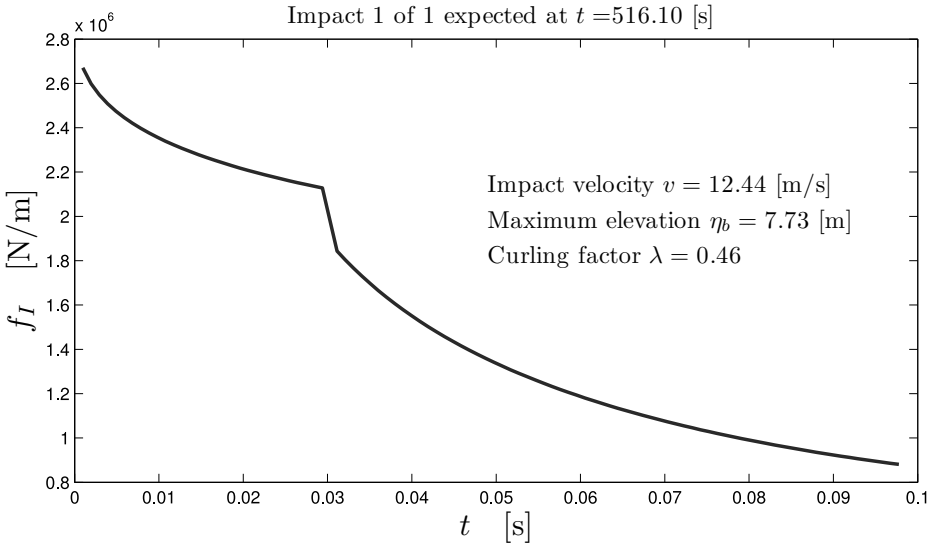

(a) Time history of the impact force throughout its duration.

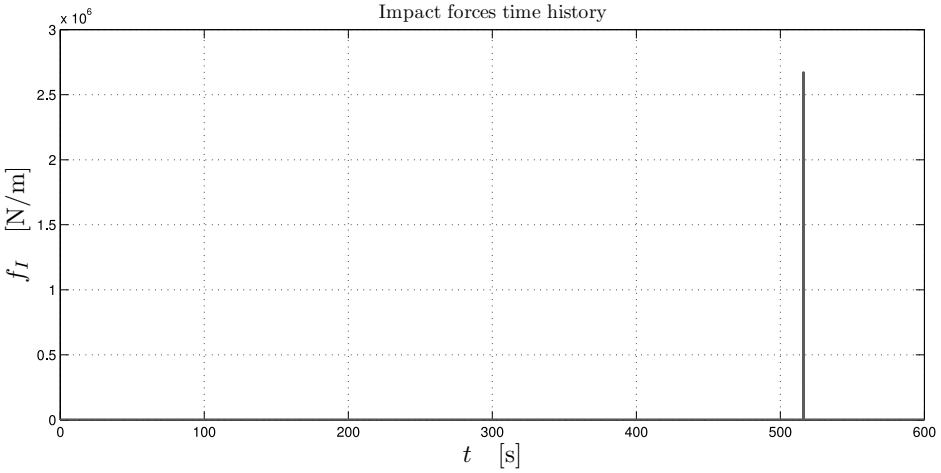

(b) Time history of the impact force throughout the total simulation time. On this scale the impact looks just like a spike.

Figure 5.63: `Simulation #02`, impact force time histories in the two different time scales.

moment arm given as $\eta_b\,(1 - 1/2\lambda)$, where λ is the curling factor [8].

Also for the fore–aft bending moment at the tower cross–section taken at the mean sea level, plotted in figure 5.66, as expected, a peak is registered at $t = 517.5\,\mathrm{s}$ due to the impact. Note also that since in this case the moment arm is twenty meters (the water depth) shorter with respect to the moment acting at the monopile foot form plot 5.65, M_{yt} results one order higher: 1.5×10^5 kN versus 3.4×10^4 kNm at

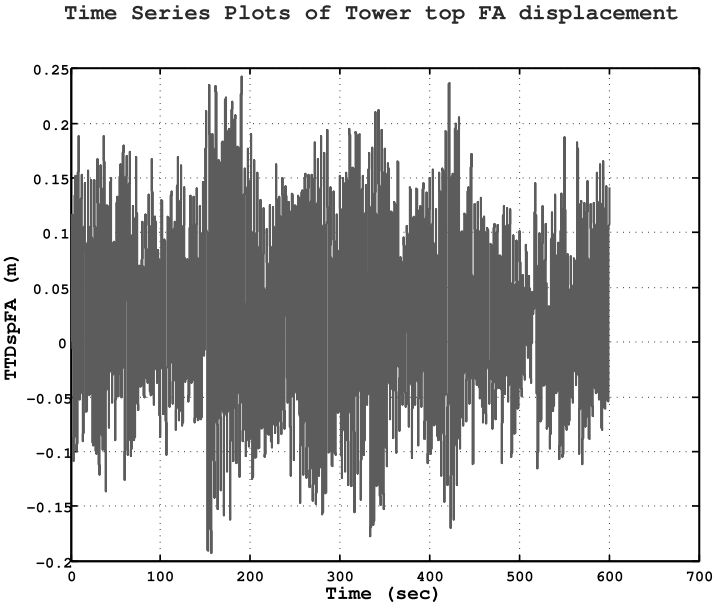

Figure 5.64: `Simulation #02`, Tower top fore–aft displacement time series.

the SWL[13]

Since for this simulation lateral and vertical wind components are also simulated, see figure 5.58, it would be interesting also to see the structural response in these other directions, to check whether the impact causes some effects.

As expected, forces, bending moments and torsion at the tower base are not completely negligible due to the lateral and vertical wind loads, however from figure 5.67 it is possible to say that no relevant effects are induced by the impact.

5.5.3 Fully coupled `Simulation #03`

The simulation presented here is particularly important for two main reasons: first it is longer than those launched up to now, and this is fundamental to have much more reliable data when evaluating the distribution of peaks due to impacts. The duration is also relevant because it permits to test the numerical stability of the code. This application shows that the code developed is reliable also for 40 min simulations.

The second very important reason for which `Simulation #03` is crucial is that it is based on "real data" input. As discussed in section 5.4, so far we have assumed the most important data to estimate the sea severity by using a simplified approach. We just relied on data and tables provided in literature and said that for 31.695 m/s wind speed at 19.5 m above the sea level, the related sea state severity should be defined in a neighborhood of $H_s = 12\,\mathrm{m}$ and $T_p = 12\,\mathrm{s}$. This is true but in this

[13] This numbers are totally indicative and have the only scope to make rough check whether the results match the expectations.

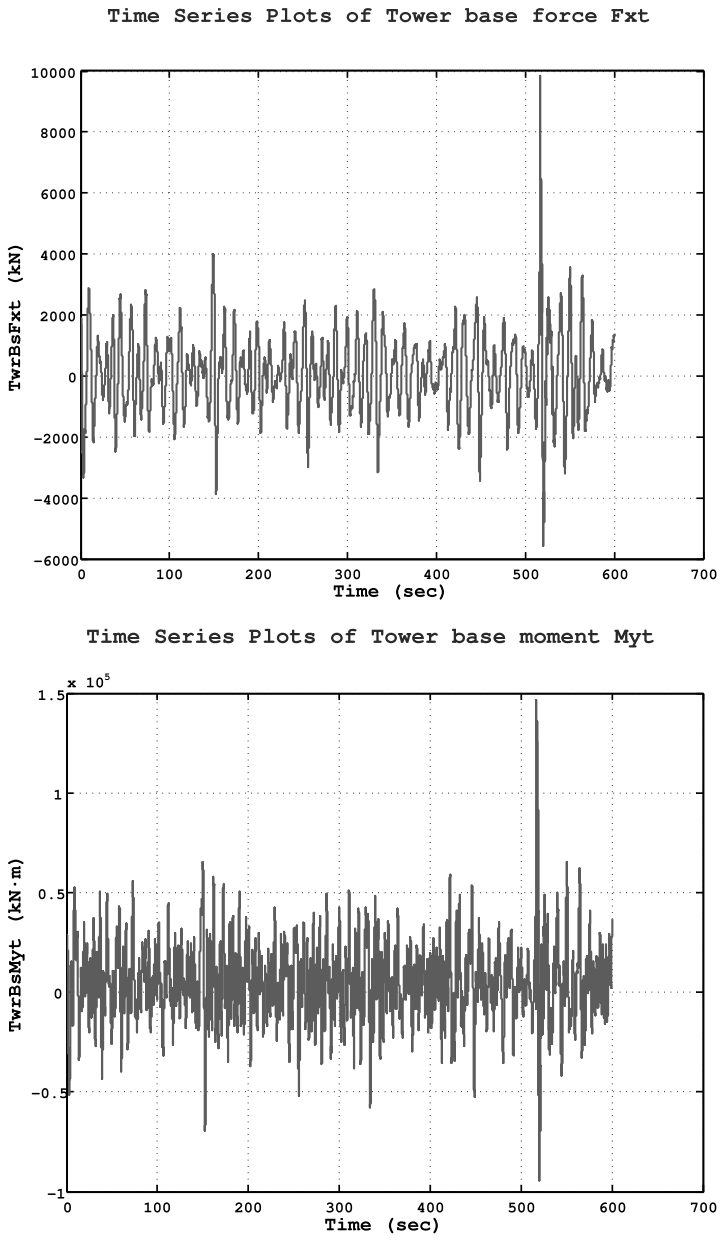

Figure 5.65: `Simulation #02`, tower base shear force F_xt and overturning moment M_yt.

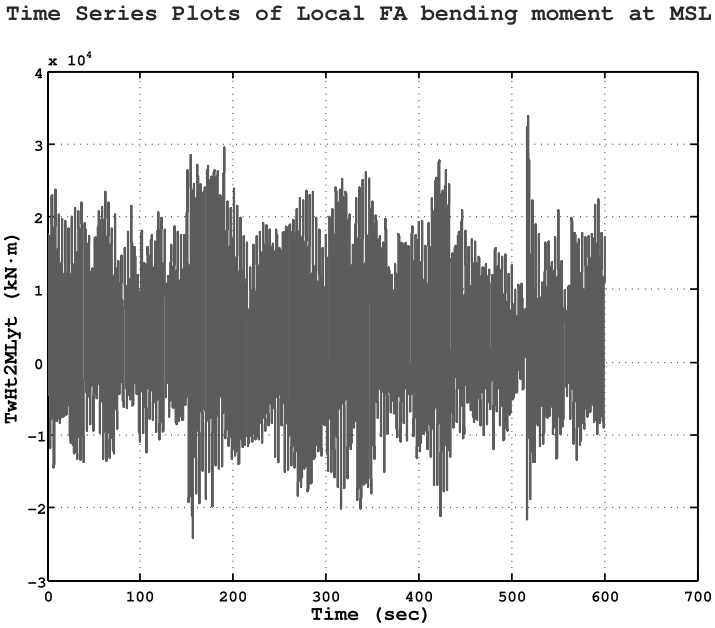

Figure 5.66: `Simulation #02`, tower top fore–aft bending moment at the tower cross–section taken approximately at the mean sea level.

case we wanted to use input parameters which have been extrapolated by real data referred to the North Sea. In [31], indeed, starting from data recorded over 3 years in the area of 2° longitude east and between 53° and 54 latitude north, the significant wave height and mean zero–crossing period with return period 50 years have been extrapolated. So in this case we are using data that we are sure they have the same return period of the wind velocity assumed. Anyhow, it should be kept in mind that the distributions for H_s and T_p have been assumed uncorrelated to the mean wind speed and this could lead to some approximation of the values. All the parameters characterizing `Simulation #03` are listed in table 5.15.

The turbulent wind is generated as in the case of `Simulation #02` and the three 50–year recurrence period turbulent wind velocity components are plotted in figure 5.68.

The 50–year return period random sea which may occur in the North Sea during a storm having the turbulent wind plotted in figure 5.68 is depicted in figure 5.69.

The zero–crossing analysis of the signal plotted in figure 5.69 detects that there could be 3 wave components with such a high steepness to break. Hence, the fully nonlinear solver is invoked three times ($nb = 3$). For each of these sub–simulations, three significant configurations of the free surface evolution are shown in the following. In all three cases, the upper subplot represents the initial time when the BEM solver is called. The three breaking wave events are shown in figures 5.70 to 5.72

The last expected impact would occur at $t = 470.03\,\mathrm{s}$. And according with the sub–domain defined above, the fully nonlinear simulator is started with an initial time $t_i = 467.03\,\mathrm{s}$. In this case the steepness is $\epsilon = \bar{\epsilon}\,((\mathsf{BrLm}\,(3)) = 0.096$ which, for

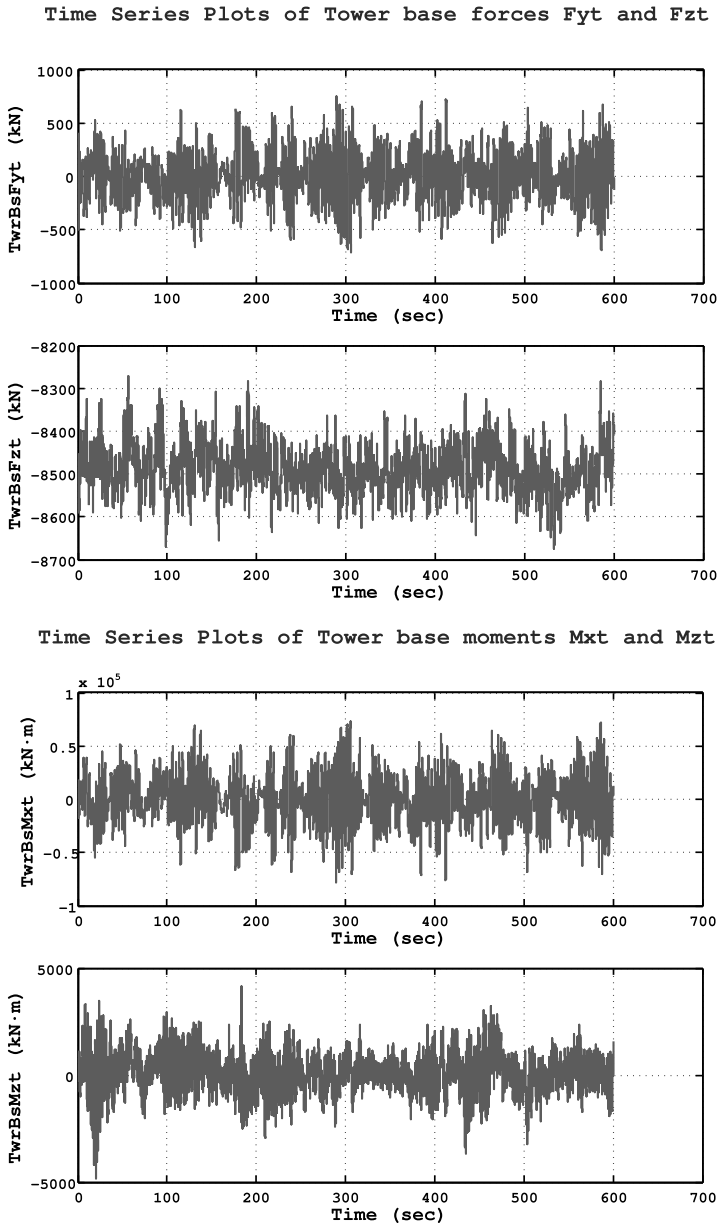

Figure 5.67: `Simulation #02`, tower base shear force F_{xt} and overturning moment M_{yt}.

U_{ref}, I_{ref}	37.5 m/s, 0.12
$U_{19.5}$, H_s, T_p	31.69 m/s, 9.80 m, 13.63 s
Spectrum type, γ	JONSWAP, 3.3
Water depth	Intermediate Water
T_{sim}, $x_{\min}$, $x_{\max}$	2400 s, −300 m, 300 m
WaveDT, DT, dt[14]	0.05 s, 0.01 s, 0.05 s
Turbine location x_t	0
Predicted number of breaking wave events	3
Number of breaking wave events occurred nb	2
Predicted breaking waves time vector $\bar{t}_b$ s	22.28, 36.05, 470.02
BrLm, Steepness ϵ	2, 3, 41
δx_t	286.27 m
δt_b	3 s
NE_f	80

Table 5.15: Data relevant to `Simulation #03`.

a case of intermediate water, is not too larger than the breaking limit. Moreover, to increase the numerical stability of the code the smoothing and regridding of the free surface have been used frequently: smoothing at each time step, regridding every three steps. This causes an unwanted dissipation of energy, which may delay the formation of the plunging breaker.

During the third simulation the expected overturning wave does not occur. See figure 5.72. However, a very steep wave forms and its effect cannot be neglected when it approaches the monopile. Although much weaker, an impact can also be induced. This last case shows that the prediction of breaking waves based on the linear theory may result inaccurate.

The three impact forces stemming from the above simulations are shown in figure 5.73.

The distribution of the impact forces over the whole simulation time is shown in figure 5.74. This plot is rather useful to understand the following results about he structural response. From this plot two remarks rise: the first two impacts are very close each other and this could induce some amplification in the global dynamics of the structure. Second, the third steep wave, which does not really plunge, is also considered an impulsive action. However, its associated impact force is much less strong due to the fact that without plunging, the crest does not reach those very high velocities of the other cases.

Figure 5.75 shows the tower top fore–aft displacement time series. It seems that the two impacts produce an increase in the displacement with a certain delay. Consider that the structure is undergoing a strong turbulent wind and its natural frequency is very far away from the impulsive action.

Concerning the state of stress, the two slamming waves that occur during the

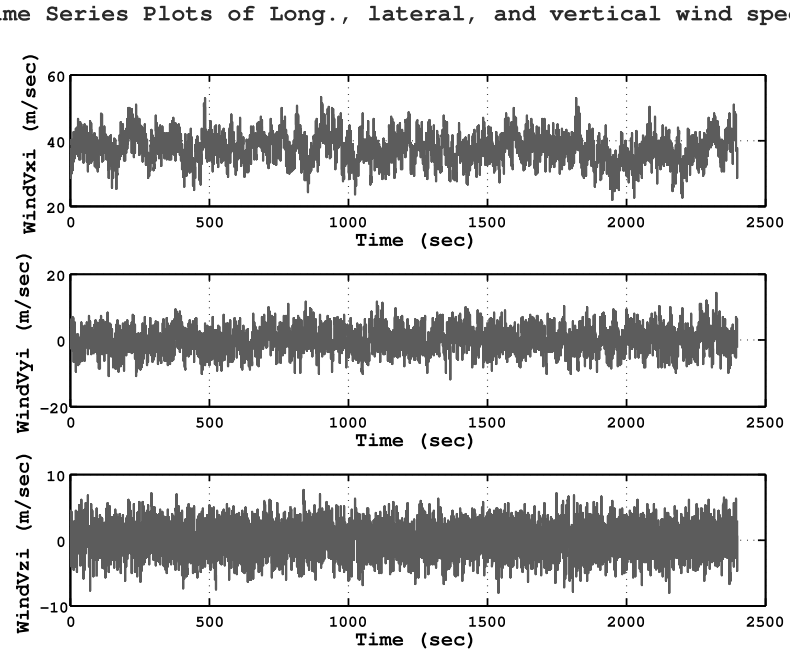

Figure 5.68: Time series of three turbulent wind speed components according to the Extreme Wind speed Model (EWM) of IEC61400-1 3rd ed. Time histories used in `Simulation #03`.

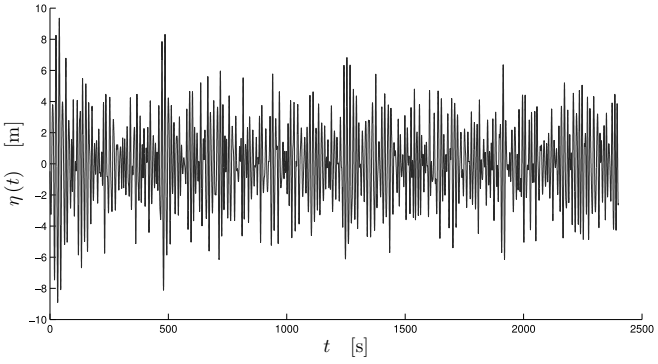

Figure 5.69: Time series of the free surface elevation at $x_t = 0$ for `Simulation #03`. Input data in table 5.14.

40 min long simulation induce on the structure a remarkable additional state of internal stress.

From output shown in plots 5.75 and 5.76 two considerations can be directly done. First of all also in this case the instantaneous augmentations of both the shear tower base force F_{xt} and the bending tower base moment M_{yt} are phenomenal. They bring the average peak value from approximately 2×10^3 kNm to nearly

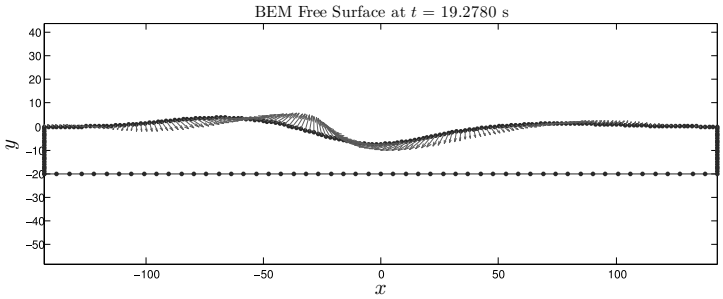

(a) Initial time.

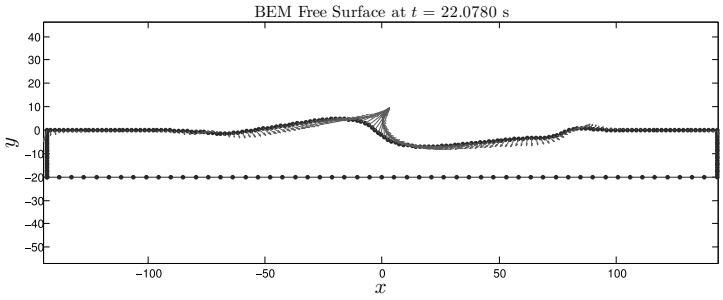

(b) Generic intermediate time step.

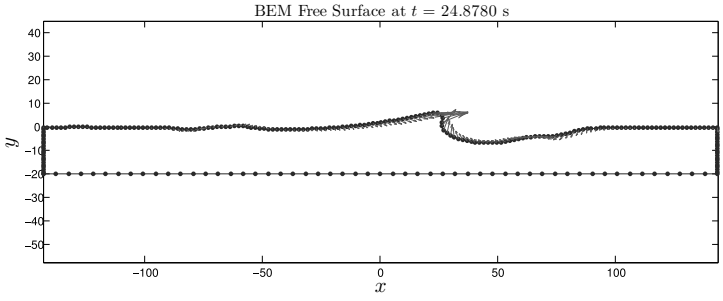

(c) Time at which data to compute the impact force are taken.

Figure 5.70: `Simulation #03`, first breaking wave event. Three snapshots of fully nonlinear free surface evolution.

8×10^3 kNm. The second thing that can be observed is the effect of the third non–breaking wave. Since it has included into the simulation as a breaking wave, the force it exerts is almost in the range of the standard maxima due to plain Morison's equation. Therefore, this instructive simulation tells us that without the formation of the jet the effect on the structure is totally different. The last remark we can add is that the peaks tend to decay very rapidly, indeed the negative peak is already less intense. This of course much depends on the global system dynamics.

Another interesting structural output which deserves attention is the internal bending moment at the still water level. In this cross–section the structure registers the additional couple due to the impact given by the impact force $M_I = F_I d_I$,

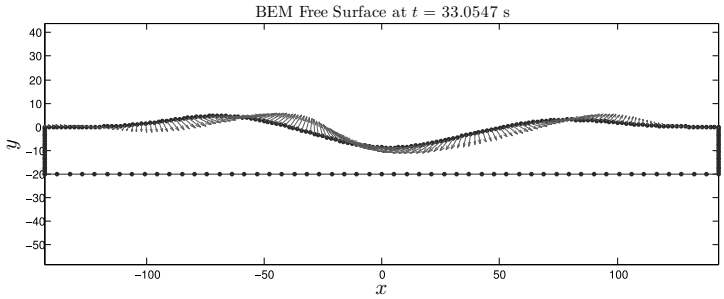

(a) Initial time.

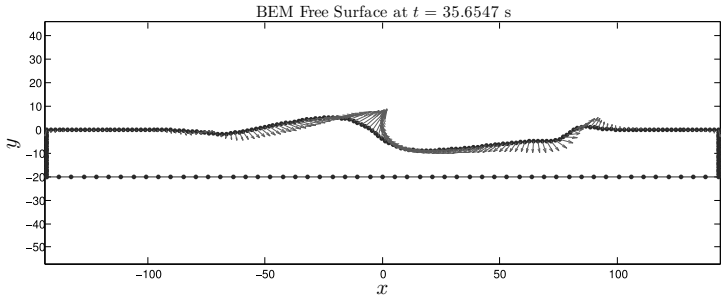

(b) Generic intermediate time step.

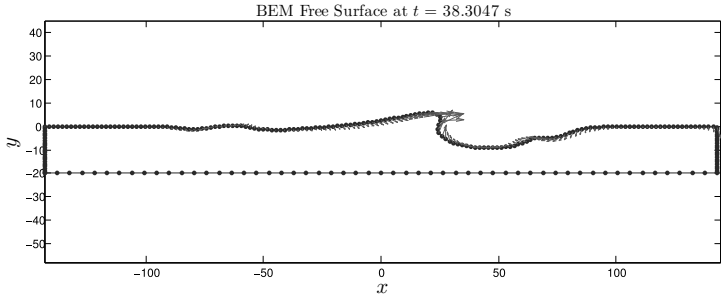

(c) Time at which data to compute the impact force are taken.

Figure 5.71: `Simulation #03`, second breaking wave event. Three snapshots of fully nonlinear free surface evolution.

where $F_I = f_I \lambda \eta_b$ is the impact force described in section 4.5 and d_I denotes the moment arm.

5.5.4 Fully coupled `Simulation #04`

This simulation is characterized by the data set reported in table 5.16. The wind conditions are unchanged with respect to the previous case, while sea state severity parameters have been slightly modified. The total simulation time is 15 min. This simulation differs from the others mainly in the number of impacts.

The three components of the extreme turbulent wind are plotted in figure 5.78.

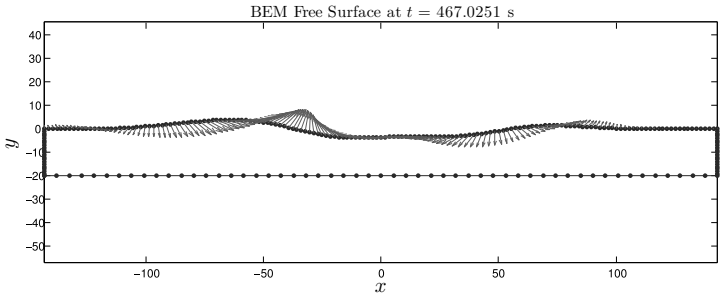

(a) Initial time.

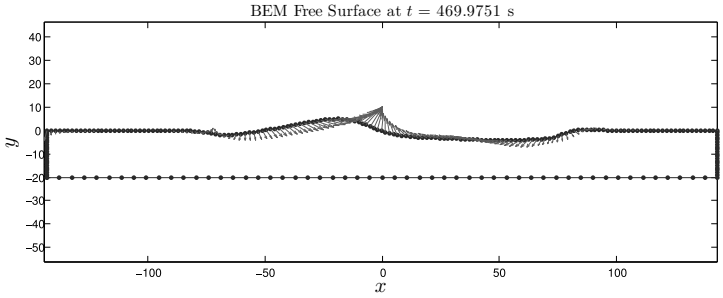

(b) Generic intermediate time step.

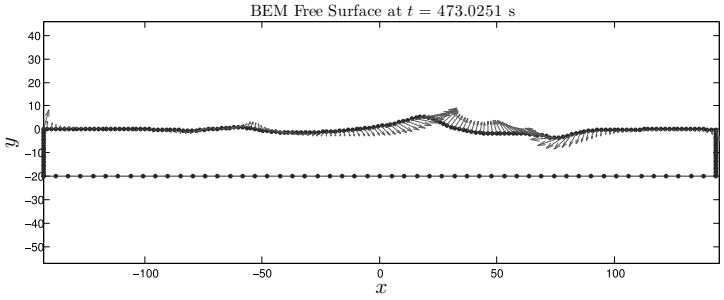

(c) Time at which data to compute the impact force are taken.

Figure 5.72: `Simulation #03`, third (expected) breaking wave event. Three snapshots of fully nonlinear free surface evolution.

The zero–crossing analysis of the free surface at the wind turbine location detects four breaking waves, thus the fully nonlinear plunging breaker simulator is called four times, i.e. $nb = 4$.

For each of these sub–simulations three significant configurations of the free surface evolution are shown in figures 5.79 to 5.82. In all four cases, the upper subplot represents the initial time when the BEM solver is called.

From figures 5.79 to 5.82 it can be seen that the first breaking wave event is not a real overturning phenomenon. Or at least the simulation duration $[t_{b_1} - \delta t_b, t_{b_1} + \delta t_b]$ was not enough to capture the complete plunging. There are many reasons for which sometimes the predicted breaking event does not actually happens. For sure it must

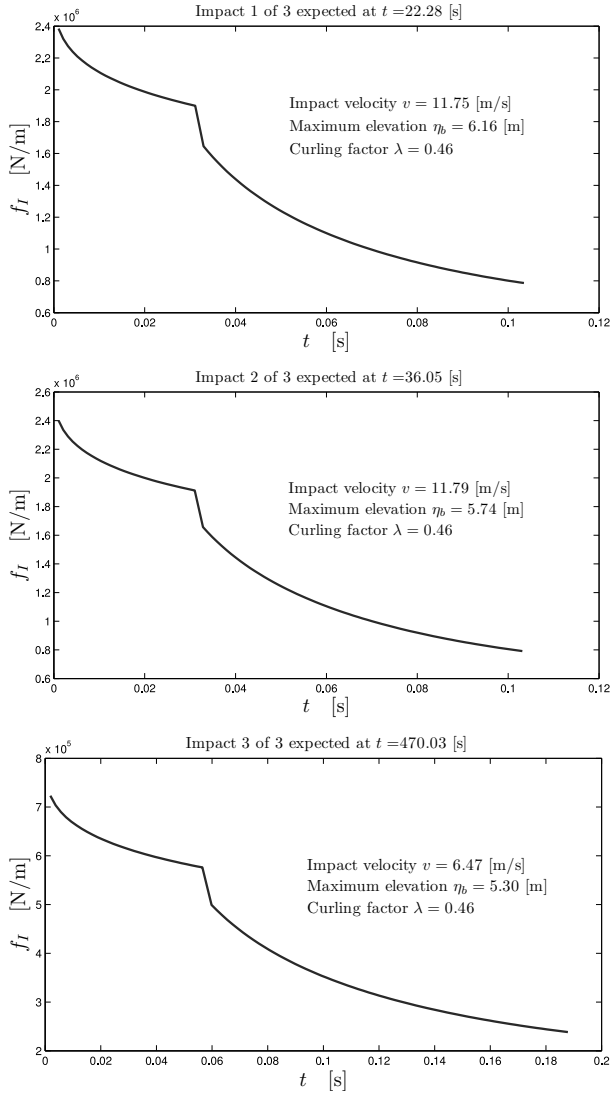

Figure 5.73: `Simulation #03`, impact forces computed according to section 4.5.

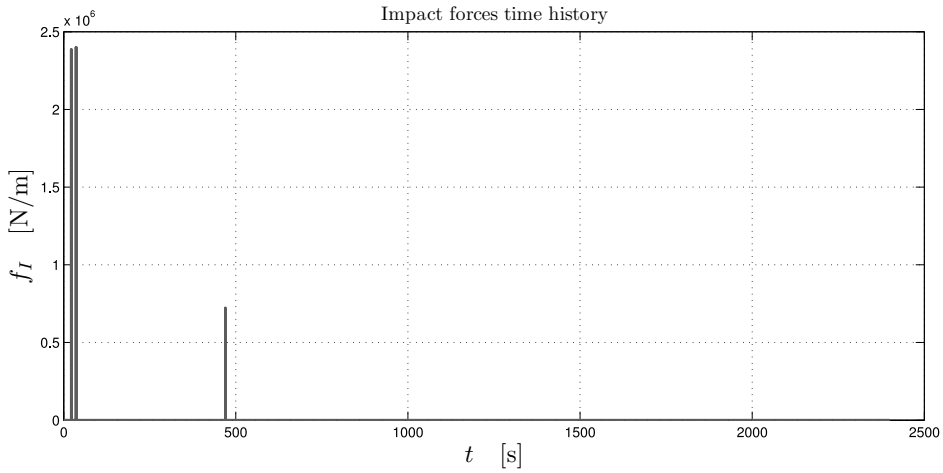

Figure 5.74: `Simulation #03`, impact forces time history over the all simulation time T_{sim}.

U_{ref}, I_{ref}	37.5 m/s, 0.12
$U_{19.5}$, H_s, T_p	31.69 m/s, 11.50 m, 10.60 s
Spectrum type, γ	JONSWAP, 3.3
Water depth	Intermediate Water
T_{sim}, $x_{\min}$, $x_{\max}$	900 s, −300 m, 300 m
WaveDT, DT, dt[15]	0.05 s, 0.01 s, 0.05 s
Turbine location x_t	0
Predicted number of breaking waves	4
Number of breaking waves occurred nb	3
Predicted breaking waves times $\bar{t}_b$ s	72.15, 114.56, 482.49, 551.06
BrLm	7, 11, 53, 60
Steepness ϵ (at breaking)	0.134, 0.133, 0.146, 0.144
δx_t	205.02 m
δt_b	2 s
NE_f	80

Table 5.16: Data relevant to `Simulation #04`.

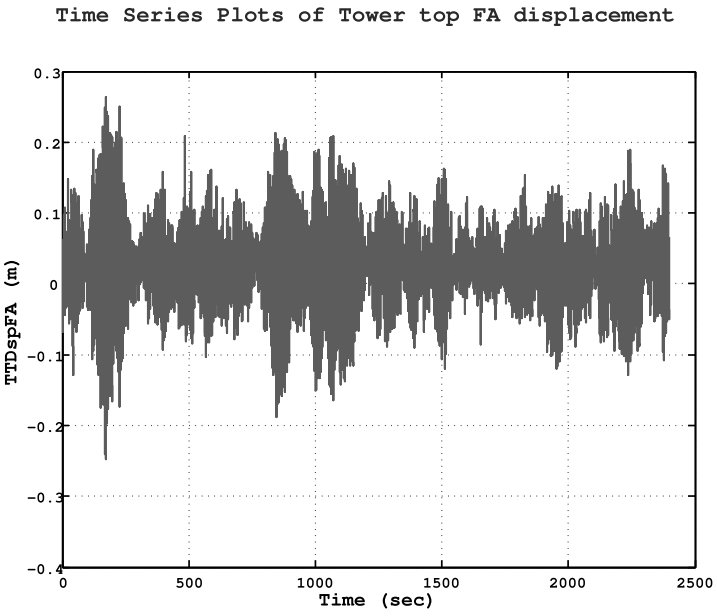

Figure 5.75: `Simulation #03`, tower top fore–aft displacement time series.

be remarked that the breaking limit criterion is a theoretical value which in certain situations (e.g. linear wave theory, as in our case) can be less reliable, secondly it could happen that the very small amount of energy dissipated by the smoothing subroutine, which is generally not affecting the solution, in this sensitive cases can influence.

However, the crest shown in figure 5.79 is steep enough to think that when hitting a pile a certain impulsive effect is also produced. Therefore it has also been included in to the total number of impact forces passed to FAST.

The four impact forces stemming from the above simulations are shown in figure 5.83.

The distribution of the all impact forces over the whole simulation time is shown in figure 5.84. As for the previous case, this plot is rather useful for qualitative judgment of the extreme structural response. From this plot it is evident that the impact associated with the third breaking wave, represented in figure 5.81, is the strongest. Even though its elevation is not higher than the other cases, the water particles at the cusp have an average velocity of 15.05 m/s which makes the crash really strong.

Figure 5.85 shows the tower top fore–aft displacement time series. It seems that the first two impacts induce an increase of the tower top displacements with peaks of about 25 cm. The third impact does not produce an instantaneous effect on the displacement, anyway amplifications are registered during the third a fourth slams.

On the contrary, the tower base forces and moments reflect instantaneously the effects of the impacts. Peaks in figure 5.86, in fact, strictly follow the impacts distribution over the all simulated time as shown in figure 5.84.

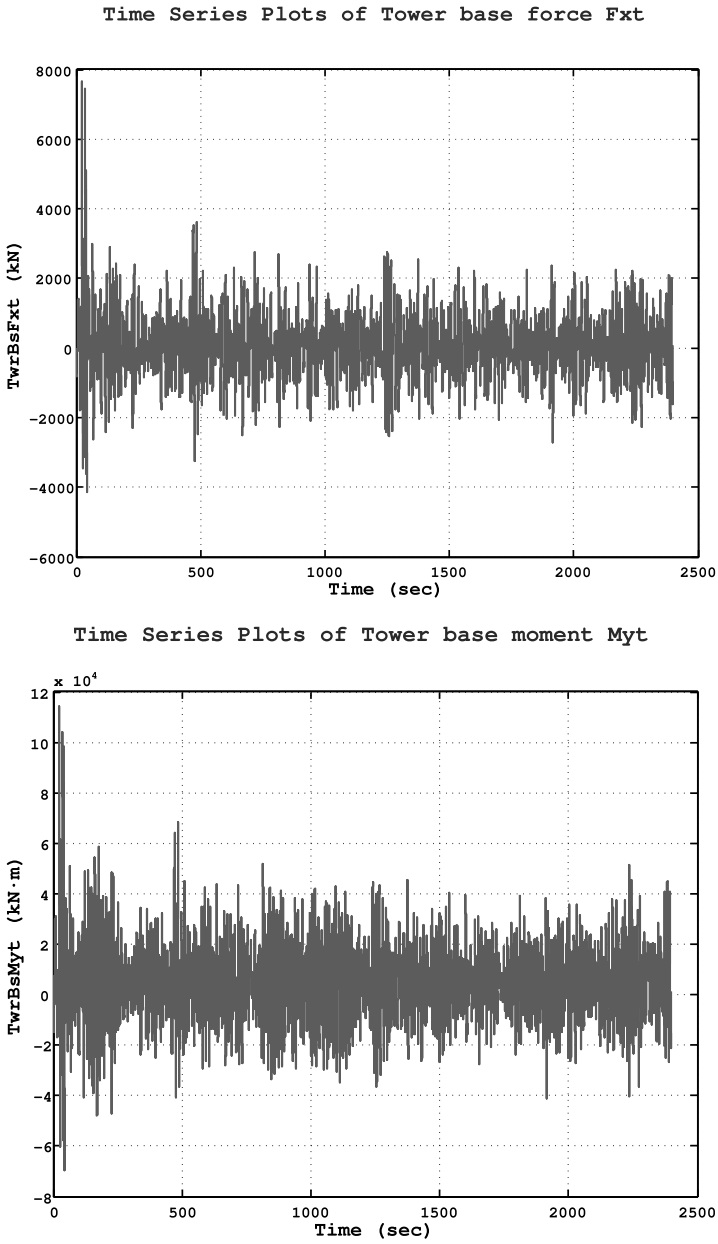

Figure 5.76: `Simulation #03`, tower base shear force F_{xt} and overturning moment M_{yt}.

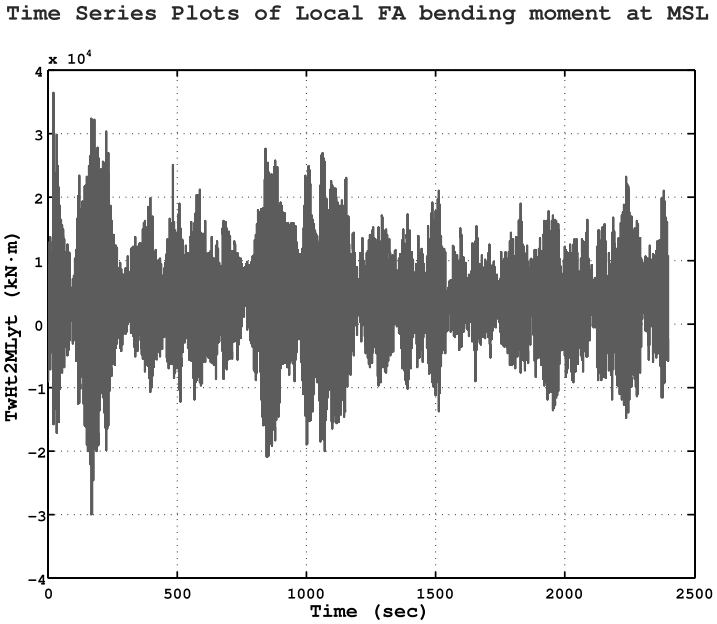

Figure 5.77: Simulation #03, tower top fore–aft bending moment at the tower cross–section taken approximately at the mean sea level.

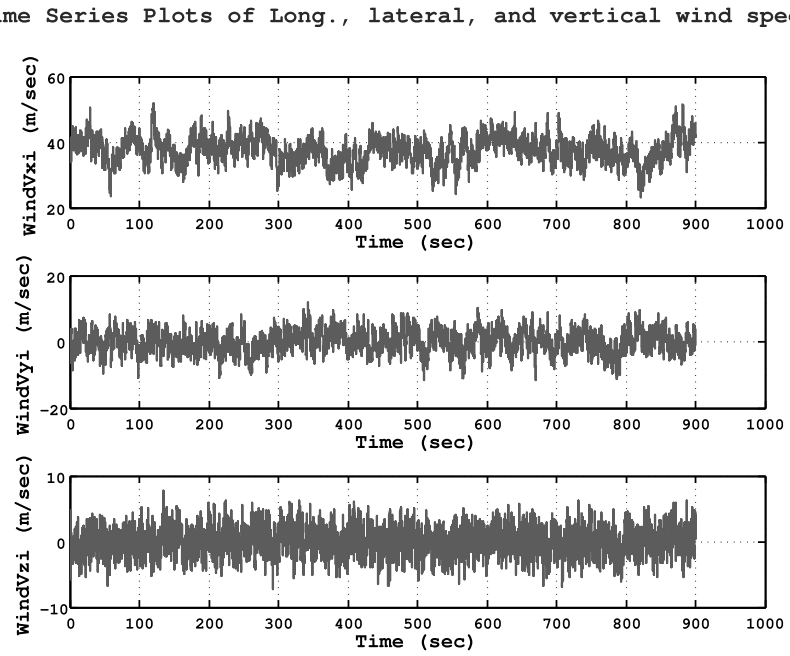

Figure 5.78: Time series of three turbulent wind speed components according to the Extreme Wind speed Model (EWM) of IEC61400-1 3rd ed. Time histories used in Simulation #04.

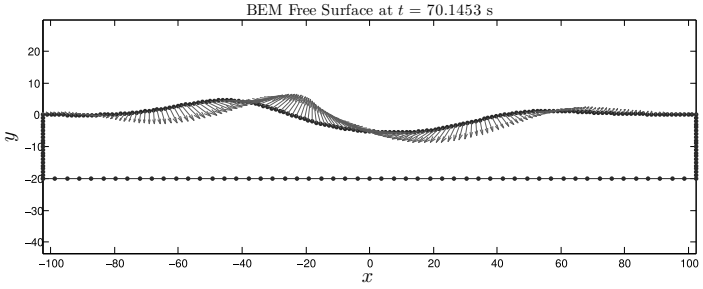

(a) Initial time.

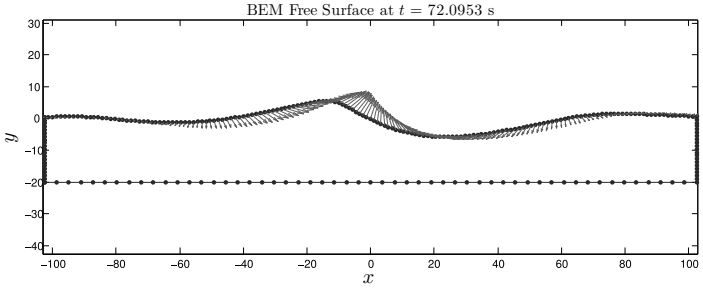

(b) Generic intermediate time step.

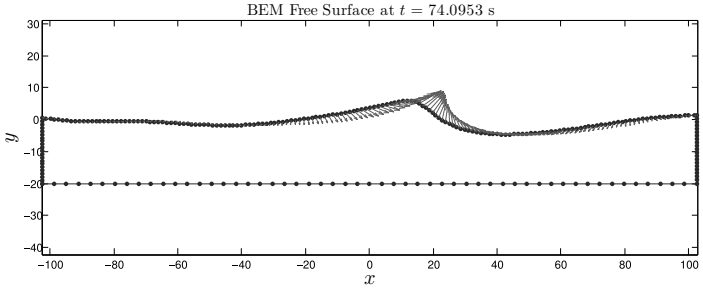

(c) Time at which data to compute the impact force are taken.

Figure 5.79: `Simulation #04`, first breaking event. Three snapshots of fully nonlinear free surface evolution.

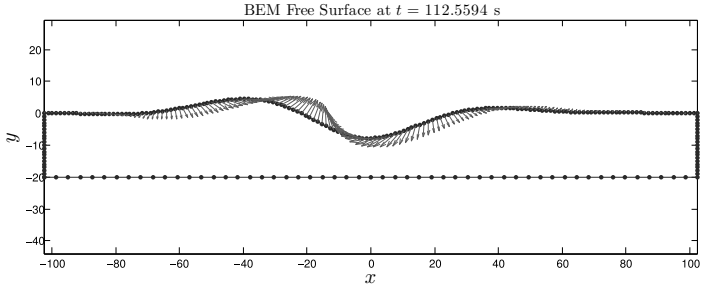

(a) Initial time.

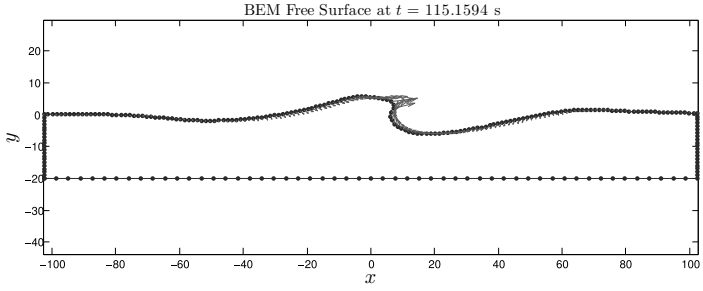

(b) Generic intermediate time step.

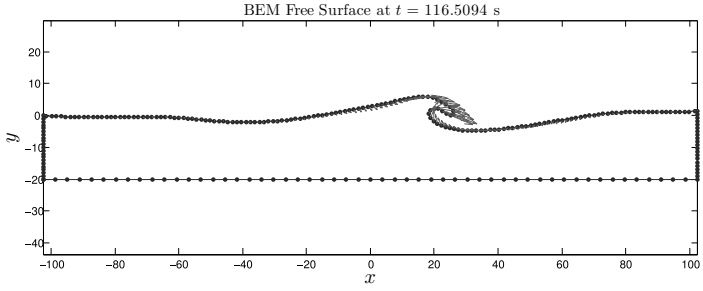

(c) Time at which data to compute the impact force are taken.

Figure 5.80: `Simulation #04`, second breaking event. Three snapshots of fully nonlinear free surface evolution.

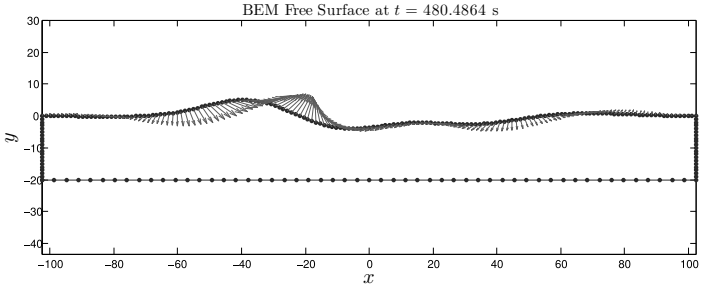

(a) Initial time.

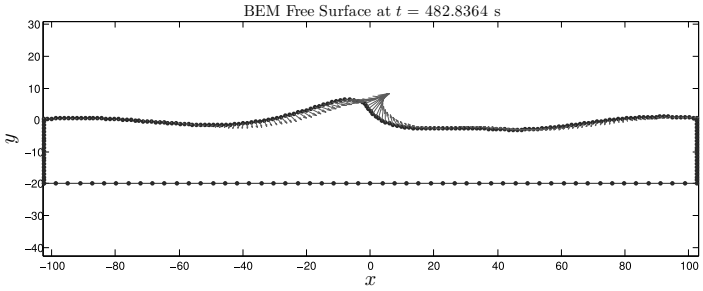

(b) Generic intermediate time step.

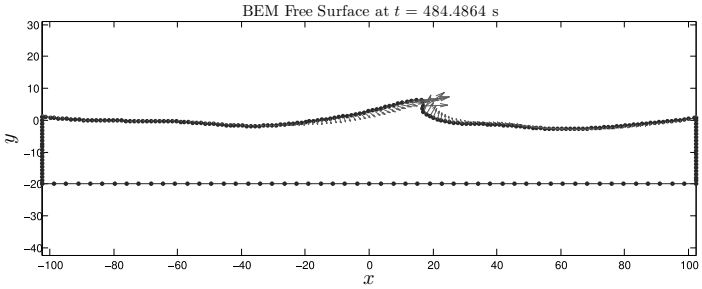

(c) Time at which data to compute the impact force are taken.

Figure 5.81: `Simulation #04`, third breaking event. Three snapshots of fully nonlinear free surface evolution.

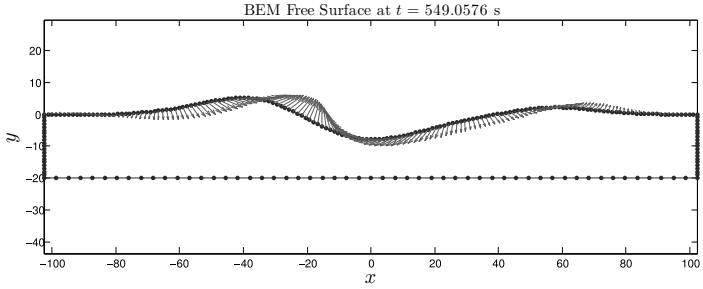

(a) Initial time.

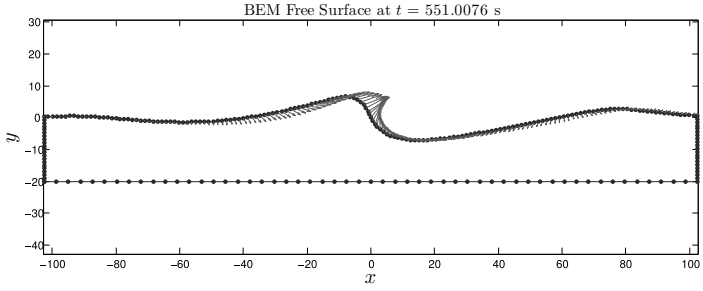

(b) Generic intermediate time step.

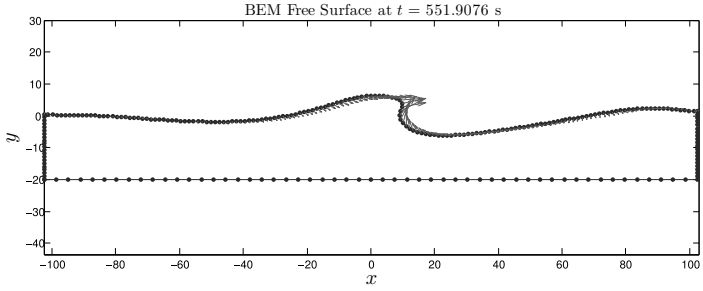

(c) Time at which data to compute the impact force are taken.

Figure 5.82: `Simulation #04`, forth breaking event. Three snapshots of fully nonlinear free surface evolution.

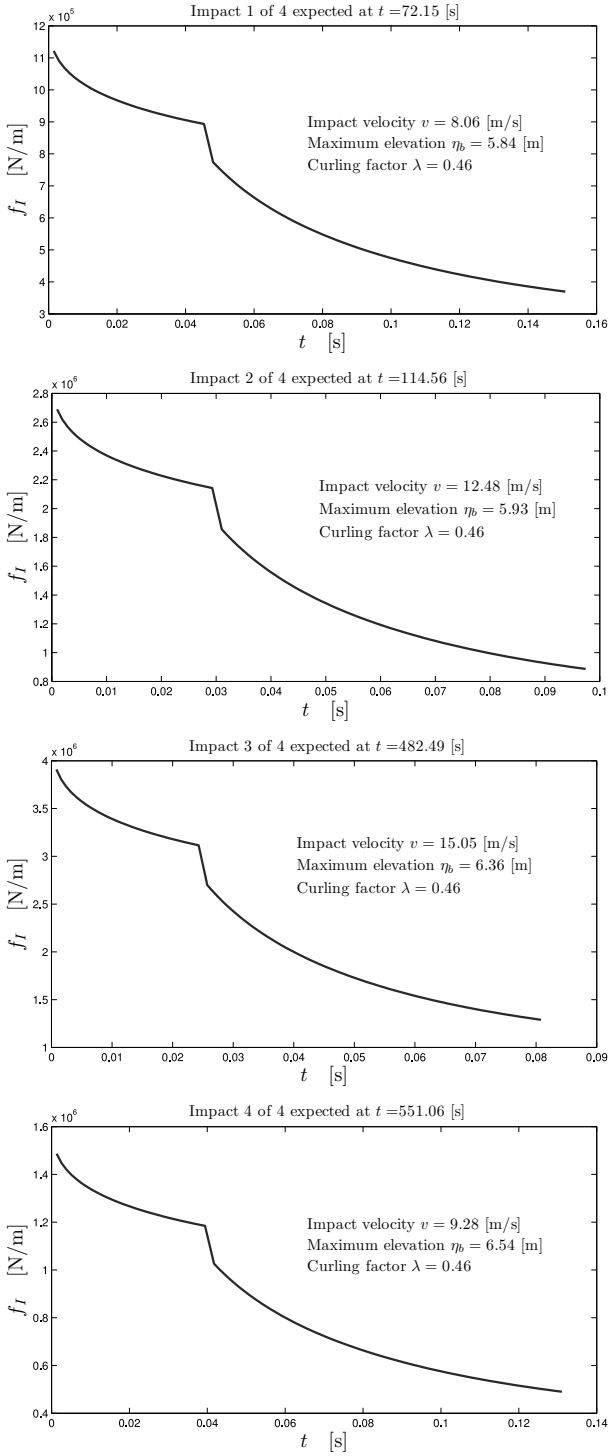

Figure 5.83: `Simulation #04`, the four impact forces computed according to section 4.5.

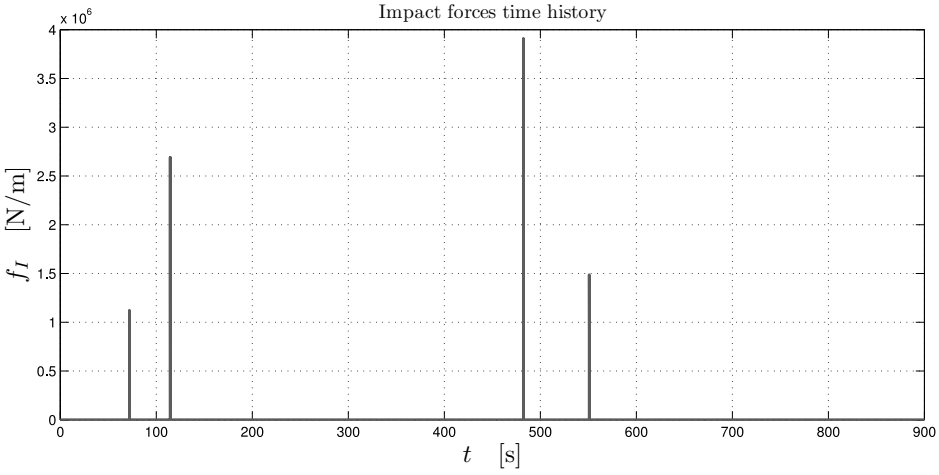

Figure 5.84: `Simulation #04`, impact forces time history over the all simulation time T_{sim}.

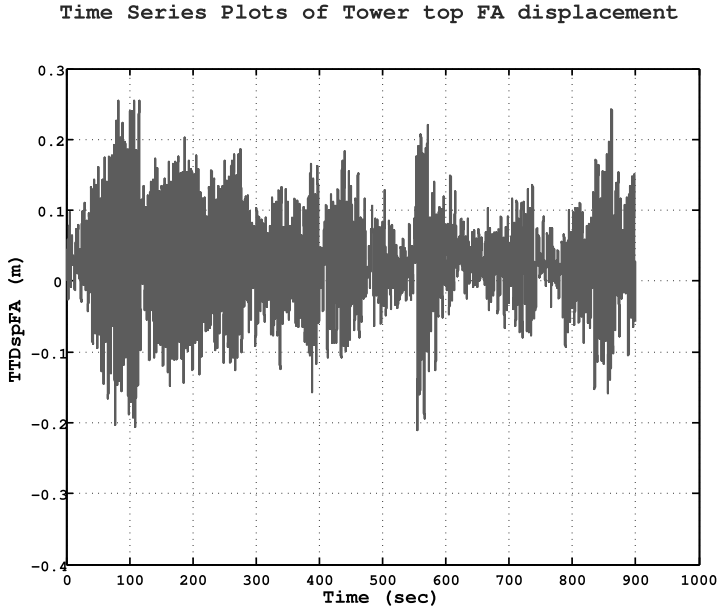

Figure 5.85: `Simulation #04`, tower top fore–aft displacement time series.

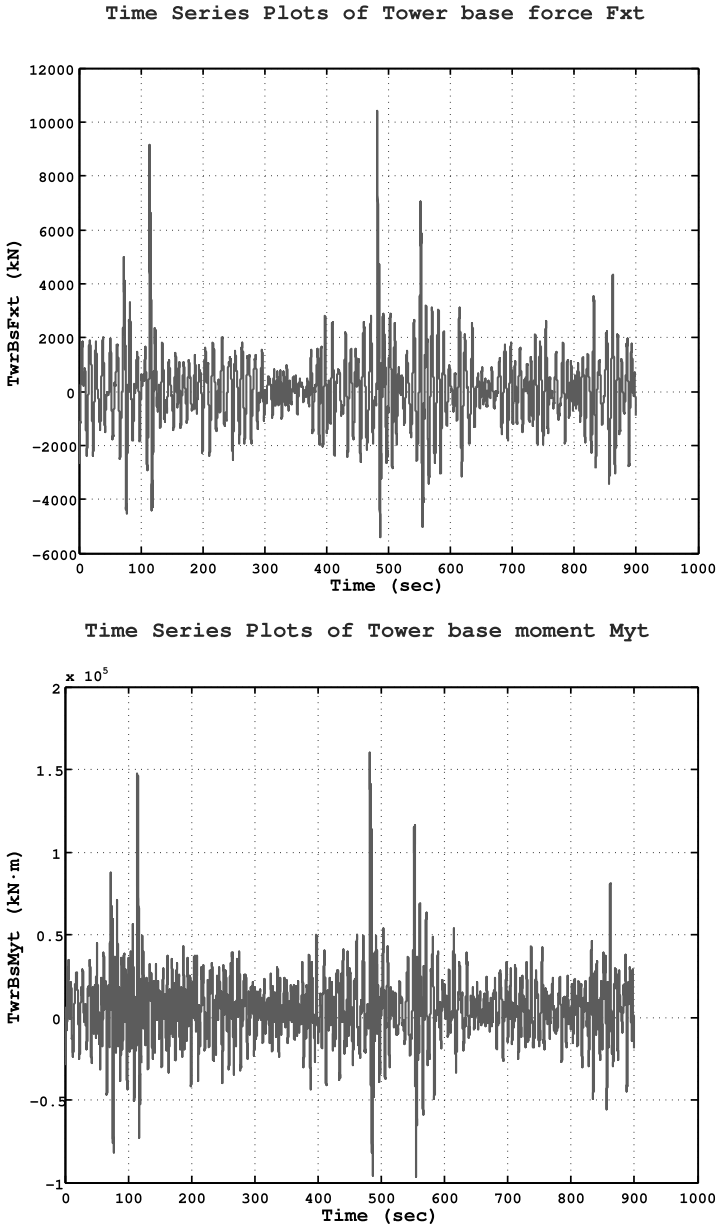

Figure 5.86: `Simulation #04`, tower base shear force F_{xt} and overturning moment M_{yt}.

Chapter6
Achievements and final remarks

This concluding chapter summarizes the principal achievements of this thesis. Moreover, the important implications of the proposed numerical tool on the structural risk assessment phase are underlined.

6.1 Implications of the proposed model on the structural safety and Risk Assessment

At this point of the work some crucial and spontaneous questions rise up: what are the practical consequences of such a model? Why should it be used instead of the traditional impact models? Would not it be easier to use directly the semi–empirical deterministic impact wave models available in literature?

Let us start from the last issue. Modern design approaches aims at employing tools (especially numerical tools in this context), which are more and more representative of the reality (reduction of model uncertainties) and at the same time guarantee an acceptable cost in terms of computational time. In fact, to minimize the model uncertainties, one could model in a very refined scale the fluid–structure interaction. Unfortunately, this approach does not meet the second fundamental need when designing offshore wind turbine, that is the limited computational time available.

The new numerical model developed in this thesis precisely represents a compromise for the two major needs above mentioned. It is able, indeed, to simulate offshore monopile–supported wind turbines exposed to wave impacts with very high accuracy without penalizing the computational effort normally required. This is possible thanks to two main features of the computational strategy developed: i) the domain decomposition linear–nonlinear; ii) the implementation of the Boundary Element Method–based solver which, among others, has the brilliant advantage to reduce the problem under consideration by one dimension.

Usually, impact forces are computed with some semi–empirical formula derived mainly from experiments. Just to give an example, in [12] and [10] it is recommend to compute the impact pressure p as follows

$$p = \rho \kappa_1 v^2 \tag{6.1}$$

where $\kappa_1 = 5.98$ for impact due to waves breaking in proximity of the vertical cylinder (this is always our case), while $\kappa_1 = 2.74$ when the pile is hit by broken waves. ρ is the water density and v is the impact velocity given as follows

$$v = 0.48 \times 1.092 \frac{gT}{2\pi} \tag{6.2}$$

Enzo Marino, *An integrated nonlinear wind-waves model for offshore wind turbines*
ISBN 978-88-6655-051-8 (print) ISBN 978-88-6655-053-2 (online)

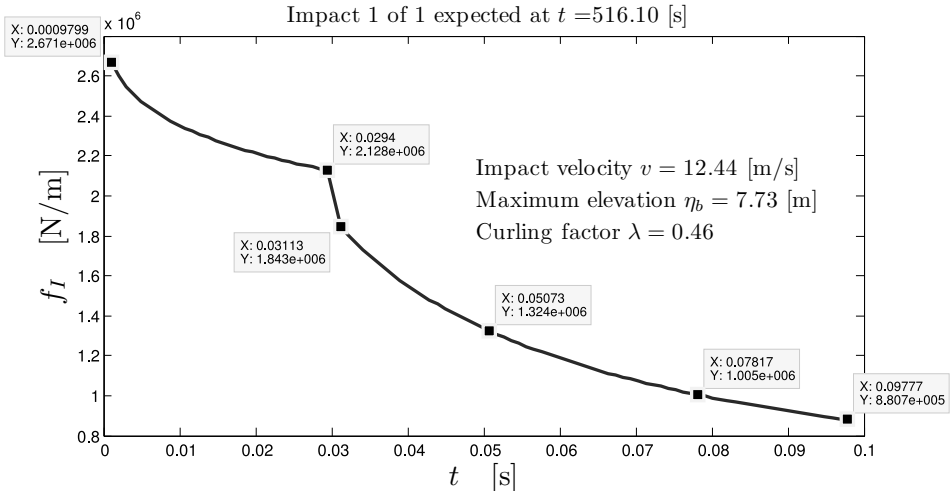

Figure 6.1: Impact force through its duration taken from `Simulation #01`.

If we recall the impact in `Simulation #02`, it is possible to compare the the simulated impact velocity with the predicted one by the above semi–empirical model. The simulated impact velocity was $v = 12.44\,\mathrm{m/s}$, while the wave period associated with that wave component was $T = 10\,\mathrm{s}$. With these data the above model would lead to an impact velocity of $8.14\,\mathrm{m/s}$, while our simulation shows that the strongest impact occur when the velocity reaches $12.44\,\mathrm{m/s}$. Figure 6.1 is recalled here to remind some key values concerning this impact.

The difference between the two impact velocities gives an idea on how large is the range of variation and approximation of semi–empirical models. Therefore, the first thing to say about the model developed in the thesis is that it is able to capture the wave impacts much more accurately and thus forces transferred to the structure are much more reliable. This, by the way, is what we announced in Chapter 1 when the reduction of model uncertainties was mentioned. In fact, by using our model the extreme response of offshore wind turbines can be more realistically captured and this induces remarkable consequences on the ultimate loads assessment.

The implications mentioned above bring us back to the issue opened in Chapter 2 when the crucial phase of the Risk Assessment was discussed. As we said, here the scope is the quantification of structural risk. To this aim, by recalling the definition

$$Risk = Probability\ of\ failure \times Losses \qquad \text{[Losses unit/time]}$$

it appears that the prediction of the state of failure is deeply conditioned on the peaks distribution of each simulation, therefore the utilization of the proposed numerical approach becomes of primary importance at this stage of the general risk management framework.

In this paragraph the important consequences of the proposed model on the vulnerability term of equation (5.1), written as

$$Vulnerability = P\left(M_{yt} > M_{yt}^{*} | U = U_{50}\right) \tag{6.3}$$

are highlighted by comparing the structural response obtained with the proposed wave impact model with the usual non–impact linear wave approach.

Notice from equation (6.3) that the approach followed in this thesis to investigate the extreme response of offshore wind turbines is the one referred to as "external conditions–based" approach, see Chapter 2. This means that the extreme response is not extrapolated from simulations at wind speeds in the range of the cut–in and cut–out, but directly reproduced by assigning extreme loads.

After running a certain number of simulations, whose input (loads) differ each other only by the seeds used to generate the extreme wind and waves, statistical properties of each realization should be analyzed. Together with the randomness of the sea and the turbulent wind, to make even wider the difference between two different arbitrarily selected simulations is the randomness of the impulsive contributions due to breaking waves. The latter makes necessary to have at disposal a minimum number of runs. Due to limited time, here it is not possible to run a large number of simulations at least 10 min long each. Hence, just to describe the procedure it will be assumed that one selected time series for the case considering the impacts forces and one realization without impact forces are selected and assumed to be representative of all the others. Moreover, for all the remaining of the work, the structural response taken as reference is the overturning moment at the tower base M_{yt}.

Let us consider the case of M_{yt} associated with `Simulation #04` which is recalled in figure 6.2. Subplot 6.2(a) represents the response when no impact is considered. Let us say that this is the output that one would obtain without the numerical tool developed in this thesis. On the contrary, subplot 6.2(b) shows for the same sea severity, established by the same extreme turbulent wind, the response including the wave impacts.

The statistics of the series in subplot 6.2(a) is given as follows

```
   Minimum       Mean    Maximum     StdDev   Skewness       Range
-8.291e+004 5.198e+003 8.538e+004 1.893e+004 -2.272e-003 1.683e+005
```

while the statistics of the series in 6.2(b) is the following

```
   Minimum       Mean    Maximum     StdDev   Skewness      Range
-9.632e+004 5.256e+003 1.601e+005 1.979e+004 3.494e-001 2.564e+005
```

A much clearer comparison is possible by the superposition of the two responses as plotted in figure 6.3. To extract local maxima form the series a peak–over–threshold is used [90], [91]. The method is suitable to select the largest value between positive slope up-crossings of the threshold and to eliminate the majority of smaller amplitude extremes that are less significant for the current purpose. The choice of the threshold is pretty important to investigate the statistics of the response and several methods are available [90] but since it is not the main point here, it is just used the threshold recommended by IEC61400-1, annex F, which is the mean value of the original series plus 1.4 the standard deviation.

Figure 6.4 compares the exceeding probability distributions for both the model taking into account the wave impacts and the model considering only Morison's contributions (solid red line and solid blue line, respectively). As expected, the upper tail of the impact model distribution keeps always above the distribution without impacts. If the distribution of the structural ultimate strength were also plotted in

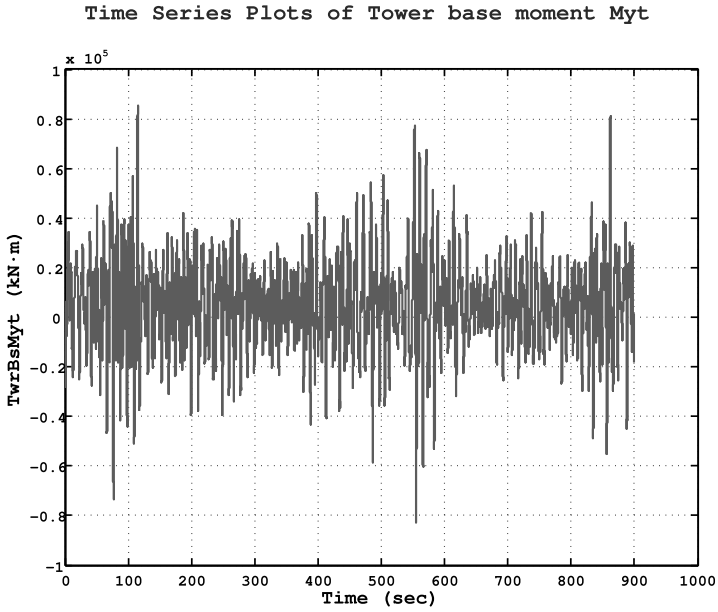

(a) Without impacts.

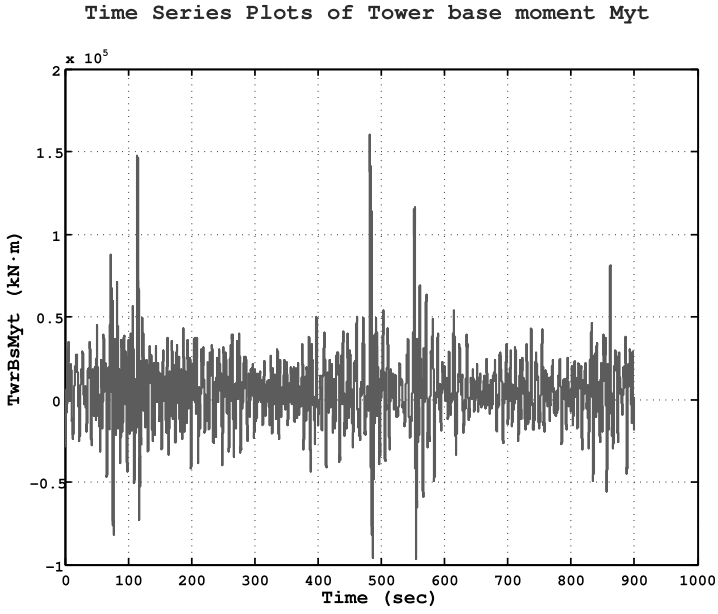

(b) With impacts.

Figure 6.2: Comparison of tower base overturning moment M_yt due to EWM plus a JONSWAP irregular sea with and without the impulsive contributions due to breaking waves.

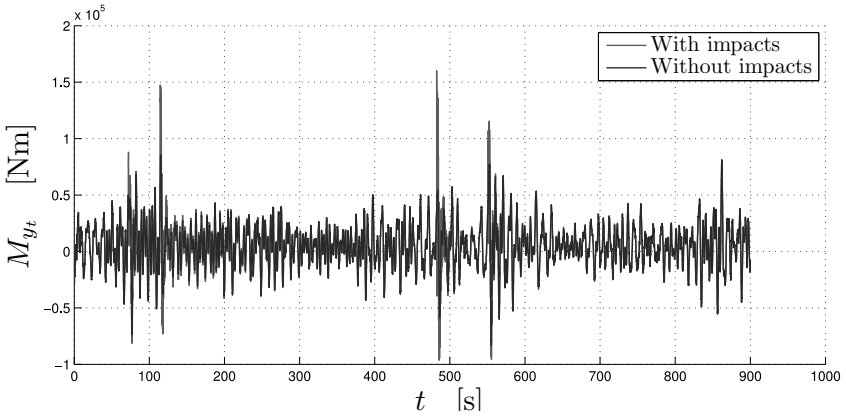

(a) Superposition of the responses time series.

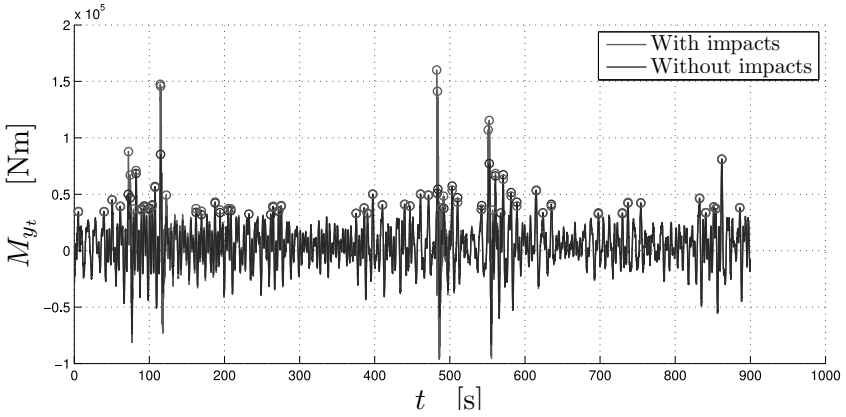

(b) Peaks selected by the threshold fixed as the mean value plus 1.4 times the standard deviation.

Figure 6.3: Comparison of tower base overturning moment M_{yt} due to EWM plus a JONSWAP irregular sea with and without the impulsive contributions due to breaking waves.

the same figure, it would result clear that the distribution without impacts leads to an overestimation of the structural capabilities giving rise to unsafe conclusions when assessing the probability of failure.

The empirical exceeding probability distributions of peaks shown in figure 6.3 is plotted in figure 6.4. It is fitted with a Generalized Extreme Value Distribution (GEV) as presented in figure 6.5.

For the sake of simplicity we can imagine that the ultimate moment strength M^*_{yt} the tower can supply is a deterministic value. So we can draw a vertical line intercepting the two distributions plotted in figures 6.4 or 6.5 in two points representing the probabilities that such an ultimate value is not exceeded for the model with impacts and for the model without impacts, respectively. These two values prove that the model without impacts leads to relay on a certain level of structural

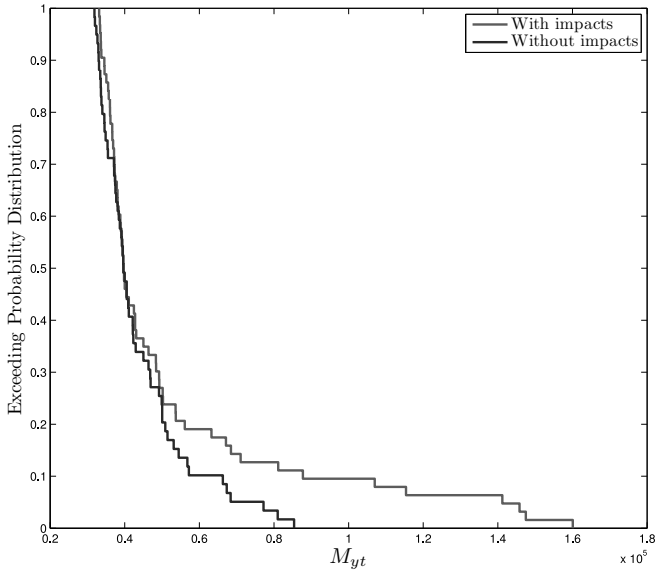

Figure 6.4: Comparison of the exceeding probability distributions of the tower base bending moment M_{yt} with and without considering the impulsive forces due to overturning plunging breakers.

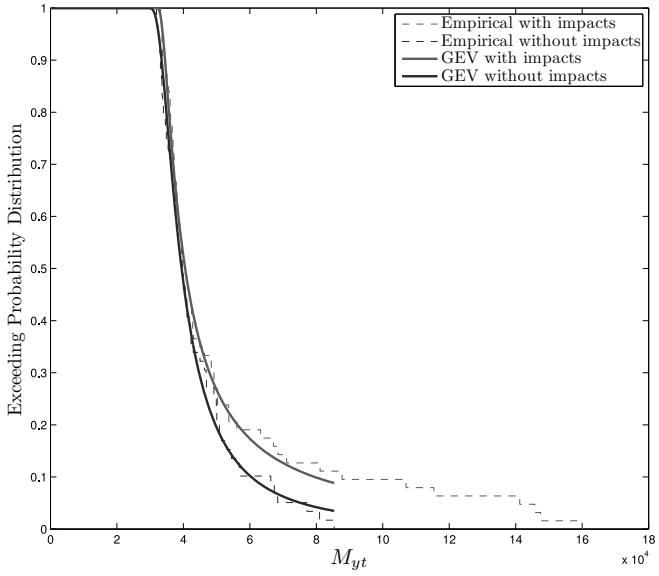

Figure 6.5: Comparison of the fitted GEV exceeding probability distributions of the tower base bending moment M_{yt} with and without considering the impulsive forces due to overturning plunging breakers.

safety which is actually wrong. In other words, the structural safety is overestimated

because the real probability that M_{yt}^{*} is not exceeded is given by the distribution accounting for the wave impacts. On the other hand, in the opposite situation, let us say in a design phase, one could fix a certain structural reliability which in this case can be represented by a horizontal line drawn on figure 6.4. The model not accounting for the impacts would lead to demand a lower ultimate bending strength than the more realistic one described by the distribution accounting for the impacts. Hence, we have that at

Design stage: Given the P_{fail}, the non-impact wave model will always demand a lower design load;

Verification stage Given the ultimate structural strength M_{yt}^{*}, the non-impact wave model will always underestimate the P_{fail} of the *System*.

The above remarks are extremely relevant from a qualitative point of view and they pave the way for the development of a systematic methodology in assessing the ultimate loads for offshore wind turbines by employing the proposed model. However, in this context, since the probability distributions have been obtained only from one simulation, a reliable quantification of the error in the assessment of the probability of failure due to the inaccuracy of the model not accounting for the impacts cannot be provided.

6.2 Summary and conclusions

At the very end of this work it remains to draw a balance of what was planned to achieve within this research and what has been really attained.

We started in Chapter 1 with a general overview about the European and world wind energy scenario. In this framework the most pressing priorities established by the European Commission to meet the challenging targets in terms of offshore wind energy have been recalled in order to provide some undiscussed motivations of general interest. In addition to them, further motivations have been identified by discovering some important lacks in modeling offshore wind turbines. In particular, while for fatigue design of offshore energy converters the current approach is satisfactory, when dealing with extreme wind and waves conditions very dangerous consequence in evaluating the structural safety may be induced by adopting standard methods alone. Departing from this background we theorized that an improved numerical model capable of capturing more realistically the response of a system exposed to an extreme environment could lead to a more accurate structural risk assessment. To this aim, after devoting some attention to the basic concepts concerning the rotor aerodynamics in Chapter 3, a fully nonlinear water waves simulator has been developed in Chapter 4. The code, written entirely within this research work, implements a higher–order Boundary Element Methods (BEM) to discretize in space Laplace's equation governing the gravity waves propagation. Then, integrating in time the kinematic and dynamic boundary conditions - following indeed the so called Mixed Eulerian–Lagrangian scheme -, it is able to simulate fully nonlinear waves generated by several types of initial and boundary conditions. A numerical wave tank, equipped with an absorbing beach, has also been simulated and comparisons with experimental measurements, along with analytical results (when available),

validated the numerical tool. The Boundary Element Method–based code permits to reproduce plunging breaking waves up to the time the tongue re–enters into the free surface.

The capabilities of the software developed in Chapter 4 have been used to set up an impact wave model which in turn has been embedded into a stochastic environment. Indeed, the first part of Chapter 5 is devoted to the implementation of a logic that, once an extreme random sea is generated, whenever breaking waves occur, the fully nonlinear code is called to perform a refined analysis over a pace–time sub–domain defined as a neighborhood centered in the wind turbine location at the time of the expected breaking wave. Next, in the second part of Chapter 5, forces stemming from overturning breaking waves are passed to the hydro–aero–elastic simulator which permits to simulate the whole offshore wind turbine system when exposed to severe conditions. Results of such coupled model have then been thoroughly commented throughout the chapter. More synthetically, in this thesis:

- A new numerical procedure to simulate extreme response of Offshore Wind Turbines has been developed:
  - The BEM-based code reproduces with high accuracy the overturning plunging breakers;
  - An analytical impact model permits to compute the impulsive forces subsequently passed to the aerolelastic solver;
  - The deterministic simulator has been successfully embedded into a stochastic environment;
- Peaks in the structural response due to slapping waves can be up to three times higher than peaks induced by the standard linear wave approach.

Finally, in this conclusive chapter we came back to what theorized at the beginning of the thesis, and in particular we tried to face those issues raised in Chapter 2. Here it has been shown that the new numerical model meets all the expectations. In fact:

- The model developed significantly contributes to turn the simulation of offshore wind turbines exposed to random wave impacts into a mature stage;
- It represents a more reliable tool in predicting ultimate loading conditions;
- It poses a crucial issue about the accuracy in evaluating the structural safety when non-impact models are employed because dangerous impact waves would be completely missed;
- The model developed aims at being a design tool as it increases the model accuracy without penalizing the computational cost normally required;
- An accurate extreme value analysis is necessary for a full quantification of the Structural Vulnerability.

AppendixA
Linear wave formulas

Wind generated waves can be grouped in two main categories:

Deep water waves, also referred to as **short waves.** The water is considered deep if the water depth d is larger than half the wavelength L, so $d > L/2$. These relatively short waves do not "feel" the sea floor.

Shallow water waves, also known as **long waves.** The water is considered to be shallow if the water depth d is less than 1/20 of the wavelength. Namely, $d < L/20$. In this case the sea bottom has a significant influence on the characteristics of these relatively short waves.

Thus, in the case of **shallow water** conditions (finite water depth) the kinematic and dynamic quantities for a single-harmonic (regular) wave are given as follows:

Velocity potential

$$\phi(p,t) = \frac{ga}{\omega}\frac{\cosh k(y+d)}{\cosh kd}\sin(kx-\omega t) \tag{A.1}$$

Dispersion relation

$$\omega^2 = gk\tanh(kd) \tag{A.2}$$

Wavelength-wave period relation

$$L = T\sqrt{gd} \tag{A.3}$$

Free surface elevation

$$\eta(x,t) = a\cos(kx-\omega t) \tag{A.4}$$

Dynamic pressure

$$p_D(p,t) = -\rho gy + \rho ga\frac{\cosh k(y+d)}{\cosh kd}\cos(kx-\omega t) \tag{A.5}$$

Particle displacement along the x–axis

$$\xi(p,t) = -a\frac{\cosh k(y+d)}{\sinh kd}\sin(kx-\omega t) \tag{A.6}$$

Particle displacement along the y–axis

$$\eta(p,t) = a\frac{\sinh k(y+d)}{\sinh kd}\cos(kx-\omega t) \tag{A.7}$$

Enzo Marino, *An integrated nonlinear wind-waves model for offshore wind turbines*
ISBN 978-88-6655-051-8 (print) ISBN 978-88-6655-053-2 (online) © 2011 Firenze University Press

Velocity along the x–axis

$$v^x(p,t) = a\omega \frac{\cosh k(y+d)}{\sinh kd} \cos(kx - \omega t) \tag{A.8}$$

Velocity along the y–axis

$$v^y(p,t) = a\omega \frac{\sinh k(y+d)}{\sinh kd} \sin(kx - \omega t) \tag{A.9}$$

Acceleration along the x–axis

$$a^x(p,t) = a\omega^2 \frac{\cosh k(y+d)}{\sinh kd} \sin(kx - \omega t) \tag{A.10}$$

Acceleration along the y–axis

$$a^y(p,t) = -a\omega^2 \frac{\sinh k(y+d)}{\sinh kd} \cos(kx - \omega t) \tag{A.11}$$

Whereas, in **deep water** conditions (infinite water depth), the kinematic and dynamic quantities for a single-harmonic (regular) wave are given as follows:

Velocity potential

$$\phi(p,t) = e^{ky} \sin(kx - \omega t) \tag{A.12}$$

Dispersion relation

$$\omega^2 = gk \tag{A.13}$$

Wavelength-wave period relation

$$L = \frac{gT^2}{2\pi} \tag{A.14}$$

Free surface elevation

$$\eta(x,t) = a\cos(kx - \omega t) \tag{A.15}$$

Dynamic pressure

$$p_D(p,t) = -\rho g y + g a e^{ky} \cos(kx - \omega t) \tag{A.16}$$

Particle displacement along the x–axis

$$\xi(p,t) = -a e^{ky} \sin(kx - \omega t) \tag{A.17}$$

Particle displacement along the y–axis

$$\eta(p,t) = a e^{ky} \cos(kx - \omega t) \tag{A.18}$$

Velocity along the x–axis

$$v^x(p,t) = a\omega e^{ky} \cos(kx - \omega t) \tag{A.19}$$

Velocity along the y–axis

$$v^y(p,t) = a\omega e^{ky}\sin(kx - \omega t) \tag{A.20}$$

Acceleration along the x–axis

$$a^x(p,t) = a\omega^2 e^{ky}\sin(kx - \omega t) \tag{A.21}$$

Acceleration along the y–axis

$$a^y(p,t) = -a\omega^2 e^{ky}\cos(kx - \omega t) \tag{A.22}$$

where $a = H/2$ is the wave amplitude, k is the wave number, ω is the circular frequency, d the water depth. The coordinates (x, y) of points p are referred to a Cartesian system having the y–axis upwardly oriented and the x axis positive in the wave propagation direction with the origin on the still water level.

AppendixB
Numerical dicretization of Laplace's equation

B.1 Green's formulation

Laplace's equation (4.8) discussed in Chapter 4 together with the boundary and initial conditions represents a Boundary Value Problem (BVP) whose approximate solution is obtained by means of weighted residual methods [38]. The weighting function $\phi^*(p, p_c)$ is the Green function that, for a 2D problem, reads as follows

$$\phi^*(p, p_c) = \frac{1}{2\pi} \ln \frac{1}{R} \tag{B.1}$$

where $R = \sqrt{(x_p - x_{p_c})^2 + (y_p - y_{p_c})^2}$ is the distance between the point p and the collocation point p_c. By means of equation (B.1) as well as the first and second Green's identities, the BVP is turned into the following Boundary Integral Equation (BIE).

$$c(p_c)\,\phi(p_c) + \int_\Gamma \phi(p)\, q^*(p, p_c)\, \mathrm{d}\Gamma - \int_\Gamma \phi^*(p, p_c)\, q(p)\, \mathrm{d}\Gamma = 0 \tag{B.2}$$

where

$$q(p) = \nabla\phi(p) \cdot \bar{n} \tag{B.3}$$

$$q^*(p, p_c) = \nabla\phi^*(p, p_c) \cdot \bar{n} \tag{B.4}$$

are respectively the flux (normal velocity component) and the normal derivative of the Green function. The coefficient $c(p_c)$ depends on the positions of the collocation point p_c. In general it is given as $\vartheta/2\pi$, where ϑ denotes the internal angle in radians of the corner at p_c. When there is no corner, that is when $\vartheta = \pi$, i.e. when p_c lies on a smooth boundary, then $c = 1/2$; when the collocation point is internal to the fluid domain $c = 1$ and finally when p_c is outside the domain $c = 0$ [38].

The boundary integral equation (B.2) is discretized into *NE* isoparametric quadratic elements in such a way nodal values belonging to j–th element are approximated as follows

$$\phi^{(j)} = \sum_{k=1}^{3} \varphi_k(s)\, \phi_k^{(j)} \tag{B.5}$$

$$q^{(j)} = \sum_{k=1}^{3} \varphi_k(s)\, q_k^{(j)} \tag{B.6}$$

Enzo Marino, *An integrated nonlinear wind-waves model for offshore wind turbines*
ISBN 978-88-6655-051-8 (print) ISBN 978-88-6655-053-2 (online) © 2011 Firenze University Press

so that equation (B.2) becomes

$$c\left(p_c\right)\phi\left(p_c\right)+\sum_{j=1}^{NE}\int_{\Gamma_j}\sum_{k=1}^{3}\varphi_k\left(s\right)\phi_k^{(j)}q_{p_c}^{*(j)}\mathrm{d}\Gamma+ \\ -\sum_{j=1}^{NE}\int_{\Gamma_j}\sum_{k=1}^{3}\varphi_k\left(s\right)q_k^{(j)}\phi_{p_c}^{*(j)}\mathrm{d}\Gamma \tag{B.7}$$

where

$$q_{p_c}^{*(j)}=-\frac{\left(x^{(j)}-x_{p_c}\right)n_x^{(j)}+\left(y^{(j)}-y_{p_c}\right)n_y^{(j)}}{2\pi\left[\left(x^{(j)}-x_{p_c}\right)^2+\left(y^{(j)}-y_{p_c}\right)^2\right]} \tag{B.8}$$

and

$$\phi_{p_c}^{*(j)}=-\frac{1}{4\pi}\ln\left[\left(x^{(j)}-x_{p_c}\right)^2+\left(y^{(j)}-y_{p_c}\right)^2\right] \tag{B.9}$$

The shape functions adopted in equation (B.7) are as follows

$$\varphi_1\left(s\right)=\frac{1}{2}s\left(s-1\right);\quad \varphi_2\left(s\right)=\left(1-s\right)\left(1+s\right);\quad \varphi_3\left(s\right)=\frac{1}{2}s\left(1+s\right) \tag{B.10}$$

Integrals in equation (B.7) can be transformed into integrals over the shape functions domain $[-1,1]$ as follows

$$c\left(p_c\right)\phi\left(p_c\right)+\sum_{j=1}^{NE}\int_{-1}^{1}\sum_{k=1}^{3}\varphi_k\left(s\right)\phi_k^{(j)}q_{p_c}^{*(j)}\left(s\right)\mathcal{J}^{(j)}(s)\mathrm{d}s+ \\ -\sum_{j=1}^{NE}\int_{-1}^{1}\sum_{k=1}^{3}\varphi_k\left(s\right)q_k^{(j)}\phi_{p_c}^{*(j)}\left(s\right)\mathcal{J}^{(j)}(s)\mathrm{d}s=0 \tag{B.11}$$

If the collocation point p_c assumes in turn all NN boundary nodes, the above equation becomes

$$c_i\phi_i+\sum_{j=1}^{NE}\sum_{k=1}^{3}h_{ik}^{(j)}\phi_k^{(j)}-\sum_{j=1}^{NE}\sum_{k=1}^{3}g_{ik}^{(j)}q_k^{(j)}=0\qquad i=1:NN \tag{B.12}$$

that is

$$c_i\phi_i+h_{i1}^{(1)}\phi_1^{(1)}+h_{i2}^{(1)}\phi_2^{(1)}+h_{i3}^{(1)}\phi_3^{(1)}+\ldots+h_{i1}^{(NE)}\phi_1^{(NE)}+h_{i2}^{(NE)}\phi_2^{(NE)}+h_{i3}^{(NE)}\phi_3^{(NE)}+ \\ -g_{i1}^{(1)}\phi_1^{(1)}-g_{i2}^{(1)}\phi_2^{(1)}-g_{i3}^{(1)}\phi_3^{(1)}-\ldots-g_{i1}^{(NE)}\phi_1^{(NE)}-g_{i2}^{(NE)}\phi_2^{(NE)}-g_{i3}^{(NE)}\phi_3^{(NE)}=0$$

where it has been set

$$h_{ik}^{(j)}=\int_{-1}^{1}q_i^{*(j)}\left(s\right)\varphi_k\left(s\right)\mathcal{J}^{(j)}(s)\mathrm{d}s \tag{B.13}$$

$$g_{ik}^{(j)}=\int_{-1}^{1}\phi_i^{*(j)}\left(s\right)\varphi_k\left(s\right)\mathcal{J}^{(j)}(s)\mathrm{d}s \tag{B.14}$$

The number NN of boundary nodes is given by $NN = 2NE$+number of corners of the domain Ω.

To compute the velocity of particles internal to the fluid domain, the gradient of the velocity potential is obtained by differentiating equation (B.12). Thus, if the collocation point p_c assumes in turn all NN_{int} where the velocity is sought, the gradient of the velocity potential writes as follows

$$v_i^x = \sum_{j=1}^{NE}\sum_{k=1}^{3} g_{ik,x}^{(j)} q_k^{(j)} - \sum_{j=1}^{NE}\sum_{k=1}^{3} h_{ik,x}^{(j)} \phi_k^{(j)} \qquad i = 1 : NN_{int} \tag{B.15}$$

$$v_i^y = \sum_{j=1}^{NE}\sum_{k=1}^{3} g_{ik,y}^{(j)} q_k^{(j)} - \sum_{j=1}^{NE}\sum_{k=1}^{3} h_{ik,y}^{(j)} \phi_k^{(j)} \qquad i = 1 : NN_{int} \tag{B.16}$$

where

$$g_{ik,x}^{(j)} = \int_{-1}^{1} \phi_{i,x}^{*(j)}(s)\, \varphi_k(s)\, \mathcal{J}^{(j)}(s) \mathrm{d}s \tag{B.17}$$

$$g_{ik,y}^{(j)} = \int_{-1}^{1} \phi_{i,y}^{*(j)}(s)\, \varphi_k(s)\, \mathcal{J}^{(j)}(s) \mathrm{d}s \tag{B.18}$$

$$h_{ik,x}^{(j)} = \int_{-1}^{1} q_{i,x}^{*(j)}(s)\, \varphi_k(s)\, \mathcal{J}^{(j)}(s) \mathrm{d}s \tag{B.19}$$

$$h_{ik,y}^{(j)} = \int_{-1}^{1} q_{i,y}^{*(j)}(s)\, \varphi_k(s)\, \mathcal{J}^{(j)}(s) \mathrm{d}s \tag{B.20}$$

For the sake of completeness, the gradient of the fundamental solution and its normal derivative for the i–th internal point are also given in the following

$$\phi_{i,x}^{*(j)} = -\frac{1}{4\pi} \frac{2\left(x^{(j)} - x_i\right)}{\left(x^{(j)} - x_i\right)^2 + \left(y^{(j)} - y_i\right)^2} \tag{B.21}$$

$$\phi_{i,y}^{*(j)} = -\frac{1}{4\pi} \frac{2\left(y^{(j)} - y_i\right)}{\left(x^{(j)} - x_i\right)^2 + \left(y^{(j)} - y_i\right)^2} \tag{B.22}$$

and

$$q_{i,x}^{*(j)} = -\frac{\left[\left(x^{(j)} - x_i\right)^2 + \left(y^{(j)} - y_i\right)^2\right] n_x^{(j)} - 2\left[\left(x^{(j)} - x_i\right) n_x^{(j)} + \left(y^{(j)} - y_i\right) n_y^{(j)}\right]\left(x^{(j)} - x_i\right)}{2\pi\left[\left(x^{(j)} - x_i\right)^2 + \left(y^{(j)} - y_i\right)^2\right]^2} \tag{B.23}$$

$$q_{i,y}^{*(j)} = -\frac{\left[\left(x^{(j)} - x_i\right)^2 + \left(y^{(j)} - y_i\right)^2\right] n_y^{(j)} - 2\left[\left(x^{(j)} - x_i\right) n_x^{(j)} + \left(y^{(j)} - y_i\right) n_y^{(j)}\right]\left(y^{(j)} - y_i\right)}{2\pi\left[\left(x^{(j)} - x_i\right)^2 + \left(y^{(j)} - y_i\right)^2\right]^2} \tag{B.24}$$

The Jacobian $\mathcal{J}^{(j)}(s)$ referred to the j–th boundary element is evaluated by differentiating the shape functions as follows

$$\mathcal{J}^{(j)}(s) = \sqrt{\left(\frac{\mathrm{d}x^{(j)}}{\mathrm{d}s}\right)^2 + \left(\frac{\mathrm{d}y^{(j)}}{\mathrm{d}s}\right)^2} \tag{B.25}$$

where the above derivatives are computed as follows

$$\frac{\mathrm{d}x^{(j)}}{\mathrm{d}s} = \sum_{k=1}^{3} \frac{\mathrm{d}\varphi_k}{\mathrm{d}s} x_k^{(j)} \tag{B.26}$$

$$\frac{\mathrm{d}y^{(j)}}{\mathrm{d}s} = \sum_{k=1}^{3} \frac{\mathrm{d}\varphi_k}{\mathrm{d}s} y_k^{(j)} \tag{B.27}$$

Finally, equation (B.12) can be rewritten in matrix form as follows

$$c_i \phi_i + \hat{H}_{iq} \phi_q = G_{iq} q_q \tag{B.28}$$

for which

$$H_{iq} \phi_q = G_{iq} q_q \tag{B.29}$$

where $H_{iq} = c_i \delta_{iq} + \hat{H}_{iq}$ and e $i = 1 : NN$ and $q = 1 : 3NE$.

In the same way, equations (B.15) and (B.16) can be written in matrix form as follows

$$v_i^x = G_{iq,x} q_q - H_{iq,x} \phi_q \tag{B.30}$$

$$v_i^y = G_{iq,y} q_q - H_{iq,y} \phi_q \tag{B.31}$$

where $i = 1 : NN_{int}$ and $q = 1 : 3NE$.

As soon as the primary unknowns of the system are computed (see the next two sections) the gradient of the velocity potential expressed by equations (B.30) and (B.31) can be readily computed.

B.1.1 Assembling

The matrix system (B.29), as well as (B.30) and (B.31), are of course not square because each boundary element has been treated as a single part without being connected with its two adjacent elements. An assembling algorithm is therefore required. The connectivity matrix has the following form

$$\mathbf{Conn} = \left[\begin{array}{c|ccc} \textit{Element} & \text{n1} & \text{n2} & \text{n3} \\ \hline 1 & n_1^{(1)} & n_2^{(1)} & n_3^{(1)} \\ \cdots & \cdots & \cdots & \cdots \\ j-1 & n_1^{(j-1)} & n_2^{(j-1)} & n_3^{(j-1)} \\ j & n_1^{(j)} & n_2^{(j)} & n_3^{(j)} \\ j+1 & n_1^{(j+1)} & n_2^{(j+1)} & n_3^{(j+1)} \\ \cdots & \cdots & \cdots & \cdots \\ NE & n_1^{(NE)} & n_2^{(NE)} & n_3^{(NE)} \end{array}\right]$$

Once the connectivity matrix has been defined, algorithm 4 turns the system matrices H and G into the square form HH and GG, respectively. By means of the same algorithm, matrices $H_{,x}$, $H_{,y}$, $G_{,x}$ and $G_{,y}$ are transformed in the square forms denoted by $HH_{,x}$, $HH_{,y}$, $GG_{,x}$ and $GG_{,y}$.

Algorithm 4: Assembling

input : H and G of size $NN \times 3NE$
output: HH and GG of size $NN \times NN$

for $i = 1$ **to** NN **do**
  for $j = 1$ **to** NE **do**
    for $k = 2$ **to** 4 **do**
      $index = \mathbf{Conn}\,(j, k)$
      $q = 3j - 3 + (k - 1)$
      $HH\,(i, index) = HH\,(i, index) + H\,(i, q)$
      $GG\,(i, index) = GG\,(i, index) + G\,(i, q)$

B.1.2 Reordering the system and continuity conditions

The system

$$HH_{ij}\phi_j = GG_{ij}q_j \tag{B.32}$$

needs to be rearranged according to the boundary condition type in order to get an algebraic system in the standard form

$$A_{ij}X_j = b_i \tag{B.33}$$

where all the unknown are collected in $\bar{X}$ and all the known terms, among velocity potential and flux, are collected in $\bar{b}$.

Singularities at the upper left and upper right corners of the domain, where two different boundary conditions coexist, have been removed by the so called "double–node technique". However, this expedient causes that for each of the two corners the matrix $\bar{A}$ has two identical row and consequently the system results singular. To avoid this the continuity condition is inserted according to [43] (see section 4.3 of the paper).

Finally, once the system unknowns are found, the gradient of the velocity potential at points internal to the fluid domain is computed as follows

$$v_i^x = GG_{ij,x}q_j - HH_{ij,x}\phi_j \tag{B.34}$$

$$v_i^y = GG_{iq,y}q_j - HH_{iq,y}\phi_j \tag{B.35}$$

where $i = 1 : NN_{int}$ and $j = 1 : NN$.

B.2 Numerical dervatives

Once the velocity potential is known on the free surface, the tangential component of the particle velocity at each node is computed by the following numerical scheme

$$v_f^t = \nabla\phi \cdot \bar{t} \tag{B.36}$$

It is straightforward to prove that the above equation can be rewritten as follows

$$v_f^t = \left(\frac{\partial\phi}{\partial x}\frac{\mathrm{d}x}{\mathrm{d}s} + \frac{\partial\phi}{\partial y}\frac{\mathrm{d}y}{\mathrm{d}s}\right)\frac{1}{\mathcal{J}(s)} = \frac{\mathrm{d}\phi}{\mathrm{d}s}\frac{1}{\mathcal{J}(s)} \tag{B.37}$$

where for the j-th element the velocity potential derivative with respect to the curvilinear coordinate s, as well as the derivatives involved in the Jacobian, are obtained by differentiating the shape functions as follows

$$\frac{\mathrm{d}\phi}{\mathrm{d}s} = \frac{\mathrm{d}\varphi_i}{\mathrm{d}s}\phi_i^{(j)} \tag{B.38}$$

$$\frac{\mathrm{d}x}{\mathrm{d}s} = \frac{\mathrm{d}\varphi_i}{\mathrm{d}s}x_i^{(j)} \tag{B.39}$$

$$\frac{\mathrm{d}y}{\mathrm{d}s} = \frac{\mathrm{d}\varphi_i}{\mathrm{d}s}y_i^{(j)} \tag{B.40}$$

B.3 Gradient of the velocity field

Let us start form the gradient of the velocity field

$$\nabla\bar{v} = \begin{pmatrix} v_{x,x} & v_{x,y} \\ v_{x,y} & v_{y,y} \end{pmatrix}$$

The curve $\Gamma_f : I\!R \to I\!R^2$, i.e. the free surface, is parameterized as follows

$$s \mapsto \Gamma_f(s) = \begin{cases} x(s) \\ y(s) \end{cases}$$

The velocity field is also parameterized as follows

$$s \mapsto \bar{v}(s) = \begin{cases} v^x(x(s), y(s), t) \\ v^y(x(s), y(s), t) \end{cases}$$

The chain rule allows to write the following partial derivatives

$$\frac{\partial v^x}{\partial s} = \frac{\partial v^x}{\mathrm{d}x}\frac{\mathrm{d}x}{\mathrm{d}s} + \frac{\partial v^x}{\mathrm{d}y}\frac{\mathrm{d}y}{\mathrm{d}s} \tag{B.41}$$

$$\frac{\partial v^y}{\partial s} = \frac{\partial v^y}{\mathrm{d}x}\frac{\mathrm{d}x}{\mathrm{d}s} + \frac{\partial v^y}{\mathrm{d}y}\frac{\mathrm{d}y}{\mathrm{d}s} \tag{B.42}$$

Next, the continuity equation assures that

$$\frac{\partial v^x}{\partial x} = -\frac{\partial v^y}{\partial y} \tag{B.43}$$

while the irrotational flow hypothesis allows to write

$$\frac{\partial v^y}{\partial x} = \frac{\partial v^x}{\partial y} \tag{B.44}$$

and both of the above equations transform the system of equations (B.41) and (B.42) into

$$\frac{\partial v^x}{\partial s} = \frac{\partial v^x}{\partial x}\frac{\mathrm{d}x}{\mathrm{d}s} + \frac{\partial v^y}{\partial x}\frac{\mathrm{d}y}{\mathrm{d}s} \tag{B.45}$$

$$\frac{\partial v^y}{\partial s} = \frac{\partial v^y}{\partial x}\frac{\mathrm{d}x}{\mathrm{d}s} + \frac{\partial v^x}{\partial x}\frac{\mathrm{d}y}{\mathrm{d}s} \tag{B.46}$$

which can be solved for $\frac{\partial v^x}{\partial x}$ and $\frac{\partial v^y}{\partial x}$ to get

$$\frac{\partial v^x}{\partial x} = \frac{1}{\mathcal{D}}\left(\frac{\partial v^x}{\partial s}\frac{\mathrm{d}x}{\mathrm{d}s} - \frac{\partial v^y}{\partial s}\frac{\mathrm{d}y}{\mathrm{d}s}\right) \tag{B.47}$$

$$\frac{\partial v^y}{\partial x} = \frac{1}{\mathcal{D}}\left(\frac{\partial v^y}{\partial s}\frac{\mathrm{d}y}{\mathrm{d}s} + \frac{\partial v^y}{\mathrm{d}s}\frac{\mathrm{d}x}{\mathrm{d}s}\right) \tag{B.48}$$

$$\tag{B.49}$$

where

$$\mathcal{D}(s) = \mathcal{J}(s)^2 = \left(\frac{\mathrm{d}x}{\mathrm{d}s}\right)^2 + \left(\frac{\mathrm{d}y}{\mathrm{d}s}\right)^2 \tag{B.50}$$

Finally the second term of the right-hand side of equation (4.21) becomes

$$\frac{Dv^x}{Dt} = \dot{v}_f^x + v_{f,x}^x v^x + v_{f,y}^x v^y \tag{B.51}$$

$$\frac{Dv^y}{Dt} = \dot{v}_f^y + v_{f,x}^y v^x + v_{f,y}^y v^y \tag{B.52}$$

where the components $\frac{\partial v^y}{\partial y}$ and $\frac{\partial v^x}{\partial y}$ have been found by using the continuity and irrotational equations.

B.4 Tests of convergence

In order to check the reliability of the BEM code it is important first to show the reliability of the solution of the steady Laplace's equation. This is in fact the core of the numerical wave simulator because at each time step a stationary problem is solved.

To this aim in the first two tests a very well known problem in solid mechanics is presented: the Saint Venant torsional problem. Indeed, given a cylindrical beam, i. e. a solid with one dimension dominating with respect to the others, and denoting its cross section by $\mathcal{A}$, the whole state of stress induced by a torsional couple is known when either the *stress function* ψ or the *warping function* φ are known. Details on the torsion problem are available in [92].

The last case regards a a general potential problem defined on a square domain with mixed boundary condition of the type as in the case of water waves.

B.4.1 Torsion: Dirichlet's problem

The problem can be formulated in terms of the *stress function* ψ as follows

$$\begin{cases} \nabla^2\psi(x_1,x_2) = 0 & \forall\ p \in \mathcal{A} \\ \psi(x_1,x_2) = \frac{1}{2}\left(x_1^2 + x_2^2\right) & \forall\ p \in \partial\mathcal{A} \end{cases} \tag{B.53}$$

When the cross section $\mathcal{A}$ has an elliptical shape, the analytical solution writes as follows

$$\psi = \frac{a^2b^2}{a^2+b^2} + \frac{1}{2}\frac{a^2-b^2}{a^2+b^2}(x_1 - x_2) \tag{B.54}$$

where a and b are the major and minor axes of the ellipse.

NE	2	4	8	16	32	64
$errL_2^2$	74.9129	0.7892	0.0017	0.0000	0.0000	0.0000
$errL_2$	8.6552	0.8884	0.0408	0.0028	0.0001	0.0000

Table B.1: $errL_2^2$ and $errL_2$ of *stress function* for different boundary mesh.

Given such a domain, for four boundary discretizations more and more refined we compare the numerical and analytical solutions by using the norm L_2 of the error computed as

$$errL_2 = \sqrt{\sum_{i=1}^{n} \left(\phi_i^{Anal.} - \phi_i^{Num.}\right)^2} \tag{B.55}$$

where n is the number of points uniformly distributed across the domain $\mathcal{A}$ at which the two solutions are evaluated. See the red dots into the domains plotted in figure B.1. The figure shows different boundary discretizations form a number of boundary elements $NE = 2$ up to $NE = 64$.

The error decrease quadratically and approaches zero with sixteen elements. See figure B.2. The rate of convergence is pretty satisfactory.

B.4.2 Torsion: Neumann's problem

The excellent result shown in the previous section needs to be confirmed also in the case when mixed boundary conditions are applied (as the case of our numerical wave simulator) where discontinuities occur. As already mentioned, this problem is faced by introducing the double–node technique. To test such a circumstance, the domain is here restricted only to one quarter of the all ellipse.

$$\begin{cases} \nabla^2\varphi\,(x_1, x_2) = 0 \quad \forall\ p \in \mathcal{A} \\ \nabla\varphi \cdot \bar{n} = x_2 n_1 - x_1 n_2 \quad \forall\ p \in \partial\mathcal{A} \end{cases} \tag{B.56}$$

In the case of Dirichlet's problem no corners were involved, thus the double–node method was not necessary. On the contrary, for the one forth of ellipse, there are three corners. For those where Neumann-Dirichlet boundary conditions are assigned the double–node technique works quite well after implementing the the kinematic and continuity conditions proposed in [43]. But at the symmetry point, in the center of the ellipse, the Dirichlet–Dirichlet condition produces two identical equations. Hence the system is again singular. To avoid this, the two nodes have been shifted of a very small quantity inside the elements [38]. With this expedient results are sufficiently accurate.

The domain discretization is shown in figure B.3. While the Root Mean Square Error convergence in shown in table B.2 and figure B.4.

B.4.3 Potential problem on a square domain

In this case a square domain Ω whose boundaries $\Gamma_b, \Gamma_{i_2}, \Gamma_f, \Gamma_{i_1}$ are straigth lines with lengths $L_b = L_{i_2} = L_f = L_{i_1} = 1\,\mathrm{m}$ is considered. The Neumann boundary

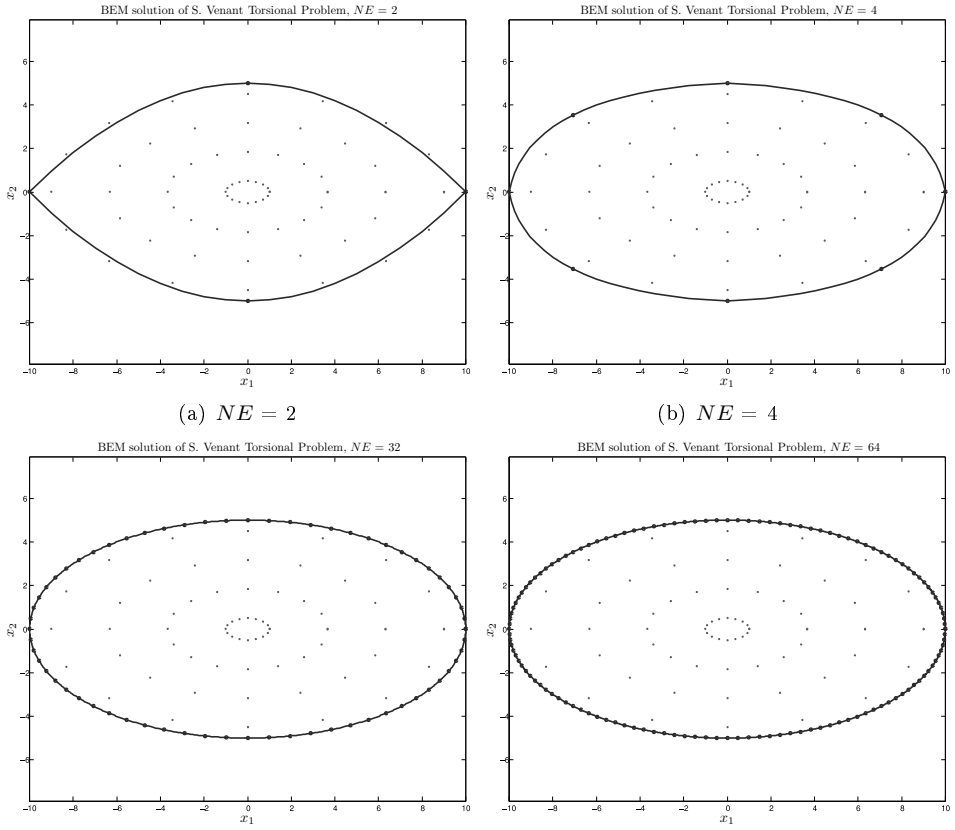

(a) $NE = 2$ (b) $NE = 4$

(c) $NE = 32$ (d) $NE = 64$

Figure B.1: Mesh refinement in the case of an elliptical cross section, domain for a Dirichlet's torsional problem.

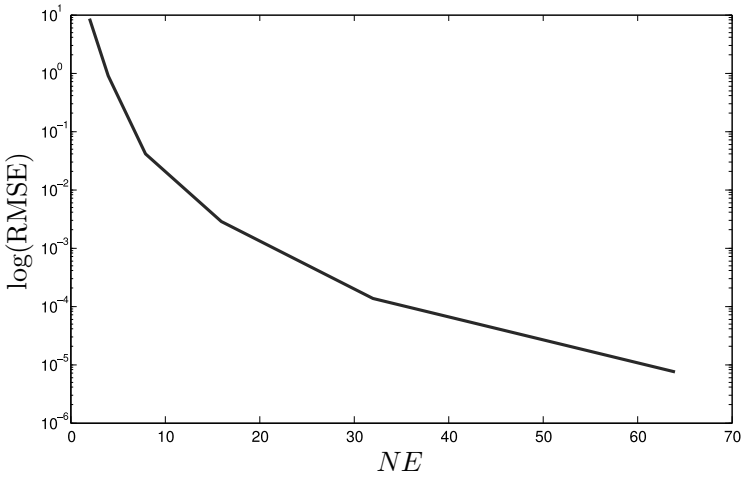

Figure B.2: Convergence of $errL_2$ in the case of Dirichlet's torsion problem.

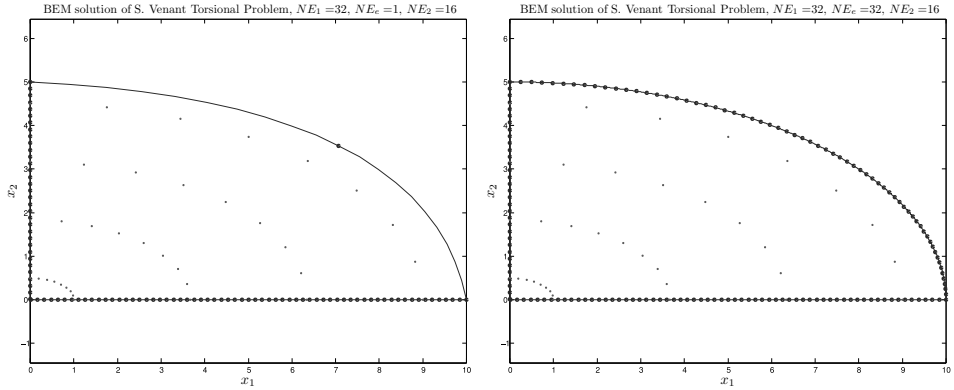

(a) $NE_1, NE_e, NE_2 = 32, 1, 16$ (b) $NE_1, NE_e, NE_2 = 32, 128, 16$

Figure B.3: Mesh refinement in the case of an elliptical cross section, domain for a Neumann's torsional problem.

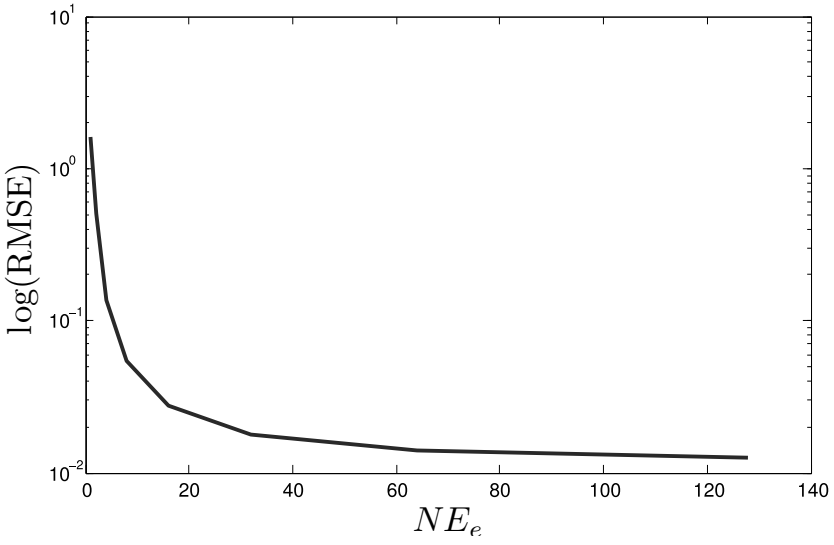

Figure B.4: Convergence of $errL_2$ in the case of Neumann's torsion problem.

NE_e	1	2	4	8	16	32	64	128
$errL_2^2$	2.5598	0.2588	0.0183	0.0029	0.0008	0.0003	0.0002	0.0002
$errL_2$	1.5999	0.5087	0.1353	0.0539	0.0278	0.0177	0.0139	0.0125

Table B.2: $errL_2^2$ and $errL_2$ of *torsion function* for different boundary mesh.

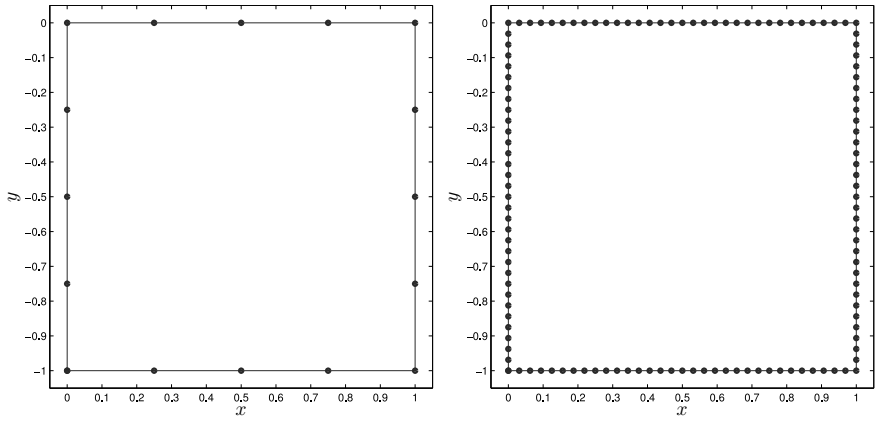

(a) Number of elements per side $NE = 2$ (b) Number of elements per side $NE = 16$

Figure B.5: Two discretizations for the solution of the potential problem defined on a square domain.

conditions are prescribed as follows

$$\frac{\partial \Phi(p)}{\partial \bar{n}} = \begin{cases} a\cos(a(y+d)) & \forall p \in \Gamma_{i_1} \\ -ae^{-a}\cos(a(y+d)) & \forall p \in \Gamma_{i_2} \\ 0 & \forall p \in \Gamma_b \end{cases}$$

while on the remaining boundary the Dirichlet condition is $\Phi(p) = 0 \ \forall p \in \Gamma_f$. a is a constant equals to $3\pi/2$ and $d = L_{i_1} = L_{i_2}$ is the distance between the upper and lower boundaries (in the next cases it will be the water depth). The exact solution of this problem is $\Phi(p) = e^{-ax}\cos(a(y+d))$.

The vector $\bar{X}$ collecting all the unknowns of the problem concatenates $2NE_b + 1$ elements that are the potential function over Γ_b, $2NE_{i_2} + 1$ elements that are the potential function over Γ_{i_2}, $2NE_f + 1$ elements that are the fluxes over Γ_f and finally $2NE_{i_1} + 1$ elements that are the potential function over Γ_{i_1}.

To investigate the error convergence of the steady second order boundary element solver, the global error $errL_2$ has been evaluated as function of the number of elements per boundary. All the four boundaries have been discretized with the same number of elements. See figure B.5.

Figure B.6 shows the convergence of the error computed as

$$errL_2 = \sqrt{\sum_{k=1}^{k=n} (X^k - X_a^k)^2} \tag{B.57}$$

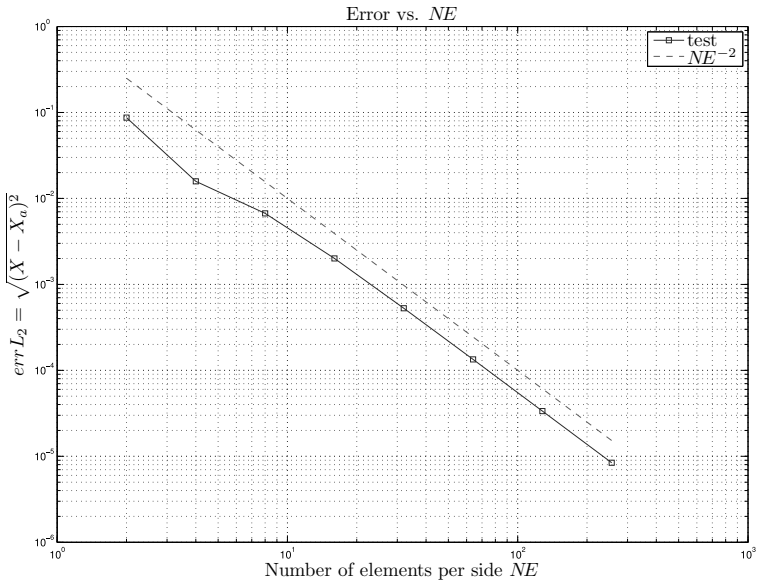

Figure B.6: Error convergence of the error.

where X and X_a are the vectors collecting the numerical and the exact analytical solution, respectively, only on the boundary.

The global error decreases quadratically as the number of element per boundary NE increases. This rate of convergence is justified by the order of the boundary elements discussed above. When the number of elements per side is quite low, when it doubles from 2 to 4, the convergence is even faster then quadratic.

Bibliography

[1] E. Hau. *Wind Turbines: Fundamentals, Technologies, Application, Economics.* Springer, 2006.

[2] IEC 61400-3 Wind Turbines Part 3: Design requirements for offshore wind turbines, Edition 1.0 2009-02.

[3] T. Plifke, S.T. Sperbeck, M. Urban, U. Peil, and H. Budelmann. A standardized methodology for managing disaster risk - an attempt to remove ambiguity. In *Proceedings of the 5th International Probabilistic Workshop, Ghent, Belgium*, 2007.

[4] T. Burton, D. Sharpe, N. Jenkins, and E. Bossanyi. *Wind Energy Handbook.* John Wiley & Sons, Ltd, 2001.

[5] T. Sarpkaya and M. Isaacson. *Mechanics of Wave Forces on Offshore Structures.* Van Nostrand Reinhold Company, 1981.

[6] D.G. Dommermuth, D.K.P. Yue, W.M. Lin, R.J. Rapp, E.S. Chan, and W.K. Melville. Deep-water plunging breakers: a comparison between potential theory and experiments. *Journal of Fluid Mechanics*, 189:423–442, 1988.

[7] Design of offshore wind turbine structures. Technical report, Offshore Standard Det Norske Veritas DNV-OS-J101.

[8] J. Wienke and H. Oumeraci. Breaking wave impact force on a vertical and inclined slender pile–theoretical and large-scale model investigations. *Coastal Engineering*, 52(5):435 – 462, 2005.

[9] J.M. Jonkman and L. Buhl Jr. Marshall. FAST user's guide. Technical report, NREL, 2005.

[10] S. Chakrabarti, editor. *Handbook of Offshore Engineering.* Elsevier Ltd., 2005.

[11] M.K. Ochi. *Ocean waves: the stochastic approach.* Cambridge Ocean Technology Series, 2005.

[12] M.K. Ochi. A series of JONSWAP wave spectra for offshore structure design. In *2nd International Conference on the Behaviour of offshore Structure*, pages 45–86, 1979.

[13] G. Clauss, E. Lehmann, and C. Ostergaard. *Offshore Structures: Conceptual Design and Hydromechanics.* Springer, London, UK, 1992.

[14] J.M.J. Journée and W.W. Massie. *Offshore Hydrodynamics*. Delft University of Technology, 2001.

[15] Global Wind Report. Technical report, GWEC, Global Wind Energy Council, 2008.

[16] O. Ditlevsen and H.O. Madsen. *Structural Reliability Method*. John Wiley & Sons Ltd, 1996.

[17] E.J. Plate. Flood risk and flood management. *Journal of Hydrology*, 267(1-2):2 – 11, 2002.

[18] M.H. Faber. *Risk and Safety in Civil, Surveying and Environmental Engineering*. Swiss Federal Institute of Technology, 2005.

[19] J.D. Sørensen. *Structural Risk Theory And Risk Analysis*. 2004.

[20] G. Augusti, C. Borri, and H.J. Niemann. Is aeolian risk as significen as other environmantal risks? *Reliability Engineering and System Safety*, 74:227–237, 2001.

[21] O. Ditlevsen. Stochastic model for joint wave and wind loads on offshore structures. *Structural Safety*, 24:139–163, 2002.

[22] M. Ciampoli, F. Petrini, and G. Augusti. A procedure for performance-based wind engineering. In *ICOSSAR 2009*, 2009.

[23] C. Mannini and G. Bartoli. The problem of uncertainty in the measurement of aerodynamic derivatives. In *ICOSSAR*, 2009.

[24] C. Mannini. *Flutter Vulnerability Assessment of Flexible Bridges*. PhD thesis, University of Florence - TU Braunschweig, 2006.

[25] P.W. Cheng. *A reliability based design methodology for extreme respnse of offsore wind turbines*. PhD thesis, DUWIND, Delft University Wind Energy Research Institute, 2002.

[26] P.W. Cheng, G.J.W. van Bussel, G.A.M. van Kuik, and J.H. Vugts. Reliability-based design methods to determine the extreme response distribution of offshore wind turbines. *Wind Energy*, 6:1–22, 2003.

[27] K. Johannessen. Joint distribution for wind and waves in the northern north sea. In *Proceedings of the Eleventh International Offshore and Polar Engineering Conference*, 2001.

[28] O. Ditlevsen and H.O. Madsen. *Structural Reliability Methods*. 2007.

[29] S. Zachary, G. Feld, G. Ward, and J. Wolfram. Multivariate extrapolation in the offshore environment. *Applied Ocean Research*, 20(5):273 – 295, 1998.

[30] M. Rosenblatt. Remarks on a multivariate transformation. *Annals of Mathematical Statistics*, 23:470–472, 1952.

[31] C.H. Kim. *Nonlinear Waves and Offshore Structures.* Worl Scientific - Advanced Series on Ocean Engineering - Vol. 27, 2008.

[32] Y. Goda. *Random Seas And Design Of Maritime Structures.* Advanced Series On Ocean Engineering, Volume 15 - World Scientific Publishing Company, 2000.

[33] C.A. Brebbia and S. Walker. *Dynamic analysis of offshore structures.* Newnes-Butterworths, 1979.

[34] M.O.L. Hansen. *Aerodynamics of Wind Turbines.* Earthscan, 2008.

[35] P.J. Moriarty and A.C. Hansen. Aerodyn theory manual. Technical report, NREL/EL-500-36881, 2005.

[36] IEC 61400-1 wind Turbines Part 1: Design requirements, Edition 3.0 2005-08.

[37] S. K. Chakrabarti. *Hydrodynamics of Offshore Structures.* WIT Press (UK), 1998.

[38] C.A. Brebbia and J. Dominguez. *Boundary Elements, An Introductory Course.* WIT Press, Boston, Southamton, 1998.

[39] P. Boccotti. *Wave Mechanics for Ocean Engineering.* Elsevier Oceanography Series, 2000.

[40] M.S. Longuet-Higgins and E.D. Cokelet. The deformation of steep surface waves on water. i. a numerical method of computation. *Proceedings of the Royal Society of London. Series A, Mathematical and Physical Sciences*, 350(1660):1–26, 1976.

[41] J.W. Dold and D.H. Peregrine. An efficient boundary integral method for steep unsteady water waves. *Numerical Methods for Fluid Dynamics II*, pages 671–679, 1986.

[42] S.T. Grilli, J. Skourup, and I.A. Svedsen. An efficient boundary element method for nonlinear water waves. *Engineering Analysis with Boundary Elements*, 6(2):97–107, 1989.

[43] S.T. Grilli and I.A. Svendsen. Corner problems and global accuracy in the boundary element solution of nonlinear wave flows. *Engineering Analysis with Boundary Elements*, 7(4):178 – 195, 1990.

[44] T. Nakayama. Boundary element analysis of nonlinear water wave problems. *International Journal for Numerical Methods in Engineering*, 19(7):953–970, 1983.

[45] T. Nakayama. A computational method for simulating transient motions of an incompressible inviscid fluid with a free surface. *International Journal for Numerical Methods in Fluids*, 10(6):683–695, 1990.

[46] V. Vinayan and S. A. Kinnas. A bem for the propagation of nonlinear planar free-surface waves. *Electronic Journal of Boundary Elements*, 5(1):17–40, 2007.

[47] W. Bai and R. Eatock Taylor. Fully nonlinear simulation of wave interaction with fixed and floating flared structures. *Ocean Engineering*, 36(3-4):223 – 236, 2009.

[48] W. Koo and M.-H. Kim. Freely floating-body simulation by a 2d fully nonlinear numerical wave tank. *Ocean Engineering*, 31(16):2011 – 2046, 2004.

[49] X.T. Zhang, B.C. Khoo, and J. Lou. Wave propagation in a fully nonlinear numerical wave tank: A desingularized method. *Ocean Engineering*, 33(17-18):2310 – 2331, 2006.

[50] J. N. Newman. *Marine Hydrodynamics*. The MIT Press, 1977.

[51] W.M. Lin. *Nonlinear motion of the free surface near a moving body*. PhD thesis, Massachusetts Institut of Technology, 1984.

[52] J. Lighthill. *Waves in fluids*. Cambridge University Press, 2011.

[53] T. Srisupattarawanit, R. Niekamp, and H.G. Matthies. Simulation of nonlinear random finite depth waves coupled with an elastic structure. *Computer Methods in Applied Mechanics and Engineering*, 195(23-24):3072 – 3086, 2006. Incompressible CFD.

[54] T. Srisupattarawanit. *Simulation of Offshore Wind Turbines by Computational Multi-Physics*. PhD thesis, Technischen Universität Carolo-Wilhelmina zu Braunschweig, 2007.

[55] R. Machane and E. Canot. High-order schemes in boundary element methods for transient non-linear free surface problems. *International Journal for Numerical Methods in Fluids*, 24(10):1049–1072, 1997.

[56] W. Tsai and D. K. P. Yue. Computation of nonlinear free-surface flows. *Annual Review of Fluid Mechanics*, 28:249–278, 1996.

[57] J.W. Dold. An efficient surface-integral algorithm applied to unsteady gravity waves. *Journal of Computational Phisycs*, 103:90 – 115, 1992.

[58] P. Wang, Y. Yitao, and M.P. Tulin. An efficient numerical tank for non-linear water waves, based on the multi-subdomain approach with bem. *International Journal for Numerical Methods in Fluids*, 20:1315–1336, 1995.

[59] D.E. Medina, J.A. Liggett, R.A. Birchwood, and K.E. Torrance. A consistent boundary element method for free surface hydrodynamic calculations. *International Journal for Numerical Methods in Fluids*, 12:835 – 857, 1991.

[60] S.T. Grilli. Depth inversion in shallow water based on nonlinear properties of shoaling periodic waves. *Coastal Engineering*, 35(3):185 – 209, 1998.

[61] J. Horrillo S.T. Grilli. Numerical generation and absorption of fully nonlinear periodic waves. *Journal of Engineering Mechanics*, 123, 1997.

[62] R. Subramanya S.T. Grilli. Quasi-singular integrals in the modeling of nonlinear water waves in shallow water. *Engineering Analysis with Boundary Elements*, 13(2):181 – 191, 1994.

[63] S.T. Grilli and I.A. Svendsen. Corner problems and global accuracy in the boundary element solution of nonlinear wave flows. *Engineering Analysis with Boundary Elements*, 7(4):178 – 195, 1990.

[64] R. Cointe. Numerical simulation of a wave channel. *Engineering Analysis with Boundary Elements*, 7(4):167 – 177, 1990.

[65] N. Drimer and Y. Agnon. An improved low-order boundary element method for breaking surface waves. *Wave Motion*, 43(3):241 – 258, 2006.

[66] J. R. Morison, M. P. O'Brien, J. W. Johnson, and S. A. Schaaf. The force exerted by surface wave on piles. *Petroleum Transactions (American Institute of Mining Engineers)*, 189:149–154, 1950.

[67] R.G. Dean and R.A. Dalrymple. *Water Wave Mechanics for Engineers and Scientists*. World Scientific - Advanced Series on Ocean Engineering - Volume 2, 1984.

[68] J.D. Wheeler. Methods for calculating forces produced by irregular waves. *Journal of Petroleum Technology*, 249:359–367, 1970.

[69] G. Cuomo, W. Allsop, T. Bruce, and J. Pearson. Breaking wave loads at vertical seawalls and breakwaters. *Coastal Engineering*, 57(4):424 – 439, 2010.

[70] M.K. Ochi and C.-H. TSAI. Prediction of impact pressure induced by breaking waves on vertical cylinders in random seas. *Applied ocean research*, 6:157–163, 1984.

[71] J. Wienke. *Druckschlagbelastung auf schlanke zylindrische Bauwerke durch brechende Wellen-theoretische und großmaßstäbliche Laboruntersuchungen - PhD thesis (in German)*. PhD thesis, TU Braunschweig, http://www.biblio.tu-bs.de, 2001.

[72] M. Kitahata Y. Goda, S. Haranaka. Study on impulsive breaking wave forces on piles. *Report Port and Harbour Technical Research Institute*, 6(5):1 – 30, 1966.

[73] H. Wagner. Über stoßund gleitvorgänge an der oberfläche von flüssigkeiten. *Zeitschrift für angewandte Mathematik und Mechanik*, 12(4):193 – 215, 1932.

[74] R. Cointe. Hydrodynamic impact analysis of a cylinder. *Journal of Offshore Mechanics and Arctic Engineering*, 109:237– 243, 1987.

[75] J. Jonkman, S. Butterfield, W. Musial, and G. Scott. Definition of a 5-MW reference wind turbine for offshore system development. Technical report, NREL, 2009.

[76] H.J.T. Kooijman, C. Lindenburg, D. Winkelaar, and E.L. van der Hooft. Dowec 6 mwpre-design aero-elastic modelling of the dowec 6 mw pre-design in phatas. Technical report, DOWEC-F1W2-HJK-01-046/9 public version, 2003.

[77] C. Lindenburg. Aeroelastic modelling of the lmh64-5 blade. Technical report, DOWEC Dutch Offshore Wind Energy Converter 1997 2003 Public Reports, 2002.

[78] E.-S. Chan. Mechanics of deep water plunging-wave impacts on vertical structures. *Coastal Engineering*, 22(1-2):115 – 133, 1994. Special Issue Vertical Breakwaters.

[79] E-S. Chan, H.-F. Cheong, and B.-C. Tan. Laboratory study of plunging wave impacts on vertical cylinders. *Coastal Engineering*, 25(1-2):87 – 107, 1995.

[80] S.R. Winterstein, T.C. Ude, C.A. Cornell, P. Bjergager, and S. Haver. Environmental parameters for extreme response: Inverse form with omission factors. In *Proceedings, ICOSSAR-93*, 1993.

[81] P. Stansell. Distributions of freak wave heights measured in the north sea. *Applied Ocean Research*, 26(1-2):35 – 48, 2004.

[82] G. Muraleedharan, A.D. Rao, P.G. Kurup, N.U. Nair, and M. Sinha. Modified weibull distribution for maximum and significant wave height simulation and prediction. *Coastal Engineering*, 54(8):630 – 638, 2007.

[83] E.L. Andreas and S. Wang. Predicting significant wave height off the northeast coast of the united states. *Ocean Engineering*, 34(8-9):1328 – 1335, 2007.

[84] C. Guedes Soares and M. Scotto. Modelling uncertainty in long-term predictions of significant wave height. *Ocean Engineering*, 28(3):329 – 342, 2001.

[85] J.A. Ferreira and C.G. Soares. Modelling distributions of significant wave height. *Coastal Engineering*, 40(4):361 – 374, 2000.

[86] I. Rychlik. A note on significant wave height. *Ocean Engineering*, 23(6):447 – 454, 1996.

[87] J. Mathisen and E. Bitner-Gregersen. Joint distributions for significant wave height and wave zero-up-crossing period. *Applied Ocean Research*, 12(2):93 – 103, 1990.

[88] L.R. Muir and A.H. El-Shaarawi. On the calculation of extreme wave heights: A review. *Ocean Engineering*, 13(1):93 – 118, 1986.

[89] M. Darbyshire and L. Draper. Forecasting wind generated sea–waves. *Engineering*, 195(5), April 1963.

[90] P.J. Moriarty, W.E. Holley, and S.P. Butterfield. Extrapolation of extreme and fatigue loads using probabilistic methods. *NREL, Technical Report*, NRET/TP-500-34421, 2004.

[91] P.H. Madsen and K.P. Marshall Buhl. Predicting ultimate loads for wind turbine design. In *AIAA/ASME Wind Energy Symposium*, 1999.

[92] C. Borri, M. Betti, and E. Marino. *Lectures on Solid Mechanics*. Firenze University Press, 2008.

[93] A. Andres, A. Argyriadis, P. Dalhoff, C. Nath, and S. Schwartz. *Standars and Certification*, chapter 11, pages 225–269. Multi-Science Publishing Co. Ltd, 2009.

[94] W. Bai and R. Eatock Taylor. Higher-order boundary element simulation of fully nonlinear wave radiation by oscillating vertical cylinders. *Applied Ocean Research*, 28(4):247 – 265, 2006.

[95] P. Brevig, M. Greenhow, and T. Vinje. Extreme wave forces on submerged wave energy devices. *Applied Ocean Research*, 4(4):219 – 225, 1982.

[96] A.T. Brewer and L.A. Godoy. On interaction between static and dynamic loads in instability of symmetric or asymmetric structural systems. *Journal of Sound and Vibration*, 147(1):105 – 114, 1991.

[97] L.L. Broderick and J.W. Leonard. Nonlinear response of membranes to ocean waves using boundary and finite elements. *Ocean Engineering*, 22(7):731 – 745, 1995.

[98] L.L. Broderick and J.W. Leonard. Nonlinear water-wave structure interaction. *Computers & Structures*, 44(4):837 – 842, 1992. Special Issue: Computational Structures Technology.

[99] L.L. Broderick and J.W. Leonard. Selective review of boundary element modelling for the interaction of deformable structures with water waves. *Engineering Structures*, 12(4):269 – 276, 1990.

[100] G.N. Bullock, C. Obhrai, D.H. Peregrine, and H. Bredmose. Violent breaking wave impacts. Part 1: Results from large-scale regular wave tests on vertical and sloping walls. *Coastal Engineering*, 54(8):602 – 617, 2007.

[101] X. Cai, H.P.Langtangen, B.F. Nielsen, and A. Tveito. A finite element method for fully nonlinear water waves,. *Journal of Computational Physics*, 143(2):544 – 568, 1998.

[102] S.K. Chakrabarti. Loads and responses. In Subrata K. Chakrabarti, editor, *Handbook of Offshore Engineering*, pages 133 – 196. Elsevier, London, 2005.

[103] Y.-H. Chang, K.-S. Hwang, and H.-H. Hwung. Large-scale laboratory measurements of solitary wave inundation on a 1:20 slope. *Coastal Engineering*, 56(10):1022 – 1034, 2009.

[104] H. Chanson and L. Jaw-Fang. Plunging jet characteristics of plunging breakers. *Coastal Engineering*, 31(1-4):125 – 141, 1997.

[105] M. Christou, C.H. Hague, and C. Swan. The reflection of nonlinear irregular surface water waves. *Engineering Analysis with Boundary Elements*, 33(5):644 – 653, 2009.

[106] E. von Collani, A. Binder, W. Sans, A. Heitmann, and K. Al-Ghazali. Design load definition by lexpol. *Wind Energy*, 11:637–653, 2008.

[107] O.M. Faltinsen. *Sea loads on ships and offshore structures*. Cambridge Ocean Technology Series, 1990.

[108] L.A. Godoy. Displacements induced by breaking waves on axially loaded cylindrical shells. *Applied Ocean Research*, 7(3):152 – 157, 1985.

[109] L.A. Godoy, S. R. Idelsohn, and E. Barbero. On load interaction in the non linear buckling analysis of cylindrical shells. *Advances in Engineering Software and Workstations*, 13(1):46 – 50, 1991.

[110] L.A. Godoy, V.C.M. de Souza, and J.G.A. Croll. Transient dynamics of cylinders under wave slamming. *Thin-Walled Structures*, 3(1):67 – 79, 1985.

[111] C.H. Hague and C. Swan. A multiple flux boundary element method applied to the description of surface water waves. *Journal of Computational Physics*, 228(14):5111 – 5128, 2009.

[112] W. He. Numerical simulation of nonlinear radiation water surface wave caused by large-amplitude oscillation of a cylinder. *Communications in Nonlinear Science and Numerical Simulation*, 4(1):24 – 28, 1999.

[113] B. J. Jonkman and M. L. Buhl Jr. *TurbSim User's Guide for Version 1.40*. Revised September 12, 2008 for TurbSim version 1.40.

[114] A. Khayyer and H. Gotoh. Modified moving particle semi-implicit methods for the prediction of 2d wave impact pressure. *Coastal Engineering*, 56(4):419 – 440, 2009.

[115] A. Khayyer, H. Gotoh, and S. Shao. Enhanced predictions of wave impact pressure by improved incompressible sph methods. *Applied Ocean Research*, 31(2):111 – 131, 2009.

[116] M.S. Kirkgoz, A.K. Tanrikulu, and C. Dündar. Dynamic analysis of a vertical plate exposed to breaking wave impact. *Ocean Engineering*, 31(13):1623 – 1635, 2004.

[117] M.S. Kirkgöz. Influence of water depth on the breaking wave impact on vertical and sloping walls. *Coastal Engineering*, 18(3-4):297 – 314, 1992.

[118] M.S. Kirkgöz and M.S. Aköz. Geometrical properties of perfect breaking waves on composite breakwaters. *Ocean Engineering*, 32(16):1994 – 2006, 2005.

[119] M.S. Kirkgöz and M. Mamak. Impulse modelling of wave impact pressures on vertical wall. *Ocean Engineering*, 31(3-4):343 – 352, 2004.

[120] K.M.T. Kleefsman, G. Fekken, A.E.P. Veldman, B. Iwanowski, and B. Buchner. A volume-of-fluid based simulation method for wave impact problems. *Journal of Computational Physics*, 206(1):363 – 393, 2005.

[121] W.C. Koo and M.H. Kim. Fully nonlinear wave-body interactions with surface-piercing bodies. *Ocean Engineering*, 34(7):1000 – 1012, 2007.

[122] A. Kyte and A. Tørum. Wave forces on vertical cylinders upon shoals. *Coastal Engineering*, 27(3-4):263 – 286, 1996.

[123] P. Lin. A numerical study of solitary wave interaction with rectangular obstacles. *Coastal Engineering*, 51(1):35 – 51, 2004.

[124] Enzo Marino. *An integrated nonlinear wind-waves model for offshore wind turbines*. PhD thesis, University of Florence-TU–Braunschweig, 2010.

[125] E. Marino, C. Borri, and C. Lugni. Influence of wind-waves energy transfer on the impulsive hydrodynamic loads acting on offshore wind turbines. *Journal of Wind Engineering and Industrial Aerodynamics*, In Press, Corrected Proof:–, 2011.

[126] E. Marino, C. Borri, and U. Peil. A fully nonlinear wave model to account for breaking wave impact loads on offshore wind turbines. *Journal of Wind Engineering and Industrial Aerodynamics*, 99(4):483 – 490, 2011.

[127] D.Z. Ning, J. Zang, S.X. Liu, R. Eatock Taylor, B. Teng, and P.H. Taylor. Free-surface evolution and wave kinematics for nonlinear uni-directional focused wave groups. *Ocean Engineering*, 36(15-16):1226 – 1243, 2009.

[128] P. Osuna, A.J. Souza, and J. Wolf. Effects of the deep-water wave breaking dissipation on the wind-wave modelling in the irish sea. *Journal of Marine Systems*, 67(1-2):59 – 72, 2007.

[129] U. Peil and C. Corte. Numerical simulation of breacking wave load on offshore wind turbines. In *Proceedings of EACWE4-The Fourth European and African Conference on Wind Engineering*, 2005.

[130] W. Romanczyk. Instability of nonlinear standing waves in front of a vertical wall. *Journal of Fluids and Structures*, 23(5):733 – 753, 2007.

[131] J. Skourup, M. J. Sterndorff, and E. A. Hansen. Numerical modelling of wave-structure interaction by a three-dimensional nonlinear boundary element method: A step towards the numerical wave tank. *Ocean Engineering*, 19(5):437 – 460, 1992.

[132] V. Sriram, S.A. Sannasiraj, and V. Sundar. Simulation of nonlinear free surface dispersive shallow water waves. *Journal of Hydro-environment Research*, 1(2):126 – 132, 2007.

[133] P.K. Stansby and M. Isaacson. Recent developments in offshore hydrodynamics: workshop report. *Applied Ocean Research*, 9(3):118 – 127, 1987.

[134] H. Sun and O.M. Faltinsen. Water impact of horizontal circular cylinders and cylindrical shells. *Applied Ocean Research*, 28(5):299 – 311, 2006.

[135] H.G. Sung and H.S. Choi. Implicit formulation with the boundary element method for nonlinear radiation of water waves. *Engineering Analysis with Boundary Elements*, 34(5):511 – 529, 2010.

[136] C. Swan, P. H. Taylor, and H. van Langen. Observations of wave-structure interaction for a multi-legged concrete platform. *Applied Ocean Research*, 19(5-6):309 – 327, 1997.

[137] R.H. Swift. Prediction of breaking wave forces on vertical cylinders. *Coastal Engineering*, 13(2):97 – 116, 1989.

[138] H. Söding, J. J. Blok, H. H. Chen, K. Hagiwara, M. Isaacson, J. Jankowski, E. R. Jefferys, J. Mathisen, I. Rask, J-P. Richer, J. U. Römeling, and P. Varsta. Environmental forces of offshore structures: a state-of-the-art review. *Marine Structures*, 3(1):59 – 81, 1990.

[139] C.Z. Wang, G.X. Wu, and K.R. Drake. Interactions between nonlinear water waves and non-wall-sided 3d structures. *Ocean Engineering*, 34(8-9):1182 – 1196, 2007.

[140] Q.X. Wang. Unstructured MEL modelling of nonlinear unsteady ship waves. *Journal of Computational Physics*, 210(1):368 – 385, 2005.

[141] Z. Wang, Q. Zou, and D. Reeve. Simulation of spilling breaking waves using a two phase flow CFD model. *Computers & Fluids*, 38(10):1995 – 2005, 2009.

[142] G.X. Wu and R. Eatock Taylor. The coupled finite element and boundary element analysis of nonlinear interactions between waves and bodies. *Ocean Engineering*, 30(3):387 – 400, 2003.

[143] S. Yan and Q.W. Ma. Numerical simulation of fully nonlinear interaction between steep waves and 2d floating bodies using the QALE-FEM method. *Journal of Computational Physics*, 221(2):666 – 692, 2007.

[144] Y. Yuksel and R. Narayanan. Breaking wave forces on horizontal cylinders close to the sea bed. *Coastal Engineering*, 23(1-2):115 – 133, 1994.

[145] X.T. Zhang, B.C. Khoo, and J. Lou. Application of desingularized approach to water wave propagation over three-dimensional topography. *Ocean Engineering*, 34(10):1449 – 1458, 2007.

PREMIO FIRENZE UNIVERSITY PRESS
TESI DI DOTTORATO

Coppi E., *Purines as Transmitter Molecules. Electrophysiological Studies on Purinergic Signalling in Different Cell Systems*, 2007

Natali I., *The Ur-Portrait.* Stephen Hero *ed il processo di creazione artistica in* A Portrait of the Artist as a Young Man, 2007

Petretto L., *Imprenditore ed Università nello start-up di impresa. Ruoli e relazioni critiche*, 2007

Mannini M., *Molecular Magnetic Materials on Solid Surfaces*, 2007

Bracardi M., *La Materia e lo Spirito. Mario Ridolfi nel paesaggio umbro*, 2007

Bemporad F., *Folding and Aggregation Studies in the Acylphosphatase-Like Family*, 2008

Buono A., *Esercito, istituzioni, territorio. Alloggiamenti militari e «case Herme» nello Stato di Milano (secoli XVI e XVII)*, 2008

Castenasi S., *La finanza di progetto tra interesse pubblico e interessi privati*, 2008

Gabbiani C., *Proteins as Possible Targets for Antitumor Metal Complexes: Biophysical Studies of their Interactions*, 2008

Colica G., *Use of Microorganisms in the Removal of Pollutants from the Wastewater*, 2008

Inzitari M., *Determinants of Mobility Disability in Older Adults: Evidence from Population-Based Epidemiologic Studies*, 2009

Di Carlo P., *I Kalasha del Hindu Kush: ricerche linguistiche e antropologiche*, 2009

Pace R., *Identità e diritti delle donne. Per una cittadinanza di genere nella formazione*, 2009

Macrì F., *Verso un nuovo diritto penale sessuale. Diritto vivente, diritto comparato e prospettive di riforma della disciplina dei reati sessuali in Italia*, 2009

Vignolini S., *Sub-Wavelength Probing and Modification of Complex Photonic Structures*, 2009

Decorosi F., *Studio di ceppi batterici per il biorisanamento di suoli contaminati da Cr(VI)*, 2009

Di Patti F., *Finite-Size Effects in Stochastic Models of Population Dynamics: Applications to Biomedicine and Biology*, 2009

Polito C., *Molecular imaging in Parkinson's disease*, 2010

Fedi M., *«Tuo lumine». L'accademia dei Risvegliati e lo spettacolo a Pistoia tra Sei e Settecento*, 2010

Orsi V., *Crisi e Rigenerazione nella valle dell'Alto Khabur (Siria). La produzione ceramica nel passaggio dal Bronzo Antico al Bronzo Medio*, 2010

Fondi M., *Bioinformatics of genome evolution: from ancestral to modern metabolism. Phylogenomics and comparative genomics to understand microbial evolution*, 2010

Marino E., *An Integrated Nonlinear Wind-Waves Model for Offshore Wind Turbines*, 2010

Romano R., *Smart Skin Envelope. Integrazione architettonica di tecnologie dinamiche e innovative per il risparmio energetico*, 2010

Finito di stampare presso
Grafiche Cappelli Srl – Osmannoro (FI)